Direct Complex Envelope Sampling of Bandpass Signals With M-Channel Blindly Calibrated Time-Interleaved ADCs

By

MANSOOR WAHAB

DISSERTATION

Submitted in partial satisfaction of the requirements for the degree of

DOCTOR OF PHILOSOPHY

in

Electrical and Computer Engineering

in the

OFFICE OF GRADUATE STUDIES

of the

UNIVERSITY OF CALIFORNIA

DAVIS

Approved:

Bernard C. Levy, Chair

Khaled Abdel-Ghaffar

Zhi Ding

Committee in Charge

2023

To my teachers

"Wisdom... comes not from age, but from education and learning."

-Anton Chekhov

Abstract

Direct Complex Envelope Sampling of Bandpass Signals With M-Channel Blindly Calibrated Time-Interleaved ADCs

Classical receiver architectures demodulate a high frequency bandpass signal to baseband before sampling the in-phase and quadrature components. With the advent of high-speed analog-to-digital converters (ADCs) and wide bandwidth sample-and-hold (S/H) circuits, it has become practicable to sample a bandpass signal directly without any demodulation operation and then process it with robust DSP technology. Direct sampling methods do present their own challenges. When a single channel is used to digitize the signal, not all frequencies above the Nyquist rate are allowed and only signals in certain frequency bands can be sampled at this minimum rate. As first shown by Kohlenberg, the restriction on spectral location can be removed with a two-channel time-interleaved ADC (TIADC) where two ADCs separated by a timing skew independently sample the signal.

In this dissertation, we propose a general and flexible technique for sampling the complex envelope of a bandpass signal using a nonuniformly interleaved M-channel TIADC. The bandpass signal is sampled directly by the sub-ADCs, and the overall TIADC sampling frequency is at or slightly above the Nyquist rate. Reconstruction of the complex envelope entails inverting a matrix of filters resulting in some TIADC timing skews being forbidden. The proposed sampling scheme requires the implementation of M digital FIR filters and can be used to digitize bandpass signals with any carrier frequency in software defined radio applications. Reconstruction analysis is provided for the case of two, three, and four channels. Multi-tone and MSK signals are used in simulations to validate the proposed method and assess its performance. Quadrature sampling, a special case of the two-channel TIADC that assumes certain parameter relations, is investigated as an approximation technique.

It is well known that gain and timing skew mismatches can severely degrade TIADC performance. To mitigate the effect of these mismatches on complex envelope reconstruction, we

present a novel blind calibration method which assumes that there exists a frequency band where the complex envelope signal has no power, due for example to oversampling. Mismatches give rise to errors in this band, which are extracted and used to estimate adaptively the gain and timing skew mismatches. Simulations with multi-tone, MSK, and bandlimited white noise signals demonstrate calibration can significantly improve reconstruction performance measured in the mean-square error (MSE) sense. Suggestions for further research are provided.

Acknowledgments

The completion of my doctoral studies would not have been possible without the continuous support of several people. First and foremost, I would like to express my sincere gratitude to Prof. Bernard Levy for serving as my undergraduate and then graduate advisor. Words cannot adequately express my admiration for him as an expert in the field and a mentor. I thank him for the time and energy he has invested in guiding me as a student and helping me become a decent researcher. His teaching and management of courses are one of the best in the department, and I have had the privilege of serving as his teaching assistant during several quarters. I owe my success in undergraduate teaching to him. I will greatly miss our long conversations in his office on various topics ranging from filter design to winemaking.

I have to thank my dissertation committee members Prof. Khaled Abdel-Ghaffar and Prof. Zhi Ding. They have both played a significant role in my education. Prof. Ghaffar has taught me circuits, digital communication, error correction, and much more. Working under him as a teaching assistant, I learned effective ways to teach the challenging subject of probability to undergraduate students. Prof. Ding taught me DSP at the graduate level and had his door open to me anytime I needed advice. His thought-provoking questions have contributed to the quality of the research presented in this dissertation.

I'm forever indebted to my DSP teachers Prof. Alan Oppenheim, Prof. Ronald Schafer, Prof. John Proakis, and Dr. Dimitris Manolakis whose books I have read over and over to master my craft. My knowledge of the field would not be where it is today had it not been for their relentless commitment to signal processing education. I hope to achieve their level of pedagogical success one day.

Finally, I would be remiss if I didn't mention my family who were highly encouraging all throughout my studies even if they didn't understand much of my work. My parents never failed to take care of my basic needs. My two sisters and their husbands made themselves

available whenever I needed them. My adorable nieces eased my worries with their innocence. I thank them all for their unconditional love and support.

Contents

Abstract iii

Acknowledgments v

List of Figures xiii

List of Tables xv

1 Introduction **1**

1.1 Receiver Architectures 1

1.2 Time-Interleaved ADCs 4

1.3 Dissertation Contributions and Organization 6

2 Background Material **9**

2.1 Signal Basics 9

2.2 The Sampling Theorem for Baseband Signals 13

2.3 Multirate Basics 17

2.4 Bandpass Signal Representation 21

2.5 First-Order and Second-Order Bandpass Sampling 23

2.6 Stochastic Optimization 28

3 Complex Envelope Sampling with M-channel Time-Interleaved ADCs **35**

3.1 Complex Envelope Sampling Model 37

3.2 Complex Envelope Reconstruction 44

3.3 Reconstruction for $M = 2, 3, 4$ 53

3.4 Simulations 64

4 Quadrature Sampling and Approximation 85

4.1 Quadrature Sampling and Reconstruction 86

4.2 Simulations 88

5 Blind Calibration of Gain and Timing Mismatches in M-channel Bandpass Sampling Time-Interleaved ADCs 93

5.1 Blind TIADC Calibration Method 95

5.2 Quadratic Approximation of $J(\hat{\boldsymbol{\theta}})$ 106

5.3 Calibration Analysis 123

5.4 Simulations 127

6 Conclusions and Future Work 142

6.1 Suggestions for Further Research 144

A Reconstruction Filters for the Four-Channel TIADC 146

B Impulse Responses of the Gradient Filters for the Two-Channel TIADC 149

C Linearization of Reconstruction Filters around a General Point (g^p, d^p) Close to the True Parameter (g, d) for the Two-Channel TIADC 151

Bibliography 155

List of Figures

1.1 Heterodyne receiver 2

1.2 Homodyne receiver 2

1.3 Direct sampling receiver 3

1.4 Direct interleaved sampling receiver 4

1.5 M-channel time-interleaved ADC 5

2.1 L-fold expander 17

2.2 L-fold decimator/compressor 19

2.3 Magnitude spectrum of a bandpass signal 21

2.4 Forbidden (gray) and allowed (white) sampling frequencies in first-order sampling of bandpass signals 27

3.1 M-th order time-interleaved sampling of bandpass signal $x_c(t)$ 37

3.2 ℓ-th image band 38

3.3 Discrete-time bandpass sampling model. 44

3.4 A mathematical model for recovery of $c^{[L]}(n)$ from $x_0(n), \ldots, x_{M-1}(n)$. 51

3.5 A causal implementation of the reconstruction block diagram in Fig. 3.4 . . . 52

3.6 Reconstruction regions for the four-channel TIADC: a) $\omega_b > 0$, b) $\omega_b < 0$ . . 64

3.7 PSD of signals $x_0(n)$ and $x_1(n)$ for a two-channel TIADC in the presence of additive white noise. 67

3.8 Magnitude responses of FIR filters $\check{H}_0(e^{j\omega})$ and $\check{H}_1(e^{j\omega})$ of order $N = 60$ for the two-channel TIADC. 67
3.9 PSD of the estimated envelope $\hat{c}(n)$ computed with FIR filters of order $N = 60$ for a two-channel TIADC with timing skew $d^0 = 0.425$. 68
3.10 PSD of the estimated envelope $\hat{c}(n)$ computed with FIR filters of order $N = 300$ for a two-channel TIADC with timing skew $d^0 = 0.425$. 69
3.11 PSD of the estimated envelope $\hat{c}(n)$ computed with FIR filters of order $N = 60$ for a two-channel TIADC with timing skew $d = 0.410$ close to a forbidden value. 70
3.12 PSD of the estimated envelope $\hat{c}(n)$ computed with FIR filters of order $N = 60$ for a two-channel TIADC with gain $g - g^0 = 0.01$ and timing $d - d^0 = -0.0025$ mismatches. 71
3.13 MSE in different image bands $1 \leq \ell \leq 20$ computed with filters of order $N = 60$ for a two-channel TIADC with timing skew $d = (\ell + 1/4)/(2\ell)$. . . . 72
3.14 PSD of the estimated envelope $\hat{c}(n)$ computed with FIR filters of order $N = 60$ for a three-channel TIADC with timing skews $d_1^0 = 0.425$ and $d_2^0 = 0.85$. . . . 73
3.15 Magnitude responses of FIR filters $\check{H}_0(e^{j\omega})$,$\check{H}_1(e^{j\omega})$, and $\check{H}_2(e^{j\omega})$ of order $N = 60$ for the three-channel TIADC. 74
3.16 PSD of the estimated envelope $\hat{c}(n)$ computed with FIR filters of order $N = 40$ for a three-channel TIADC with timing skews $d_1^0 = 0.425$ and $d_2^0 = 0.85$. . . . 75
3.17 PSD of the estimated envelope $\hat{c}(n)$ computed with FIR filters of order $N = 60$ for a three-channel TIADC with timing skews $d_1 = 0.41$ and $d_2 = 0.81$ close to forbidden values. 75
3.18 PSD of the estimated envelope $\hat{c}(n)$ computed with FIR filters of order $N = 60$ for a three-channel TIADC with gain $g_1 - g_1^0 = 0.01$, $g_2 - g_2^0 = 0.02$ and timing $d_1 - d_1^0 = -0.0025$, $d_2 - d_2^0 = -0.0050$ mismatches. 76
3.19 Verification of the sampling model in Fig. 3.3 for the four-channel TIADC using a multi-tone complex envelope. 78

3.20 PSD of signals $x_0(n), x_1(n), x_2(n)$, and $x_3(n)$ for a four-channel TIADC in the presence of additive white noise. 79
3.21 Magnitude responses of FIR filters $\check{H}_0(e^{j\omega})$,$\check{H}_1(e^{j\omega})$,$\check{H}_2(e^{j\omega})$, and $\check{H}_3(e^{j\omega})$ of order $N = 80$ for the four-channel TIADC. 79
3.22 PSD of the estimated envelope $\hat{c}^{[2]}(n)$ computed with FIR filters of order $N = 80$ for a four-channel TIADC with timing skews $d_1^0 = 0.375$, $d_2^0 = 0.625$, and $d_3^0 = 0.875$. 80
3.23 PSD of the estimated envelope $\hat{c}^{[2]}(n)$ computed with FIR filters of order $N = 80$ for a four-channel TIADC with gain $g_1 - g_1^0 = 0.01$, $g_2 - g_2^0 = 0.025$, $g_3 - g_3^0 = 0.05$ and timing $d_1 - d_1^0 = -0.0025$, $d_2 - d_2^0 = -0.0050$, $d_3 - d_3^0 = -0.0075$ mismatches. 80
3.24 PSD of the theoretical envelope $c^{[2]}(n)$ of a MSK signal sampled with a four-channel TIADC with timing skews $d_1^0 = 0.375$, $d_2^0 = 0.625$, and $d_3^0 = 0.875$. . 83
3.25 PSD of the estimated MSK envelope $\hat{c}^{[2]}(n)$ computed with filters of order $N = 80$ for a four-channel TIADC with timing skews $d_1^0 = 0.375$, $d_2^0 = 0.625$, and $d_3^0 = 0.875$. 83

4.1 PSD of the estimated envelope $\hat{c}(n)$ for $\varepsilon = \omega_b = 0$ computed with FIR filters of order $N = 16$ for a two-channel TIADC with quadrature timing skew $d^0 = 0.05$. 89
4.2 MSE for the entire range of ε values computed with FIR filters of order $N = 10, 20, 30$ in the case of quadrature timing skew $d^0 = 0.05$. 90
4.3 MSE for $-200\pi < \varepsilon < 200\pi$ computed with FIR filters of order $N = 10, 20, 30$ in the case of quadrature timing skew $d^0 = 0.05$. 91
4.4 MSE for the entire range of ε values computed with FIR filters of order $N = 10, 20, 30$ in the case of quadrature timing skew $d^0 = 0.05$ with 0.10% timing mismatch. 91

5.1 Adaptive reconstruction filter implementation and error signal computation, where $1 \leq i \leq M-1$. 104
5.2 Zoomed in i-th reconstruction and calibration channel from Fig. 5.1 for $1 \leq i \leq M-1$. 105
5.3 Magnitudes of FIR approximation of reconstruction filters $H_{i,l}(e^{j\omega})$ with $i, l = 0, 1$ for a Kaiser window of length $N+1 = 61$ and parameter $\beta = 6$. 128
5.4 Magnitude of bandpass FIR filter H_{BP} obtained by using a window of length 81 and parameter $\beta = 8$. 129
5.5 PSD of the estimated envelope $\hat{c}(n)$ computed with FIR approximations of order $N = 60$ of reconstruction filters H_0 and H_1 for the true TIADC parameters g and d. 130
5.6 PSD of the estimated envelope $\hat{c}(n)$ computed with first order structure of Fig. 5.1 for nominal TIADC parameters $g^0 = 1$, $d^0 = 0.425$ and actual mismatches $\gamma = 0.01$, $\delta = -0.0025$ using filters of order $N = 60$. 130
5.7 Gain mismatch estimates for a four-tone complex input sequence of length $L_s = 5 \times 10^4$ samples, and constant adaptation step sizes $\mu_\gamma = 10^{-3}$ amd $\mu_\delta = 10^{-5}$. 131
5.8 Timing skew mismatch estimates for a four-tone complex input sequence of length $L_s = 5 \times 10^4$ samples, and constant adaptation step sizes $\mu_\gamma = 10^{-3}$ amd $\mu_\delta = 10^{-5}$. 131
5.9 PSD of the estimated envelope $\hat{c}(n)$ before calibration. 132
5.10 PSD of the estimated envelope $\hat{c}(n)$ after calibration with constant adaptation step sizes. 133
5.11 Gain mismatch estimates for a four-tone complex input sequence of length $L_s = 5 \times 10^4$ samples, and time-varying adaptation step sizes $\mu_\gamma(n) = 5/n$ and $\mu_\delta(n) = (2 \times 10^{-3})/n$. 134

5.12 Timing skew mismatch estimates for a four-tone complex input sequence of length $L_s = 5 \times 10^4$ samples, and time-varying adaptation step sizes $\mu_\gamma(n) = 5/n$ and $\mu_\delta(n) = (2 \times 10^{-3})/n$. 134
5.13 PSD of the estimated envelope $\hat{c}(n)$ after calibration with time-varying adaptation step sizes. 135
5.14 PSD of the actual sampled bandlimited white noise complex envelope. 137
5.15 Gain mismatch estimates for a bandlimited white noise complex envelope, with $L_s = 10^5$ samples, and constant adaptation step sizes $\mu_\gamma = 5 \times 10^{-4}$ and $\mu_\delta = 5 \times 10^{-6}$. 137
5.16 Timing skew mismatch estimates for a bandlimited white noise complex envelope, with $L_s = 10^5$ samples, and constant adaptation step sizes $\mu_\gamma = 5 \times 10^{-4}$ and $\mu_\delta = 5 \times 10^{-6}$. 138
5.17 PSD of the sampled bandlimited white noise complex envelope after calibration with constant adaptation step sizes. 138
5.18 PSD of the sampled MSK envelope. 139
5.19 Gain mismatch estimates for MSK complex envelope, with $L_s = 10^5$ samples, and constant adaptation step sizes $\mu_\gamma = 1.2 \times 10^{-3}$ and $\mu_\delta = 0.15 \times 10^{-5}$. . . 140
5.20 Timing skew mismatch estimates for MSK complex envelope, with $L_s = 10^5$ samples, and constant adaptation step sizes $\mu_\gamma = 1.2 \times 10^{-3}$ and $\mu_\delta = 0.15 \times 10^{-5}$. 141
5.21 PSD of the sampled MSK complex envelope after calibration with constant adaptation step sizes. 141

List of Tables

2.1 DTFT Properties 11

3.1 Detailed step-by-step instructions for computing the impulse responses of reconstruction filters $H_0(e^{j\omega}), \ldots, H_{M-1}(e^{j\omega})$. 50

3.2 MSE vs N for a two-channel TIADC with timing skew $d^0 = 0.425$. 69

3.3 MSE for a two-channel TIADC with filters of order $N = 60$ in the presence of gain mismatches ($g^0 = 1$). 71

3.4 MSE for a two-channel TIADC with filters of order $N = 60$ in the presence of timing mismatches ($d^0 = 0.425$). 71

3.5 MSE for a two-channel TIADC with filters of order $N = 60$ in the presence of gain and timing mismatches ($g^0 = 1$, $d^0 = 0.425$). 71

3.6 MSE vs ℓ for a two-channel TIADC with filters of order $N = 60$ and timing skew mismatch $d = (\ell + 1/4)/(2\ell) - 0.0010$. 72

3.7 MSE vs N for the three-channel TIADC with timing skews $d_1^0 = 0.425$ and $d_2^0 = 0.85$. 74

3.8 MSE for the three-channel TIADC with filters of order $N = 60$ in the presence of gain mismatches ($g_1^0 = 1$, $g_2^0 = 1$). 77

3.9 MSE for the three-channel TIADC with filters of order $N = 60$ in the presence of timing mismatches ($d_1^0 = 0.425$, $d_2^0 = 0.85$). 77

3.10 MSE for the three-channel TIADC with filters of order $N = 60$ in the presence of gain and timing mismatches ($g_1^0 = 1$, $g_2^0 = 1$, $d_1^0 = 0.425$, $d_2^0 = 0.85$). . . . 77

3.11 MSE vs N for the four-channel TIADC with timing skews $d_1^0 = 0.375$, $d_2^0 = 0.625$, and $d_3^0 = 0.875$. 79
3.12 MSE for the four-channel TIADC with filters of order $N = 80$ in the presence of gain mismatches ($g_1^0 = 1$, $g_2^0 = 1$, $g_3^0 = 1$). 81
3.13 MSE for the four-channel TIADC with filters of order $N = 80$ in the presence of timing mismatches ($d_1^0 = 0.375$, $d_2^0 = 0.625$, $d_3^0 = 0.875$). 81
3.14 MSE for the four-channel TIADC with filters of order $N = 80$ in the presence of gain and timing mismatches ($g_1^0 = 1$, $g_2^0 = 1$, $g_3^0 = 1$, $d_1^0 = 0.375$, $d_2^0 = 0.625$, $d_3^0 = 0.875$). 81
3.15 MSE vs N for the envelope of a MSK signal sampled with a four-channel TIADC with timing skews $d_1^0 = 0.375$, $d_2^0 = 0.625$, and $d_3^0 = 0.875$. 82
3.16 MSE for the MSK envelope computed with filters of order $N = 80$ in the presence of a four-channel TIADC gain and timing mismatches ($g_1^0 = g_2^0 = g_3^0 = 1$, $d_1^0 = 0.375$, $d_2^0 = 0.625$, $d_3^0 = 0.875$). 84

5.1 The MSE and final estimated mismatches after one and two calibrations (with constant adaptation step sizes) as the image band index ℓ increases. 136
5.2 MSK complex envelope reconstruction performance (MSE) before and after calibration (with constant adaptation step size) for various timing skew mismatches. 141

Chapter 1

Introduction

1.1 Receiver Architectures

Conventional radar or communication receivers typically rely on mixing and filtering operations prior to signal digitization [1]. They downconvert a high frequency bandpass signal to baseband (directly or in stages) and correlate it with two quadrature oscillators to obtain the in-phase and quadrature signal components which are then sampled by two separate analog-to-digital converters (ADCs). Most receivers utilize some variant of a *heterodyne* architecture shown in Fig. 1.1. The RF front-end bandpass filter H_S selects the signal of interest $x_c(t)$ and rejects interference from out-of-band and image band signals. After the signal is downconverted from carrier to an intermediate frequency (IF), it is passed through the filter H_{IF} which reduces distortion and dynamic range requirements simplifying subsequent filtering, amplification, and demodulation [2]. The heterodyne receiver offers great performance in terms of selectivity and sensitivity. However, this is achieved with the use of high Q-factor non-integrable RF and IF filters which increase production costs. Furthermore, IF needs to be carefully selected to provide sufficient image rejection and robust channel selection.

A common alternative is the *homodyne* receiver with the *direct conversion* architecture shown in Fig. 1.2. After $x_c(t)$ is selected by the filter H_S, it is downconverted directly to

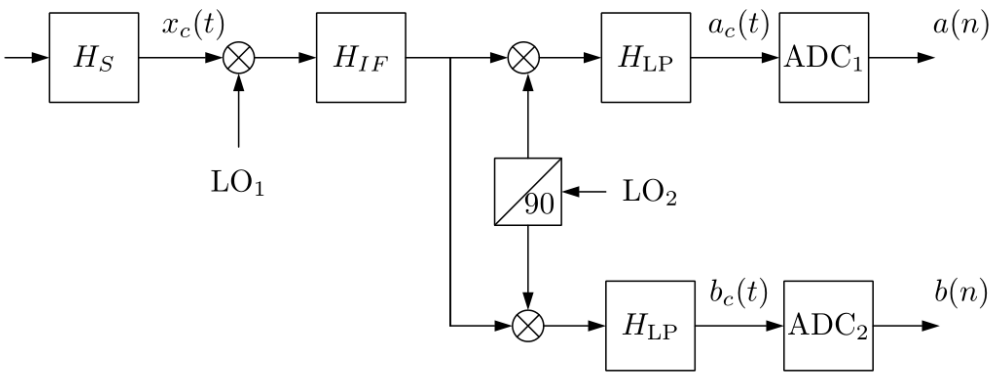


Figure 1.1: Heterodyne receiver

baseband without an IF stage. This allows for a more integrable RF front-end design and reduces the number of discrete components. Despite this significant advantage, homodyne receivers introduce certain problems that are either manageable or entirely absent in heterodyne architectures. LO leakage to the antenna and consequent DC-offsets that arise from self-mixing create in-band interference. Heterodyne receivers address this by eliminating the DC-offsets with the IF filter. Other issues associated with homodyne receivers include I/Q mismatches, sensitivity to even-order distortions, and flicker ($1/f$) noise of devices [3].

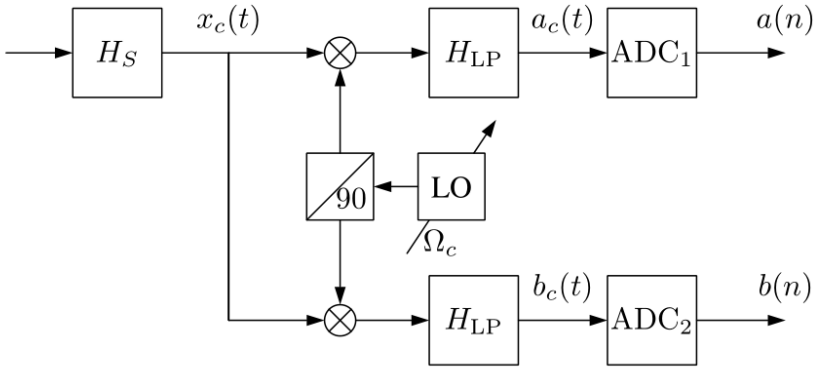


Figure 1.2: Homodyne receiver

The inherent challenges present in conventional receivers motivate a better architecture with fewer analog components. An RF mixer in particular is a non-linear device that intro-

duces intermodulation and harmonic distortion, and can be a considerable source of noise and power loss [4]. With the advent of high-speed ADCs and wide bandwidth sample-and-hold (S/H) circuits [5], *direct sampling* methods have become popular in processing bandpass signals. As shown in Fig. 1.3, $x_c(t)$ can be digitized directly without downconversion which significantly reduces receiver complexity. Here, the filter H_s can be a highly tunable RF MEMS filter as presented in [6–9].

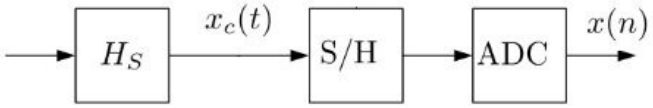


Figure 1.3: Direct sampling receiver

A direct sampling receiver is highly attractive for software radio applications where it is desirable to perform analog to digital conversion as close to the antenna as possible and leave all the heavy processing (filtering, frequency shifting, etc.) to DSP software [10]. Unfortunately, when a single ADC is used in digitization not all sampling frequencies above the Nyquist rate are permissible, where the Nyquist rate is the frequency equaling twice the signal bandwidth [11, 12], [13, Sec. 6.4]. Extra constraints on the sampling frequency are needed to prevent aliasing between the negative and positive spectral images of the bandpass signal. These constraints depend on the location of the frequency band occupied by the bandpass signal. Moreover, only signals in certain frequency bands can be sampled at the Nyquist rate. This creates a significant challenge for software radio receivers since different sampling frequencies need to be selected for signals in different bands, even if they have the same bandwidth. A simple way of overcoming spectral mixing of negative and positive images is to employ Hilbert transform sampling, where two channels are used to sample the signal and its Hilbert transform [14]. This equates to sampling a single analytic signal which only has a positive frequency support with Fourier spectrum the same (up to a scale) as the positive spectrum of the original bandpass signal. Although this approach

works for all sampling frequencies above the Nyquist rate, its main disadvantage is designing a practical analog Hilbert transformer [15].

Kohlenberg [11] was the first to recognize as early as 1953 that the restrictions on the sampling frequency in direct sampling receivers can be removed if instead of a single ADC, two separate ADCs operating with a time skew are used to sample the bandpass signal. This time-interleaved scheme shown in Fig. 1.4 does not require a Hilbert transformer. Each ADC has a sampling rate half of the total sampling frequency. Except for certain values of the timing offset between the sampling times of the ADCs, Kohlenberg showed that a signal in any band can be sampled at the Nyquist rate and then reconstructed via two filters from the two time-interleaved sample sequences.

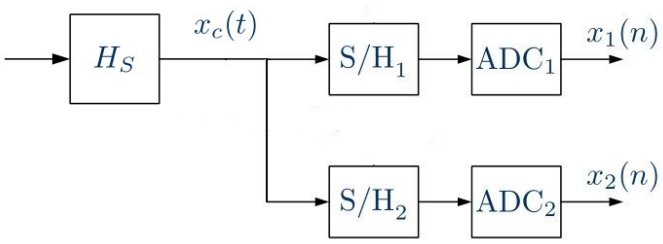


Figure 1.4: Direct interleaved sampling receiver

1.2 Time-Interleaved ADCs

Kohlenberg's second-order sampling is a simple two-channel case of a general M-channel time-interleaved ADC (TIADC) shown in Fig. 1.5. In this architecture first proposed by Black and Hodges [16], M slower converters are stacked in parallel to alternately sample the analog signal $x_c(t)$ and effectively act as a single high-speed ADC. The sampling rate of each sub-ADC is M times lower than that of the whole system and can be below the Nyquist rate. Each channel has its own dedicated S/H circuit that must have a large enough bandwidth for the entire signal. M sequential time-delayed clocks with equal period produce a periodic sampling pattern which can be uniform or nonuniform depending on the chosen

timing offsets between the channels clocks. With a digital multiplexer (MUX), the outputs of the sub-ADCs are combined into a single digital signal $y(n)$ operating at the total sampling frequency which must be above the Nyquist rate to avoid aliasing.

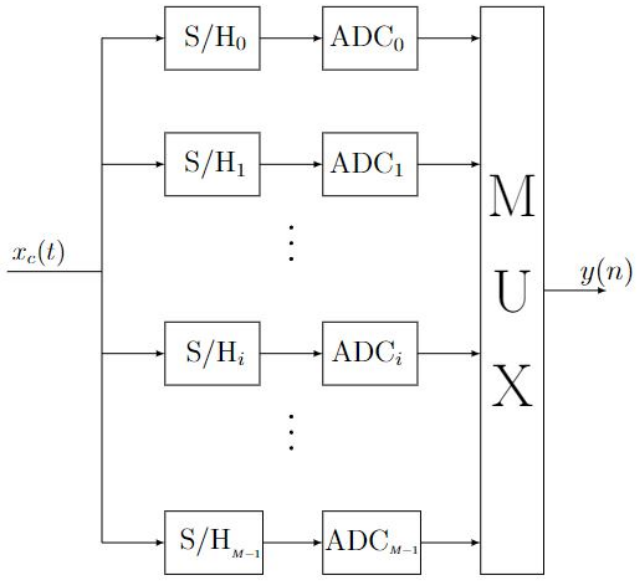


Figure 1.5: M-channel time-interleaved ADC

For high speed and high resolution applications, a TIADC can be a more energy-efficient sampling architecture compared to a single ADC [17, Sec. 1.2]. Unfortunately, mismatch errors arise when several ADCs are interleaved [18]. For maximum performance, it is required that the channels be perfectly matched and that each channel's clock registers a new data sample at the specified instant. Due to hardware imperfections and limitations, however, this is not achievable in practice. There can be DC level offsets between the sub-ADCs which appear in the output signal spectrum as spurious tones at integer multiples of sub-ADC sampling rate. The sub-ADCs can have different gains resulting in gain mismatches. The clocks' sampling instants can be corrupted by skew mismatches and jitter effects which introduce timing mismatches in the TIADC [19]. Clock skew mismatches are deterministic and mostly due to device mismatches or power supply disturbances. Jitter error is random changes on the clock edges mostly due to device noise. Finally, mismatches in bandwidths

of the S/H circuits create bandwidth mismatches between the channels [20]. Gain, timing, and bandwidth mismatches all create unwanted input signal images at integer multiples of sub-ADC sampling rate.

All mismatches are a source of noise and degrade the signal-to-noise-and-distortion ratio (SNDR) in TIADCs. Preliminary spectrum and signal-to-noise ratio (SNR) analysis was performed for timing mismatches in [21, 22] and for offset and gain mismatches in [23]. Explicit formulas for the combined offset, gain, and timing mismatch effects are derived in [24] for $M = 2, 4$. Extensive SNDR derivations are provided in [25] for the general M-channel case with arbitrary offset, gain, and timing mismatches. All these results except for [23] are limited to sinusoidal narrow-band inputs. For wide-band wide-sense stationary (WSS) and wise-sense cyclostationary (WSCS) signals, the SNR under timing mismatches is derived in terms of second-order statistics in [26]. Finally, for a general deterministic bandlimited input the SNR formula is given in [27] as a function of the signal bandwidth for a two-channel TIADC with timing mismatches.

Correction of mismatches can be performed via TIADC calibration. Offset errors can be corrected entirely in hardware [28], or alternatively via more clever calibration techniques based on the least-mean square (LMS) algorithm [29, 30] or random chopper sampling [31]. Correction of gain, timing, and bandwidth mismatches is generally more nuanced. These mismatches can be calibrated in the analog domain [29] or digitally with robust signal processing algorithms [32–35]. The field of TIADC calibration has seen tremendous growth in the past two decades, and some major results are mentioned in Chapter 5 of this dissertation.

1.3 Dissertation Contributions and Organization

In this dissertation, we propose a novel and flexible direct sampling and reconstruction scheme for the complex envelope of a bandpass signal using a blindly calibrated M-channel TIADC. Sampling is performed at or slightly above the Nyquist rate for all signals indepen-

dent of the location of their frequency band. Reconstruction is all digital and requires the implementation of M generally complex-valued digital FIR filters and a digital modulator. Unlike previous publications on bandpass sampling using TIADCs, our universal method reconstructs the sampled complex envelope of the bandpass signal instead of the analog bandpass signal itself and so it combines sampling and demodulation into one joint algorithm. A fully blind calibration technique that requires small oversampling is proposed to correct gain and timing mismatches of the TIADC which can severely degrade reconstruction performance. To the best knowledge of the author, this dissertation is the *first* to provide a *complete and rigorous* treatment for blind calibration of a nonuniform M-channel bandpass sampling TIADC.

The main contributions of this dissertation are Chapters 3, 4, and 5. The rest of the dissertation is organized as follows. In Chapter 2, we review pertinent background material that is needed for later chapters. This includes the Fourier transform, baseband sampling, multirate sampling, first-order and second-order bandpass sampling, and finally stochastic optimization. Chapter 3 introduces the complex envelope sampling and reconstruction models for the general M-channel case and provides reconstructions details for $M = 2, 3, 4$. Numerous simulations with multi-tone and MSK signals are used validate the models and analyze the method performance. Chapter 4 examines a special case of $M = 2$ known as quadrature sampling which we demonstrate can function as a robust approximation technique. Chapter 5 starts with a brief literature overview of calibration techniques and then describes in detail the novel blind gain and timing mismatch calibration algorithm for a M-channel TIADC. Extensive simulations with three different types of signals are used to reinforce the theory behind the calibration method. It is assumed that offset errors have already been corrected, and we do not consider bandwidth mismatch correction [36–41] since bandwidth mismatches usually play a secondary role to gain and timing mismatches. Chapter 6 draws conclusions and points to directions for further research.

Our notation generally follows the signal processing notation used in [42] with slight

modifications when needed/desired. New notation is explained in the text when introduced. Boldface letters are used for vectors and matrices.

Chapter 2

Background Material

2.1 Signal Basics

Definitions

Since this dissertation deals primarily with processing of signals, it is useful to start with the definition of a signal. Defined rigorously, a 1-D signal x is mapping of the form

$$x : D \to \mathbb{F}, \tag{2.1}$$

where $\mathbb{F} = \mathbb{R}$ or $\mathbb{C}$ is the field of real or complex numbers, and $D = \mathbb{R}$ if the signal is continuous in time or $D = \mathbb{Z}$ (the set of all integers) if the signal is discrete in time. For the sake of simplicity, we adopt the standard signal processing notation for signals:

$$\begin{aligned} x_c(t) : &\quad \text{a continuous-time signal for } t \in \mathbb{R} \\ x(n) : &\quad \text{a discrete-time signal for } n \in \mathbb{Z}. \end{aligned}$$

The signals $x_c(t)$ and $x(n)$ can real or complex. Throughout the dissertation, we refer to $x_c(t)$ as an analog signal and $x(n)$ as a digital signal.

The Fourier Transform

Let the L^1-norm of $x_c(t)$ be defined as

$$\|x_c\|_1 := \int_{-\infty}^{\infty} |x_c(t)| dt \,, \tag{2.2}$$

and $L^1(\mathbb{R}) := \{x_c \,:\, \|x_c\|_1 < \infty\}$ be the space of all signals $x_c(t)$ with finite L^1-norm. Then for any $x_c \in L^1(\mathbb{R})$, the continuous-time Fourier transform (CTFT) [43, 44] is defined by

$$X_c(j\Omega) = \int_{-\infty}^{\infty} x_c(t) e^{-j\Omega t} dt, \tag{2.3}$$

where $\Omega \in \mathbb{R}$ is the angular frequency and $j = \sqrt{-1}$. The function $X_c(j\Omega)$ is generally complex-valued and describes the *frequency* content of $x_c(t)$. If $X_c(j\Omega) \in L^1(\mathbb{R})$, the inverse transform

$$x_c(t) = \frac{1}{2\pi} \int_{-\infty}^{\infty} X_c(j\Omega) e^{j\Omega t} d\Omega \tag{2.4}$$

recovers the time-domain signal $x_c(t)$ from its frequency-domain representation. In compact form, the relationship is written as

$$x_c(t) \overset{\mathcal{FT}}{\longleftrightarrow} X_c(j\Omega),$$

where $\mathcal{FT}$ stands for the Fourier transform.

For a discrete-time signal $x(n)$ in the Banach space $\ell^1(\mathbb{Z}) = \{x \,:\, \|x\|_1 < \infty\}$ equipped with the norm

$$\|x\|_1 := \sum_{n \in \mathbb{Z}} |x(n)| \,, \tag{2.5}$$

the discrete-time Fourier transform (DTFT) is defined as

$$X(e^{j\omega}) = \sum_{n \in \mathbb{Z}} x(n) e^{-j\omega n} \,, \tag{2.6}$$

where ω is a continuous variable representing angular frequency. Since $X(e^{j\omega}) = X(e^{j(\omega+2\pi k)})$ for all $k \in \mathbb{Z}$, it suffices to analyze $X(e^{j\omega})$ over a band of length 2π. The convenient choice is the interval $[-\pi, \pi)$. The complex-valued $X(e^{j\omega})$ can be written in polar form

$$X(e^{j\omega}) = |X(e^{j\omega})|e^{j\angle X(e^{j\omega})} \tag{2.7}$$

with $|X(e^{j\omega})|$ representing the magnitude and $\angle X(e^{j\omega})$ the phase. Given $X(e^{j\omega}) \in L^1[-\pi, \pi]$, we can construct the original signal $x(n)$ through the inverse discrete-time Fourier Transform (IDTFT)

$$x(n) = \frac{1}{2\pi} \int_{-\pi}^{\pi} X(e^{j\omega}) e^{j\omega n} d\omega \,. \tag{2.8}$$

The relationship can be expressed compactly as

$$x(n) \overset{\mathcal{FT}}{\longleftrightarrow} X(e^{j\omega}) \,.$$

Table 2.1 shows selected DTFT properties that are used in this dissertation. The proofs for these properties are quite straightforward and can be found in [42, Sec. 2.9]. The symbol $*$ denotes the convolution operator, X^* denotes complex conjugation of X, and $\Re\{\cdot\}$ stands for the real part.

Signal $x(n)$, $y(n)$	DTFT $X(e^{j\omega})$, $Y(e^{j\omega})$
$ax(n) + by(n), \quad a, b \in \mathbb{R}$	$aX(e^{j\omega}) + bY(e^{j\omega})$
$x(n-d), \quad d \in \mathbb{R}$	$X(e^{j\omega})e^{-j\omega d}$
$x(n)e^{j\omega_0 n}, \quad \omega_0 \in \mathbb{R} \mod 2\pi$	$X(e^{j(\omega-\omega_0)})$
$x(n) * y(n)$	$X(e^{j\omega})Y(e^{j\omega})$
$\Re\{x(n)\}$	$\frac{1}{2}[X(e^{j\omega}) + X^*(e^{-j\omega})]$

Table 2.1: DTFT Properties

It is important to note that $x_c \in L^1(\mathbb{R})$ and $x \in \ell^1(\mathbb{Z})$ are sufficient but not necessary for the existence of $X_c(j\Omega)$ and $X(e^{j\omega})$, respectively. For example, the signal $x(n) = \sin(\omega_c n)/(\pi n)$ for $0 < \omega_c < \pi$, belongs to the Hilbert space $\ell^2(\mathbb{Z}) = \{x : \sum_{n\in\mathbb{Z}} |x(n)|^2 < \infty\}$ and not $\ell^1(\mathbb{Z})$ but still has a Fourier transform which is a boxcar function centered at zero (a lowpass filter with cutoff frequency ω_c). In this case, the equality in (2.6) is meant in the sense of mean-square convergence [44]. It is possible to define the Fourier transform for more generalized signals [45] that do not belong to either ℓ^1 or ℓ^2 such as $x(n) = e^{j\omega_0 n}$ for some $\omega_0 \in \mathbb{R} \mod 2\pi$. This signal has DTFT $X(e^{j\omega}) = 2\pi\delta(\omega - \omega_0)$ for $\omega \in [-\pi, \pi)$, where $\delta(\omega)$ is the Dirac function, which can be easily verified with the inverse transform (2.8) using Dirac function properties. In this dissertation, we assume all signals have Fourier transforms and do not concern ourselves with the exact nature of Fourier transform existence.

Linear Time-Invariant Systems

The output $y(n)$ of a discrete single-input single-output (SISO) linear system to an input $x(n)$ can be written as

$$y(n) = \sum_{k=-\infty}^{\infty} h(n,k)x(k), \tag{2.9}$$

where $h(n,k)$ is the time-varying system impulse response denoting the response at time n to an impulse applied at time k. With the additional assumption of time invariance, the input-output relationship reduces to a convolution operation

$$y(n) = \sum_{k=-\infty}^{\infty} h(n-k)x(k) = \sum_{k=-\infty}^{\infty} h(k)x(n-k) = x(n) * h(n)\,, \tag{2.10}$$

where the second equality can be shown with a simple change of variable. In frequency domain, the output is

$$Y(e^{j\omega}) = X(e^{j\omega})H(e^{j\omega}) \tag{2.11}$$

which follows directly from property four in Table 2.1.

2.2 The Sampling Theorem for Baseband Signals

In many applications, the discrete-time signal $x(n)$ originates from an analog signal $x_c(t)$ via a process called sampling. The sampling theorem has its roots in the works of Whittaker [46], Nyquist [47], Kotel'nikov [48], Raabe [49], Shannon [50], and Someya [51] and is one of the most important discoveries of the 20th century. Although it is often credited to electrical engineers Harry Nyquist and Claude Shannon, a strong case is made by the German mathematician and harmonic analysis specialist Paul Butzer that the Japanese scientist Kinnosuke Ogura was the first to establish the result in [52] which remained mostly unknown outside of Japan until 1992 [53]. Using complex analysis, Butzer et al. [54] have rigorously proven that Ogura's first theorem in [52] is equivalent to the classical reconstruction from samples formula found in DSP textbooks.

In simplest terms, the sampling theorem states that a bandlimited baseband finite energy analog signal is *entirely* and *uniquely* represented by its samples taken at a rate at least twice the signal bandwidth. We now demonstrate this mathematically following closely the analysis presented in [42, Chap. 4]. Given a sampling period T_s, the digital signal $x(n)$ can be related to the analog signal $x_c(t)$ in time domain as

$$x(n) = x_c(nT_s), \quad n \in \mathbb{Z}. \tag{2.12}$$

Establishing the relationship in frequency domain is straightforward but requires some work. Let

$$x_s(t) = x_c(t) \cdot \sum_{n\in\mathbb{Z}} \delta(t - nT_s) = \sum_{n\in\mathbb{Z}} x_c(nT_s)\delta(t - nT_s) = \sum_{n\in\mathbb{Z}} x(n)\delta(t - nT_s) \tag{2.13}$$

be a continuous periodic signal that is equal to $x_c(t)$ at $nT_s, \forall n \in \mathbb{Z}$ and is zero elsewhere. The digital signal $x(n)$ can be considered a time normalized version of $x_s(t)$ with mapping: $nT_s \to n$. From (2.13), we have

$$X_s(j\Omega) = \sum_{n\in\mathbb{Z}} x(n)e^{-j\Omega nT_s} = X(e^{j\omega})\big|_{\omega=\Omega T_s} = X(e^{j\Omega T_s}), \tag{2.14}$$

where $e^{-j\Omega nT_s}$ is the CTFT of $\delta(t - nT_s)$, and the second equality follows directly from (2.6). $X_s(j\Omega)$ can also be expressed in terms $X_c(j\Omega)$ by recalling that multiplication in time domain is equivalent to convolution in frequency domain with a scaling factor. Using the fact

$$\sum_{n\in\mathbb{Z}} \delta(t - nT_s) \xleftrightarrow{\mathcal{FT}} \Omega_s \sum_{k\in\mathbb{Z}} \delta(\Omega - k\Omega_s), \tag{2.15}$$

where $\Omega_s = 2\pi/T_s$ is called the sampling frequency, we have

$$\begin{aligned} X_s(j\Omega) &= \frac{1}{2\pi}\big[X_c(j\Omega) * \Omega_s \sum_{k\in\mathbb{Z}} \delta(\Omega - k\Omega_s)\big] \\ &= \frac{1}{T_s}\sum_{k\in\mathbb{Z}} X_c\big(j(\Omega - k\Omega_s)\big). \end{aligned} \tag{2.16}$$

From (2.14) and (2.16), it becomes evident that

$$X(e^{j\omega}) = \frac{1}{T_s}\sum_{k\in\mathbb{Z}} X_c\big(j(\frac{\omega}{T_s} - k\frac{2\pi}{T_s})\big) \tag{2.17}$$

consists of an infinite number of amplitude and frequency scaled copies of $X_c(j\Omega)$ shifted by 2π. We are now ready to state and prove the sampling theorem, but first need a few simple definitions.

Definition 1. $L^2(\mathbb{R}) := \{x_c \ : \ \int_{\mathbb{R}} |x_c(t)|^2 dt < \infty\}$ *is the space of finite energy analog signals.*

Definition 2. $\mathcal{BL}_{B/2}(\mathbb{R}) := \{x_c \in L^2(\mathbb{R}) \ : \ X_c(j\Omega) = 0 \ \forall \ |\Omega| > \frac{B}{2}\}$ *is the space of finite energy analog signals bandlimited to frequency $B/2$ (the signal bandwidth).*

Theorem 1. *Let $x_c(t) \in \mathcal{BL}_{B/2}(\mathbb{R}) \subset L^2(\mathbb{R})$. If $T_s \leq 2\pi/B$, then $x_c(t)$ is completely*

determined by its samples at $t = nT_s, n \in \mathbb{Z}$ *and can be constructed* $\forall t$ *via interpolation*

$$x_c(t) = \sum_{n\in\mathbb{Z}} x(n) \frac{\sin(\frac{\pi}{T_s}(t - nT_s)}{\frac{\pi}{T_s}(t - nT_s)}. \tag{2.18}$$

Proof. The key is to carefully analyze the spectrum of the signal $x_s(t)$ in equation (2.16). Since $x_c(t) \in \mathcal{BL}_{B/2}(\mathbb{R})$, its k-th frequency shifted copy $X_c(j(\Omega - k\Omega_s))$ has a nonzero frequency support only on the interval $I_k = [-B/2 + |k|\Omega_s\,, B/2 + |k|\Omega_s\,]$. If $\Omega_s \geq B$ (or equivalently $T_s \leq 2\pi/B$), then

$$\bigcap_{k\in\mathbb{Z}} I_k = \emptyset$$

ignoring boundary points, and the desired copy $X_c(j\Omega)$ on I_0 can be obtained with simple windowing

$$X_c(j\Omega) = X_s(j\Omega) \cdot H(j\Omega), \tag{2.19}$$

where

$$H(j\Omega) = \begin{cases} T_s & |\Omega| \leq \Omega_{co} = \frac{\Omega_s}{2} = \frac{\pi}{T_s} \\ 0 & \text{otherwise} \end{cases} \tag{2.20}$$

is a lowpass filter with gain T_s and cutoff frequency $\Omega_{co} = \pi/T_s$ that satisfies $B/2 \leq \Omega_{co} \leq \Omega_s - B/2$. The filter impulse response is

$$h(t) = T_s \frac{\sin(\Omega_{co}t)}{\pi t} = \frac{\sin(\frac{\pi}{T_s}t)}{\frac{\pi}{T_s}t}\,. \tag{2.21}$$

Converting expression (2.19) to time domain, we have

$$x_c(t) = x_s(t) * h(t) = \sum_{n\in\mathbb{Z}} x(n)h(t - nT_s) \tag{2.22}$$

which simplifies to (2.18) after substituting (2.21) for $h(t)$. □

The interpolator $h(t)$ has the properties: i) $h(0) = 1$, ii) $h(nT_s) = 0$, for $n = \pm1, \pm2, \ldots$,

which ensure that the constructed signal in (2.18) equals to $x(n)$ at sampling times nT_s. The minimum acceptable sampling frequency $\Omega_s = B$ equaling twice the signal bandwidth is referred to as the Nyquist rate. If $\Omega_s < B$, then $\bigcap_{k\in\mathbb{Z}} I_k \neq \emptyset$ and the spectral copies $X_c(j(\Omega - k\Omega_s))$ overlap causing *aliasing*. Recovering $x_c(t)$ via interpolation may still be possible but only for low frequencies. In general, aliasing has catastrophic consequences since it can result in a reconstructed signal fundamentally different from the original.

At the maximum alias-free sampling period $T_s = 2\pi/B$ corresponding to the Nyquist rate, an alternative interpretation of the sampling theorem involves recognizing that the orthonormal set $\{\psi_n(t)\}_{n\in\mathbb{Z}}$, i.e.,

$$< \psi_n(t), \psi_m(t) > = \int_{\mathbb{R}} \psi_n(t)\psi_m(t)dt = \delta(n-m), \tag{2.23}$$

where $\psi_n(t) = (1/\sqrt{T_s})h(t-nT_s)$, forms an orthonormal basis (ONB) for the space $\mathcal{BL}_{B/2}(\mathbb{R})$ [55, Sec. 2.4]. The interpolation equation (2.18) then simply represents the series expansion of $x_c(t)$ with coefficients

$$< x_c(t), \psi_n(t) >= \int_{\mathbb{R}} x_c(t)\psi_n(t)dt = \sqrt{T_s}\, x(n)\,. \tag{2.24}$$

The analysis leading up to Theorem 1 was performed with a single ADC sampling $x_c(t)$ to produce the digital representation $x(n)$. It can be extended to second-order sampling where a two-channel TIADC takes samples at times $t = nT_s'$ and $t = (n+d)T_s'$ for some $0 < d < 1$. Here, $T_s' = (2\pi)/\Omega_s'$ is the sampling period of each sub-ADC, and the overall sampling frequency $\Omega_s = 2\Omega_s'$ is required to satisfy the sampling theorem ($\Omega_s \geq B$). As derived in detail in [14], a lowpass filter is used in each channel to interpolate its samples, and the resulting signals from the two channels are added to reconstruct the original analog signal. The use of two slower ADCs instead of a single ADC with twice as high sampling frequency can be advantageous for sampling wide-band signals with a large bandwidth.

Generalizations and various extensions of the sampling theorem are discussed in [56–59].

2.3 Multirate Basics

In many signal processing applications it is desirable to change the sampling rate of a digital signal $x(n) = x_c(nT_s)$ to a new sampling frequency $\widehat{\Omega}_s = 2\pi/\widehat{T}_s$, i.e., we wish to obtain a new sequence

$$\widehat{x}(n) = x_c(n\widehat{T}_s). \tag{2.25}$$

In theory, this can be accomplished by reconstructing $x_c(t)$ from $x(n)$ using (2.18) and then sampling it with the new period $\widehat{T}_s$. However, going back to the analog domain is unnecessary since resampling can be accomplished entirely in the digital domain with the use of two well-known multirate blocks (expander and decimator). An in-depth treatment of multirate systems is provided in [60]. Here, we only cover the two basic blocks that play a crucial role in the development of the sampling and reconstruction models presented in Chapter 3.

If $\widehat{T}_s < T_s$, then the net effect is an increase in the sampling rate. We explore this case first. Suppose we wish to increase the sampling frequency by an integer factor $L > 1$, i.e., it is desired to have $\widehat{T}_s = T_s/L$ and hence $\widehat{x}(n) = x_c(nT_s/L)$. This can be accomplished by cascading an *L-fold expander* shown in Fig. 2.1 with a lowpass filter with gain L and cutoff frequency π/L. The expander inserts $L-1$ zeros between each sample of $x(n)$, and the low pass filter acts as an interpolator assigning new values to these zeros. The output of the expander in time domain can be expressed as

$$x_e(n) = \sum_{k\in\mathbb{Z}} x(k)\delta(n-kL) = \begin{cases} x(n/L) & n \text{ is integer-multiple of } L \\ 0 & \text{otherwise}, \end{cases} \tag{2.26}$$

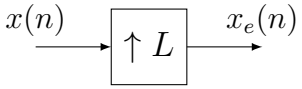


Figure 2.1: L-fold expander

and in compact form, we write

$$x_e(n) = x(n)\big|_{\uparrow L} \,. \tag{2.27}$$

In frequency domain, the spectrum is compressed by a factor of L changing the period from 2π to $2\pi/L$.

Proof. This follows directly from the definition of DTFT (2.6).

$$\begin{aligned} X_e(e^{j\omega}) &= \sum_{n\in\mathbb{Z}}\sum_{k\in\mathbb{Z}} x(k)\delta(n-kL)e^{-j\omega n} \\ &= \sum_{k\in\mathbb{Z}} x(k)e^{-j\omega kL} \underbrace{\sum_{n\in\mathbb{Z}} \delta(n-kL)}_{1} \\ &= X(e^{j\omega L}). \end{aligned} \tag{2.28}$$

□

The digital low pass filter

$$h(n) = L\frac{\sin(\frac{\pi n}{L})}{\pi n} = \frac{\sin(\frac{\pi n}{L})}{\frac{\pi n}{L}} \tag{2.29}$$

needed after the expander to generate the desired signal $\widehat{x}(n) = x_c(nT_s/L)$ changes the spectrum periodicity back to 2π as required for the Fourier transform a digital signal.

If $\widehat{T}_s = LT_s > T_s$ for integer $L > 1$, then the net effect is a decrease in the sampling rate resulting in a new signal $\widehat{x}(n) = x_c(nLT_s)$. The process of reducing the sampling rate of a digital signal is referred to as downsampling. It can be accomplished via an *L-fold decimator* shown in Fig. 2.2 with the time domain relationship $x_d(n) = x(nL)$ which indicates that the decimator compresses $x(n)$ by only retaining its samples that are integer-multiple of L. We use the compact form

$$x_d(n) = x(n)\big|_{\downarrow L} \tag{2.30}$$

whenever convenient. In frequency domain, the spectrum of the decimated signal $x_d(n)$ consists of L frequency stretched and shifted copies of $X(e^{j\omega})/L$.

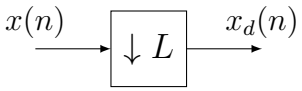


Figure 2.2: L-fold decimator/compressor

Proof. Let $s_L(n) = \sum_{k\in\mathbb{Z}} \delta(n - kL)$ be a digital L-periodic impulse train, and consider the signal

$$z(n) = x(n) \cdot s_L(n) = \sum_{k\in\mathbb{Z}} x(kL)\delta(n - kL) = \sum_{k\in\mathbb{Z}} x_d(k)\delta(n - kL) \tag{2.31}$$

with Fourier transform

$$Z(e^{j\omega}) = \sum_{k\in\mathbb{Z}} x_d(k)e^{-j\omega kL} = X_d(e^{j\omega L})\,. \tag{2.32}$$

Equivalently, $X_d(e^{j\omega}) = Z(e^{j\frac{\omega}{L}})$. From (2.31), it follows that

$$Z(e^{j\omega}) = \frac{1}{2\pi} X(e^{j\omega}) \circledast S_L(e^{j\omega}), \tag{2.33}$$

where $\circledast$ denotes circular convolution and

$$S_L(e^{j\omega}) = \frac{2\pi}{L} \sum_{k=0}^{L-1} \delta(\omega - k\frac{2\pi}{L}) \tag{2.34}$$

is the DTFT of $s_L(n)$. Using (2.34) inside (2.33) leads to

$$Z(e^{j\omega}) = \frac{1}{L} \sum_{k=0}^{L-1} X(e^{j(\omega - \frac{2\pi}{L}k)})\,. \tag{2.35}$$

Finally, applying the relationship derived in (2.32), we have

$$X_d(e^{j\omega}) = \frac{1}{L} \sum_{k=0}^{L-1} X(e^{j(\frac{\omega}{L} - \frac{2\pi}{L}k)}) \tag{2.36}$$

which is periodic with 2π. □

Since downsampling involves throwing away samples, it can result in aliasing if too many samples are discarded. A large downsampling factor L can cause $X(e^{j\frac{\omega}{L}})$ and its 2π-shifted copies to occupy a band of width larger than 2π and hence overlap. A common remedy is to lowpass filter the signal $x(n)$ to frequency π/L prior to decimation. This ensures spectral copies are contained entirely in intervals of length 2π and do not alias with each other. The downside of this prefiltering is that possibly important frequency information in the range $\pi/L < \omega < \pi$ is lost.

In all the above derivations L was assumed to be an integer. It is, however, possible to increase or decrease the sampling rate of a digital signal by a non-integer rational factor. This generally requires putting $x(n)$ through an all digital system consisting of an expander, a lowpass filter, and a decimator [42, Sec. 4.6]. If it is desired to change the sampling frequency from Ω_s to a new frequency $\widehat{\Omega}_s = (L_1/L_2)\Omega_s$, then the expander needs be assigned the integer factor L_1 and the decimator the integer factor L_2. The lowpass filter has gain L_1 and cutoff frequency $\omega_c = \min(\pi/L_1, \pi/L_2)$. If $L_1 > L_2$, there is an increase in the sampling rate, and otherwise a decrease if $L_2 > L_1$. A practical problem arises when the values of L_1 and L_2 are large. It becomes difficult to implement a lowpass filter with a very small bandwidth. Fortunately, a multistage implementation [61] can be employed where the expander and decimator factors are decomposed as

$$\begin{aligned} L_1 &= \prod_{i=1}^{S} L_{1,i} \\ L_2 &= \prod_{i=1}^{S} L_{2,i} \,, \end{aligned} \tag{2.37}$$

where $L_{1,i}$ and $L_{2,i}$ are much smaller integers and S is the number of stages. The i-th stage is comprised of an expander with factor $L_{1,i}$, a lowpass filter with gain $L_{1,i}$ and cutoff frequency $\omega_{c_i} = \min(\pi/L_{1,i}\,, \pi/L_{2,i})$, and a decimator with factor $L_{2,i}$. The S stages are cascaded and effectively act a single system changing the sampling rate by the desired factor L_1/L_2.

Although not always common, it is useful to adopt a notation that distinguishes between

digital signals with different sampling rates. If $x(n) = x_c(nT_s)$, then the notation

$$x^{[L]}(n) = x_c(n\frac{T_s}{L}) \tag{2.38}$$

with integer $L \geq 2$ can be used to denote a new signal with a sampling rate L times higher than that of $x(n)$. We make use of this notation throughout Chapters 3 and 5.

2.4 Bandpass Signal Representation

A real signal $x_c(t)$ is called a bandpass signal if its Fourier transform $X_c(j\Omega) \neq 0$ only for $\Omega \in \Omega_+ \cup \Omega_-$, where $\Omega_+ = [\Omega_L, \Omega_H]$ is called the positive frequency band and $\Omega_- = [-\Omega_H, -\Omega_L]$ the negative frequency band. For an amplitude modulated signal with bandwidth B and carrier frequency Ω_c , $\Omega_L = \Omega_c - B/2$, $\Omega_H = \Omega_c + B/2$, and $\Omega_H - \Omega_L = B$. An example of the Fourier magnitude spectrum of a bandpass signal is shown in Fig. 2.3. Our goal in this section is to derive various time domain representations for the bandpass signal $x_c(t)$.

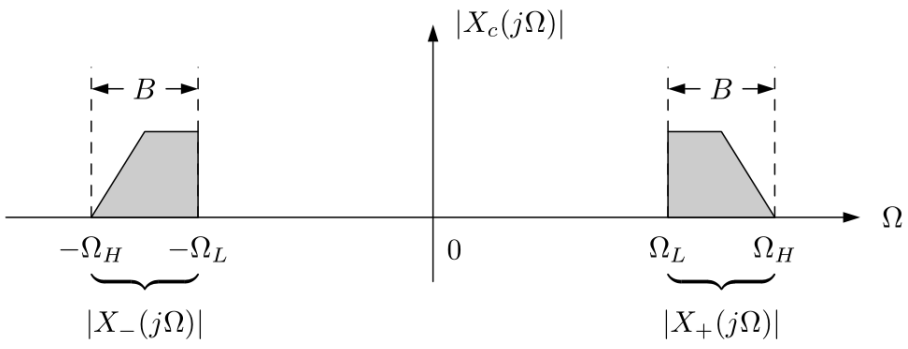


Figure 2.3: Magnitude spectrum of a bandpass signal

We start with the simple fact that for a real $x_c(t)$, its Fourier transform satisfies

$$X_c(-j\Omega) = X_c^*(j\Omega), \tag{2.39}$$

which implies that knowledge of $X_c(j\Omega)$ on Ω_+ alone is sufficient. Recalling the inverse

Fourier transform equation (2.4), we have

$$\begin{aligned} x_c(t) &= \frac{1}{2\pi}\int_{-\infty}^{\infty} X_c(j\Omega)e^{j\Omega t}d\Omega \\ &= \frac{1}{2\pi}\Big[\int_{-\infty}^{0} X_c(j\Omega)e^{j\Omega t}d\Omega + \int_{0}^{\infty} X_c(j\Omega)e^{j\Omega t}d\Omega\Big] \\ &= \frac{1}{2\pi}\Big[\int_{0}^{\infty} X_c(-j\Omega)e^{-j\Omega t}d\Omega + \int_{0}^{\infty} X_c(j\Omega)e^{j\Omega t}d\Omega\Big] \\ &= \frac{1}{2\pi}\Big[\int_{0}^{\infty} X_c^*(j\Omega)e^{-j\Omega t}d\Omega + \int_{0}^{\infty} X_c(j\Omega)e^{j\Omega t}d\Omega\Big] \\ &= \Re\left\{\frac{1}{2\pi}\int_{0}^{\infty} 2X_c(j\Omega)e^{j\Omega t}d\Omega\right\} \\ &= \Re\{x_c^a(t)\}, \end{aligned} \tag{2.40}$$

where the third equality comes from a change of variables, the fourth equality is a consequence of (2.39), and the fifth equality stems from the identity $a + a^* = 2\Re\{a\}$ for $a \in \mathbb{C}$. The signal

$$x_c^a(t) = \frac{1}{2\pi}\int_{0}^{\infty} 2X_c(j\Omega)e^{j\Omega t}d\Omega \tag{2.41}$$

is called the *analytic signal* of $x_c(t)$ whose Fourier transform can be expressed as

$$X_c^a(j\Omega) = \begin{cases} 2X_c(j\Omega) & \Omega \geq 0 \\ 0 & \Omega < 0 \end{cases} = 2X_c(j\Omega)\cdot U(\Omega), \tag{2.42}$$

where

$$U(\Omega) = \begin{cases} 1 & \Omega \geq 0 \\ 0 & \Omega < 0 \end{cases} \tag{2.43}$$

is the unit step function. Applying the inverse Fourier transform to both sides of (2.42), we obtain the time domain relationship

$$x_c^a(t) = 2x_c(t) * \big[\frac{1}{2}\delta(t) + \frac{j}{2\pi t}\big] = x_c(t) + jx_c(t) * \frac{1}{\pi t} = x_c(t) + j\widehat{x}_c(t), \tag{2.44}$$

where $\widehat{x}_c(t)$ is the Hilbert transform [62] of $x_c(t)$. Since $X_c^a(j\Omega) \neq 0$ only for $\Omega \in \Omega_+$, it can be frequency shifted to baseband to generate the signal bandlimited to frequency $B/2$,

$$c_c(t) = x_c^a(t)e^{-j\Omega_c t} \tag{2.45}$$

which is referred to as the *complex envelope* of $x_c(t)$. From (2.40) and (2.45) follows the most common bandpass signal representation

$$x_c(t) = \Re\{c_c(t)e^{j\Omega_c t}\}. \tag{2.46}$$

Letting $c_c(t) = a_c(t)+jb_c(t)$, where $a_c(t)$ and $b_c(t)$ are also bandlimited to $B/2$, the expression (2.46) can be simplified to contain only real sinusoidal functions

$$\begin{aligned} x_c(t) &= a_c(t)\cos(\Omega_c t) - b_c(t)\sin(\Omega_c t) \\ &= |c_c(t)|\cos(\Omega_c t + \angle c_c(t))\,, \end{aligned} \tag{2.47}$$

where $|c_c(t)| = \sqrt{a_c^2(t) + b_c^2(t)}$ and $\angle c_c(t) = \tan^{-1}[b_c(t)/a_c(t)]$. The baseband signals $a_c(t)$ and $b_c(t)$ are referred to as the in-phase and quadrature components of $x_c(t)$, respectively.

2.5 First-Order and Second-Order Bandpass Sampling

In many publications, a bandpass signal is sampled with a sampling rate on the order of its carrier frequency. For the purpose of sampling it is treated as a baseband signal with highest frequency Ω_H, and a sampling frequency $\Omega_s \geq 2\Omega_H$ is chosen to satisfy Theorem 1. Unfortunately, this approach becomes highly uneconomical for bandpass signals with large carrier frequencies. For example, consider a signal with carrier frequency $\Omega_c/(2\pi) = 5.5$ GHz and bandwidth $B/(2\pi) = 1$ GHz. Sampling this signal at or above $2 \times (5.5 + 0.5) = 12$ GHz is far from optimal considering the signal bandwidth is twelve times lower than the minimum

sampling rate.

It has been known for sometime that a bandpass signal can be sampled with a rate on the order of its bandwidth B [11,12]. Just as in the case of baseband signals, a minimum sampling frequency equaling twice the signal bandwidth (the Nyquist rate) can be used to sample a bandpass signal $x_c(t)$ if it meets certain spectral location criteria. Unlike the baseband case, however, not all sampling frequencies $\Omega_s > 2B$ are permissible. Extra precaution is needed to avoid overlap/aliasing between $X_+(j(\Omega - l\Omega_s))$ and $X_-(j(\Omega - m\Omega_s))$ for all $l, m \in \mathbb{Z}$, where $X_+(j\Omega)$ and $X_-(j\Omega)$ denote the signal spectrum on Ω_+ and Ω_-, respectively. Strict conditions can be derived for aliasing avoidance and to guarantee signal reconstruction from its samples. This leads to the first-order sampling theorem for bandpass signals.

Definition 3. $\mathcal{BP}_B(\mathbb{R}) := \{x_c \in L^2(\mathbb{R}) \ : \ X_c(j\Omega) = 0 \ \forall \ |\Omega| < \Omega_L \ , \ |\Omega| > \Omega_H = \Omega_L + B\}$ *is the space of finite energy bandpass analog signals with bandwidth* $B = \Omega_H - \Omega_L$ *and frequency support* $[-\Omega_H, -\Omega_L] \cup [\Omega_L, \Omega_H]$.

Theorem 2. *Let* $x_c(t) \in \mathcal{BP}_B(\mathbb{R}) \subset L^2(\mathbb{R})$. *If* $\Omega_s = 2\pi/T_s$ *satisfies conditions*

$$\begin{aligned} \frac{2}{k}\frac{\Omega_H}{B} \leq \frac{\Omega_s}{B} \leq \frac{2}{k-1}\left(\frac{\Omega_H}{B} - 1\right) \\ 1 \leq k \leq \left\lfloor \frac{\Omega_H}{B} \right\rfloor, \end{aligned} \tag{2.48}$$

where $\lfloor a \rfloor = \max\{p \in \mathbb{Z} \mid p \leq a\}$ *is the floor function, then the sampling process resulting in the digital signal* $x(n) = x_c(nT_s)$ *is alias free. Moreover,* $x_c(t)$ *is completely determined by its samples at* $t = nT_s, n \in \mathbb{Z}$ *and can be reconstructed* $\forall t$ *via interpolation*

$$x_c(t) = \sum_{n \in \mathbb{Z}} x(n) g(t - nT_s), \tag{2.49}$$

using

$$g(t) = 2\frac{\sin(\frac{B}{2}t)}{\frac{\pi t}{T_s}}\cos(\Omega_c t). \tag{2.50}$$

Proof. Let $\mathcal{F}_s$ be the set of all *forbidden sampling frequencies*, i.e., Ω_s that result in aliasing. Then

$$\begin{aligned}\forall\, \Omega_s \in \mathcal{F}_s\ , \exists\, \Omega_p \in [\Omega_L, \Omega_H],\ \Omega_n \in [-\Omega_H, -\Omega_L] \text{ and } a, b \in \mathbb{Z}\ \text{ s.t.} \\ \Omega_p + a\Omega_s = \Omega_n + b\Omega_s. \end{aligned} \tag{2.51}$$

We can rewrite $\Omega_p + a\Omega_s = \Omega_n + b\Omega_s$ as $\Omega_p - \Omega_n = (b-a)\Omega_s = k\Omega_s$ for some $k \in \mathbb{N}$. Since $\Omega_p - \Omega_n \in [2\Omega_L, 2\Omega_H]$, (2.51) can be stated more compactly as

$$\forall\, \Omega_s \in \mathcal{F}_s\ , \exists\, k \in \mathbb{N}\ \text{ s.t. }\ 2\Omega_L \leq k\Omega_s \leq 2\Omega_H \tag{2.52}$$

which is both necessary and sufficient for aliasing as further elaborated in [63]. Normalizing by kB and recalling $\Omega_L = \Omega_H - B$, the two-sided inequality in (2.52) can be rewritten as

$$\frac{2}{k}\left(\frac{\Omega_H}{B} - 1\right) \leq \frac{\Omega_s}{B} \leq \frac{2}{k}\frac{\Omega_H}{B}. \tag{2.53}$$

Treating Ω_H/B as the independent variable and Ω_s/B as the dependent variable, (2.53) indicates that for a fixed k the forbidden sampling rates lie inside a strip. The set $\mathcal{F}_s$ is then a collection of all the strips. The allowed sampling rates are located in between the $(k-1)$-th and k-th forbidden regions and are therefore specified by two inequalities

$$\begin{aligned}\frac{\Omega_s}{B} &\leq \frac{2}{k-1}\left(\frac{\Omega_H}{B} - 1\right) \\ \frac{\Omega_s}{B} &\geq \frac{2}{k}\frac{\Omega_H}{B},\end{aligned} \tag{2.54}$$

which can be solved for k to yield

$$k \leq \frac{\Omega_H}{B}. \tag{2.55}$$

Combining the inequalities in (2.54) and recalling that k is a positive integer gives the complete characterization of *allowed sampling frequencies* specified in (2.48).

The sampled spectrum is described by (2.16). When the sampling is alias free, the original signal can be extracted with a bandpass filter centered at $\pm\Omega_c$ with gain T_s and bandwidth B in a straightforward manner

$$X_c(j\Omega) = X_s(j\Omega) \cdot G(j\Omega), \tag{2.56}$$

where

$$G(j\Omega) = \begin{cases} T_s & |\Omega \pm \Omega_c| \leq B/2 \\ 0 & \text{otherwise} \end{cases} \tag{2.57}$$

has the inverse transform expressed in (2.50). The interpolation formula (2.49) is the time-domain analog of (2.56). □

A graphical representation of conditions (2.48) shown in Fig. 2.4 greatly aids in visualizing the forbidden and allowed regions. Given the signal bandwidth B and highest frequency Ω_H, a vertical line can be drawn at Ω_H/B. All the line segments that fall inside the white region constitute the permissible sampling frequencies for the signal of interest. It follows that signals with the same bandwidth but different carrier frequency may require distinct sampling rates. This is highly undesirable for radio receivers that digitize signals in different bands. The theoretical minimum $\Omega_s = 2B$ is allowed only when $\Omega_H = mB$ for $m \in \mathbb{N}$. This special case known as *integer band positioning* is highly impractical as any small deviation in the carrier frequency and/or sampling rate will lead to choosing a forbidden sampling frequency. The authors in [12] propose appending a guard band to the signal, but this unnecessarily increases the bandwidth. Finally, for $k = 1$ the sampling condition in (2.48) simplifies to $\Omega_s \geq 2\Omega_H$ which is the familiar sampling theorem for baseband signals. As mentioned earlier, sampling at or above $2\Omega_H$ is highly wasteful when the modulation frequency Ω_c is orders higher than the signal bandwidth B.

The constraints (2.48) on the sampling frequency arise due to $x_c(t)$ having frequency content over two disjoint bands Ω_+ and Ω_-. Since the analytic signal $x_c^a(t)$ (2.41) has only

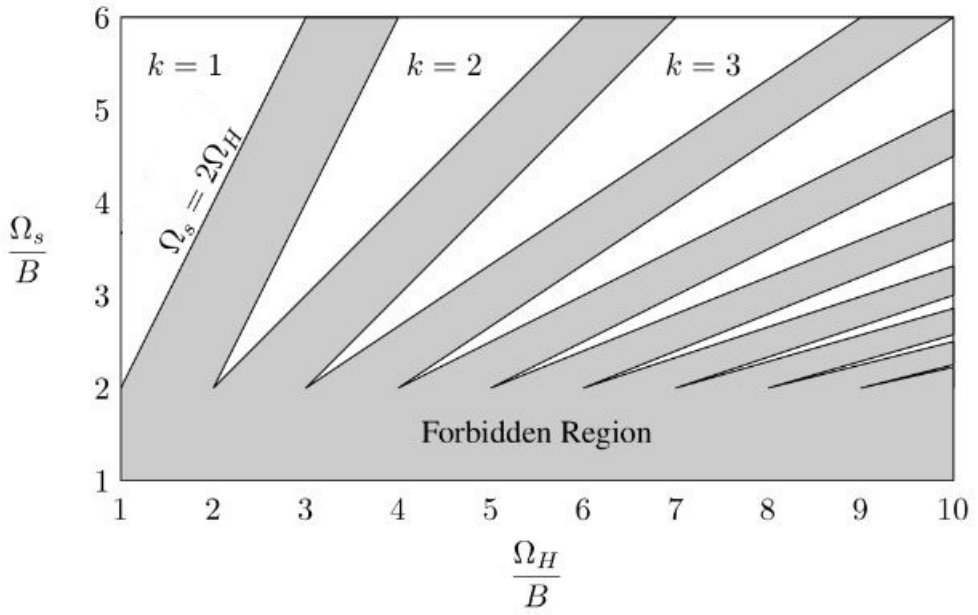


Figure 2.4: Forbidden (gray) and allowed (white) sampling frequencies in first-order sampling of bandpass signals

a one-sided frequency support over Ω_+ with spectrum the same (up to a scale) as $x_c(t)$, sampling this signal bypasses the spectral mixing issues associated with sampling $x_c(t)$. According to (2.44), sampling $x_c^a(t)$ entails a two-channel sampling of $x_c(t)$ and its Hilbert transform $\widehat{x}_c(t)$. If $T_s' = 2\pi/\Omega_s'$ with $\Omega_s' = \Omega_s/2 \geq B$, then the sampled signal

$$x^a(n) = x_c^a(nT_s') = x_c(nT_s') + j\widehat{x}_c(nT_s') = x(n) + j\widehat{x}(n) \tag{2.58}$$

has a rate of $\Omega_s'/2\pi$ complex samples per second, or $\Omega_s/2\pi$ real samples per second. Since sampling is alias free, $x_c^a(t)$ can be recovered from its samples via interpolation

$$\begin{aligned} x_c^a(t) &= \sum_{n\in\mathbb{Z}} x^a(n) g^a(t - nT_s') \\ &= \sum_{n\in\mathbb{Z}} x(n) g^a(t - nT_s') + j \sum_{n\in\mathbb{Z}} \widehat{x}(n) g^a(t - nT_s'), \end{aligned} \tag{2.59}$$

using a complex bandpass filter with gain T_s' over Ω_+ and zero elsewhere

$$g^a(t) = \frac{\sin(\frac{B}{2}t)}{\frac{\pi t}{T'_s}} e^{j\Omega_c t}. \tag{2.60}$$

Recalling the relationship (2.40), the signal of interest $x_c(t)$ can then be reconstructed from its samples and its Hilbert transform samples as

$$x_c(t) = \sum_{n\in\mathbb{Z}} x(n)\Re\{g^a(t-nT'_s)\} - \sum_{n\in\mathbb{Z}} \widehat{x}(n)\Im\{g^a(t-nT'_s)\}, \tag{2.61}$$

where $\Im\{\cdot\}$ refers to taking the imaginary part. The challenge of this method lies in the design of a practical analog Hilbert transformer.

A more attractive alternative proposed by Kohlenberg [11] that does not involve a Hilbert transformer consists of using second-order time-interleaved sampling, where the signal $x_c(t)$ is sampled at time instants $t = nT'_s$ and $t = (n+d)T'_s$ for $0 < d < 1$. Then for the minimum rate $\Omega_s = 2\Omega'_s = 2B$ but except for some values of d such as $d = 1/2$, the interpolation

$$x_c(t) = \sum_{n\in\mathbb{Z}} x(n)s(t-nT'_s) + \sum_{n\in\mathbb{Z}} x(n+d)s(-t+(n+d)T'_s), \tag{2.62}$$

where $x(n+d) = x_c((n+d)T'_s)$, reconstructs $x_c(t)$ from its two streams of samples no matter the signal carrier frequency. Proof of this theorem and expression for $s(t)$ can be found in [11] and [13, Sec. 6.4].

Second-order (two-channel) time-interleaved sampling removes the sampling frequency restriction imposed by first-order sampling. All signals independent of their band location can be sampled at the minimum rate $2B$. It turns out this result generalizes to M-th order sampling as discussed in Chapter 3.

2.6 Stochastic Optimization

Consider the stochastic optimization problem that seeks to find $\boldsymbol{\theta}_0 \in \mathbb{R}^n$ s.t.

$$\boldsymbol{\theta}_0 = \arg\min_{\boldsymbol{\theta}\in\mathbb{R}^n} J(\boldsymbol{\theta}), \tag{2.63}$$

where the objective function

$$J(\boldsymbol{\theta}) = E_{\mathbf{Z}}[Q(\mathbf{Z},\boldsymbol{\theta})] = \int_{\mathbb{R}^q} Q(\mathbf{z},\boldsymbol{\theta}) f_{\mathbf{Z}}(\mathbf{z}) d\mathbf{z} \tag{2.64}$$

is convex. Here, $\mathbf{Z}$ is a random vector in $\mathbb{R}^q$ with probability density function (PDF) $f_{\mathbf{Z}}(\mathbf{z})$, and $E[\cdot]$ denotes the expectation operator. Assuming $J(\boldsymbol{\theta})$ is twice continuously differentiable, it has a gradient

$$\nabla_{\boldsymbol{\theta}} J(\boldsymbol{\theta}) = \begin{bmatrix} \frac{\partial J(\boldsymbol{\theta})}{\partial \theta_1} \\ \frac{\partial J(\boldsymbol{\theta})}{\partial \theta_2} \\ \vdots \\ \frac{\partial J(\boldsymbol{\theta})}{\partial \theta_n} \end{bmatrix} \tag{2.65}$$

and $n \times n$ Hessian matrix

$$\mathbf{H}(\boldsymbol{\theta}) = \nabla^2_{\boldsymbol{\theta}} J(\boldsymbol{\theta}) \tag{2.66}$$

with (i,j) entry $\dfrac{\partial^2 J(\boldsymbol{\theta})}{\partial\theta_i \partial\theta_j}$ for $1 \le i,j \le n$. The function $J(\boldsymbol{\theta})$ is then strictly convex if and only if either one of the following conditions hold true [65]:

i) $J(\alpha\boldsymbol{\theta}_1 + (1-\alpha)\boldsymbol{\theta}_2) < \alpha J(\boldsymbol{\theta}_1) + (1-\alpha)J(\boldsymbol{\theta}_2) \quad \forall\, \boldsymbol{\theta}_1, \boldsymbol{\theta}_2 \in \mathbb{R}^n$ s.t. $\boldsymbol{\theta}_1 \neq \boldsymbol{\theta}_2$, and any α s.t. $0 < \alpha < 1$.

ii) $\mathbf{H}(\boldsymbol{\theta}) > \mathbf{0} \quad \forall\, \boldsymbol{\theta} \in \mathbb{R}^{\mathbf{n}}$, i.e., the Hessian matrix is positive definite.

The second condition is often more useful in practice as it allows an easy way to distinguish convex from concave functions after finding the stationary point $\nabla_{\boldsymbol{\theta}} J(\boldsymbol{\theta}) = 0$. Convex functions have the important property that if $\boldsymbol{\theta}_0$ is a local minimum over a convex subset of $\mathbb{R}^n$, then it is a global minimum. Moreover, in the vicinity of $\boldsymbol{\theta}_0$, $J(\boldsymbol{\theta})$ admits the positive definite quadratic approximation

$$J(\boldsymbol{\theta}) \approx \frac{1}{2}(\boldsymbol{\theta} - \boldsymbol{\theta}_0)^T \mathbf{H}(\boldsymbol{\theta_0})(\boldsymbol{\theta} - \boldsymbol{\theta_0}). \tag{2.67}$$

The Gradient Descent

A class of optimization algorithms that iteratively solve (2.63–2.64) rely on gradient information to achieve minimization. The simplest of these is the *steepest descent* method

$$\boldsymbol{\theta}(n+1) = \boldsymbol{\theta}(n) - \mu(n)\nabla_{\boldsymbol{\theta}} J(\boldsymbol{\theta}(n)), \tag{2.68}$$

where $\boldsymbol{\theta}(n)$ for $n = 0, 1, 2, \ldots$ is the estimate at iteration n, $\mu(n)$ is the step size at iteration n, and $\boldsymbol{\theta}(n+1)$ is the estimate at the next iteration $n+1$. At each step, the direction of search is taken in opposite direction to the gradient at the current estimate $\boldsymbol{\theta}(n)$. This is justified with the simple fact that the direction of gradient indicates the maximal rate of increase in $J(\boldsymbol{\theta})$, and thus taking steps in the opposite direction ensures rapid decrease. The step size $\mu(n)$ at each iteration can be selected using a perfect line search or a weak search technique such as Armijo's method that is based on Wolfe's conditions [66, Section 8.2]. Alternatively, a constant step size $\mu(n) = \mu$ can be chosen to reduce algorithm complexity.

For a strongly convex $J(\boldsymbol{\theta})$, the steepest descent converges to the optimal solution $\boldsymbol{\theta}_0$ at a linear rate, but the speed of convergence depends on the condition number of the Hessian matrix which is defined as the ratio of largest to smallest eigenvalue of $\mathbf{H}(\boldsymbol{\theta}_0)$ [67, Sec. 3.3]. This follows from the quadratic approximation (2.67). A large condition number causes an exaggerated zigzag behavior in iterations and can severely degrade the convergence of the algorithm.

To evaluate the gradient of $J(\boldsymbol{\theta})$ in (2.68), some statistical information is needed to carry out the expectation in (2.64). This information can be the PDF $f_{\mathbf{Z}}(\mathbf{z})$ or the first and second order statistics of $\mathbf{Z}$ in the case of a quadratic $Q(\mathbf{Z}, \boldsymbol{\theta})$. Unfortunately, a statistical model of $\mathbf{Z}$ is often not available in practical situations. Instead, we can use the observations $\mathbf{Z}(t)$ for $1 \leq t \leq T$, where at each fixed time $\mathbf{Z}(t)$ is $f_{\mathbf{Z}}(\mathbf{z})$ distributed, to justify the approximation

$$\frac{1}{T}\sum_{t=1}^{T} Q(\mathbf{Z}(t), \boldsymbol{\theta}) \approx E_{\mathbf{Z}}[Q(\mathbf{Z}, \boldsymbol{\theta})] \tag{2.69}$$

by the strong law of large numbers (SLLN) for large T. This result holds asymptotically as $T \to \infty$ when the observations $\mathbf{Z}(t)$ are independent and identically distributed (iid) and $Q(\mathbf{Z}(t), \boldsymbol{\theta})$ has a finite variance. If the observations are not iid, then the random process $\mathbf{Z}(t)$ has to obey strong mixing conditions. From (2.69) it follows that the approximation

$$\nabla_{\boldsymbol{\theta}} J(\boldsymbol{\theta}) \approx \frac{1}{T} \sum_{t=1}^{T} \nabla_{\boldsymbol{\theta}} Q(\mathbf{Z}(t), \boldsymbol{\theta}) \tag{2.70}$$

can be used in (2.68). This approach can be viewed as a batch minimization technique that processes all observations $\mathbf{Z}(t)$, $1 \leq t \leq T$ at the same time.

The Stochastic Gradient Descent

Instead of processing all the observations at once, we can perform the minimization (2.63–2.64) adaptively using a new observation as it becomes available. The stochastic gradient descent (SGD) proposed in 1951 by Robbins and Monro [68] skips the expectation operation when evaluating the gradient of $J(\boldsymbol{\theta})$. It applies the gradient operator directly to $Q(\mathbf{Z}(n), \boldsymbol{\theta})$, where $\mathbf{Z}(n)$ is a stationary random process with unknown statistics, which results in the iteration

$$\boldsymbol{\theta}(n+1) = \boldsymbol{\theta}(n) - \mu(n) \nabla_{\boldsymbol{\theta}} Q(\mathbf{Z}(n), \boldsymbol{\theta}(n)). \tag{2.71}$$

Assuming $\mu(n) = \mu$ is a very small constant step size, the iteration (2.71) can be justified by observing that the effect of L consecutive updates can be expressed as

$$\boldsymbol{\theta}(n+L) = \boldsymbol{\theta}(n) - \mu \sum_{k=n}^{n+L-1} \nabla_{\boldsymbol{\theta}} Q(\mathbf{Z}(k), \boldsymbol{\theta}(k)). \tag{2.72}$$

Since μ is very small, $\boldsymbol{\theta}(k) \approx \boldsymbol{\theta}(n)$ for $n \leq k \leq n+L-1$. Then by the SLLN we have

$$\frac{1}{L} \sum_{k=n}^{n+L-1} \nabla_{\boldsymbol{\theta}} Q(\mathbf{Z}(k), \boldsymbol{\theta}(n)) \approx \nabla_{\boldsymbol{\theta}} E_{\mathbf{Z}(n)}[Q(\mathbf{Z}(n), \boldsymbol{\theta}(n))] = \nabla_{\boldsymbol{\theta}} J(\boldsymbol{\theta}(n)). \tag{2.73}$$

Using this approximation in (2.72) results in

$$\boldsymbol{\theta}(n+L) \approx \boldsymbol{\theta}(n) - \mu L \nabla_{\boldsymbol{\theta}} J(\boldsymbol{\theta}(n)) = \boldsymbol{\theta}(n) - \widehat{\mu} \nabla_{\boldsymbol{\theta}} J(\boldsymbol{\theta}(n)), \tag{2.74}$$

the right hand side of which has the exact form of steepest descent iteration (2.68) with constant step size $\widehat{\mu} = \mu L$. Thus, for L sufficiently large that still ensures $\boldsymbol{\theta}(k)$ doesn't vary much over the interval $[n, n+L-1]$, blocks of L consecutive stochastic gradient iterations behave like single gradient iterations of $J(\boldsymbol{\theta})$. The step size for stochastic gradient is much smaller than the steepest descent step size.

Classical adaptive algorithms such as LMS and recursive least squares (RLS) can be analyzed using the energy conservation relation proposed by Sayed [69]. This approach has the advantage that it does not assume a small step size. Its scope, however, is limited since not all adaptive algorithms obey an energy conservation relation. A more general method for analyzing the convergence of adaptive algorithms using an ordinary differential equation (ODE) was pioneered by Ljung [70, 71] and studied in depth by Benveniste, Métivier, and Priouret [72]. For SGD this technique forms an ODE by averaging the adaptive updating mechanism of the SGD iteration and views the estimates $\boldsymbol{\theta}(n)$ in (2.71) as random fluctuations around the ODE trajectory. When the ODE has a unique and stable equilibrium point $\boldsymbol{\theta}_*$, it should ideally coincide with the global minimum $\boldsymbol{\theta}_0$ of the convex function $J(\boldsymbol{\theta})$ we wish to minimize. If this is not the case, the adaptive algorithm is biased. In the rest of this section, we outline the basics of the ODE method which is used in Chapter 5 to examine the convergence behavior of the novel mismatch calibration algorithm.

The SGD algorithm (2.71) with constant step size μ can be expressed as

$$\boldsymbol{\theta}(n+1) = \boldsymbol{\theta}(n) + \mu \mathbf{T}(\mathbf{Z}(n), \boldsymbol{\theta}(n)) \tag{2.75}$$

with

$$\mathbf{T}(\mathbf{Z}(n), \boldsymbol{\theta}) = -\nabla_{\boldsymbol{\theta}} Q(\mathbf{Z}(n), \boldsymbol{\theta}). \tag{2.76}$$

The ODE corresponding to (2.75) is specified by the mean vector field

$$\frac{d\boldsymbol{\theta}}{dt} = \boldsymbol{t}(\boldsymbol{\theta}) = E_{\mathbf{Z}(n)}[\mathbf{T}(\mathbf{Z}(n), \boldsymbol{\theta})] \tag{2.77}$$

with initial condition $\boldsymbol{\theta}(0) = \boldsymbol{\theta}_i$ denoting the initial estimate in the adaptive algorithm (2.75). In evaluating $\boldsymbol{t}(\boldsymbol{\theta})$, the parameter $\boldsymbol{\theta}$ is held "frozen" so that the distribution of $\mathbf{Z}(n)$ is stationary in (2.77). Using the definition of $J(\boldsymbol{\theta})$ from (2.64), we obtain

$$\frac{d\boldsymbol{\theta}}{dt} = -\nabla_{\boldsymbol{\theta}} J(\boldsymbol{\theta}), \tag{2.78}$$

which means that for SGD algorithms the ODE is a gradient flow, i.e., its trajectories follow steepest descent lines of $J(\boldsymbol{\theta})$. Furthermore,

$$\frac{dJ(\boldsymbol{\theta}(t))}{dt} = \nabla_{\boldsymbol{\theta}}^T J(\boldsymbol{\theta}(t)) \frac{d\boldsymbol{\theta}}{dt} = -||\nabla_{\boldsymbol{\theta}} J(\boldsymbol{\theta}(t))||^2 \tag{2.79}$$

implies that along trajectories of the ODE, the objective function $J(\boldsymbol{\theta}(t))$ serves as a Lyapunov function and is monotone decreasing until a stationary point $\boldsymbol{\theta}_0$ satisfying $\nabla_{\boldsymbol{\theta}} J(\boldsymbol{\theta}_0) = 0$ is reached. For a convex $J(\boldsymbol{\theta})$ there is only one stationary point corresponding to its global minimum.

Convergence analysis of adaptive algorithms via the ODE method relies on two theorems proved rigorously in [72]. The first theorem pertains to the transient phase of the algorithms. Succinctly, it states that for a small constant step size μ the n-th estimate $\boldsymbol{\theta}(n)$ of the adaptive algorithm (2.75) is within a standard deviation proportional to $\mu^{1/2}$ of the point $\boldsymbol{\theta}_c(\mu n)$, where $\boldsymbol{\theta}_c(t)$ is the ODE trajectory. This can be visualized by thinking of the ODE trajectory as the center of a tube with radius proportional to $\mu^{1/2}$ and adaptive algorithm trajectories varying randomly within this tube. The second theorem deals with the steady-state behavior of adaptive algorithms. It assumes the ODE has a unique stable equilibrium

point $\boldsymbol{\theta}_*$ and that for SGD the negative of the Hessian matrix of $J(\boldsymbol{\theta})$ at this point

$$\mathbf{A}(\boldsymbol{\theta}_*) = -\mathbf{H}(\boldsymbol{\theta}_*) = -\nabla^2_{\boldsymbol{\theta}} J(\boldsymbol{\theta}_*) \tag{2.80}$$

is asymptotically stable, i.e., all its eigenvalues are strictly in the left half plane. The theorem then states that as μ decreases to zero, the estimates $\boldsymbol{\theta}(n)$ asymptotically become Gaussian distributed with mean $\boldsymbol{\theta}_*$ and covariance matrix $\mu\mathbf{P}$, where the matrix $\mathbf{P} > 0$ satisfies a Lyapunov equation. Thus, a smaller μ guarantees more accurate asymptotic estimates fluctuating tightly around the desired minimum.

Chapter 3

Complex Envelope Sampling with M-channel Time-Interleaved ADCs

Several papers have extended Kohlenberg's second-order time-interleaved bandpass sampling result to the case where M nonuniformly interleaved ADCs each operating at Ω_s/M, where Ω_s is the total sampling rate of the TIADC, sample the bandpass signal and then M filters are used to reconstruct the signal. Kida and Kuroda [73] derived a general expression for the M reconstruction filters but only for the minimum sampling rate $\Omega_s = 2B$. Coulson [74] provided clear formulas for reconstruction filters in time domain with sampling frequency as a parameter and showed that each filter consists of M bandpass filters when the minimum sampling rate $\Omega_s = 2B$ is used. Although flexible and not limited to the minimum rate, his method is developed entirely in the analog domain. For digital implementation, oversampling at $\Omega_s \geq 2MB$ is required to obtain alias-free digital versions of reconstruction filters. Lin and Vaidyanathan [75] generalized Coulson's result to a broader class of bandpass signals consisting of M disjoint spectral components and extended their method to signals in 2-D and discrete-time. They demonstrated stability of reconstruction, but did not focus on filter derivation.

In this chapter we propose a flexible and universal sampling scheme for a bandpass signal

$x_c(t) \in \mathcal{BP}_B(\mathbb{R})$ using a nonuniform M-channel TIADC with timing offsets $d_i T_s'$, where the timing skews satisfy $0 < d_{i-1} < d_i < 1$ for $i = 1, 2, \ldots, M-1$ and $T_s' = 2\pi/\Omega_s'$ denotes the sub-ADC sampling period. The sampling frequency of the overall ADC is $\Omega_s = M\Omega_s'$. We require Ω_s at the minimum to be at the Nyquist rate $2B$ when M is even and slightly above $2B$ for M odd. No assumption is made about the carrier frequency Ω_c, signal bandwidth B, and timing skews d_i, except that the carrier frequency Ω_c is greater than $B/2$, which ensures that the signal considered is a bandpass signal. Our *contributions* are the following:

1) In contrast to [73–75] that recover the original signal, we reconstruct the sampled complex envelope of the bandpass signal from the M sequences produced by the TIADC. So our method encompasses sampling, demodulation, and I and Q components separation all in one DSP device. This makes it attractive as a communications receiver front-end deployed to digitize signals in any frequency band.

2) Unlike [73, 74], both our sampling and reconstruction models are developed entirely in digital domain, and thus no digitization of analog filters is needed. We show that the evaluation of the sampled complex envelope requires the implementation of M complex-valued digital FIR filters and a discrete-time modulator. Detailed step-by-step instructions for computing these digital reconstruction filters are given. This can assist in implementation of the proposed technique. An in-depth reconstruction analysis is provided for the cases $M = 2, 3, 4$.

3) Existing works on nonuniform time-interleaved bandpass sampling do not examine reconstruction performance in the presence of TIADC mismatches. In the simulations presented in Section 3.4, we investigate the performance of our method both under ideal conditions and when the TIADC suffers from gain and timing mismatches. Using multi-tone and MSK signals, it is demonstrated that the effect of mismatches on complex envelope reconstruction can be significant.

The results of this chapter have been published by the author in [76].

3.1 Complex Envelope Sampling Model

In Fig. 3.1, we consider M-th order time-interleaved sampling of $x_c(t) \in \mathcal{BP}_B(\mathbb{R})$ with mathematical representation (2.46). Here, $M \geq 2$, T_s' denotes the sub-ADC sampling period, and $\Omega_s' = 2\pi/T_s'$ is the sub-ADC sampling frequency. The sampling frequency of the overall ADC is $\Omega_s = M\Omega_s'$. It is independent of Ω_c and assumed to be greater than or equal to the Nyquist rate $2B$. The timing offset between ADC_0 and ADC_i is $D_i = d_i T_s'$, where timing skews d_i satisfy $0 < d_i < 1$ and $d_{i-1} < d_i$ for $i = 1, 2, \ldots, M-1$. For $d_i = i/M$, the combination of M sub-ADCs forms a uniform ADC with sampling period $T_s = T_s'/M$. As discussed in Section 2.5, uniform sampling presents challenges in sampling rate selection. For all other $d_i \neq i/M$, the overall ADC has a nonuniform but periodic sampling pattern.

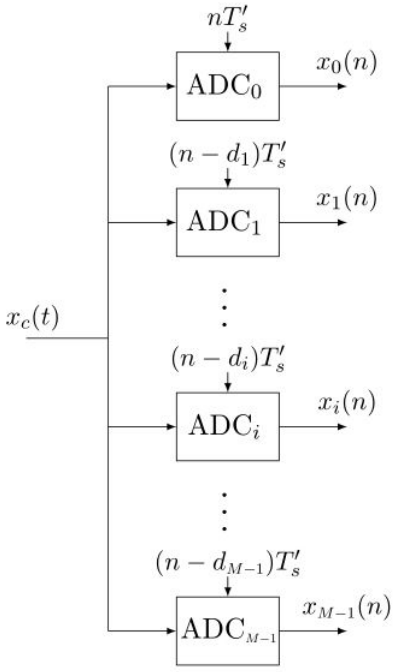


Figure 3.1: M-th order time-interleaved sampling of bandpass signal $x_c(t)$

Let $\ell \in \mathbb{N}$ be defined as

$$\ell = \text{round}(\frac{\Omega_c}{\Omega_s'}), \tag{3.1}$$

so that Ω_c belongs to the frequency band $[(\ell - 1/2)\Omega_s', (\ell + 1/2)\Omega_s']$ which corresponds to

the location of the ℓ-th image copy of a sampled baseband signal and is therefore referred to here as the ℓ-th image band. It is assumed that $\ell \geq 1$, so that $x_c(t)$ is a bandpass signal. The band $[(\ell - 1/2)\Omega_s', (\ell + 1/2)\Omega_s']$ includes the 2ℓ-th and $2\ell + 1$-th Nyquist zones of the sub-ADCs, and ℓ can be expressed in terms of the Nyquist zone index p as $\ell = \lfloor p/2 \rfloor$. The carrier frequency Ω_c maps in the digital domain to the discrete modulation frequency $|\omega_b| \leq \pi$ given by

$$\omega_b = \Omega_c T_s' \bmod 2\pi = \Big(\frac{\Omega_c}{\Omega_s'} - \ell\Big)2\pi \, . \tag{3.2}$$

The ℓ-th image band is demonstrated in Fig. 3.2. We have $\omega_b = 0$ only when $\Omega_c = \ell\Omega_s'$. Although elegant and simple, picking a sampling rate integer fraction of the carrier frequency may not be feasible in hardware.

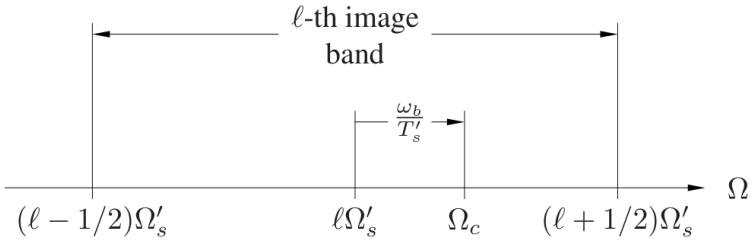


Figure 3.2: ℓ-th image band

Sampling: Let $\mathcal{E}(M) \geq 0$ be the oversampling parameter function defined as

$$\mathcal{E}(M) = \begin{cases} 0 & \text{if } M \text{ is even} \\ \frac{2}{M-1} & \text{if } M \text{ is odd} \end{cases} \tag{3.3}$$

for $M \geq 2$. Then to ensure the overall TIADC sampling frequency is at or above the Nyquist rate, we pick

$$\Omega_s \geq (2 + \mathcal{E}(M))B = \begin{cases} 2B & \text{if } M \text{ is even} \\ \frac{M}{M-1}2B & \text{if } M \text{ is odd.} \end{cases} \tag{3.4}$$

Since $\Omega_s' = \Omega_s/M$, we have

$$\Omega_s' \geq \frac{(2+\mathcal{E}(M))B}{M} = \begin{cases} \frac{2B}{M} = \frac{B}{L} & \text{if } M \text{ is even} \\ \frac{2B}{M-1} = \frac{B}{L} & \text{if } M \text{ is odd} , \end{cases} \tag{3.5}$$

where $L = \lfloor M/2 \rfloor$. If m is an even positive integer, then both $M = m$ and $M = m+1$ result in $L = m/2$. So, the sub-ADC sampling frequency is bounded below by the same value when m or $m+1$ number of channels are used. For M even, the overall ADC sampling frequency Ω_s is bounded below by the Nyquist rate $2B$. For M odd, the lower bound is slightly higher but approaches the Nyquist rate as M grows large since $M/(M-1) \to 1$ as $M \to \infty$. The justification for slight oversampling in the case of odd M is discussed at the end of the section.

Given (3.4) and recalling the Nyquist rate for $c_c(t)$ is B ($2 \times \text{BW}\{c_c(t)\} = 2 \times B/2 = B$), the envelope $c_c(t)$ may experience undersampling by a factor of L when the sub-ADCs sample $x_c(t)$. This introduces a second form of aliasing in addition to aliasing between the negative and positive spectral images. Let $c^{[L]}(n) = c_c(nT_s'/L)$ be the complex envelope sampled at or above its Nyquist rate and $C(e^{j\omega})$ its DTFT which contains all information about the envelope. The sampled sequences $x_i(n)$, $0 \leq i \leq M-1$ from Fig. 3.1 can then be computed as follows.

$$x_0(n) = x_c(nT_s') = \Re\{c_c(nT_s')e^{j\Omega_c T_s' n}\},$$

where $c_c(nT_s') = c_c(Ln\frac{T_s'}{L}) = c^{[L]}(Ln)$. By observing

$$e^{j\Omega_c T_s' n} = e^{j(\omega_b + 2\pi\ell)n} = e^{j\omega_b n},$$

the digital signal $x_0(n)$ can be expressed as

$$x_0(n) = \Re\{c^{[L]}(Ln)e^{j\omega_b n}\}. \tag{3.6}$$

Similarly, if

$$e^{j\Omega_c T_s'(n-d_i)} = e^{j(\omega_b+2\pi\ell)(n-d_i)} = e^{j\omega_b(n-d_i)}e^{-j2\pi\ell d_i},$$

then for $1 \le i \le M-1$ the sampled sequence $x_i(n)$ can be expressed as

$$\begin{aligned} x_i(n) &= x_c((n-d_i)T_s') = x_c(L(n-d_i)\frac{T_s'}{L}) \\ &= \Re\{c^{[L]}(L(n-d_i))e^{j\Omega_c T_s'(n-d_i)}\} \\ &= \Re\{c^{[L]}(L(n-d_i))e^{j\omega_b(n-d_i)}e^{-j2\pi\ell d_i}\} \\ &= \Re\{c^{[L]}(Ln-Ld_i)e^{j\frac{\omega_b}{L}(Ln-Ld_i)}e^{-j2\pi\ell d_i}\}. \end{aligned} \tag{3.7}$$

In the last expression, $c^{[L]}(n-Ld_i)$ is a shorthand notation for

$$c^{[L]}(n-Ld_i) = f_i(n) * c^{[L]}(n), \tag{3.8}$$

where

$$f_i(n) = \frac{\sin(\pi(n-Ld_i))}{\pi(n-Ld_i)} \tag{3.9}$$

is the impulse response of the periodic fractional delay filter specified by

$$F_i(e^{j\omega}) = e^{-j\omega Ld_i} \tag{3.10}$$

for $-\pi < \omega \le \pi$. More generally, the 2π periodic filter $F_i(e^{j\omega})$ can be expressed as

$$F_i(e^{j\omega}) = e^{-j(\omega-q(\omega))Ld_i} \tag{3.11}$$

for all ω, where for $l \in \mathbb{Z}$

$$q(\omega) = l2\pi \quad \text{for} \quad (2l-1)\pi \le \omega < (2l+1)\pi \tag{3.12}$$

represents the quantized value of ω produced by an infinite quantizer with step size 2π.

From (3.7), $x_i(n)$ for $1 \leq i \leq M-1$ can be written as $x_i(n) = \Re\{s_i(n)\}$ with

$$s_i(n) = c^{[L]}(Ln - Ld_i)e^{j\frac{\omega_b}{L}(Ln-Ld_i)}e^{-j2\pi\ell d_i}. \tag{3.13}$$

The Fourier transform of sequence $s_i(n)$ denoted by $S_i(e^{j\omega})$ can be computed in steps:

$$\begin{aligned}
c^{[L]}(n) &\overset{\mathcal{FT}}{\longleftrightarrow} C(e^{j\omega}) \\
c^{[L]}(n - Ld_i) &\overset{\mathcal{FT}}{\longleftrightarrow} C(e^{j\omega})F_i(e^{j\omega}) \\
c^{[L]}(n - Ld_i)e^{j\frac{\omega_b}{L}n} &\overset{\mathcal{FT}}{\longleftrightarrow} C(e^{j(\omega-\frac{\omega_b}{L})})F_i(e^{j(\omega-\frac{\omega_b}{L})}) \\
c^{[L]}(n - Ld_i)e^{j\frac{\omega_b}{L}(n-Ld_i)} &\overset{\mathcal{FT}}{\longleftrightarrow} C(e^{j(\omega-\frac{\omega_b}{L})})F_i(e^{j(\omega-\frac{\omega_b}{L})})e^{-j\omega_b d_i} \\
c^{[L]}(n - Ld_i)e^{j\frac{\omega_b}{L}(n-Ld_i)}e^{-j2\pi\ell d_i} &\overset{\mathcal{FT}}{\longleftrightarrow} C(e^{j(\omega-\frac{\omega_b}{L})})F_i(e^{j(\omega-\frac{\omega_b}{L})})e^{-j(\omega_b+2\pi\ell)d_i}
\end{aligned}$$

and finally downsampling by L ($n \to nL$) results in $s_i(n)$ from (3.13) with Fourier transform

$$\begin{aligned}
S_i(e^{j\omega}) &= \frac{1}{L}\sum_{k=0}^{L-1} F_i(e^{j(\frac{\omega}{L}-\frac{\omega_b}{L}-\frac{2\pi}{L}k)})C(e^{j(\frac{\omega}{L}-\frac{\omega_b}{L}-\frac{2\pi}{L}k)})e^{-j(\omega_b+2\pi\ell)d_i} \\
&= \frac{1}{L}\sum_{k=0}^{L-1} F_i(e^{j(\frac{\omega}{L}-\frac{2\pi}{L}k)})G_i(e^{j(\frac{\omega}{L}-\frac{2\pi}{L}k)})C(e^{j(\frac{\omega}{L}-\frac{\omega_b}{L}-\frac{2\pi}{L}k)})
\end{aligned} \tag{3.14}$$

where

$$\begin{aligned}
G_i(e^{j\frac{\omega}{L}}) &\triangleq \frac{F_i(e^{j(\frac{\omega}{L}-\frac{\omega_b}{L})})}{F_i(e^{j\frac{\omega}{L}})}e^{-j(\omega_b+2\pi\ell)d_i} \\
&= e^{-j\left[q(\frac{\omega}{L})-q(\frac{\omega}{L}-\frac{\omega_b}{L})\right]Ld_i}e^{-j2\pi\ell d_i}.
\end{aligned} \tag{3.15}$$

For $\omega_b > 0$, we obtain

$$q\left(\frac{\omega}{L}\right) - q\left(\frac{\omega}{L}-\frac{\omega_b}{L}\right) = \begin{cases} 2\pi & -\pi L \leq \omega < -\pi L + \omega_b \\ 0 & -\pi L + \omega_b \leq \omega < \pi L\,, \end{cases} \tag{3.16}$$

$$G_i(e^{j\frac{\omega}{L}}) = \begin{cases} e^{-j2\pi(\ell+L)d_i} & -\pi L \leq \omega < -\pi L + \omega_b \\ e^{-j2\pi\ell d_i} & -\pi L + \omega_b \leq \omega < \pi L \,, \end{cases} \tag{3.17}$$

and therefore, $G_i(e^{j(\frac{\omega}{L}-\frac{2\pi}{L}k)})$ from (3.14) can be expressed as

$$\begin{aligned} G_i(e^{j(\frac{\omega}{L}-\frac{2\pi}{L}k)}) &= G_i(e^{j\frac{\omega}{L}})\Big|_{\omega\to\,\omega-2\pi k} \\ &= \begin{cases} e^{-j2\pi(\ell+L)d_i} & -\pi(L-2k) \leq \omega < -\pi(L-2k) + \omega_b \\ e^{-j2\pi\ell d_i} & -\pi(L-2k) + \omega_b \leq \omega < \pi(L+2k) \end{cases} \end{aligned} \tag{3.18}$$

for $0 \leq k \leq L-1$. For $\omega_b < 0$, we have

$$q\left(\frac{\omega}{L}\right) - q\left(\frac{\omega}{L} - \frac{\omega_b}{L}\right) = \begin{cases} 0 & -\pi L \leq \omega < \pi L + \omega_b \\ -2\pi & \pi L + \omega_b \leq \omega < \pi L \,, \end{cases} \tag{3.19}$$

$$G_i(e^{j\frac{\omega}{L}}) = \begin{cases} e^{-j2\pi\ell d_i} & -\pi L \leq \omega < \pi L + \omega_b \\ e^{-j2\pi(\ell-L)d_i} & \pi L + \omega_b \leq \omega < \pi L \,, \end{cases} \tag{3.20}$$

and consequently

$$G_i(e^{j(\frac{\omega}{L}-\frac{2\pi}{L}k)}) = \begin{cases} e^{-j2\pi\ell d_i} & -\pi(L-2k) \leq \omega < \pi(L+2k) + \omega_b \\ e^{-j2\pi(\ell-L)d_i} & \pi(L+2k) + \omega_b \leq \omega < \pi(L+2k) \end{cases} \tag{3.21}$$

for $0 \leq k \leq L-1$. The filter $G_i(e^{j(\frac{\omega}{L}-\frac{2\pi}{L}k)})$ is $2\pi L$ periodic. It is a frequency scaled and shifted version of $G_i(e^{j\omega})$ which is 2π periodic as any DTFT and can be expressed as

$$G_i(e^{j\omega}) = \begin{cases} e^{-j2\pi(\ell+L)d_i} & -\pi \leq \omega < -\pi + \frac{\omega_b}{L} \\ e^{-j2\pi\ell d_i} & -\pi + \frac{\omega_b}{L} \leq \omega < \pi \end{cases} \tag{3.22}$$

for $\omega_b > 0$, and

$$G_i(e^{j\omega}) = \begin{cases} e^{-j2\pi\ell d_i} & -\pi \le \omega < \pi + \frac{\omega_b}{L} \\ e^{-j2\pi(\ell - L)d_i} & \pi + \frac{\omega_b}{L} \le \omega < \pi \end{cases} \tag{3.23}$$

for $\omega_b < 0$. Its impulse response is given by

$$\begin{aligned} g_i(n) = \; & \frac{(-1)^n \mathrm{sgn}(\omega_b)}{j2\pi n}\big(e^{j\frac{\omega_b}{L}n} - 1\big) \\ & \times \big(e^{-j2\pi \mathrm{sgn}(\omega_b) L d_i} - 1\big) e^{-j2\pi\ell d_i} \end{aligned} \tag{3.24}$$

for $n \neq 0$, where

$$\mathrm{sgn}(\omega) = \begin{cases} 1 & \omega > 0 \\ -1 & \omega < 0 \end{cases} \tag{3.25}$$

denotes the sign function, and

$$g_i(n) = \frac{e^{-j2\pi\ell d_i}}{2\pi}\big(2\pi - \frac{|\omega_b|}{L} + \frac{|\omega_b|}{L} e^{-j2\pi \mathrm{sgn}(\omega_b) L d_i}\big) \tag{3.26}$$

for $n = 0$.

The sampling model can be represented in block diagram form shown in Fig. 3.3. In this model, $F_i(e^{j\omega})$ is fully determined by the TIADC parameters L and d_i, whereas the filter $G_i(e^{j\omega})$ depends on the image band index ℓ of Ω_c and its relative location ω_b within this band in addition to L and d_i. Thus, from a software defined radio perspective, $G_i(e^{j\omega})$ changes if the frequency band of the signal of interest varies, but $F_i(e^{j\omega})$ stays the same. Compressors in the model indicate the outputs $\{x_0(n), \ldots, x_{M-1}(n)\}$ have a sampling rate L times lower than the input $c^{[L]}(n)$. The oversampling parameter (3.3) ensures L is an integer given by $L = \lfloor M/2 \rfloor$ instead of $L = M/2$ which is noninteger for M odd. This helps avoid lowpass filtering associated with a noninteger sampling rate change discussed in Section 2.3 which would increase the complexity of the model in Fig. 3.3.

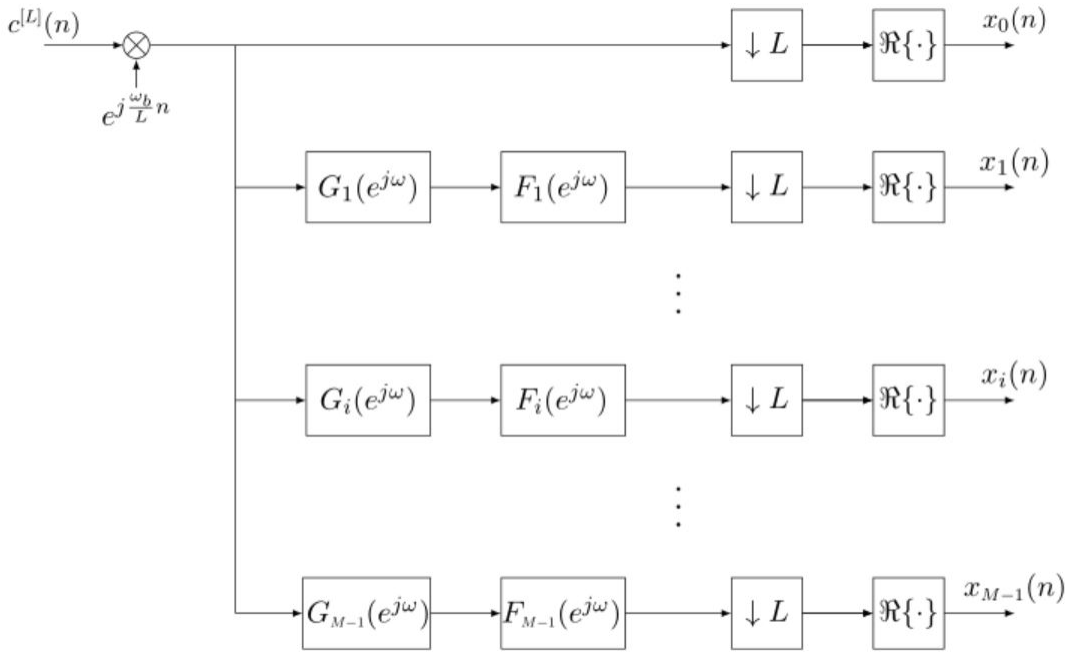


Figure 3.3: Discrete-time bandpass sampling model.

3.2 Complex Envelope Reconstruction

We consider the problem of recovering $c^{[L]}(n)$ from $x_i(n)$, $0 \leq i \leq M-1$. Since $c^{[L]}(n)$ is complex, $C(e^{j\omega})$ is devoid of symmetries, so knowledge of $C(e^{j\omega})$ over the entire frequency band $[-\pi, \pi]$ is needed to recover $c^{[L]}(n)$. Recalling the fifth DTFT property from Table 2.1 and given

$$S_0(e^{j\omega}) = \frac{1}{L}\sum_{k=0}^{L-1} C(e^{j(\frac{\omega}{L}-\frac{\omega_b}{L}-\frac{2\pi}{L}k)}), \tag{3.27}$$

we have

$$X_0(e^{j\omega}) = \frac{1}{2L}\sum_{k=0}^{L-1} C(e^{j(\frac{\omega}{L}-\frac{\omega_b}{L}-\frac{2\pi}{L}k)}) + C^*(e^{-j(\frac{\omega}{L}+\frac{\omega_b}{L}+\frac{2\pi}{L}k)}). \tag{3.28}$$

Before computing $X_i(e^{\omega})$ for $1 \leq i \leq M-1$, we make a few observations and simplifications.

$$\begin{aligned} F_i^*(e^{-j\frac{\omega}{L}}) &= e^{+j\left[-\frac{\omega}{L}-q(-\frac{\omega}{L})\right]Ld_i} = e^{-j\left[\frac{\omega}{L}+q(-\frac{\omega}{L})\right]Ld_i} \\ &= e^{-j\left[\frac{\omega}{L}-q(\frac{\omega}{L})\right]Ld_i} = F_i(e^{j\frac{\omega}{L}}), \end{aligned}$$

where we have used the fact that $q(-\frac{\omega}{L}) = -q(\frac{\omega}{L})$. If

$$F_i(e^{j(\frac{\omega}{L}-\frac{2\pi}{L}k)}) = e^{-j\left[\frac{\omega}{L}-\frac{2\pi}{L}k-q(\frac{\omega}{L}-\frac{2\pi}{L}k)\right]Ld_i},$$

then let

$$f_{i,k}(e^{j\frac{\omega}{L}}) \;=\; \frac{F_i(e^{(j\frac{\omega}{L}-\frac{2\pi}{L}k)})}{F_i(e^{j\frac{\omega}{L}})} = e^{+j2\pi kd_i}e^{-j\left[q(\frac{\omega}{L})-q(\frac{\omega}{L}-\frac{2\pi}{L}k)\right]Ld_i} \tag{3.29}$$

which using

$$q\left(\frac{\omega}{L}\right) - q\left(\frac{\omega}{L}-\frac{2\pi}{L}k\right) = \begin{cases} 2\pi & -\pi L \le \omega < -\pi L + 2\pi k \\ 0 & -\pi L + 2\pi k \le \omega < \pi L \end{cases}$$

can be computed to be

$$\begin{aligned} f_{i,k}(e^{j\frac{\omega}{L}}) \;&=\; e^{+j2\pi kd_i} \times \begin{cases} e^{-j2\pi Ld_i} & -\pi L \le \omega < -\pi L + 2\pi k \\ 1 & -\pi L + 2\pi k \le \omega < \pi L \end{cases} \\ &= \begin{cases} e^{-j2\pi(L-k)d_i} & -\pi L \le \omega < -\pi L + 2\pi k \\ e^{+j2\pi kd_i} & -\pi L + 2\pi k \le \omega < \pi L\,. \end{cases} \end{aligned} \tag{3.30}$$

Note that $f_{i,0}(e^{j\frac{\omega}{L}}) = 1$. Using the relation $F_i(e^{j(\frac{\omega}{L}-\frac{2\pi}{L}k)}) = f_{i,k}(e^{j\frac{\omega}{L}})F_i(e^{j\frac{\omega}{L}})$ from (3.29), the expression (3.14) can be rewritten as

$$S_i(e^{j\omega}) = \frac{F_i(e^{j\frac{\omega}{L}})}{L}\sum_{k=0}^{L-1} f_{i,k}(e^{j\frac{\omega}{L}})G_i(e^{j(\frac{\omega}{L}-\frac{2\pi}{L}k)})C(e^{j(\frac{\omega}{L}-\frac{\omega_b}{L}-\frac{2\pi}{L}k)}) \tag{3.31}$$

which leads to

$$\begin{aligned} X_i(e^{j\omega}) = \frac{F_i(e^{j\frac{\omega}{L}})}{2L}\Bigg\{ &\sum_{k=0}^{L-1} f_{i,k}(e^{j\frac{\omega}{L}})G_i(e^{j(\frac{\omega}{L}-\frac{2\pi}{L}k)})C(e^{j(\frac{\omega}{L}-\frac{\omega_b}{L}-\frac{2\pi}{L}k)}) \\ &+ \sum_{k=0}^{L-1} f^*_{i,k}(e^{-j\frac{\omega}{L}})G^*_i(e^{-j(\frac{\omega}{L}+\frac{2\pi}{L}k)})C^*(e^{-j(\frac{\omega}{L}+\frac{\omega_b}{L}+\frac{2\pi}{L}k)})\Bigg\} \end{aligned} \tag{3.32}$$

for $1 \leq i \leq M-1$, where

$$f_{i,k}^*(e^{-j\frac{\omega}{L}}) = \begin{cases} e^{-j2\pi k d_i} & -\pi L \leq \omega < \pi L - 2\pi k \\ e^{+j2\pi(L-k)d_i} & \pi L - 2\pi k \leq \omega < \pi L \, . \end{cases} \tag{3.33}$$

Reconstruction: We first expand all the sequences $x_i(n)$ by a factor of L to compensate for the effect of undersampling.

$$\begin{aligned} X_0^e(e^{j\omega}) &= X_0(e^{j\omega})\Big|_{\uparrow L} = X_0(e^{j\omega L}) \\ &= \frac{1}{2L}\sum_{k=0}^{L-1} C(e^{j(\omega-\frac{\omega_b}{L}-\frac{2\pi}{L}k)}) + C^*(e^{-j(\omega+\frac{\omega_b}{L}+\frac{2\pi}{L}k)}) \end{aligned} \tag{3.34}$$

and

$$\begin{aligned} X_i^e(e^{j\omega}) &= X_i(e^{j\omega})\Big|_{\uparrow L} = X_i(e^{j\omega L}) \\ &= \frac{F_i(e^{j\omega})}{2L}\Bigg\{ \sum_{k=0}^{L-1} f_{i,k}(e^{j\omega}) G_i(e^{j(\omega-\frac{2\pi}{L}k)}) C(e^{j(\omega-\frac{\omega_b}{L}-\frac{2\pi}{L}k)}) \\ &\quad + \sum_{k=0}^{L-1} f_{i,k}^*(e^{-j\omega}) G_i^*(e^{-j(\omega+\frac{2\pi}{L}k)}) C^*(e^{-j(\omega+\frac{\omega_b}{L}+\frac{2\pi}{L}k)}) \Bigg\} \end{aligned} \tag{3.35}$$

for $1 \leq i \leq M-1$, where

$$f_{i,k}(e^{j\omega}) = \begin{cases} e^{-j2\pi(L-k)d_i} & -\pi \leq \omega < -\pi + \frac{2\pi}{L}k \\ e^{+j2\pi k d_i} & -\pi + \frac{2\pi}{L}k \leq \omega < \pi \end{cases} \tag{3.36}$$

and

$$f_{i,k}^*(e^{-j\omega}) = \begin{cases} e^{-j2\pi k d_i} & -\pi \leq \omega < \pi - \frac{2\pi}{L}k \\ e^{+j2\pi(L-k)d_i} & \pi - \frac{2\pi}{L}k \leq \omega < \pi \, . \end{cases} \tag{3.37}$$

In time domain, $L-1$ zeros are inserted between the consecutive samples of $x_i(n)$,

$$x_i^e(n) = x_i(n)\Big|_{\uparrow L} = \begin{cases} x_i(\frac{n}{L}) & n = 0, \pm L, \pm 2L, \ldots \\ 0 & \text{otherwise}\,. \end{cases} \tag{3.38}$$

Expressions (3.34–3.35) indicate that $X_i^e(e^{j\omega})$, $0 \le i \le M-1$ is a linear combination of a total of $2L$ envelope variants, the superposition of which makes it impossible to recover the desired $C(e^{j\omega})$ from a single channel alone. However, combining the information from all $X_i^e(e^{j\omega})$, we can write the problem in matrix-vector form as

$$\begin{bmatrix} X_0^e(e^{j\omega}) \\ F_1^{-1}(e^{j\omega})X_1^e(e^{j\omega}) \\ \vdots \\ F_i^{-1}(e^{j\omega})X_i^e(e^{j\omega}) \\ \vdots \\ F_{M-1}^{-1}(e^{j\omega})X_{M-1}^e(e^{j\omega}) \end{bmatrix} = \mathbf{M}(e^{j\omega}) \begin{bmatrix} \mathbf{C}(e^{j\omega}) \\ \mathbf{C}^*(e^{-j\omega}) \end{bmatrix}, \tag{3.39}$$

where

$$\mathbf{C}(e^{j\omega}) = \begin{bmatrix} C(e^{j(\omega - \frac{\omega_b}{L})}) \\ \vdots \\ C(e^{j(\omega - \frac{\omega_b}{L} - \frac{2\pi}{L}k)}) \\ \vdots \\ C(e^{j(\omega - \frac{\omega_b}{L} - \frac{2\pi}{L}(L-1))}) \end{bmatrix} \tag{3.40}$$

is an $L \times 1$ vector and complex conjugation is performed element-wise. The $M \times 2L$ matrix $\mathbf{M}(e^{j\omega})$ is given by

$$\mathbf{M}(e^{j\omega}) = \frac{1}{2L}\begin{bmatrix} \mathbf{P}(e^{j\omega}) & \mathbf{P}^*(e^{-j\omega}) \end{bmatrix} \tag{3.41}$$

with the matrix

$$\mathbf{P}(e^{j\omega}) = \begin{bmatrix} 1 & \cdots & 1 & \cdots & 1 \\ G_1(e^{j\omega}) & \cdots & f_{1,k}(e^{j\omega})G_1(e^{j(\omega-\frac{2\pi}{L}k)}) & \cdots & f_{1,L-1}(e^{j\omega})G_1(e^{j(\omega-\frac{2\pi}{L}(L-1))}) \\ \vdots & \ddots & \vdots & \ddots & \vdots \\ G_i(e^{j\omega}) & \cdots & f_{i,k}(e^{j\omega})G_i(e^{j(\omega-\frac{2\pi}{L}k)}) & \cdots & f_{i,L-1}(e^{j\omega})G_i(e^{j(\omega-\frac{2\pi}{L}(L-1))}) \\ \vdots & \ddots & \vdots & \ddots & \vdots \\ G_{M-1}(e^{j\omega}) & \cdots & f_{M-1,k}(e^{j\omega})G_{M-1}(e^{j(\omega-\frac{2\pi}{L}k)}) & \cdots & f_{M-1,L-1}(e^{j\omega})G_{M-1}(e^{j(\omega-\frac{2\pi}{L}(L-1))}) \end{bmatrix} \tag{3.42}$$

being of size $M \times L$. In (3.41), * refers to complex conjugation of each entry of $\mathbf{P}(e^{j\omega})$ without applying the transpose operator to the matrix. The first row of $\mathbf{M}(e^{j\omega})$ consists of all ones and is the information row associated with $X_0^e(e^{j\omega})$ from (3.34).

The matrix $\mathbf{M}(e^{j\omega})$ is a function of timing skews d_i. From (3.39), envelope reconstruction entails inverting $\mathbf{M}(e^{j\omega})$ so a set that characterizes the *forbidden timing skews* can be expressed as

$$\mathcal{F} = \big\{(d_1, \ldots, d_i, \ldots, d_{M-1}) \;\big|\; \mathbf{M}^{\text{inv}}(e^{j\omega}) \text{ does not exist}\big\}, \tag{3.43}$$

where $\mathbf{M}^{\text{inv}}(e^{j\omega})$ is a generalized inverse of $\mathbf{M}(e^{j\omega})$ of size $2L \times M$ that satisfies $\mathbf{M}^{\text{inv}}(e^{j\omega})\mathbf{M}(e^{j\omega}) = \mathbf{I}_{2L}$ (the identity matrix of size $2L \times 2L$) and is given by

$$\mathbf{M}^{\text{inv}}(e^{j\omega}) = \begin{cases} \mathbf{M}^{-1}(e^{j\omega}) & \text{if } M \text{ is even} \\ \mathbf{M}_{\text{left}}^{-1}(e^{j\omega}) & \text{if } M \text{ is odd} \end{cases} \tag{3.44}$$

with

$$\mathbf{M}_{\text{left}}^{-1}(e^{j\omega}) = \big(\mathbf{M}^H(e^{j\omega})\mathbf{M}(e^{j\omega})\big)^{-1}\mathbf{M}^H(e^{j\omega}), \tag{3.45}$$

where ^{H} denotes the Hermitian transpose. The left inverse $\mathbf{M}_{\text{left}}^{-1}(e^{j\omega})$ exists if $\mathbf{M}(e^{j\omega})$ has full column rank, i.e., $\text{rank}(\mathbf{M}(e^{j\omega})) = 2L$. The component of interest on the RHS of (3.39)

is $C(e^{j(\omega-\frac{\omega_b}{L})})$ which can be expressed as

$$C\big(e^{j(\omega-\frac{\omega_b}{L})}\big) = \underbrace{\begin{bmatrix}1 & 0 & \dots & 0\end{bmatrix}}_{1\times 2L}\mathbf{M}^{\text{inv}}(e^{j\omega})\begin{bmatrix}1 & & & \\ & F_1^{-1}(e^{j\omega}) & & 0 \\ & & \ddots & \\ & 0 & & F_{M-1}^{-1}(e^{j\omega})\end{bmatrix}\begin{bmatrix}X_0^e(e^{j\omega}) \\ \vdots \\ X_i^e(e^{j\omega}) \\ \vdots \\ X_{M-1}^e(e^{j\omega})\end{bmatrix}. \tag{3.46}$$

If we define a row vector of reconstruction filters as

$$\begin{aligned}\mathbf{H}(e^{j\omega}) &= \big[H_0(e^{j\omega}),\dots,H_i(e^{j\omega}),\dots,H_{M-1}(e^{j\omega})\big] \\ &= \mathbf{\Phi}(e^{j\omega})\,\text{diag}\big\{1,F_1^{-1}(e^{j\omega}),\dots,F_i^{-1}(e^{j\omega}),\dots,F_{M-1}^{-1}(e^{j\omega})\big\}\end{aligned} \tag{3.47}$$

with

$$\begin{aligned}\mathbf{\Phi}(e^{j\omega}) &= \big[\Phi_0(e^{j\omega}),\dots,\Phi_i(e^{j\omega}),\dots,\Phi_{M-1}(e^{j\omega})\big] \\ &= \underbrace{\begin{bmatrix}1 & 0 & \dots & 0\end{bmatrix}}_{1\times 2L}\mathbf{M}^{\text{inv}}(e^{j\omega}),\end{aligned} \tag{3.48}$$

then (3.46) can be compactly written as

$$C\big(e^{j(\omega-\frac{\omega_b}{L})}\big) = \sum_{i=0}^{M-1} H_i(e^{j\omega})X_i^e(e^{j\omega}). \tag{3.49}$$

In time domain, the filter $H_i(e^{j\omega})$ for $1 \le i \le M-1$ is simply a noninteger advance of $\Phi_i(e^{j\omega})$. We have

$$\begin{aligned}h_0(n) = \phi_0(n) &\overset{\mathcal{FT}}{\longleftrightarrow} H_0(e^{j\omega}) = \Phi_0(e^{j\omega}) \\ h_i(n) = \phi_i(n+Ld_i) &\overset{\mathcal{FT}}{\longleftrightarrow} H_i(e^{j\omega}) = \Phi_i(e^{j\omega})F_i^{-1}(e^{j\omega}),\end{aligned} \tag{3.50}$$

where

$$\phi_i(n + Ld_i) = \phi_i(n) * \frac{\sin(\pi(n + Ld_i))}{\pi(n + Ld_i)}. \tag{3.51}$$

Note from (3.48) that only the first row of $\mathbf{M}^{\text{inv}}(e^{j\omega})$ is needed for computing the filters $H_i(e^{j\omega})$, $0 \le i \le M-1$. Since the entries of the matrix $\mathbf{P}(e^{j\omega})$ in (3.42) are piecewise constant over $[-\pi, \pi]$, the matrix $\mathbf{M}(e^{j\omega})$, its inverse $\mathbf{M}^{\text{inv}}(e^{j\omega})$, and filters $H_i(e^{j\omega})$ are all piecewise constant as well. Table 3.1 below provides comprehensive instructions for computing the impulse responses of reconstruction filters.

Steps for computing $h_i(n)$, $0 \le i \le M-1$	
1.	Compute $L = \lfloor M/2 \rfloor$, ℓ (3.1), and ω_b (3.2).
2.	Choose a vector of TIADC timing skews $(d_1, \ldots, d_i, \ldots, d_{M-1})$.
3.	Compute the piecewise constant filters $f_{i,k}(e^{j\omega})$ (3.36) and $G_i(e^{j(\omega-(2\pi/L)k)})$ (3.22–3.23) for $1 \le i \le M-1$, $1 \le k \le L-1$.
4.	Compute the piecewise constant matrix $\mathbf{M}(e^{j\omega})$ (3.41–3.42) for $\omega \in [-\pi, \pi)$.
5.	Check $\text{rank}(\mathbf{M}(e^{j\omega})) = 2L$ in all frequency segments within the interval $[-\pi, \pi]$. If not, go back to step 2 and pick another timing skew vector.
6.	Compute the piecewise constant matrix $\mathbf{M}^{\text{inv}}(e^{j\omega})$ (3.44–3.45) for $\omega \in [-\pi, \pi)$.
7.	For $0 \le i \le M-1$, let $\Phi_i(e^{j\omega}) = \mathbf{M}^{\text{inv}}_{1,i}(e^{j\omega})$ and compute its impulse response $\phi_i(n)$.
8.	Let $h_0(n) = \phi_0(n)$ and $h_i(n) = \phi_i(n + Ld_i)$, $1 \le i \le M-1$, where $\phi_i(n + Ld_i)$ is obtained through a noninteger advance filter as specified in (3.51).

Table 3.1: Detailed step-by-step instructions for computing the impulse responses of reconstruction filters $H_0(e^{j\omega}), \ldots, H_{M-1}(e^{j\omega})$.

Since $C(e^{j(\omega-\frac{\omega_b}{L})})$ (3.49) is the DTFT of the modulated signal $r^{[L]}(n) = c^{[L]}(n)e^{j(\omega_b/L)n}$, $c^{[L]}(n)$ can be recovered by demodulating $r^{[L]}(n)$. Given $c^{[L]}(n) = a^{[L]}(n) + jb^{[L]}(n)$ which follows from the definition of the complex envelope in Section 2.4, the sampled in-phase signal $a^{[L]}(n)$ and quadrature signal $b^{[L]}(n)$ can be easily decoupled from the knowledge of $c^{[L]}(n)$ by extracting its real and imaginary parts, respectively.

The block diagram in Fig. 3.4 shows complete reconstruction of $c^{[L]}(n)$ requires M L-fold

expanders, M filters, and one modulator. To approximate the filters by causal FIR filters of order $N = 2K$, a K-samples delay needs to be included in the implementation as demonstrated in Fig. 3.5. The new filters $\check{H}_i(e^{j\omega})$ with $i = 0, \ldots, M-1$ are FIR approximations of the filters $e^{-j\omega K} H_i(e^{j\omega})$ obtained by applying a Kaiser window of length $2K+1$ to their ideal impulse responses. In this case, the output $\hat{c}^{[L]}(n-K)$ of the causal reconstruction block diagram is only an estimate of the complex envelope at time $n-K$. While the sequences $x_i(n)$ are real, the impulse responses $h_i(n)$ are in general complex. Therefore, the complexity of the reconstruction technique depicted in Fig. 3.5 when FIR filters of order N are used is $2M(N+1)$ real multiplications and one complex multiplication per complex envelope sample (the complex multiplication is needed to implement the discrete-time demodulation by $e^{-j(\omega_b/L)(n-K)}$).

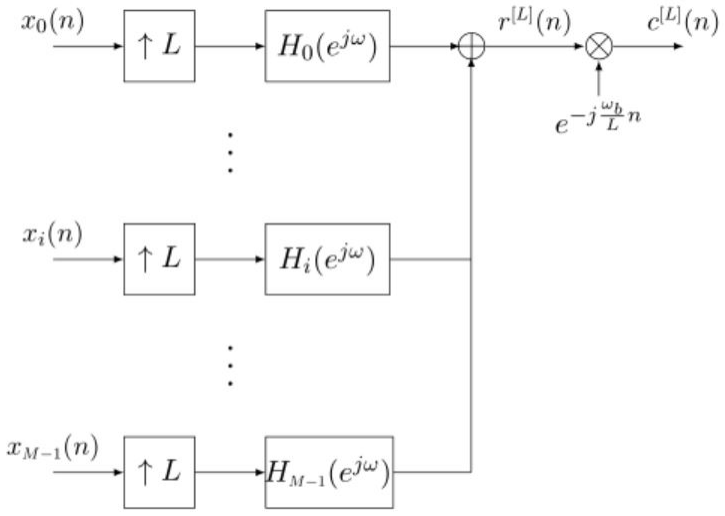


Figure 3.4: A mathematical model for recovery of $c^{[L]}(n)$ from $x_0(n), \ldots, x_{M-1}(n)$.

The use of FIR filters to reconstruct the sampled complex envelope $c^{[L]}(n)$ of a bandpass signal by processing M nonuniformly interleaved sample sequences $x_i(n)$, $0 \leq i \leq M-1$ can be justified by observing that it was shown in Section IV of [78] that the uniform samples of a bandlimited signal can be reconstructed to an arbitrary degree of accuracy by finite length interpolation of nonuniform samples as long as the average sampling rate of this nonuniform sampling scheme is above the Nyquist rate. However, two noteworthy differences with [78] is

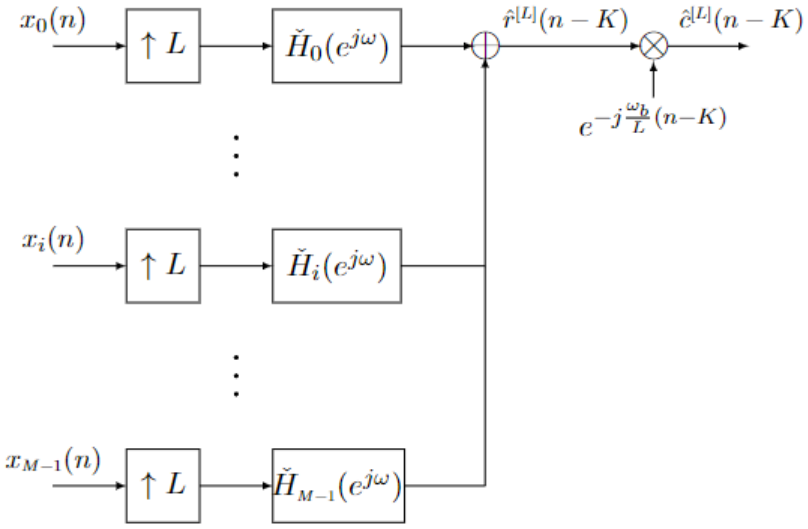


Figure 3.5: A causal implementation of the reconstruction block diagram in Fig. 3.4

that we consider here the reconstruction of the sampled envelope instead of the signal itself, and because each sequence $x_i(n)$ is uniformly sampled, FIR filters can be employed instead of more general interpolation filters.

Although our proposed TIADC complex envelope sampling and reconstruction technique described in the last two sections presents some apparent similarities with the multicoset sampling method described in [79–81], the two methods are actually different. The multicoset sampling technique considers a fast sampling scheme, which in our notation would correspond to using a sampling period T_s, and given the uniform samples $x(n) = x_c(nT_s)$, it retains only a finite number $p < M$ of substreams $x_i(m) = x(mM + c_i)$ with c_i integer satisfying $0 \leq c_1 < c_2 < \ldots < c_p < M - 1$. Roughly speaking coset sampling retains only p out of M uniform samples for each sample block of length M, and the "cosets" correspond to the subgrid $\{n = mM + c_i, m \in \mathbb{Z}\}$ of $\mathbb{Z}$. Like all TIADC sampling techniques, our method produces also M interlaced sequences $x_i(m) = x_c((m + d_i)MT_s)$ where $d_0 = 0 < d_1 < \ldots < d_{M-1} < 1$ represent the irregular timing skews, but $d_iM = c_i$ is usually *not integer*. Accordingly, the reconstruction technique described in [80, 81] which relies on the construction of left inverses of Vandermonde matrices is not applicable. Thus our bandpass sampling technique relies on a more general TIADC structure than considered

in multicoset sampling. Note also that we employ all M sub-ADC sequences instead of p out of M substreams. The problem we consider is both simpler and more complicated than the multiband sampling problem addressed by multicoset sampling techniques. It is simpler, since we consider bandpass signals with frequency content over $[\Omega_L, \Omega_H]$ and $[-\Omega_H, -\Omega_L]$, whereas for multiband sampling, the frequency content usually consists of several disjoint bands in an interval of length B. Multicoset sampling is able to achieve sampling rates approaching the Landau rate [82] which is below the Nyquist rate $2B$ since the effective bandwidth of the signal is less than B. This can be extremely efficient when the signal has a sparse spectrum. Our problem is also more difficult, since the proposed receiver is not concerned with sampling and reconstructing the received analog signal, but rather its complex envelope, so it encompasses in a single DSP device an entire communications receiver front-end, which typically would involve demodulation, I and Q components separation, and sampling. A few general analogies do exist between our proposed TIADC sampling method and multicoset sampling. For example, the invertibility condition for matrix $\mathbf{M}(e^{j\omega})$ in equation (3.41) (which is used to characterize the forbidden timing skews) is very roughly similar to the full row rank condition of Vandermonde matrix $\mathbf{W}_L(\mathcal{C}, \mathcal{K})$ in [80].

3.3 Reconstruction for $M = 2, 3, 4$

In this section, we derive and analyze reconstruction details for the two-channel, three-channel, and four-channel TIADC. When $M = 2, 3$ with $L = 1$, the sub-ADC sampling frequency Ω_s' defined in (3.5) is greater than or equal to B (the Nyquist rate of $c_c(t)$). This ensures the only form of aliasing present is from overlap between the negative and positive spectral images. For $L \geq 2$, Ω_s' can be less than B which introduces additional aliasing from frequency overlap occurring between neighboring positive copies independent of negative spectral images and frequency overlap occurring between neighboring negative copies independent of positive spectral images. This is observed in the case of four channels

where robust filters are needed to remove the effects of two sources of aliasing.

Two-Channel TIADC

Since $M = 2$ and $L = 1$, compressors are void in the sampling model in Fig. 3.3, and expanders drop from the reconstruction model in Fig. 3.4. We drop the subscript on d, $F(e^{j\omega})$, and $G(e^{j\omega})$ since the timing skew and filters exist only for one channel. The reconstruction matrix has simple form

$$\mathbf{M}(e^{j\omega}) = \frac{1}{2}\begin{bmatrix} 1 & 1 \\ G(e^{j\omega}) & G^*(e^{-j\omega}) \end{bmatrix} \tag{3.52}$$

and is invertible as long as its determinant

$$D(e^{j\omega}) = \det\big(\mathbf{M}(e^{j\omega})\big) = \frac{1}{4}(G^*(e^{-j\omega}) - G(e^{j\omega})) \tag{3.53}$$

is nonzero. We find

$$D(e^{j\omega}) = \begin{cases} \frac{j}{2}\sin(2\pi\ell d) & 0 \le |\omega| \le \pi - |\omega_b| \\ \frac{j}{2}e^{j\pi\mathrm{sgn}(\omega)d}\sin(\pi(2\ell + \mathrm{sgn}(\omega_b))d) & \pi - |\omega_b| < |\omega| < \pi\,. \end{cases} \tag{3.54}$$

Accordingly, the determinant $D(e^{j\omega})$ will be nonzero as long as the timing skew d is such that both $\sin(2\pi\ell d)$ and $\sin(\pi(2\ell + \mathrm{sgn}(\omega_b))d)$ are nonzero. If integers m, q are superscripts on d, the set of forbidden timing skews defined in (3.43) for the two-channel TIADC can be expressed as

$$\mathcal{F} = \left\{ \begin{array}{l|c} d^m = \frac{m}{2\ell} & 1 \le m \le 2\ell - 1 \\ d^q = \frac{q}{2\ell + \mathrm{sgn}(\omega_b)} & 1 \le q \le 2\ell + \mathrm{sgn}(\omega_b) - 1 \end{array} \right\}. \tag{3.55}$$

Note that for $m = \ell$, we have $d^m = 1/2$, so as expected, the half sampling period is a forbidden timing skew, since in this case the TIADC reduces to a uniform ADC with sampling period $T_s = T_s'/2$. Also, observe that the assumption that Ω_c is not in the baseband, which corresponds to $\ell \ge 1$, is needed to ensure the recovery of $C(e^{j(\omega-\omega_b)})$, since when $\ell = 0$,

$D(e^{j\omega}) \equiv 0$ over the band $-(\pi - |\omega_b|) \leq \omega \leq \pi - |\omega_b|$.

When $\mathbf{M}(e^{j\omega})$ is invertible for all ω, we find

$$\begin{bmatrix} H_0(e^{j\omega}) & H_1(e^{j\omega}) \end{bmatrix} = \frac{1}{2D(e^{j\omega})} \begin{bmatrix} G^*(e^{-j\omega}) & -F^{-1}(e^{j\omega}) \end{bmatrix}. \tag{3.56}$$

Substituting the expressions for $D(e^{j\omega})$ and $G(e^{j\omega})$ inside (3.56) gives

$$H_0(e^{j\omega}) = \frac{e^{j2\pi\ell d}}{j\sin(2\pi\ell d)} = 1 - j\cot(2\pi\ell d) \tag{3.57}$$

for $|\omega| \leq \pi - |\omega_b|$ and

$$\begin{aligned} H_0(e^{j\omega}) &= \frac{e^{j\pi(2\ell+\mathrm{sgn}(\omega_b))d}}{j\sin(\pi(2\ell+\mathrm{sgn}(\omega_b))d)} \\ &= 1 - j\cot(\pi(2\ell+\mathrm{sgn}(\omega_b))d) \end{aligned} \tag{3.58}$$

for $\pi - |\omega_b| < |\omega| \leq \pi$. Observe $\Re\{H_0(e^{j\omega})\} = 1$ for all ω and the filter $\Im\{H_0(e^{j\omega})\}$ is a real and even function of ω and thus its impulse response is also real and even. So even though the filter $H_0(e^{j\omega})$ is complex, its implementation requires a single real filter. Similarly, for

$$H_1(e^{j\omega}) = \Phi_1(e^{j\omega})F^{-1}(e^{j\omega}), \tag{3.59}$$

we find

$$\Phi_1(e^{j\omega}) = \frac{j}{\sin(2\pi\ell d)} \tag{3.60}$$

for $|\omega| \leq \pi - |\omega_b|$ and

$$\Phi_1(e^{j\omega}) = \frac{je^{-j\pi\mathrm{sgn}(\omega)d}}{\sin(\pi(2\ell+\mathrm{sgn}(\omega_b))d)} \tag{3.61}$$

for $\pi - |\omega_b| < |\omega| < \pi$. The impulse responses of the two filters $H_0(e^{j\omega})$ and $H_1(e^{j\omega})$ can be

evaluated in closed form by taking the inverse Fourier transform. They are given by

$$\Re\{h_0(n)\} = \delta(n), \tag{3.62}$$

$$\begin{aligned} \Im\{h_0(n)\} &= -\cot(\pi(2\ell + \mathrm{sgn}(\omega_b))d)\delta(n) \\ &\quad + \big(\cot(\pi(2\ell + \mathrm{sgn}(\omega_b))d) - \cot(2\pi\ell d)\big) \times \frac{\sin((\pi - |\omega_b|)n)}{\pi n}, \end{aligned} \tag{3.63}$$

and

$$\Re\{\phi_1(n)\} = 0, \tag{3.64}$$

$$\begin{aligned} \Im\{\phi_1(n)\} &= \frac{\sin((\pi - |\omega_b|)n)}{\pi n \sin(2\pi\ell d)} \\ &\quad - \frac{\sin((\pi - |\omega_b|)n - \pi d)}{\pi n \sin(\pi(2\ell + \mathrm{sgn}(\omega_b)d)}\,, \end{aligned} \tag{3.65}$$

$$h_1(n) = \phi_1(n + d). \tag{3.66}$$

Three-Channel TIADC

We have $M = 3$ and $L = 1$, so again compressors and expanders become void. The non-square reconstruction matrix $\mathbf{M}(e^{j\omega})$ is given by

$$\mathbf{M}(e^{j\omega}) = \frac{1}{2}\begin{bmatrix} 1 & 1 \\ G_1(e^{j\omega}) & G_1^*(e^{-j\omega}) \\ G_2(e^{j\omega}) & G_2^*(e^{-j\omega}) \end{bmatrix} \tag{3.67}$$

which has a left inverse if $\mathrm{rank}(\mathbf{M}(e^{j\omega})) = 2$. Equivalently, the intersection of the sets with values that cause the subdeterminants of the matrix to be zero should be null. We explore

this further. Let

$$\mathbf{M_1}(e^{j\omega}) = \frac{1}{2}\begin{bmatrix} 1 & 1 \\ G_1(e^{j\omega}) & G_1^*(e^{-j\omega}) \end{bmatrix} \tag{3.68}$$

$$\mathbf{M_2}(e^{j\omega}) = \frac{1}{2}\begin{bmatrix} 1 & 1 \\ G_2(e^{j\omega}) & G_2^*(e^{-j\omega}) \end{bmatrix} \tag{3.69}$$

$$\mathbf{M_3}(e^{j\omega}) = \frac{1}{2}\begin{bmatrix} G_1(e^{j\omega}) & G_1^*(e^{-j\omega}) \\ G_2(e^{j\omega}) & G_2^*(e^{-j\omega}) \end{bmatrix} \tag{3.70}$$

be the submatrices of $\mathbf{M}(e^{j\omega})$. The determinants of these 2×2 matrices and when they are equal to zero can be computed in a similar way as for the two-channel TIADC. If integers $m_1, m_2, m_3, q_1, q_2, q_3$ are superscripts, then

$$\begin{aligned} D_1(e^{j\omega}) &= \det\big(\mathbf{M_1}(e^{j\omega})\big) = \frac{1}{4}(G_1^*(e^{-j\omega}) - G_1(e^{j\omega})) \\ &= \begin{cases} \frac{j}{2}\sin(2\pi\ell d_1) & 0 \le |\omega| \le \pi - |\omega_b| \\ \frac{j}{2}e^{j\pi\mathrm{sgn}(\omega)d_1}\sin(\pi(2\ell + \mathrm{sgn}(\omega_b))d_1) & \pi - |\omega_b| < |\omega| < \pi\,, \end{cases} \end{aligned} \tag{3.71}$$

$$\mathcal{F}_1 = \left\{ \begin{array}{l} d_1^{m_1} = \frac{m_1}{2\ell} \\ d_1^{q_1} = \frac{q_1}{2\ell + \mathrm{sgn}(\omega_b)} \end{array} \middle| \begin{array}{c} D_1(e^{j\omega}) = 0,\ 1 \le m_1 \le 2\ell - 1 \\ 1 \le q_1 \le 2\ell + \mathrm{sgn}(\omega_b) - 1 \end{array} \right\}, \tag{3.72}$$

$$\begin{aligned} D_2(e^{j\omega}) &= \det\big(\mathbf{M_2}(e^{j\omega})\big) = \frac{1}{4}(G_2^*(e^{-j\omega}) - G_2(e^{j\omega})) \\ &= \begin{cases} \frac{j}{2}\sin(2\pi\ell d_2) & 0 \le |\omega| \le \pi - |\omega_b| \\ \frac{j}{2}e^{j\pi\mathrm{sgn}(\omega)d_2}\sin(\pi(2\ell + \mathrm{sgn}(\omega_b))d_2) & \pi - |\omega_b| < |\omega| < \pi\,, \end{cases} \end{aligned} \tag{3.73}$$

$$\mathcal{F}_2 = \left\{ \begin{array}{l} d_2^{m_2} = \frac{m_2}{2\ell} \\ d_2^{q_2} = \frac{q_2}{2\ell + \mathrm{sgn}(\omega_b)} \end{array} \middle| \begin{array}{c} D_2(e^{j\omega}) = 0,\ 1 \le m_2 \le 2\ell - 1 \\ 1 \le q_2 \le 2\ell + \mathrm{sgn}(\omega_b) - 1 \end{array} \right\}, \tag{3.74}$$

$$
\begin{aligned}
D_3(e^{j\omega}) &= \det\big(\mathbf{M_3}(e^{j\omega})\big) = \frac{1}{4}(G_1(e^{j\omega})G_2^*(e^{-j\omega}) - G_2(e^{j\omega})G_1^*(e^{-j\omega})) \\
&= \begin{cases} \frac{j}{2}\sin(2\pi\ell(d_2-d_1)) & 0 \le |\omega| \le \pi - |\omega_b| \\ \frac{j}{2}e^{j\pi\mathrm{sgn}(\omega)(d_1+d_2)}\sin(\pi(2\ell+\mathrm{sgn}(\omega_b))(d_2-d_1)) & \pi-|\omega_b| < |\omega| < \pi\,, \end{cases}
\end{aligned} \tag{3.75}
$$

$$
\mathcal{F}_3 = \left\{ \begin{array}{l} (d_2-d_1)^{m_3} = \frac{m_3}{2\ell} \\ (d_2-d_1)^{q_3} = \frac{q_3}{2\ell+\mathrm{sgn}(\omega_b)} \end{array} \middle| \begin{array}{c} D_3(e^{j\omega}) = 0,\ 1 \le m_3 \le 2\ell-1 \\ 1 \le q_3 \le 2\ell+\mathrm{sgn}(\omega_b)-1 \end{array} \right\}. \tag{3.76}
$$

Using these expressions, the set of forbidden timing skews for the three-channel TIADC is given by

$$
\begin{aligned}
\mathcal{F} &= \mathcal{F}_1 \cap \mathcal{F}_2 \cap \mathcal{F}_3 \\
&= \left\{ \begin{array}{l} (d_1^{m_1}, d_2^{m_2}) = \frac{1}{2\ell}(m_1, m_2) \\ (d_1^{q_1}, d_2^{q_2}) = \frac{1}{2\ell+\mathrm{sgn}(\omega_b)}(q_1, q_2) \end{array} \middle| \begin{array}{c} 1 \le m_1 < m_2 \le 2\ell-1 \\ 1 \le q_1 < q_2 \le 2\ell+\mathrm{sgn}(\omega_b)-1 \end{array} \right\},
\end{aligned} \tag{3.77}
$$

where we have used the fact that $d_2 > d_1$ (making it so $m_1 = 2\ell-1$, $q_1 = 2\ell+\mathrm{sgn}(\omega_b)-1$ drop from $\mathcal{F}_1$ and $m_2 = 1$, $q_2 = 1$ drop from $\mathcal{F}_2$).

If we define and simplify

$$
\begin{aligned}
D(e^{j\omega}) &= \det\big(4\mathbf{M}^H(e^{j\omega})\mathbf{M}(e^{j\omega})\big) \\
&= 9 - \|1 + G_1(e^{j\omega})G_1(e^{-j\omega}) + G_2(e^{j\omega})G_2(e^{-j\omega})\|^2 \\
&= 9 - \big(1 + G_1(e^{j\omega})G_1(e^{-j\omega}) + G_2(e^{j\omega})G_2(e^{-j\omega})\big) \times \\
&\qquad \big(1 + G_1(e^{j\omega})G_1(e^{-j\omega}) + G_2(e^{j\omega})G_2(e^{-j\omega})\big)^* \\
&= 6 - 2\Re\{G_1(e^{j\omega})G_1(e^{-j\omega})\} - 2\Re\{G_2(e^{j\omega})G_2(e^{-j\omega})\} - \\
&\qquad 2\Re\{G_1(e^{j\omega})G_1(e^{-j\omega})G_2^*(e^{j\omega})G_2^*(e^{-j\omega})\},
\end{aligned} \tag{3.78}
$$

then

$$
\mathbf{M}_{\text{left}}^{-1}(e^{j\omega}) = \frac{2}{D(e^{j\omega})}\times
$$

$$\begin{bmatrix} 2 - G_1^*(e^{j\omega})G_1^*(e^{-j\omega}) & 2G_1^*(e^{j\omega}) - & 2G_2^*(e^{j\omega}) - \\ \quad -G_2^*(e^{j\omega})G_2^*(e^{-j\omega}) & G_1(e^{-j\omega})\big(1 + G_2^*(e^{j\omega})G_2^*(e^{-j\omega})\big) & G_2(e^{-j\omega})\big(1 + G_1^*(e^{j\omega})G_1^*(e^{-j\omega})\big) \\ 2 - G_1(e^{j\omega})G_1(e^{-j\omega}) & 2G_1(e^{-j\omega}) - & 2G_2(e^{-j\omega}) - \\ \quad -G_2(e^{j\omega})G_2(e^{-j\omega}) & G_1^*(e^{j\omega})\big(1 + G_2(e^{j\omega})G_2(e^{-j\omega})\big) & G_2^*(e^{j\omega})\big(1 + G_1(e^{j\omega})G_1(e^{-j\omega})\big) \end{bmatrix}. \tag{3.79}$$

In calculating both (3.78) and (3.79), we have made use of simplifications

$$G_i(e^{j\omega})G_i^*(e^{j\omega}) = \|G_i(e^{j\omega})\|^2 = 1$$
$$G_i(e^{-j\omega})G_i^*(e^{-j\omega}) = \|G_i(e^{-j\omega})\|^2 = 1$$

for $i = 1, 2$. These follow directly from definitions (3.22–3.23) which can be further used to find

$$D(e^{j\omega}) = \begin{cases} D_1(d_1, d_2, \ell) & 0 \le |\omega| \le \pi - |\omega_b| \\ D_2(d_1, d_2, \ell) & \pi - |\omega_b| < |\omega| \le \pi \end{cases} \tag{3.80}$$

with

$$\begin{aligned} D_1(d_1, d_2, \ell) = 6 \;-\; & 2\big[\cos(2\pi 2\ell d_1) + \cos(2\pi 2\ell d_2) \\ & + \cos(2\pi 2\ell d_1)\cdot\cos(2\pi 2\ell d_2) + \sin(2\pi 2\ell d_1)\cdot\sin(2\pi 2\ell d_2)\big] \end{aligned} \tag{3.81}$$

and

$$\begin{aligned} D_2(d_1, d_2, \ell) = 6 \;-\; & 2\big[\cos(2\pi(2\ell + \mathrm{sgn}(\omega_b))d_1) + \cos(2\pi(2\ell + \mathrm{sgn}(\omega_b))d_2) \\ & + \cos(2\pi(2\ell + \mathrm{sgn}(\omega_b))d_1)\cdot\cos(2\pi(2\ell + \mathrm{sgn}(\omega_b))d_2) \\ & + \sin(2\pi(2\ell + \mathrm{sgn}(\omega_b))d_1)\cdot\sin(2\pi(2\ell + \mathrm{sgn}(\omega_b))d_2)\big]. \end{aligned} \tag{3.82}$$

The filters given by

$$\begin{aligned}\mathbf{\Phi}(e^{j\omega}) &= \big[\Phi_0(e^{j\omega}), \Phi_1(e^{j\omega}), \Phi_2(e^{j\omega})\big] \\ &= [1 \;\; 0]\mathbf{M}_{\text{left}}^{-1}(e^{j\omega}) \\ &= \frac{2}{D(e^{j\omega})}\times\end{aligned}$$

$$\begin{bmatrix} 2 - G_1^*(e^{j\omega})G_1^*(e^{-j\omega}) & 2G_1^*(e^{j\omega}) - & 2G_2^*(e^{j\omega}) - \\ -G_2^*(e^{j\omega})G_2^*(e^{-j\omega}) & G_1(e^{-j\omega})\big(1 + G_2^*(e^{j\omega})G_2^*(e^{-j\omega})\big) & G_2(e^{-j\omega})\big(1 + G_1^*(e^{j\omega})G_1^*(e^{-j\omega})\big) \end{bmatrix} \tag{3.83}$$

can now be computed in closed form.

$$\Phi_0(e^{j\omega}) = \begin{cases} \Phi_0^1 & 0 \le |\omega| \le \pi - |\omega_b| \\ \Phi_0^2 & \pi - |\omega_b| < |\omega| < \pi\,, \end{cases} \tag{3.84}$$

where

$$\begin{aligned}\Phi_0^1 = \frac{2}{D_1(d_1, d_2, \ell)}\big[&2 - \cos(2\pi 2\ell d_1) - \cos(2\pi 2\ell d_2) \\ &-j\big(\sin(2\pi 2\ell d_1) + \sin(2\pi 2\ell d_2)\big)\big]\end{aligned} \tag{3.85}$$

and

$$\begin{aligned}\Phi_0^2 = \frac{2}{D_2(d_1, d_2, \ell)}\big[&2 - \cos(2\pi(2\ell + \text{sgn}(\omega_b))d_1) - \cos(2\pi(2\ell + \text{sgn}(\omega_b))d_2) \\ &-j\big(\sin(2\pi(2\ell + \text{sgn}(\omega_b))d_1) + \sin(2\pi(2\ell + \text{sgn}(\omega_b))d_2)\big)\big].\end{aligned} \tag{3.86}$$

$$\Phi_1(e^{j\omega}) = \begin{cases} \Phi_1^1 & -\pi < \text{sgn}(\omega_b)\cdot\omega < -(\pi - |\omega_b|) \\ \Phi_1^2 & 0 \le |\omega| \le \pi - |\omega_b| \\ \Phi_1^3 & \pi - |\omega_b| < \text{sgn}(\omega_b)\cdot\omega < \pi\,, \end{cases} \tag{3.87}$$

where

$$\begin{aligned}\Phi_1^1 &= \frac{2}{D_2(d_1,d_2,\ell)}\big[2\cos(2\pi(\ell+\mathrm{sgn}(\omega_b))d_1) - \cos(2\pi\ell d_1)\\ &- \cos(2\pi(\ell d_1 - (2\ell+\mathrm{sgn}(\omega_b))d_2)) + j\big(2\sin(2\pi(\ell+\mathrm{sgn}(\omega_b))d_1)\\ &+ \sin(2\pi\ell d_1) + \sin(2\pi(\ell d_1 - (2\ell+\mathrm{sgn}(\omega_b))d_2))\big)\big], \end{aligned} \tag{3.88}$$

$$\begin{aligned}\Phi_1^2 = \frac{2}{D_1(d_1,d_2,\ell)}\big[&\cos(2\pi\ell d_1) - \cos(2\pi\ell(d_1-2d_2))\\ &+j\big(3\sin(2\pi\ell d_1) + \sin(2\pi\ell(d_1-2d_2))\big)\big], \end{aligned} \tag{3.89}$$

and

$$\begin{aligned}\Phi_1^3 &= \frac{2}{D_2(d_1,d_2,\ell)}\big[2\cos(2\pi\ell d_1) - \cos(2\pi(\ell+\mathrm{sgn}(\omega_b))d_1)\\ &- \cos(2\pi((\ell+\mathrm{sgn}(\omega_b))d_1 - (2\ell+\mathrm{sgn}(\omega_b))d_2))\\ &+ j\big(2\sin(2\pi\ell d_1) + \sin(2\pi(\ell+\mathrm{sgn}(\omega_b))d_1)\\ &+ \sin(2\pi((\ell+\mathrm{sgn}(\omega_b))d_1 - (2\ell+\mathrm{sgn}(\omega_b))d_2))\big)\big]. \end{aligned} \tag{3.90}$$

$$\Phi_2(e^{j\omega}) = \begin{cases} \Phi_2^1 & -\pi < \mathrm{sgn}(\omega_b)\cdot\omega < -(\pi - |\omega_b|) \\ \Phi_2^2 & 0 \le |\omega| \le \pi - |\omega_b| \\ \Phi_2^3 & \pi - |\omega_b| < \mathrm{sgn}(\omega_b)\cdot\omega < \pi\,, \end{cases} \tag{3.91}$$

where

$$\begin{aligned}\Phi_2^1 &= \frac{2}{D_2(d_1,d_2,\ell)}\big[2\cos(2\pi(\ell+\mathrm{sgn}(\omega_b))d_2) - \cos(2\pi\ell d_2)\\ &- \cos(2\pi(\ell d_2 - (2\ell+\mathrm{sgn}(\omega_b))d_1)) + j\big(2\sin(2\pi(\ell+\mathrm{sgn}(\omega_b))d_2)\\ &+ \sin(2\pi\ell d_2) + \sin(2\pi(\ell d_2 - (2\ell+\mathrm{sgn}(\omega_b))d_1))\big)\big], \end{aligned} \tag{3.92}$$

$$\Phi_2^2 = \frac{2}{D_1(d_1,d_2,\ell)}\big[\cos(2\pi\ell d_2) - \cos(2\pi\ell(d_2-2d_1)) \\ +j\big(3\sin(2\pi\ell d_2) + \sin(2\pi\ell(d_2-2d_1))\big)\big], \tag{3.93}$$

and

$$\begin{aligned}\Phi_2^3 &= \frac{2}{D_2(d_1,d_2,\ell)}\big[2\cos(2\pi\ell d_2) - \cos(2\pi(\ell+\mathrm{sgn}(\omega_b))d_2) \\ &- \cos(2\pi((\ell+\mathrm{sgn}(\omega_b))d_2 - (2\ell+\mathrm{sgn}(\omega_b))d_1)) \\ &+ j\big(2\sin(2\pi\ell d_2) + \sin(2\pi(\ell+\mathrm{sgn}(\omega_b))d_2) \\ &+ \sin(2\pi((\ell+\mathrm{sgn}(\omega_b))d_2 - (2\ell+\mathrm{sgn}(\omega_b))d_1))\big)\big].\end{aligned} \tag{3.94}$$

The impulse responses of the filters are given by

$$\phi_0(n) = \Phi_0^2\,\delta(n) + (\Phi_0^1 - \Phi_0^2) \times \frac{\sin((\pi-|\omega_b|)n)}{\pi n}, \tag{3.95}$$

$$h_0(n) = \phi_0(n). \tag{3.96}$$

$$\begin{aligned}\phi_1(n) &= \Phi_1^2 \times \frac{\sin((\pi-|\omega_b|)n)}{\pi n} \\ &+ \frac{\sin(\frac{|\omega_b|}{2}n)}{\pi n} \times \left[\Phi_1^1\, e^{-j\mathrm{sgn}(\omega_b)(\pi-\frac{|\omega_b|}{2})n} + \Phi_1^3\, e^{+j\mathrm{sgn}(\omega_b)(\pi-\frac{|\omega_b|}{2})n}\right],\end{aligned} \tag{3.97}$$

$$h_1(n) = \phi_1(n+d_1). \tag{3.98}$$

$$\begin{aligned}\phi_2(n) &= \Phi_2^2 \times \frac{\sin((\pi-|\omega_b|)n)}{\pi n} \\ &+ \frac{\sin(\frac{|\omega_b|}{2}n)}{\pi n} \times \left[\Phi_2^1\, e^{-j\mathrm{sgn}(\omega_b)(\pi-\frac{|\omega_b|}{2})n} + \Phi_2^3\, e^{+j\mathrm{sgn}(\omega_b)(\pi-\frac{|\omega_b|}{2})n}\right],\end{aligned} \tag{3.99}$$

$$h_2(n) = \phi_2(n+d_2). \tag{3.100}$$

Reconstruction filters associated with the three-channel TIADC have more challenging

closed-form expressions in comparison to the case of two channels. This is due to the left inverse being more computationally intensive than a regular inverse.

Four-Channel TIADC

Let Γ be the set of all sub-ADC sampling rates in the case of $M = 4$ and $L = 2$. Since $\inf \Gamma = B/2$ from (3.5), spectral images may have width greater than 2π in digital domain due to undersampling of the envelope. As mentioned in the beginning of the section, this creates additional aliasing that will need to be removed in the reconstruction. The matrix $\mathbf{M}(e^{j\omega})$ can be written as

$$\mathbf{M}(e^{j\omega}) = \frac{1}{4}\begin{bmatrix} 1 & 1 & 1 & 1 \\ G_1(e^{j\omega}) & e^{j2\pi \mathrm{sgn}(\omega) d_1} G_1(e^{j(\omega-\pi)}) & G_1^*(e^{-j\omega}) & e^{j2\pi \mathrm{sgn}(\omega) d_1} G_1^*(e^{-j(\omega+\pi)}) \\ G_2(e^{j\omega}) & e^{j2\pi \mathrm{sgn}(\omega) d_2} G_2(e^{j(\omega-\pi)}) & G_2^*(e^{-j\omega}) & e^{j2\pi \mathrm{sgn}(\omega) d_2} G_2^*(e^{-j(\omega+\pi)}) \\ G_3(e^{j\omega}) & e^{j2\pi \mathrm{sgn}(\omega) d_3} G_3(e^{j(\omega-\pi)}) & G_3^*(e^{-j\omega}) & e^{j2\pi \mathrm{sgn}(\omega) d_3} G_3^*(e^{-j(\omega+\pi)}) \end{bmatrix}. \tag{3.101}$$

Since the phase-shifting filters $G_i(e^{j\omega}), G_i^*(e^{-j\omega}), G_i(e^{j(\omega-\pi)}), G_i^*(e^{-j(\omega+\pi)})$ for $i = 1, 2, 3$ are piecewise, we can show the matrix $\mathbf{M}(e^{j\omega})$ is piecewise constant on six segments in the interval $[-\pi, \pi]$ as shown in Fig. 3.6 for $\omega_b > 0$ and $\omega_b < 0$. These segments can be expressed as three reconstruction regions

$$\begin{aligned} R_1 &: 0 \le |\omega| < \frac{|\omega_b|}{2} \\ R_2 &: \frac{|\omega_b|}{2} \le |\omega| < \pi - \frac{|\omega_b|}{2} \\ R_3 &: \pi - \frac{|\omega_b|}{2} \le |\omega| < \pi \end{aligned}$$

over which the inverse matrix $\mathbf{M}^{-1}(e^{j\omega})$ and reconstruction filters $H_i(e^{j\omega})$, $i = 0, 1, 2, 3$ must be computed. Unfortunately, obtaining general closed-form expressions of these filters is

no easy task since computing the general expression for the determinant and inverse of the matrix $\mathbf{M}(e^{j\omega})$ (3.101) is not simple. An analytical representation of the set of forbidden timing skews $\mathcal{F}$ is not feasible either for the same reason. However, it is easy to show that $\det(\mathbf{M}(e^{j\omega})) = 0$ in at least two of the regions R_1, R_2, R_3 for $d_1 = 1/4, d_2 = 1/2, d_3 = 3/4$ and $\ell \geq 1$. This is expected since this choice of timing skews gives a uniform ADC with sampling period $T_s = T_s'/4$.

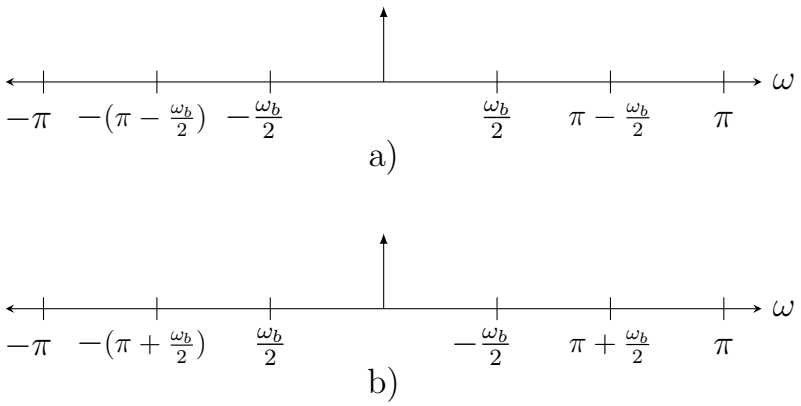


Figure 3.6: Reconstruction regions for the four-channel TIADC: a) $\omega_b > 0$, b) $\omega_b < 0$

In Appendix A, reconstruction filters and their impulse responses are computed for $\ell = 5$ and $\omega_b = \pi/2$. The values $d_1 = 0.375$, $d_2 = 0.625$, $d_3 = 0.875$ are chosen midway between forbidden timing skews that give a uniform ADC. The filters are piecewise and evaluated in each region of Fig. 3.6a). They are used in Section 3.4 to demonstrate complex envelope reconstruction in the case of four-channel TIADC.

3.4 Simulations

To validate our proposed direct sampling method, we demonstrate through various simulations complex envelope reconstruction for the two-channel, three-channel, and four-channel TIADC. Multi-tone and MSK signals are used to assess the method performance.

Reconstruction of a Multi-Tone Complex Envelope

Consider a bandpass signal $x_c(t) \in \mathcal{BP}_B(\mathbb{R})$ with carrier frequency $F_c = \Omega_c/(2\pi) = 5.15$GHz, and continuous-time envelope

$$\begin{aligned} c_c(t) &= 2\cos(400 \times 10^6 \times 2\pi t) \\ &\quad + j[\sin(400 \times 10^6 \times 2\pi t) + \cos(175 \times 10^6 \times 2\pi t)] \\ &= \frac{3}{2}e^{j400\times 10^6 \times 2\pi t} + \frac{1}{2}e^{-j400\times 10^6 \times 2\pi t} \\ &\quad + \frac{j}{2}[e^{j175\times 10^6 \times 2\pi t} + e^{-j175\times 10^6 \times 2\pi t}] \end{aligned} \tag{3.102}$$

which has bandwidth $(B/2)/(2\pi) = 400$ MHz. The bandwidth of $x_c(t)$ is then $B/(2\pi) = 800$ MHz.

For $M = 2$, the sub-ADC sampling frequency must satisfy condition (3.5),

$$\Omega_s' \geq B.$$

Choosing $F_s' = \Omega_s'/(2\pi) = 1$GHz, we can write

$$F_c = 5F_s' + 150 \ \text{ MHz}$$

which implies $\ell = 5$, i.e., F_c is located in the 5-th image band, and

$$\omega_b = \frac{150}{1000} \times 2\pi = 0.3\pi.$$

The discrete-time envelope obtained by sampling $c_c(t)$ with sampling period $T_s' = 1/F_s'$ is

$$\begin{aligned} c(n) = c_c(nT_s') &= \frac{3}{2}e^{j0.8\pi n} + \frac{1}{2}e^{-j0.8\pi n} \\ &\quad + \frac{j}{2}[e^{j0.35\pi n} + e^{-j0.35\pi n}]. \end{aligned} \tag{3.103}$$

This signal has four tones located at $\pm 0.8\pi$ and $\pm 0.35\pi$, but the tone at 0.8π has an amplitude three times larger than the tones at -0.8π and $\pm 0.35\pi$.

To sample $x_c(t)$, we select a TIADC with nominal timing skew $d^0 = 0.425$, which is approximately half-way between two forbidden timing skews $d^{m=4} = 0.4$ and $d^{q=5} = 0.454$. Then the discrete-time signals generated by the sub-ADCs are given by

$$\begin{aligned} x_0(n) &= \Re\{c(n)e^{j\omega_b n}\} + v_0(n) \\ &= \frac{3}{2}\cos(0.9\pi n) + \frac{1}{2}\cos(0.5\pi n) \\ &+ \frac{1}{2}[-\sin(0.65\pi n) + \sin(0.05\pi n)] + v_0(n), \end{aligned} \tag{3.104}$$

and

$$\begin{aligned} x_1(n) &= \Re\{c(n-d^0)e^{j\omega_b(n-d^0)}e^{-j2\pi\ell d^0}\} + v_1(n) \\ &= \frac{3}{2}\cos(0.9\pi(n-d^0) - 0.9\pi) \\ &\quad + \frac{1}{2}\cos(0.5\pi(n-d^0) + \pi/4) \\ &\quad - \frac{1}{2}\sin(0.65\pi(n-d^0) - \pi/4) \\ &\quad + \frac{1}{2}\sin(0.05\pi(n-d^0) + \pi/4)] + v_1(n)\,. \end{aligned} \tag{3.105}$$

In the above expressions $v_0(n)$ and $v_1(n)$ are white noise sequences modelling the combined effect of thermal and quantization noises. The sub-ADC SNR is 61.8dB. The signals $x_0(n)$ and $x_1(n)$ have the same power spectral density (PSD) plotted in Fig. 3.7, where $f = \omega/(2\pi)$. It is computed by using the periodogram method with a Kaiser window for a data segment with 10^4 samples. The block diagram in Fig. 3.5 is used to compute the estimated envelope $\hat{c}(n)$. The FIR filters $\check{H}_0(e^{j\omega})$ and $\check{H}_1(e^{j\omega})$ shown in Fig. 3.8 have order $N = 60$ and are obtained by applying a Kaiser window with parameter $\beta = 6$ to the time-shifted by $K = N/2$ ideal impulse responses $h_0(n)$ and $h_1(n)$.

The PSD of the estimated envelope $\hat{c}(n)$ is shown in Fig. 3.9. It is again evaluated

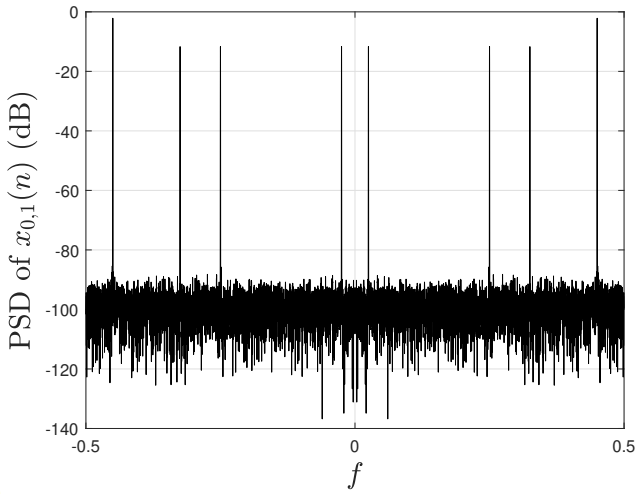


Figure 3.7: PSD of signals $x_0(n)$ and $x_1(n)$ for a two-channel TIADC in the presence of additive white noise.

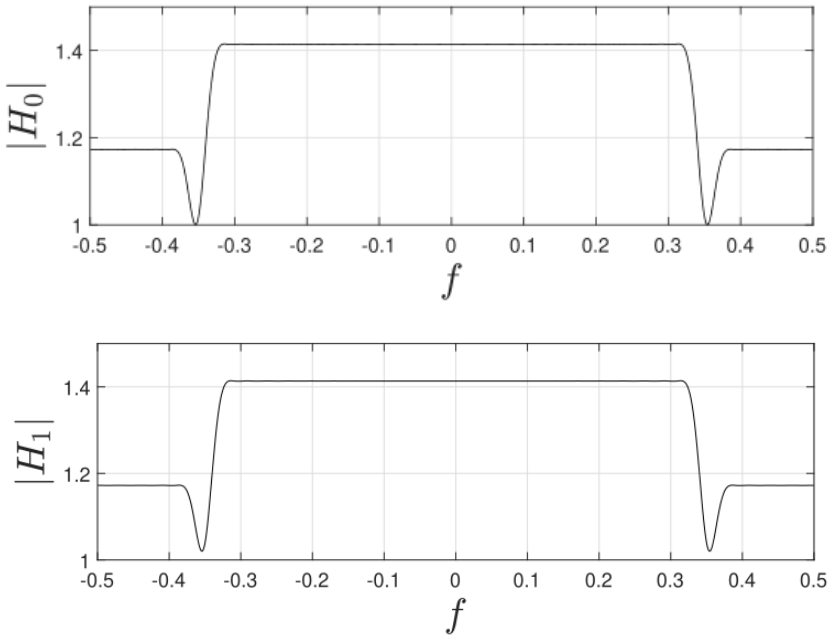


Figure 3.8: Magnitude responses of FIR filters $\check{H}_0(e^{j\omega})$ and $\check{H}_1(e^{j\omega})$ of order $N = 60$ for the two-channel TIADC.

by using the windowed complex data periodogram method for a data block of length 10^4 samples. The periodogram is scaled so that a complex tone with unit amplitude corresponds to 0dB. In addition to the four desired tones at $\pm 0.8\pi$ and $\pm 0.35\pi$, four secondary tones are present representing the residual spectral components of $e^{-j2\omega_b n}c^*(n) = e^{-j0.6\pi n}c^*(n)$,

which are located at 0.6π, 0.2π, -0.25π, and -0.95π. Since the dominant tone of $c^*(n)$ is located at -0.8π, the highest secondary tone in the PSD of $\hat{c}(n)$ is located at $0.6\pi = -0.6\pi - 0.8\pi \mod (2\pi)$, yielding a SFDR of about 65dB. It is worth also noting that the secondary tone at -0.95π is higher than the secondary tones at -0.25π and 0.2π which should in theory be at the same level. This is due to the fact that the filters $H_0(e^{j\omega})$ and $H_1(e^{j\omega})$ have discontinuities at $\pm(\pi - |\omega_b|) = \pm 0.7\pi$ so that after windowing, the filters exhibit nonideal filtering characteristics in transition bands about these discontinuity points. After modulation by $e^{-j\omega_b n} = e^{-j0.3\pi n}$, the nonideal filtering bands become located about $-\pi$ and 0.4π, which explains the higher level of the secondary tone at -0.95π. Lengthening the filters $\check{H}_i(e^{j\omega})$, $i = 0, 1$ removes this transition band effect. Significantly increasing the order of the filters makes them behave almost ideally as demonstrated in Fig. 3.10 where secondary tones have completely vanished into the noise floor and near-perfect envelope reconstruction is achieved. Finally, since the exact envelope $c(n)$ is known, the error $\tilde{c}(n) = c(n) - \hat{c}(n)$ can be evaluated. Table 3.2 displays the mean-square error (MSE) for selected values of N. Increasing the filter order beyond $N = 80$ results in negligible performance improvement as measured by the MSE.

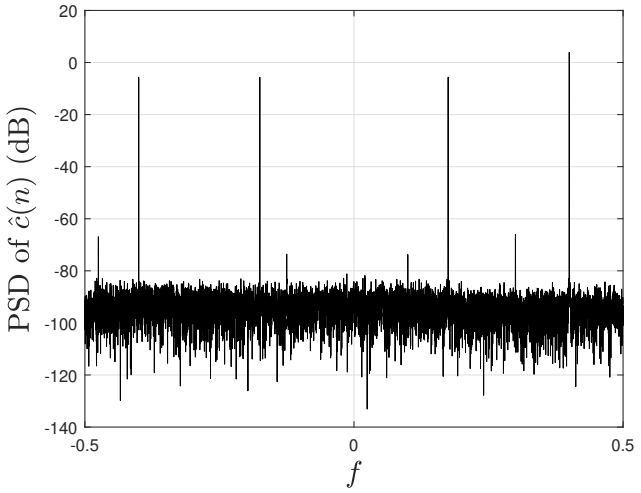


Figure 3.9: PSD of the estimated envelope $\hat{c}(n)$ computed with FIR filters of order $N = 60$ for a two-channel TIADC with timing skew $d^0 = 0.425$.

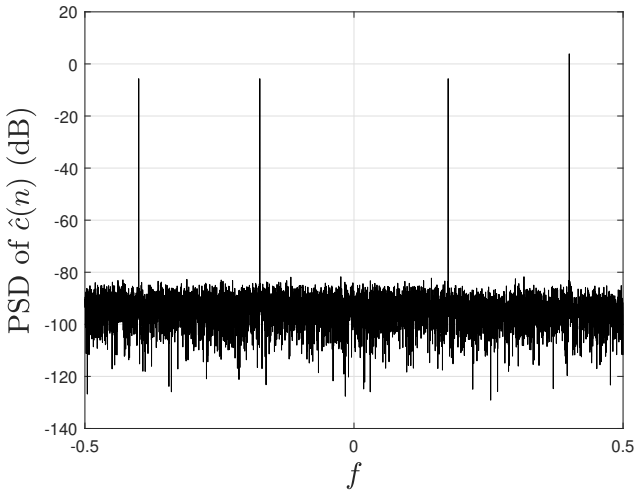


Figure 3.10: PSD of the estimated envelope $\hat{c}(n)$ computed with FIR filters of order $N = 300$ for a two-channel TIADC with timing skew $d^0 = 0.425$.

N	20	40	60	80	100	140	200	300
MSE (dB)	-34.64	-46.03	-53.42	-54.04	-54.22	-54.34	-54.38	-54.4

Table 3.2: MSE vs N for a two-channel TIADC with timing skew $d^0 = 0.425$.

To illustrate the slight degradation in performance which occurs if the timing skew d is close to a forbidden value, consider the case where $d = 0.4 + \varepsilon$ is close to forbidden value $d^{m=4} = 0.4$. The PSD of the reconstructed complex envelope for $\varepsilon = 0.01$ is shown in Fig. 3.11. The secondary tones are approximately at the same level as in Fig. 3.9, but the piecewise constant filtering operation is applied to the noise floor. This is due to the fact that since $D(e^{j\omega})$ from (3.54) is close to zero inside the interval $[-0.7\pi, 0.7\pi]$, the magnitudes of filters $H_i(e^{j\omega})$, $i = 0, 1$ are not evaluated as accurately inside this band as outside. After demodulation by $e^{-0.3\pi n}$, the effect of mismatched filter magnitudes is exhibited in bands $[-\pi, 0.4\pi]$ and $[0.4\pi, \pi]$. The reconstruction MSE is -47.27dB, so that a bad timing skew positioning results in a slight performance loss. However, a timing skew too close to a forbidden value can severely degrade reconstruction. For example, the MSE is -27.54dB for $\varepsilon = 0.001$ and -7.48dB for $\varepsilon = 0.0001$.

Up to this point the reconstruction filters $H_i(e^{j\omega})$, $i = 0, 1$ have been computed under the assumption that the two sampling channels are perfectly matched and that the timing

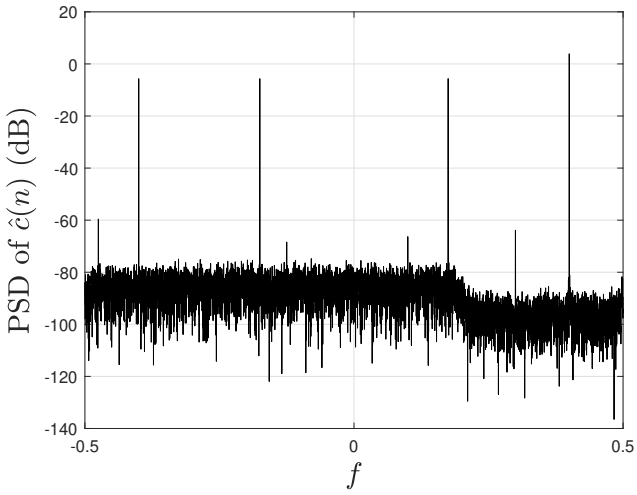


Figure 3.11: PSD of the estimated envelope $\hat{c}(n)$ computed with FIR filters of order $N = 60$ for a two-channel TIADC with timing skew $d = 0.410$ close to a forbidden value.

skew d is known exactly. To assess the effect of mismatches on the performance of the two-channel TIADC, assume that the relative gain of the second channel compared to the first channel is $g = 1.01$, and that the actual timing skew d satisfies $d = d^0 - 0.0025$, where d^0 denotes the nominal timing skew used to design the reconstruction filters. When reconstruction filters based on nominal values $g^0 = 1$ and $d^0 = 0.425$ are used to evaluate $\hat{c}(n)$, the estimated envelope has the PSD shown in Fig. 3.12. In this case the secondary tones are much higher than in Fig. 3.9 (the secondary tone at 0.6π is now at -22dB) and the MSE is only -17.80dB, so that the presence of 1% gain mismatch and 0.25% timing mismatch results in a degradation of 43dB in SFDR and 35dB in MSE performance. Tables 3.3–3.5 display the MSE for various gain and timing mismatches. This data indicates reconstruction is more sensitive to timing mismatches than to gain mismatches. This should not come as a surprise, since the expression (3.105) for $x_1(n)$ includes a $2\pi\ell d$ phase shift. Thus when the image band index ℓ is sufficiently large, a relatively small timing mismatch $d - d^0$ results in a large phase shift.

Finally, it is worth determining the performance of the two-channel TIADC in different image bands. Suppose F_s' is still fixed at 1GHz, but the carrier frequency takes on values

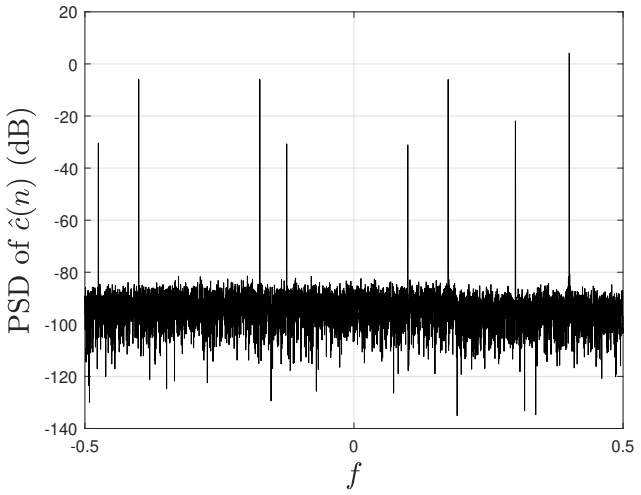


Figure 3.12: PSD of the estimated envelope $\hat{c}(n)$ computed with FIR filters of order $N = 60$ for a two-channel TIADC with gain $g - g^0 = 0.01$ and timing $d - d^0 = -0.0025$ mismatches.

$g - g^0$	1%	3%	5%	10%	15%	20%	25%
MSE (dB)	-36.64	-25.95	-22.48	-16.44	-12.91	-10.40	-8.46

Table 3.3: MSE for a two-channel TIADC with filters of order $N = 60$ in the presence of gain mismatches ($g^0 = 1$).

$d - d^0$	0.01%	0.05%	0.10%	0.15%	0.20%	0.25%	0.50%
MSE (dB)	-45.79	-31.96	-25.89	-22.34	-19.84	-17.88	-11.86

Table 3.4: MSE for a two-channel TIADC with filters of order $N = 60$ in the presence of timing mismatches ($d^0 = 0.425$).

$g - g^0$	1%	1%	2.5%	2.5%	5%	5%
$d - d^0$	0.01%	0.10%	0.10%	0.25%	0.25%	0.50%
MSE (dB)	-36.23	-25.50	-23.95	-17.43	-16.44	-11.31

Table 3.5: MSE for a two-channel TIADC with filters of order $N = 60$ in the presence of gain and timing mismatches ($g^0 = 1$, $d^0 = 0.425$).

$F_c = 1.15, 2.15, 3.15, 4.15, \ldots, 20.15$ GHz so that $1 \leq \ell \leq 20$. Fig. 3.13 shows the MSE for all ℓ where a permissible timing skew is chosen as $d = (\ell + 1/4)/(2\ell)$ and the filters are of order $N = 60$. We infer comparable performance can be achieved in all image bands. In the presence of timing mismatches, however, performance suffers as ℓ increases for reasons stated in the preceding paragraph. Table 3.6 demonstrates this in the case of 0.10% timing

mismatch.

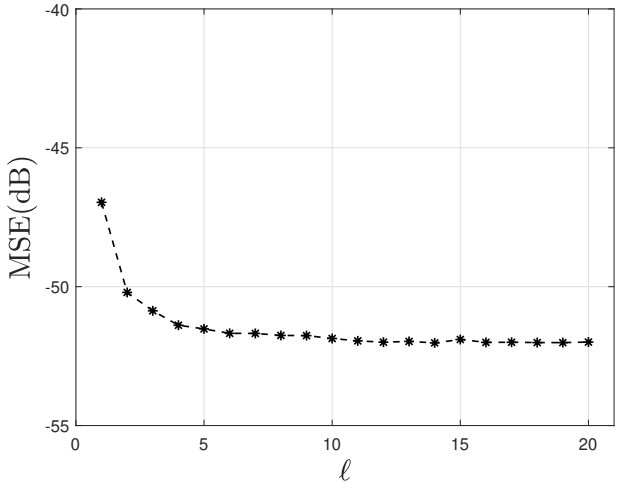


Figure 3.13: MSE in different image bands $1 \leq \ell \leq 20$ computed with filters of order $N = 60$ for a two-channel TIADC with timing skew $d = (\ell + 1/4)/(2\ell)$.

ℓ	1	2	3	5	7	10	15	20
MSE (dB)	-31.23	-29.87	-27.60	-24.07	-21.52	-18.69	-15.34	-12.97

Table 3.6: MSE vs ℓ for a two-channel TIADC with filters of order $N = 60$ and timing skew mismatch $d = (\ell + 1/4)/(2\ell) - 0.0010$.

For $M = 3$, we consider $x_c(t)$ with the same envelope given in (3.102) and the same carrier frequency $F_c = 5.15$GHz. The oversampling parameter in (3.3) is $\mathcal{E}(3) = 1$, which means the sub-ADC sampling frequency must again satisfy

$$\Omega_s' \geq B.$$

Picking $F_s' = 1$GHz just as in the case of two channels, we have the same image band index $\ell = 5$, discrete modulation frequency $\omega_b = 0.3\pi$, and sampled complex envelope specified in (3.103). Consider two forbidden timing skew vectors from the set (3.77) with $m_1 = 4, m_2 = 8, q_1 = 5$, and $q_2 = 10$:

$$(d_1^4, d_2^8) = \frac{1}{2\ell}(4, 8) = (0.4, 0.8)$$

$$(d_1^5, d_2^{10}) = \frac{1}{2\ell + \mathrm{sgn}(\omega_b)}(5, 10) = (0.454, 0.909).$$

Choosing the nominal timing skews approximately halfway between these, we obtain

$$(d_1^0, d_2^0) = (0.425, 0.85).$$

The PSD of the estimated envelope $\hat{c}(n)$ is shown in Fig. 3.14, and the frequency responses of FIR filters $\check{H}_i(e^{j\omega})$, $i = 0, 1, 2$ of order $N = 60$ with Kaiser parameter $\beta = 6$ are plotted in Fig. 3.15. Similar to the case of two channels, the reconstructed envelope has the four desired tones along with four secondary tones that diminish in magnitude as the order of the filters is increased. The dominant secondary tone at 0.6π yields a SFDR of about 58dB. The MSE is -46.9dB. The transition band effect can be observed if we lower the filters order to $N = 40$. This is demonstrated in Fig. 3.16, where the secondary tone at -0.95π is higher than the secondary tones at -0.25π and 0.2π. Table 3.7 displays the MSE for different N. Little performance is gained beyond $N = 100$ where the MSE starts to saturate around -48dB.

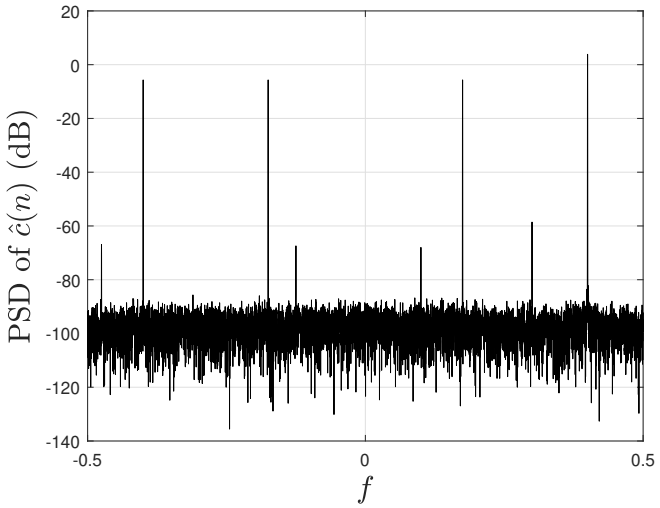


Figure 3.14: PSD of the estimated envelope $\hat{c}(n)$ computed with FIR filters of order $N = 60$ for a three-channel TIADC with timing skews $d_1^0 = 0.425$ and $d_2^0 = 0.85$.

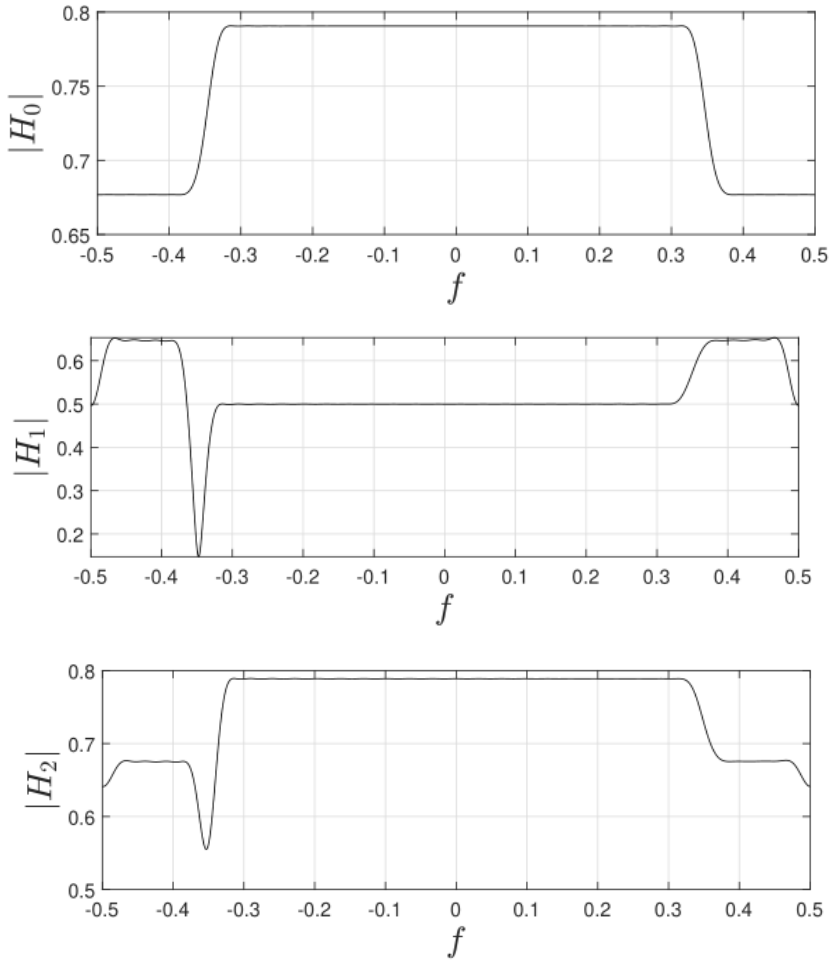


Figure 3.15: Magnitude responses of FIR filters $\check{H}_0(e^{j\omega})$,$\check{H}_1(e^{j\omega})$, and $\check{H}_2(e^{j\omega})$ of order $N = 60$ for the three-channel TIADC.

N	40	60	80	100	120	160	200	300
MSE (dB)	-41.46	-46.9	-47.49	-47.92	-48.03	-48.06	-48.08	-48.08

Table 3.7: MSE vs N for the three-channel TIADC with timing skews $d_1^0 = 0.425$ and $d_2^0 = 0.85$.

Consider the case where $d_1 = 0.4 + \varepsilon$ and $d_2 = 0.8 + \varepsilon$, i.e., the timing skews are close to the forbidden vector $(d_1^4, d_2^8) = (0.4, 0.8)$. The PSD of the reconstructed envelope for $\varepsilon = 0.01$ is shown in Fig. 3.17. Since $D_1(d_1, d_2, \ell)$ in (3.81) is close to zero, reconstruction suffers in the region $[-\pi, 0.4\pi]$. The MSE is -35.66dB, so a slight positioning in the vicinity of a forbidden timing skew vector causes a drop of roughly 11dB in performance. For $\varepsilon = 0.001$, the MSE jumps all the way up to -15.49dB. Other simulations not shown here indicate

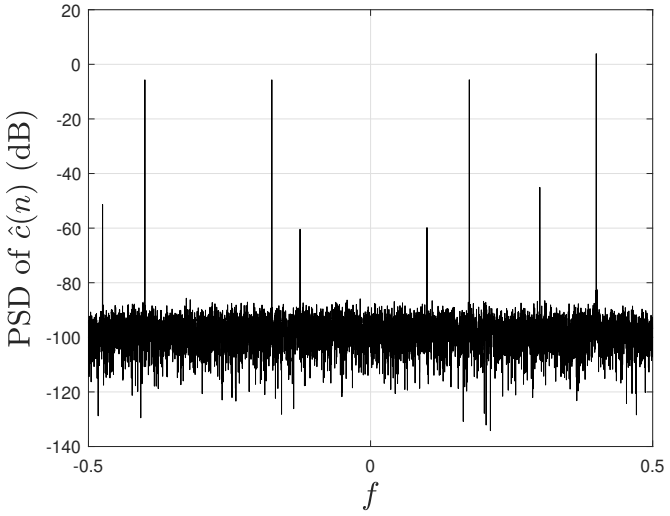


Figure 3.16: PSD of the estimated envelope $\hat{c}(n)$ computed with FIR filters of order $N = 40$ for a three-channel TIADC with timing skews $d_1^0 = 0.425$ and $d_2^0 = 0.85$.

that not all forbidden timing skew vectors are equally sensitive. For example, if we were to pick $d_1 = 0.454 + \varepsilon$ and $d_2 = 0.909 + \varepsilon$, i.e., timing skews in the vicinity of forbidden vector $(d_1^5, d_2^{10}) = (0.454, 0.909)$, the MSE would be -45.34dB for $\varepsilon = 0.01$ and -28.69dB for $\varepsilon = 0.001$.

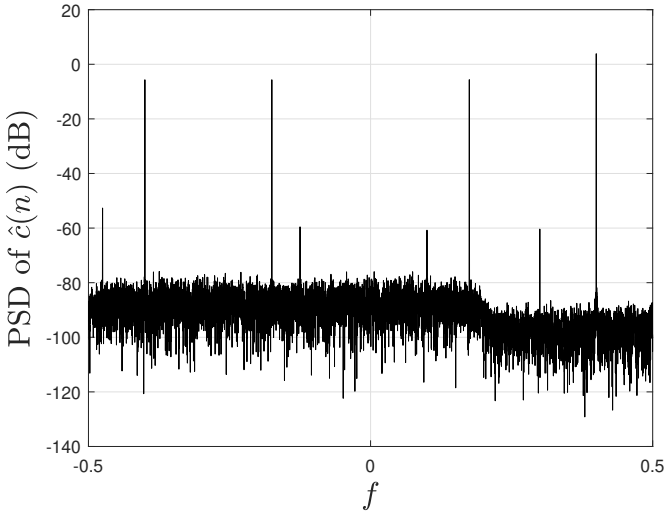


Figure 3.17: PSD of the estimated envelope $\hat{c}(n)$ computed with FIR filters of order $N = 60$ for a three-channel TIADC with timing skews $d_1 = 0.41$ and $d_2 = 0.81$ close to forbidden values.

To investigate the performance of the three-channel TIADC in the presence of gain and timing mismatches, suppose the relative gains of the second and third channel compared to the first channel are $g_1 = 1.01$ and $g_2 = 1.02$, respectively. Moreover, the actual timing skews satisfy $d_1 = d_1^0 - 0.0025$ and $d_2 = d_2^0 - 0.0050$, where d_1^0, d_2^0 denote the nominal timing skews used to design the reconstruction filters. When $\hat{c}(n)$ is evaluated with reconstruction filters based on $g_1^0 = 1$, $g_2^0 = 1$, $d_1^0 = 0.425$, and $d_2^0 = 0.85$, the estimated envelope has the PSD shown in Fig. 3.18. The presence of $1\%, 2\%$ gain mismatches and $0.25\%, 0.50\%$ timing mismatches lowers the SFDR to 19dB and gives a MSE of only -13.23dB. Tables 3.8–3.10 contain the MSE for various gain and timing mismatches. Just as in the case of two channels and for the same reasons, reconstruction is affected significantly more by the timing mismatches than gain mismatches. This can be highly problematic especially for signals with carrier frequencies in higher image bands.

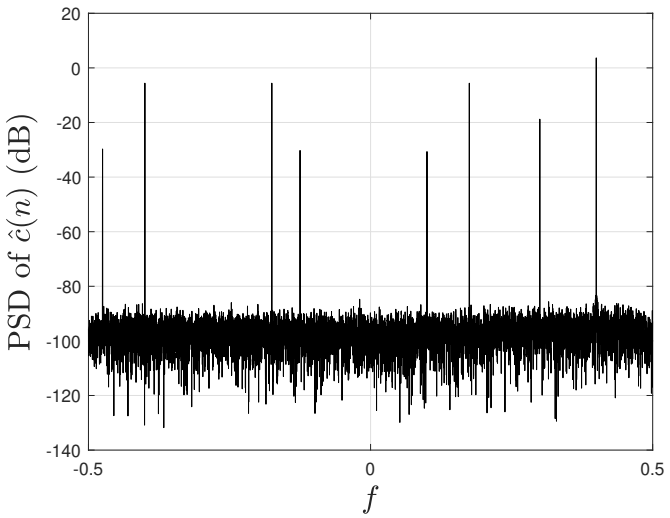


Figure 3.18: PSD of the estimated envelope $\hat{c}(n)$ computed with FIR filters of order $N = 60$ for a three-channel TIADC with gain $g_1 - g_1^0 = 0.01$, $g_2 - g_2^0 = 0.02$ and timing $d_1 - d_1^0 = -0.0025$, $d_2 - d_2^0 = -0.0050$ mismatches.

For $M = 4$, we again consider the envelope given in (3.102), but the signal $x_c(t)$ now has

$g_1 - g_1^0$	0%	1%	1%	2.5%	5%	10%	20%
$g_2 - g_2^0$	1%	1%	2%	5%	10%	15%	25%
MSE (dB)	-40.47	-39.00	-33.13	-24.54	-18.31	-14.52	-9.82

Table 3.8: MSE for the three-channel TIADC with filters of order $N = 60$ in the presence of gain mismatches ($g_1^0 = 1$, $g_2^0 = 1$).

$d_1 - d_1^0$	0.10%	0.10%	0.25%	0%	0.25%	0.5%	0.5%
$d_2 - d_2^0$	0%	0.10%	0%	0.25%	0.25%	0.5%	1%
MSE (dB)	-33.08	-26.71	-24.97	-19.48	-18.73	-12.70	-7.46

Table 3.9: MSE for the three-channel TIADC with filters of order $N = 60$ in the presence of timing mismatches ($d_1^0 = 0.425$, $d_2^0 = 0.85$).

$g_1 - g_1^0$	1%	1%	0%	1%	5%	10%	1%	12%
$g_2 - g_2^0$	1%	0%	1%	1%	5%	10%	1%	12%
$d_1 - d_1^0$	0.10%	0.25%	0%	0.25%	0.25%	0.25%	0.50%	0.50%
$d_2 - d_2^0$	0.10%	0%	0.25%	0.25%	0.25%	0.25%	0.50%	0.50%
MSE (dB)	-26.45	-24.86	-19.41	-18.65	-17.38	-14.89	-12.65	-10.67

Table 3.10: MSE for the three-channel TIADC with filters of order $N = 60$ in the presence of gain and timing mismatches ($g_1^0 = 1$, $g_2^0 = 1$, $d_1^0 = 0.425$, $d_2^0 = 0.85$).

carrier frequency $F_c = 2.625$GHz. From (3.5), we must have

$$\Omega_s' \geq \frac{B}{2} = 400 \times 10^6 \times 2\pi.$$

Choosing $F_s' = 500$ MHz satisfies this condition and gives $\ell = 5$ along with discrete modulation frequency

$$\omega_b = \frac{125}{500} \times 2\pi = \frac{\pi}{2}.$$

The discrete-time envelope obtained by sampling $c_c(t)$ with sampling period $T_s'/2 = 1/(2F_s')$ is

$$\begin{aligned} c^{[2]}(n) = c_c(n\frac{T_s'}{2}) &= \frac{3}{2}e^{j0.8\pi n} + \frac{1}{2}e^{-j0.8\pi n} \\ &\quad + \frac{j}{2}[e^{j0.35\pi n} + e^{-j0.35\pi n}] \end{aligned} \tag{3.106}$$

which is the same as (3.103) for the case of two and three channels. If we choose the nominal timing skews as $d_1^0 = 0.375$, $d_2^0 = 0.625$, and $d_3^0 = 0.875$, the filters from Appendix A can be used in reconstruction. Fig. 3.19 plots the MSE between the TIADC outputs in Fig. 3.1 with additive noise and corresponding outputs in the sampling model in Fig. 3.3. The filters $G_i(e^{j\omega})$ and $F_i(e^{j\omega})$ for $i = 1, 2, 3$ in Fig. 3.3 are approximated by FIR filters of order $N = 40, 50, 60, 80, 140, 250$ and Kaiser parameter $\beta = 6$. For $x_0(n)$, the MSE is at the noise power -60dB for all N. For $x_i(n)$, $i = 1, 2, 3$ the MSE converges to -60dB as N grows large. High filter order is of no consequence here since the goal is validation of the sampling model in Fig. 3.3 for $M = 4$ and not implementation.

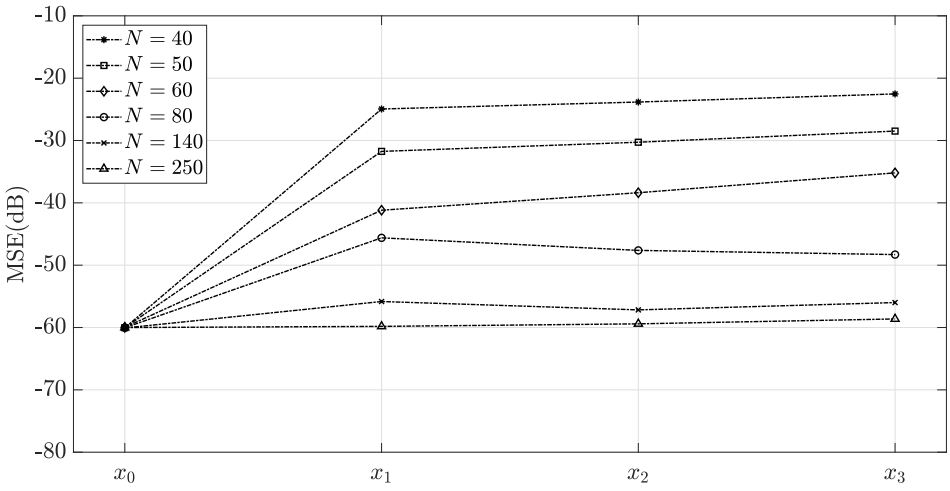


Figure 3.19: Verification of the sampling model in Fig. 3.3 for the four-channel TIADC using a multi-tone complex envelope.

The PSD of digital signals $x_0(n), x_1(n), x_2(n), x_3(n)$ is the same and plotted in Fig. 3.20. It contains tones at $\pm 0.1\pi, \pm 0.2\pi, \pm 0.8\pi$, and $\pm 0.9\pi$. The FIR reconstruction filters $\check{H}_i(e^{j\omega})$, $i = 0, 1, 2, 3$ of order $N = 80$ and Kaiser parameter $\beta = 6$ have frequency responses shown in Fig. 3.21. The PSD of the estimated envelope in Fig. 3.22 contains the four desired tones at $\pm 0.35\pi, \pm 0.8\pi$ and three secondary tones around each of these desired tones. The SFDR is 51dB and the MSE about -43dB. The secondary tones gradually disappear as the filter order N increases. From table 3.11, we observe the MSE approaches a limit of -45.51dB.

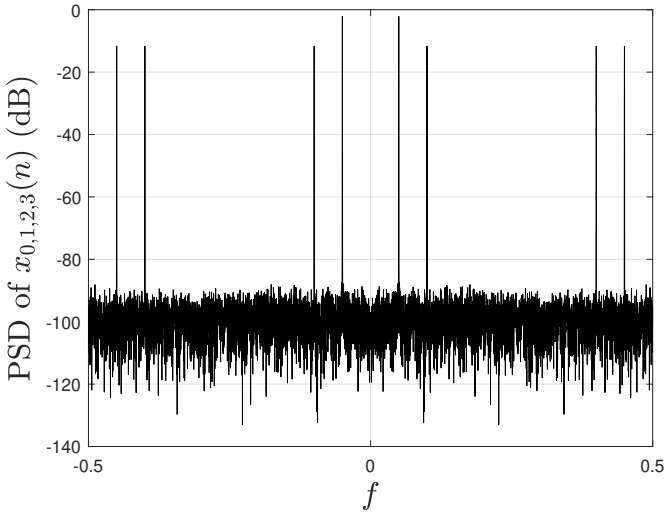


Figure 3.20: PSD of signals $x_0(n), x_1(n), x_2(n)$, and $x_3(n)$ for a four-channel TIADC in the presence of additive white noise.

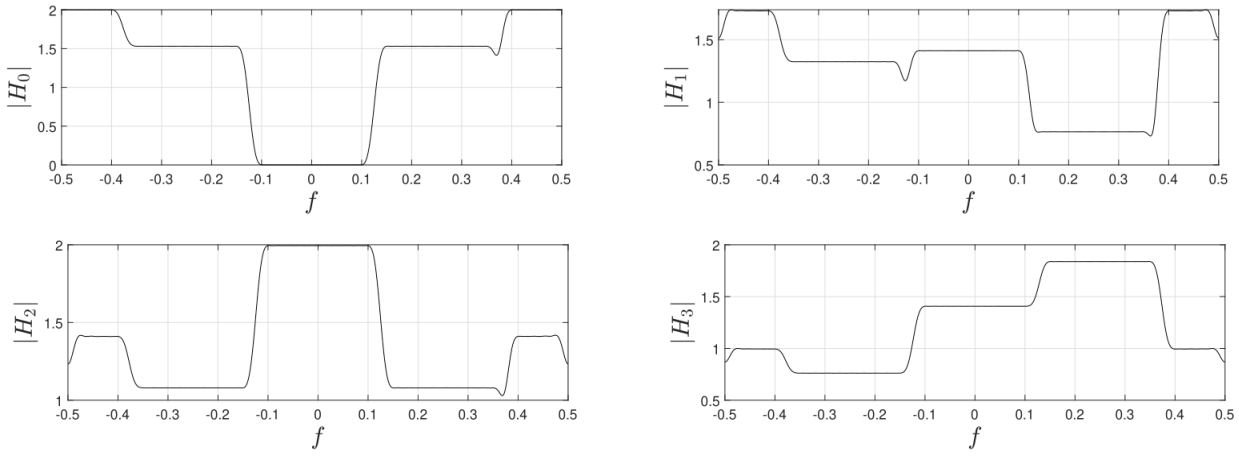


Figure 3.21: Magnitude responses of FIR filters $\check{H}_0(e^{j\omega})$,$\check{H}_1(e^{j\omega})$,$\check{H}_2(e^{j\omega})$, and $\check{H}_3(e^{j\omega})$ of order $N = 80$ for the four-channel TIADC.

N	40	60	80	100	180	300
MSE (dB)	-23.94	-36.09	-43.01	-44.79	-45.48	-45.51

Table 3.11: MSE vs N for the four-channel TIADC with timing skews $d_1^0 = 0.375$, $d_2^0 = 0.625$, and $d_3^0 = 0.875$.

Suppose the actual gains on the second, third, and fourth channel are $g_1 = 1.01$, $g_2 = 1.025$, and $g_3 = 1.05$, respectively, and the actual timing skews are given by $d_1 = d_1^0 - 0.0025$, $d_2 = d_2^0 - 0.0050$, and $d_3 = d_3^0 - 0.0075$ where d_1^0, d_2^0, d_3^0 denote the nominal timing skews

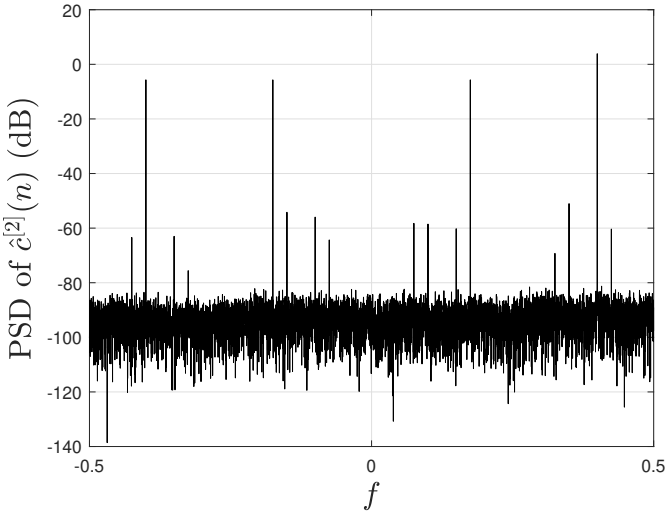


Figure 3.22: PSD of the estimated envelope $\hat{c}^{[2]}(n)$ computed with FIR filters of order $N = 80$ for a four-channel TIADC with timing skews $d_1^0 = 0.375$, $d_2^0 = 0.625$, and $d_3^0 = 0.875$.

used to design the reconstruction filters. The PSD of $\hat{c}^{[2]}(n)$ in the presence of these gain and timing mismatches is shown in Fig. 3.23. The secondary tones are significantly higher giving a SFDR of only 16dB. The MSE has jumped up to -10.49dB. Tables 3.12–3.14 present the MSE in the case of various gain and timing mismatches. Performance degradation can be significant depending on the magnitude of timing skew mismatches.

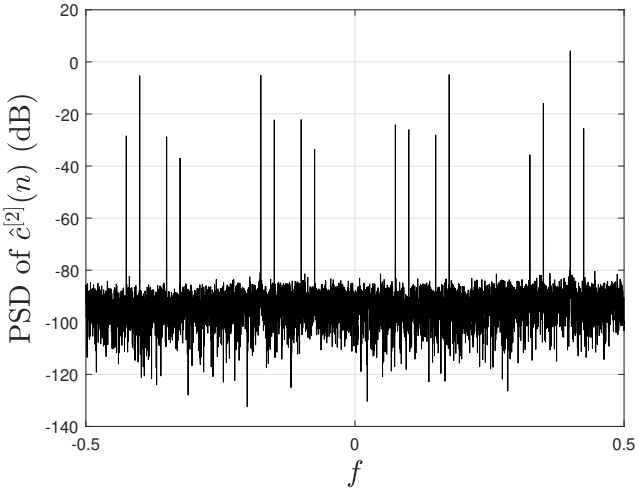


Figure 3.23: PSD of the estimated envelope $\hat{c}^{[2]}(n)$ computed with FIR filters of order $N = 80$ for a four-channel TIADC with gain $g_1 - g_1^0 = 0.01$, $g_2 - g_2^0 = 0.025$, $g_3 - g_3^0 = 0.05$ and timing $d_1 - d_1^0 = -0.0025$, $d_2 - d_2^0 = -0.0050$, $d_3 - d_3^0 = -0.0075$ mismatches.

$g_1 - g_1^0$	1%	1%	1%	7.5%	10%	10%	15%	25%
$g_2 - g_2^0$	1%	2.5%	5%	7.5%	10%	15%	15%	25%
$g_3 - g_3^0$	1%	5%	10%	7.5%	10%	20%	20%	25%
MSE (dB)	-35.99	-26.00	-19.86	-19.4	-16.91	-12.86	-12.11	-8.95

Table 3.12: MSE for the four-channel TIADC with filters of order $N = 80$ in the presence of gain mismatches ($g_1^0 = 1$, $g_2^0 = 1$, $g_3^0 = 1$).

$d_1 - d_1^0$	0%	0.10%	0.25%	0.25%	0.25%	0.5%	0.5%	1%
$d_2 - d_2^0$	0%	0.10%	0%	0%	0.50%	0.5%	0.5%	1%
$d_3 - d_3^0$	0.10%	0.10%	0%	0.25%	0.25%	0.5%	1%	1%
MSE (dB)	-28.08	-25.97	-18.36	-15.40	-14.31	-11.99	-8.05	-6.00

Table 3.13: MSE for the four-channel TIADC with filters of order $N = 80$ in the presence of timing mismatches ($d_1^0 = 0.375$, $d_2^0 = 0.625$, $d_3^0 = 0.875$).

$g_1 - g_1^0$	1%	1%	0%	5%	5%	10%	10%	12%
$g_2 - g_2^0$	1%	3%	5%	5%	7.5%	10%	15%	12%
$g_3 - g_3^0$	1%	5%	5%	5%	10%	10%	20%	12%
$d_1 - d_1^0$	0.10%	0.10%	0%	0.25%	0.50%	0.50%	0.50%	0.75%
$d_2 - d_2^0$	0.10%	0.10%	0%	0.25%	0.25%	0.50%	0.75%	0.75%
$d_3 - d_3^0$	0.10%	0.10%	0.25%	0.25%	0.25%	0.50%	0.50%	0.75%
MSE (dB)	-25.61	-22.96	-18.12	-16.65	-12.37	-10.47	-8.09	-7.25

Table 3.14: MSE for the four-channel TIADC with filters of order $N = 80$ in the presence of gain and timing mismatches ($g_1^0 = 1$, $g_2^0 = 1$, $g_3^0 = 1$, $d_1^0 = 0.375$, $d_2^0 = 0.625$, $d_3^0 = 0.875$).

Reconstruction of the Complex Envelope of a MSK Signal

We now apply the proposed reconstruction method to a practical communication signal. Suppose the bandpass signal $x_c(t) \in \mathcal{BP}_B(\mathbb{R})$ is a minimum-shift keying (MSK) signal with carrier frequency $F_c = 2.625$GHz and continuous-time envelope

$$c_c(t) = \sum_{k=-\infty}^{\infty} I_{2k}\, p(t - 2kT_b) - j \sum_{k=-\infty}^{\infty} I_{2k+1}\, p(t - (2k+1)T_b), \tag{3.107}$$

where

$$p(t) = \begin{cases} \sin(\frac{\pi t}{2T_b}) & 0 \le t \le 2T_b \\ 0 & \text{otherwise} \end{cases} \tag{3.108}$$

and $I_l \in \{-1, 1\}\ \forall l \in \mathbb{Z}$ with $\Pr(I_l = +1) = \Pr(I_l = -1) = 1/2$. The bandwidth B of $x_c(t)$ is set to the bandwidth that contains 99% of total signal power which is given by $1.2 \times (2\pi/T_b)$ [83], [84, Sec. 3.4]. Choosing $T_b = 1.5 \times 10^{-9}$ gives $B/(2\pi) = 800$ MHz.

To sample $x_c(t)$, we use the same four-channel TIADC ($M = 4$) with sub-ADC sampling frequency $F_s' = 500$MHz and nominal timing skews $d_1^0 = 0.375$, $d_2^0 = 0.625$, $d_3^0 = 0.875$. Therefore, $\ell = 5$ and $\omega_b = \pi/2$ just as in the case of a multi-tone signal. The sampled complex envelope is given by

$$c^{[2]}(n) = \sum_{k=-\infty}^{\infty} I_{2k}\, m_1(n,k) - j \sum_{k=-\infty}^{\infty} I_{2k+1}\, m_2(n,k)\ , \tag{3.109}$$

where

$$m_1(n,k) = \begin{cases} \sin\left(\frac{\pi}{3}(n-3k)\right) & 3k \le n < 3(k+1) \\ 0 & \text{otherwise} \end{cases} \tag{3.110}$$

and

$$m_2(n,k) = \begin{cases} \sin\left(\frac{\pi}{3}(n-3(k+\frac{1}{2}))\right) & \lceil 3(k+\frac{1}{2})\rceil \le n \le \lfloor 3(k+\frac{3}{2})\rfloor \\ 0 & \text{otherwise}\ . \end{cases} \tag{3.111}$$

The PSD of $c^{[2]}(n)$ is continuous as shown in Fig. 3.24. When FIR filters $\check{H}_i(e^{j\omega})$, $i = 0, 1, 2, 3$ of order $N = 80$ and Kaiser parameter $\beta = 6$ are used in reconstruction, the MSE is -35dB. The PSD of the estimated envelope $\hat{c}^{[2]}(n)$ is shown in Fig. 3.25. As observed in Table 3.15, the approximation is robust and improves with increasing N. However, longer filters are needed to match the best performance achieved (about -45dB) with a multi-tone signal. This is understandable given MSK has a higher signal complexity.

N	40	60	80	100	200	300	400
MSE (dB)	-27.6	-32.2	-35	-36.6	-39.7	-41.5	-44.1

Table 3.15: MSE vs N for the envelope of a MSK signal sampled with a four-channel TIADC with timing skews $d_1^0 = 0.375$, $d_2^0 = 0.625$, and $d_3^0 = 0.875$.

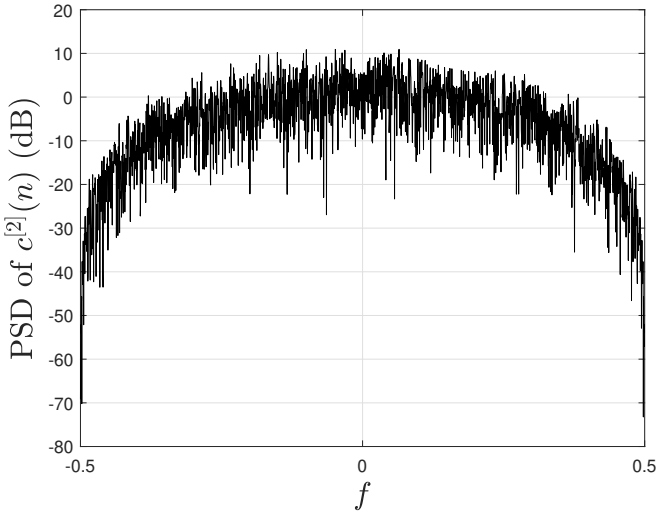


Figure 3.24: PSD of the theoretical envelope $c^{[2]}(n)$ of a MSK signal sampled with a four-channel TIADC with timing skews $d_1^0 = 0.375$, $d_2^0 = 0.625$, and $d_3^0 = 0.875$.

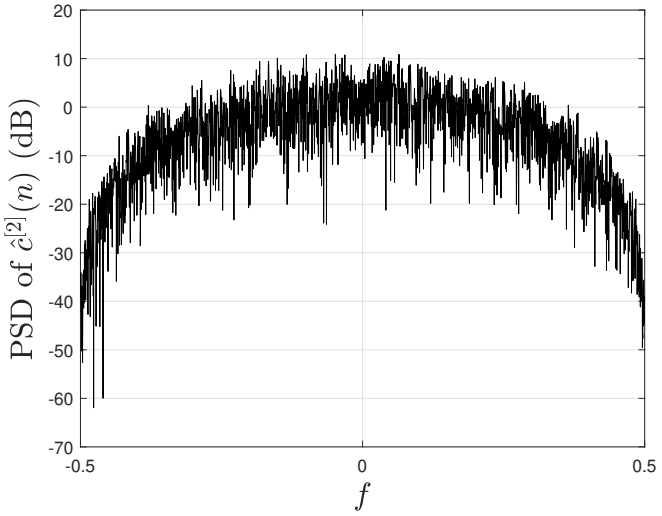


Figure 3.25: PSD of the estimated MSK envelope $\hat{c}^{[2]}(n)$ computed with filters of order $N = 80$ for a four-channel TIADC with timing skews $d_1^0 = 0.375$, $d_2^0 = 0.625$, and $d_3^0 = 0.875$.

Table 3.16 investigates performance deterioration when the TIADC suffers from gain and timing mismatches. Five percent gain mismatch and less than one percent timing mismatch in all the channels causes about a 25dB drop in MSE.

$g_1 - g_1^0$	1%	1%	1%	2%	1%	5%
$g_2 - g_2^0$	1%	3%	3%	4%	2.5%	5%
$g_3 - g_3^0$	1%	5%	5%	6%	5%	5%
$d_1 - d_1^0$	0.10%	0.10%	0.10%	0.25%	0.25%	0.75%
$d_2 - d_2^0$	0.10%	0.10%	0.15%	0.30%	0.50%	0.75%
$d_3 - d_3^0$	0.10%	0.10%	0.20%	0.35%	0.75%	0.75%
MSE (dB)	-27.69	-26.11	-23.46	-18.31	-13.55	-10.75

Table 3.16: MSE for the MSK envelope computed with filters of order $N = 80$ in the presence of a four-channel TIADC gain and timing mismatches ($g_1^0 = g_2^0 = g_3^0 = 1$, $d_1^0 = 0.375$, $d_2^0 = 0.625$, $d_3^0 = 0.875$).

Concluding Remarks

We have demonstrated successful envelope reconstruction for multi-tone and MSK signals. Performance as measured by the MSE between the theoretical and estimated envelope depends on the complexity of both the input signal and reconstruction filters. As the number of TIADC channels M increases, the number of transition regions in frequency domain of the filters also increases. Estimation suffers in these regions, and therefore the use of more channels results in relatively higher reconstruction error (worse MSE). Finally, sensitivity to gain and timing mismatches presents a significant challenge for hardware implementation. This highlights the importance of accurate TIADC calibration.

Chapter 4

Quadrature Sampling and Approximation

A special case of Kohlenberg's second-order bandpass sampling called quadrature sampling was first studied by Grace and Pitt [85]. The sub-ADC sampling rate is chosen as an integer fraction of the carrier frequency, while the timing offset is equal to a quarter of the carrier period plus possibly an integer multiple of the carrier period. The total minimum sampling rate achieved is $2B((\Omega_c/B)/\lfloor\Omega_c/B\rfloor)$ which equals to the Nyquist rate $2B$ only when the carrier frequency $\Omega_c = kB$, for some positive integer k. Using the theory of orthogonal expansions, Brown [86] sharpened this result and obtained the minimum sampling rate $2B((2\Omega_c/B)/\lfloor 2\Omega_c/B\rfloor)$ which reduces to $2B$ when $\Omega_c = mB/2$, for any positive integer m. Brown later improved his result in [87] arriving at $2B\{((2\Omega_c/B)+1)/\lfloor(2\Omega_c/B)+1\rfloor\}$, but his new method allows the carrier frequency Ω_c to vary.

Quadrature sampling is highly appealing since the data sequences generated by the sub-ADCs are the sampled in-phase and quadrature signal components, i.e., the sampled complex envelope of the bandpass signal. As shown in [87], these baseband signals have easy reconstruction formulas in terms of the samples of the original signal. The drawback of quadrature sampling is its strict parameter selection which can lead to implementation issues. Ensur-

ing the carrier frequency is exactly an integer multiple of the sub-ADC sampling frequency may not be feasible in practice. Moreover, the timing offset between the two ADCs can be really small if the carrier frequency of the signal is very large. Other choices of the sampling frequency, carrier frequency, and sub-ADC offset were explored by Sun and Signell [88, 89], but they also involve constraints that can make design of flexible receivers challenging.

In this brief chapter, we provide sampling and reconstruction details for the quadrature sampling case using derivations of the two-channel TIADC from Section 3.3 and then investigate quadrature sampling as an approximation technique. Specifically, we show reconstruction filters in the case of quadrature sampling have simple forms and can be used to estimate the complex envelope even when the carrier frequency is not exactly an integer multiple of the sub-ADC sampling rate as required for quadrature sampling. This approximation can be highly robust if filters of sufficiently large (but practical) order are used in the reconstruction. Performance as measured by MSE deteriorates when the timing skew deviates from its ideal value set by quadrature sampling due to TIADC timing mismatches.

The results of this chapter have been published by the author in [90].

4.1 Quadrature Sampling and Reconstruction

Unlike previously published results on two-channel TIADC sampling of bandpass signals, our proposed sampling and reconstruction method places no restriction on Ω_c, Ω_s, B and d beyond $\Omega_c > \Omega_s'/2 \geq B/2$ (Ω_c cannot be in the baseband and Ω_s is at a minimum at the Nyquist rate $2B$). Earlier results [85, 86, 88, 89] typically assume relations between Ω_s and Ω_c and between d and Ω_c. For example for quadrature sampling as originally proposed by Grace and Pitt [85] and further investigated by others [86, 91], $\Omega_s' = \Omega_c/\ell$ with $\ell \in \mathbb{N}$, so that Ω_c is exactly at the center of the ℓ-th image band resulting in $\omega_b = 0$. Brown's quadrature sampling [86] also permits the carrier frequency to be $\Omega_c = (\ell \pm 1/2)\Omega_s'$ which in the digital domain maps to $\omega_b = \pm\pi$, but we do not consider this case here. The timing

offset between the two ADCs in quadrature sampling is chosen as $D = T_c/4 + pT_c$ with $p \in \mathbb{Z}$ and $T_c = 2\pi/\Omega_c$. The timing skew is then given by

$$d = \frac{D}{T_s'} = \frac{1}{4\ell} + \frac{p}{\ell}\,, \tag{4.1}$$

so $2\pi\ell d = \pi/2 + 2\pi p$. The sampled sequences in (3.6) and (3.7) reduce to

$$\begin{aligned} x_0(n) &= a(n) = a_c(nT_s') \\ x_1(n) &= b(n-d) = b_c((n-d)T_s') \end{aligned} \tag{4.2}$$

so that the two sub-ADCs sample independently the in-phase and quadrature components of the bandpass signal. The phase-shifting filter in (3.22–3.23) reduces to $G(e^{j\omega}) = -j$, and the determinant of matrix $\mathbf{M}(e^{j\omega})$ becomes $D(e^{j\omega}) = j/2$ which is constant and nonzero for all $\omega \in [-\pi, \pi)$ indicating the timing skew (4.1) is not forbidden. This can also be verified from (3.55) by observing

$$d = \frac{1}{4\ell} + \frac{p}{\ell} = \frac{1/2 + 2p}{2\ell} = \frac{2p\frac{1}{2}}{2\ell} \neq \frac{m}{2\ell}$$

for $1 \leq m \leq 2\ell - 1$ and any integer p. Reconstruction filters simplify to

$$\begin{aligned} H_0(e^{j\omega}) &= 1 \\ H_1(e^{j\omega}) &= je^{j\omega d}, \end{aligned} \tag{4.3}$$

with respective impulse responses

$$\begin{aligned} h_0(n) &= \delta(n) \\ h_1(n) &= j\,\frac{\sin[\pi(n+d)]}{\pi(n+d)}\,. \end{aligned} \tag{4.4}$$

From a practical standpoint, reconstruction is greatly simplified since only a non-integer advance filter is required which can be implemented causally with insertion of a delay. In spite of its elegance, quadrature sampling does present challenges. The timing skew d in (4.1) becomes quite small for signals located in higher image bands imposing strict jitter requirements for the sampling clocks and necessitating TIADC calibration. Moreover, the carrier frequency of the received signal may not be exactly an integer multiple of the sub-ADC sampling rate. This latter issue motivates assessing envelope reconstruction in the presence of carrier frequency deviations away from its ideal value. Let $\Omega_c^0 = \ell\Omega_s'$ be the theoretical carrier frequency desired and

$$\Omega_c = \Omega_c^0 + \varepsilon \tag{4.5}$$

the actual signal carrier frequency at the receiver. The frequency offset technically satisfies $|\varepsilon| < \Omega_s'/2$, but in practice is much smaller. Evaluating (3.2) using (4.5) gives $\omega_b = \varepsilon T_s'$, so different digital signals $x_0(n)$, $x_1(n)$ are generated based on expressions (3.6–3.7) as ε varies. Although ω_b is nonzero for all $\varepsilon \neq 0$, the complex envelope can be reconstructed approximately using the quadrature case filters (4.3) which were computed under the assumption that $\omega_b = 0$. The performance of this method is analyzed in the next section.

4.2 Simulations

Consider a bandpass signal $x_c(t) \in \mathcal{BP}_B(\mathbb{R})$ with theoretical carrier frequency $F_c^0 = \Omega_c^0/(2\pi) =$ 5 GHz, and continuous-time envelope given in (3.102) with bandwidth $(B/2)/(2\pi) = 400$ MHz. The choice of sub-ADC sampling frequency $F_s' = \Omega_s'/(2\pi) = 1$ GHz is above $B/(2\pi) =$ 800 MHz to satisfy (3.5). Since

$$F_c = F_c^0 + \frac{\varepsilon}{2\pi} = 5F_s' + \frac{\varepsilon}{2\pi}\,,$$

and $|\varepsilon|/(2\pi) < F_s'/2$, we have $\ell = 5$, i.e., F_c is located in the 5-th image band. The value of ω_b varies with different ε, but is close to zero for ε sufficiently small. The discrete-time envelope obtained by sampling $c_c(t)$ with sampling period $T_s' = 1/F_s'$ is the digital signal in (3.103).

To sample $x_c(t)$, we select a TIADC with nominal timing skew $d^0 = 1/(4\ell) = 0.05$ which is the simplest case of quadrature timing skew from (4.1). In the simulations two independent white noise sequences modelling the effect of thermal and quantization noises are added to the sub-ADC outputs $x_0(n), x_1(n)$. The sub-ADC SNR is 61.8dB. In the reconstruction block diagram in Fig. 3.5, quadrature filters (4.3) are used as an approximation to the actual filters given in (3.57–3.61).

The PSD of the estimated envelope $\hat{c}(n)$ is plotted in Fig. 4.1 when $\varepsilon = 0$, i.e. $F_c = F_c^0$ and $\omega_b = 0$. This is the ideal case where the quadrature filters are the true reconstruction filters and not an approximation. The PSD is computed via the periodogram method which is scaled so that a complex tone with unit amplitude corresponds to 0dB. The FIR filters have order $N = 16$ and Kaiser parameter $\beta = 6$. The estimated envelope has correct positioning and scaling of the four desired tones indicating successful reconstruction. Given the error $\tilde{c}(n) = c(n) - \hat{c}(n)$, the MSE is -50.56dB.

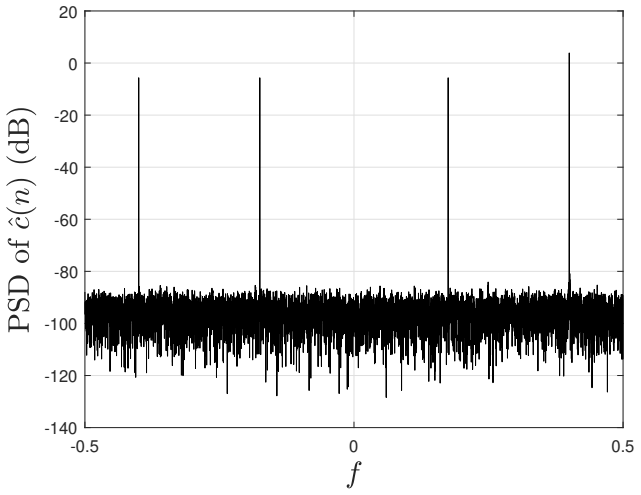


Figure 4.1: PSD of the estimated envelope $\hat{c}(n)$ for $\varepsilon = \omega_b = 0$ computed with FIR filters of order $N = 16$ for a two-channel TIADC with quadrature timing skew $d^0 = 0.05$.

The MSE is plotted in Fig. 4.2 for $|\varepsilon|/(2\pi) < F_s'/2 = 500$ MHz when different filter orders are used to estimate the envelope. Higher filter orders $N = 20, 30$ offer significant performance gain around $\varepsilon = 0$ in comparison to $N = 10$, but present little to no advantage beyond $|\varepsilon|/(2\pi) > 100$ MHz. This can be better observed in Fig. 4.3 that plots the MSE on a smaller domain focusing on more realistic values of ε. In the case of $N = 30$, frequency offsets up to ± 40 MHz can be tolerated without any performance loss. In this range $\omega_b \approx 0$, so the filters (3.57–3.61) strongly resemble quadrature filters (4.3) used in envelope estimation. However, implementing filters of length $N + 1 = 31$ may not be desirable depending on the application and power consumption constraints.

It is worth observing the MSE is not symmetric with respect to $\varepsilon = 0$. This asymmetry is due to the fact that for $\omega_b > 0$ the approximation of the dominant tone of $c(n)$ at $+0.8\pi$ is slightly worse than in the case of $\omega_b < 0$. Expressed differently, for $\omega_b > 0$ the PSD of the error function contains the dominant tone $+0.8\pi$, while for $\omega_b < 0$ it's made up entirely of nondominant tones. The asymmetry can also be observed in the tail behavior of the MSE in Fig. 4.2. For $\varepsilon > 0$ the MSE curves approach -9dB, while for $\varepsilon < 0$ they converge to -16dB.

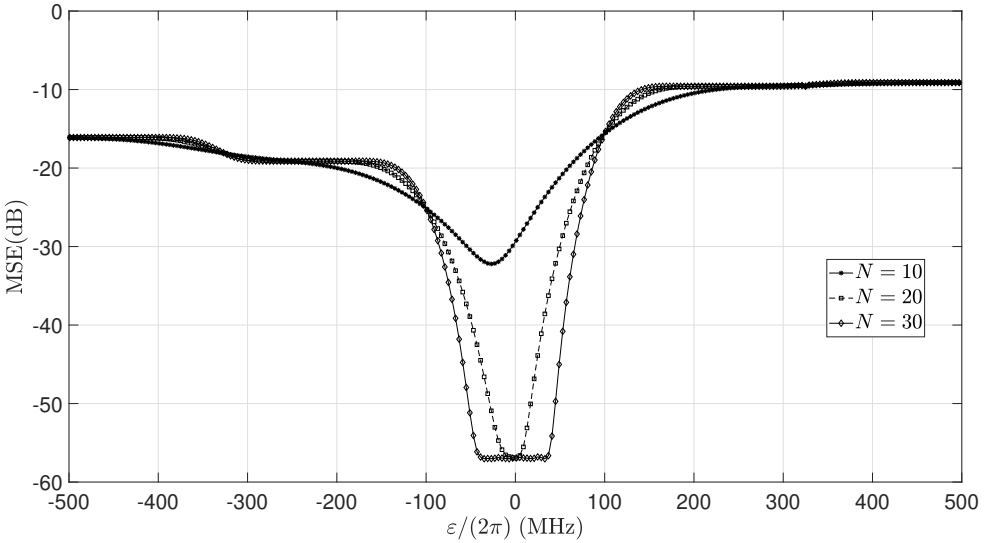


Figure 4.2: MSE for the entire range of ε values computed with FIR filters of order $N = 10, 20, 30$ in the case of quadrature timing skew $d^0 = 0.05$.

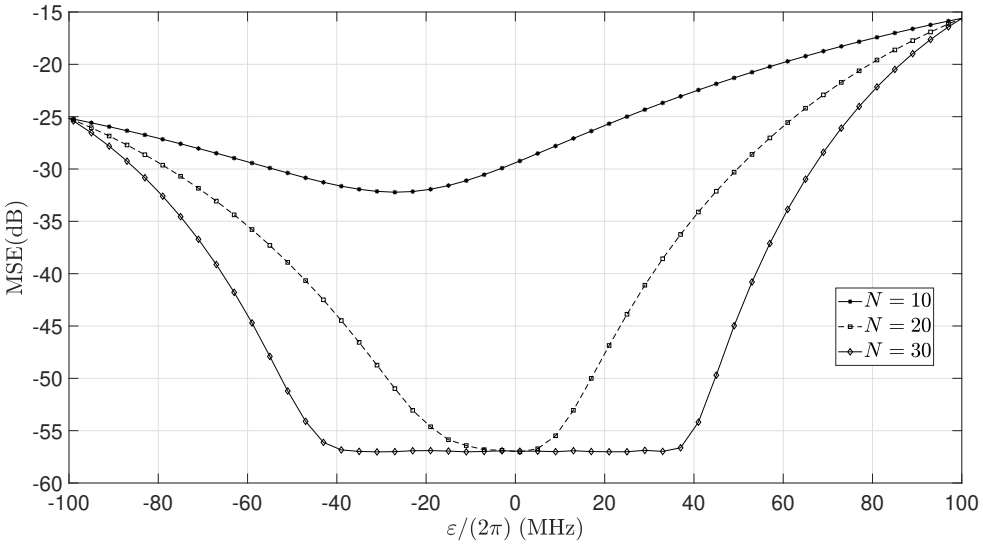


Figure 4.3: MSE for $-200\pi < \varepsilon < 200\pi$ computed with FIR filters of order $N = 10, 20, 30$ in the case of quadrature timing skew $d^0 = 0.05$.

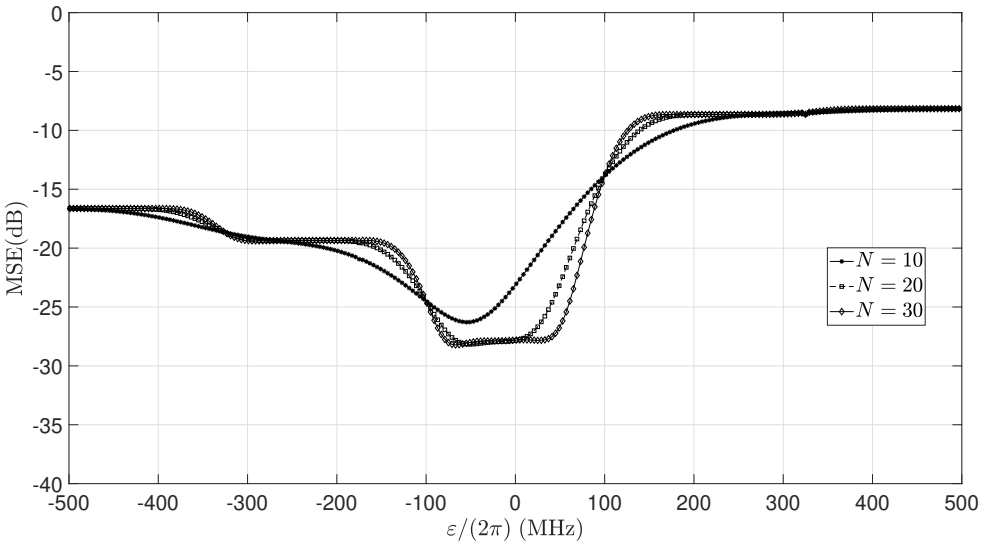


Figure 4.4: MSE for the entire range of ε values computed with FIR filters of order $N = 10, 20, 30$ in the case of quadrature timing skew $d^0 = 0.05$ with 0.10% timing mismatch.

Given the nominal quadrature timing skew $d^0 = 0.05$ is quite small, it can impose stringent jitter specifications on the two sampling clocks of the TIADC. This motivates assessing quadrature approximation performance when the TIADC suffers from timing skew mismatches. Fig. 4.4 shows the MSE curves in the case when $d - d^0 = 0.0010$, i.e., there is

a 0.10% mismatch between the nominal parameter d^0 and the true parameter d. Comparing this figure with Fig. 4.2, we note the MSE drops by 30dB in the vicinity of $\varepsilon = 0$ for $N = 20, 30$, but only by 7dB for $N = 10$. Thus, unlike in the case $N = 10$ where estimation is limited more by the low filter order than timing mismatch, higher filter orders $N = 20, 30$ lose their robust approximation when the timing skew is inaccurate. This indicates TIADC calibration is especially necessary when higher order filters are used in envelope reconstruction. The tails of the MSE curves in Fig. 4.4 have a very similar convergence behavior to the ones in Fig. 4.2.

Chapter 5

Blind Calibration of Gain and Timing Mismatches in M-channel Bandpass Sampling Time-Interleaved ADCs

As demonstrated in Chapters 3 and 4 simulations, the proposed complex envelope reconstruction technique is sensitive to TIADC gain and timing skew mismatches. This motivates a calibration algorithm that can estimate mismatches and compensate for their effect. TIADC calibration techniques can be divided in two categories, depending on whether the normal ADC operation is suspended during calibration phases. Foreground calibration techniques interrupt the ADC operation by using a known test signal and identify mismatches by using equalizer type of methods [92–94] or more recently by employing genetic algorithms [95, 96]. Background or blind methods identify mismatches while the ADC is operating normally. They rely on some a priori signal knowledge, such as the absence of signal energy in certain frequency bands (this can be achieved for example if the signal is oversampled [33, 34, 97–102]), stationarity properties of the signal [32, 103–106], or source spectrum sparsity [107,108]. Foreground methods have the disadvantage of lowering the ADC throughput, but they are highly scalable and robust to modelling inaccuracies. Background

methods are more efficient and have the advantage of being able to track continuously ADC parameter changes, but they require additional digital filtering operations. In this respect, it is important to note that majority of existing TIADC calibration methods are restricted to baseband signals and thus cannot be applied directly to our proposed bandpass TIADC architecture.

In recent years, some techniques have been developed for calibrating bandpass sampling TIADCs. For example, semi-blind methods discussed in [109–111] inject a known test signal in a frequency band free of power prior to digitization, evaluate the distortions caused by TIADC mismatches, and then remove the test signal from the TIADC output. They are, however, limited to uniformly interleaved bandpass sampling ADCs. Some fully blind techniques [112–116] also assume that the TIADC is ideally uniform and select the overall ADC sampling frequency on the basis of first-order bandpass sampling condition (2.48) to avoid aliasing. Calibration of a nonuniform bandpass TIADC does have presence in the literature (although very little). The authors in [117,118] consider timing skew calibration for Kohlenberg's [11] second-order nonuniform bandpass sampling. While [117] utilizes training signals to perform timing skew estimation, [118] relies on detection of wide-sense stationarity in the reconstructed signal for blind parameter estimation.

All of the mentioned bandpass calibration techniques sample and reconstruct the analog bandpass signal and not its envelope. In this chapter, we propose a novel bandpass calibration method tailored to the complex envelope sampling and reconstruction technique discussed in Chapter 3. Our method is universal and works for any number of channels M. We leverage the digital filtering operations used to compute the envelope in order to perform TIADC calibration. As in [33, 99], it is assumed that the signal is slightly oversampled, by say 20%. This creates a frequency band where the complex envelope does not have any spectral content. Therefore the presence of energy in this band indicates that the TIADC gain and timing skew estimates used in the reconstruction are incorrect. By implementing a complex bandpass filter which extracts the signal power in this band, we construct an

error signal whose power is minimized adaptively to estimate the gain and timing skew mismatches. We rigorously study the error signal, analyze the convergence behavior of the estimation algorithm, and demonstrate the efficacy of the proposed calibration method with simulations using multi-tone, white noise, and MSK signals.

Instead of correcting the mismatches of each channel with respect to their nominal values, the calibration method we consider corrects relative mismatches with respect to a reference channel. This is advantageous since relative channel mismatches are smaller in magnitude than absolute mismatches in each channel. Moreover, only $M-1$ instead of M sub-ADCs need to be calibrated. The common choice for the reference channel is the first sub-ADC. We follow this convention in developing our proposed calibration technique. Finally, mismatches are allowed to vary over time, but we assume the variations are small and not abrupt.

5.1 Blind TIADC Calibration Method

Consider M-channel TIADC sampling of $x_c(t) \in \mathcal{BP}_B(\mathbb{R})$ shown in Fig. 3.1. In practice, semiconductor imperfections and other hardware limitations make it impossible to match the sub-ADCs to their design specifications. For a desired sub-ADC timing skew d_i^0 with $1 \leq i \leq M-1$, due to circuit imperfections, the actual timing skew is d_i and the sub-ADC relative gain g_i differs from its ideal value $g_i^0 = 1$. Typically, the mismatches

$$\begin{aligned} \gamma_i &= g_i - g_i^0 = g_i - 1 \\ \delta_i &= d_i - d_i^0 \end{aligned} \tag{5.1}$$

are small, say about 1% or less, but they contribute to a significant loss of ADC resolution. Mismatch values are of course unknown and must be estimated. Since the first sub-ADC is used as a reference channel, its output is still given by

$$x_0(n) = \Re\{c^{[L]}(Ln)e^{j\omega_b n}\}, \tag{5.2}$$

which is the same expression as (3.6). The output of the i-th sub-ADC with gain and timing skew mismatches can be expressed as

$$\begin{aligned} x_i(n) &= g_i \times \Re\{c^{[L]}(L(n-d_i))e^{j\omega_b(n-d_i)}e^{-j2\pi\ell d_i}\} \\ &= (1+\gamma_i) \times \Re\{c^{[L]}(L(n-(d_i^0+\delta_i)))e^{j\omega_b(n-(d_i^0+\delta_i))}e^{-j2\pi\ell d_i^0}e^{-j2\pi\ell\delta_i}\} \end{aligned} \tag{5.3}$$

for $1 \leq i \leq M-1$. The fractional delay filter in Fig. 3.3 changes from (3.10) to

$$F_i(e^{j\omega}; g_i, d_i) = g_i e^{-j\omega L d_i} \tag{5.4}$$

for $-\pi < \omega \leq \pi$, where we have made explicit the dependency on g_i and d_i. The filters (3.22–3.23) and (3.37) are still given by the same expressions, but we can write them as $G_i(e^{j\omega}; d_i)$ and $f_{i,k}(e^{j\omega}; d_i)$, respectively, due to their dependency on d_i.

Let $\boldsymbol{g}, \boldsymbol{d} \in \mathbb{R}^{M-1}$ defined as

$$\begin{aligned} \boldsymbol{g} &= [g_1, \ldots, g_i, \ldots, g_{M-1}]^T \\ \boldsymbol{d} &= [d_1, \ldots, d_i, \ldots, d_{M-1}]^T \end{aligned} \tag{5.5}$$

be the vector of TIADC channel gains and timing skews, respectively. Here, ^{T} denotes the transpose operator. The reconstruction matrix (3.41) is a function of $\boldsymbol{d}$ and so from now on we write it as $\mathbf{M}(e^{j\omega}; \boldsymbol{d})$. While the first reconstruction filter $H_0(e^{j\omega}; \boldsymbol{d})$ in (3.47) depends on $\boldsymbol{d}$ only, the others $H_i(e^{j\omega}; g_i, \boldsymbol{d})$ for $1 \leq i \leq M-1$ have an additional dependency on the gain g_i of their channel. If we define

$$\boldsymbol{\theta} = \begin{bmatrix} \boldsymbol{g} \\ \boldsymbol{d} \end{bmatrix} \in \mathbb{R}^{2(M-1)}, \tag{5.6}$$

then the expression (3.49) can be stated in time domain as

$$r^{[L]}(n;\boldsymbol{\theta}) = h_0(n;\boldsymbol{d}) * x_0^e(n) + \sum_{i=1}^{M-1} h_i(n;g_i,\boldsymbol{d}) * x_i^e(n)\ , \tag{5.7}$$

where $x_i^e(n)$, $0 \leq i \leq M-1$ are the expanded TIADC outputs given in (3.38). Thus, reconstruction is a function of $\boldsymbol{\theta}$ which is unknown and must be estimated. We let $\hat{\boldsymbol{\theta}} = [\hat{\boldsymbol{g}}, \hat{\boldsymbol{d}}]^T$ be an estimate of $\boldsymbol{\theta}$ and

$$\boldsymbol{\theta}_0 = \begin{bmatrix} \boldsymbol{g}^0 \\ \boldsymbol{d}^0 \end{bmatrix} = \begin{bmatrix} g_1^0 \\ \vdots \\ g_{M-1}^0 \\ d_1^0 \\ \vdots \\ d_{M-1}^0 \end{bmatrix} = \begin{bmatrix} \mathbf{1}_{M-1} \\ d_1^0 \\ \vdots \\ d_{M-1}^0 \end{bmatrix} \tag{5.8}$$

the nominal parameter vector, where $\mathbf{1}_{M-1}$ is a column vector of size $M-1$ consisting of all ones. Since mismatches are small, it is assumed that $\boldsymbol{\theta}$, $\hat{\boldsymbol{\theta}}$, and $\boldsymbol{\theta}_0$ are all close to each other. The goal of the calibration will be to accurately estimate $\boldsymbol{\theta}$ using the known $\boldsymbol{\theta}_0$ as a starting point. The mismatch parameter vector is given by

$$\boldsymbol{\theta} - \boldsymbol{\theta}_0 = \begin{bmatrix} \boldsymbol{\gamma} \\ \boldsymbol{\delta} \end{bmatrix} \tag{5.9}$$

with gain mismatches vector

$$\boldsymbol{\gamma} = [\gamma_1, \ldots, \gamma_i, \ldots, \gamma_{M-1}]^T \tag{5.10}$$

and timing skew mismatches vector

$$\boldsymbol{\delta} = [\delta_1, \ldots, \delta_i, \ldots, \delta_{M-1}]^T \ . \tag{5.11}$$

Since $\boldsymbol{\theta}$ is unknown, its estimate $\hat{\boldsymbol{\theta}}$ can be used in reconstruction (5.7), i.e., we can use impulse responses of filters $H_0(e^{j\omega}; \hat{\boldsymbol{d}})$ and $H_i(e^{j\omega}; \hat{g}_i, \hat{\boldsymbol{d}})$, $1 \leq i \leq M-1$. However, to avoid updating the filters each time the vector $\hat{\boldsymbol{\theta}}$ is updated, we exploit the fact that the estimated mismatch vector $\hat{\boldsymbol{\theta}} - \boldsymbol{\theta}_0$ is small and thus we can perform first-order expansions of filters around the nominal vector $\boldsymbol{\theta}_0$.

$$\begin{aligned} H_0(e^{j\omega}; \hat{\boldsymbol{d}}) &= H_0(e^{j\omega}; \boldsymbol{d}^0 + \hat{\boldsymbol{\delta}}) \\ &= H_0(e^{j\omega}; \boldsymbol{d}^0) + \hat{\boldsymbol{\delta}}^T \nabla_{\hat{\boldsymbol{d}}} H_0(e^{j\omega}; \boldsymbol{d}^0) \\ &= H_0(e^{j\omega}; \boldsymbol{d}^0) + \sum_{l=1}^{M-1} \hat{\delta}_l \frac{\partial H_0}{\partial \hat{d}_l}(e^{j\omega}; \boldsymbol{d}^0) \\ &= H_{0,0}(e^{j\omega}) + \sum_{l=1}^{M-1} \hat{\delta}_l H_{0,l}(e^{j\omega}), \end{aligned} \tag{5.12}$$

where we define

$$H_{0,0}(e^{j\omega}) = H_0(e^{j\omega}; \boldsymbol{d}^0),$$

$$H_{0,l}(e^{j\omega}) = \frac{\partial H_0}{\partial \hat{d}_l}(e^{j\omega}; \boldsymbol{d}^0) \ .$$

For $1 \leq i \leq M-1$,

$$\begin{aligned} H_i(e^{j\omega}; \hat{g}_i, \hat{\boldsymbol{d}}) &= H_i(e^{j\omega}; g_i^0 + \hat{\gamma}_i, \boldsymbol{d}^0 + \hat{\boldsymbol{\delta}}) \\ &= H_i(e^{j\omega}; g_i^0, \boldsymbol{d}^0) + \hat{\gamma}_i \frac{\partial H_i}{\partial \hat{g}_i}(e^{j\omega}; g_i^0, \boldsymbol{d}^0) + \sum_{l=1}^{M-1} \hat{\delta}_l \frac{\partial H_i}{\partial \hat{d}_l}(e^{j\omega}; g_i^0, \boldsymbol{d}^0) \\ &= (1 - \hat{\gamma}_i) H_{i,0}(e^{j\omega}) + \sum_{l=1}^{M-1} \hat{\delta}_l H_{i,l}(e^{j\omega}), \end{aligned} \tag{5.13}$$

where

$$H_{i,0}(e^{j\omega}) = H_i(e^{j\omega}; g_i^0, \boldsymbol{d}^0),$$

$$H_{i,l}(e^{j\omega}) = \frac{\partial H_i}{\partial \hat{d}_l}(e^{j\omega}; g_i^0, \boldsymbol{d}^0) \ ,$$

and we have made use of the observation

$$\frac{\partial H_i}{\partial \hat{g}_i}(e^{j\omega}; g_i^0, \boldsymbol{d}^0) = -H_i(e^{j\omega}; g_i^0, \boldsymbol{d}^0).$$

We can therefore express (5.7) as

$$r^{[L]}(n; \hat{\boldsymbol{\theta}}) = r_0^{[L]}(n; \hat{\boldsymbol{d}}) + \sum_{i=1}^{M-1} r_i^{[L]}(n; \hat{g}_i, \hat{\boldsymbol{d}}) \tag{5.14}$$

with

$$\begin{aligned} r_0^{[L]}(n; \hat{\boldsymbol{d}}) &= x_0^e(n) * h_{0,0}(n) + \sum_{l=1}^{M-1} \hat{\delta}_l \big(x_0^e(n) * h_{0,l}(n)\big) \\ r_i^{[L]}(n; \hat{g}_i, \hat{\boldsymbol{d}}) &= (1-\hat{\gamma}_i)\big(x_i^e(n) * h_{i,0}(n)\big) + \sum_{l=1}^{M-1} \hat{\delta}_l \big(x_i^e(n) * h_{i,l}(n)\big), \end{aligned} \tag{5.15}$$

where $h_{0,0}(n)$, $h_{0,l}(n)$, $h_{i,0}(n)$, and $h_{i,l}(n)$ for $1 \leq i, l \leq M-1$ are impulse responses of filters $H_{0,0}(e^{j\omega})$, $H_{0,l}(e^{j\omega})$, $H_{i,0}(e^{j\omega})$, and $H_{i,l}(e^{j\omega})$, respectively.

Since the estimated parameter vector $\hat{\boldsymbol{\theta}}$ is used in reconstruction, the output signal $r^{[L]}(n; \hat{\boldsymbol{\theta}})$ differs from the exact signal $r^{[L]}(n; \boldsymbol{\theta}) = c^{[L]}(n)e^{j(\omega_b/L)n}$ that would be obtained for the correct parameter vector $\boldsymbol{\theta}$. Therefore, we can use differences between $r^{[L]}(n; \hat{\boldsymbol{\theta}})$ and the correct signal $r^{[L]}(n; \boldsymbol{\theta})$ to calibrate the TIADC. In a blind calibration method, the signal $r^{[L]}(n; \boldsymbol{\theta})$ is unknown, but we can exploit known properties of $c^{[L]}(n)$ to infer some information about $r^{[L]}(n; \boldsymbol{\theta})$ to estimate the parameter vector $\boldsymbol{\theta}$.

The blind calibration scheme we propose estimates $\boldsymbol{\theta}$ adaptively by extracting from $r^{[L]}(n; \hat{\boldsymbol{\theta}})$ an error signal $e^{[L]}(n; \hat{\boldsymbol{\theta}})$ whose power provides a measure of how far the estimated

vector $\hat{\boldsymbol{\theta}}$ is from the true vector $\boldsymbol{\theta}$. To accomplish this, we assume $c_c(t)$ is oversampled so that $c^{[L]}(n) = c_c(nT_s'/L)$ has zero power in frequencies around $\pm\pi$. This is guaranteed to happen when the sampling frequency $L\Omega_s'$ of $c_c(t)$ is above its Nyquist rate B. Therefore, we assume that the complex envelope $c_c(t)$ is oversampled with oversampling ratio

$$\alpha = \frac{L\Omega_s' - B}{L\Omega_s'} \ . \tag{5.16}$$

It is easy to show that

$$\alpha = \frac{\Omega_s - \Omega_{s,min}}{\Omega_s} \ , \tag{5.17}$$

where

$$\Omega_{s,min} = \begin{cases} 2B & \text{if } M \text{ is even} \\ \frac{M}{M-1}2B & \text{if } M \text{ is odd} \end{cases} \tag{5.18}$$

from (3.4) is the minimum permissible sampling frequency of the overall TIADC. In this case the DTFT $C(e^{j\omega})$ of the sampled envelope sequence $c^{[L]}(n)$ satisfies

$$C(e^{j\omega}) = 0 \tag{5.19}$$

over interval $[(1-\alpha)\pi, (1+\alpha)\pi]$ and all its 2π-shifted copies. This implies that when the estimated parameter vector $\hat{\boldsymbol{\theta}}$ coincides with the correct vector $\boldsymbol{\theta}$, the signal $r^{[L]}(n;\boldsymbol{\theta}) = c^{[L]}(n)e^{j(\omega_b/L)n}$ has no frequency content in the band $I = [\frac{\omega_b}{L} + (1-\alpha)\pi, \frac{\omega_b}{L} + (1+\alpha)\pi]$ and its 2π-shifted copies. Consider therefore the discrete-time bandpass filter

$$H_{\text{BP}}(e^{j\omega}) = \begin{cases} 1 & \omega \in I \mod (2\pi) \\ 0 & \text{otherwise} \ . \end{cases} \tag{5.20}$$

It can be viewed as an ideal lowpass filter for the band $[-\alpha\pi, \alpha\pi]$ modulated by $(\omega_b/L) + \pi$,

so that its impulse response is given by

$$h_{BP}(n) = (-e^{j\frac{\omega_b}{L}})^n \frac{\sin(\alpha\pi n)}{\pi n} \ . \tag{5.21}$$

Then, let

$$e^{[L]}(n;\hat{\boldsymbol{\theta}}) = h_{BP}(n) * r^{[L]}(n;\hat{\boldsymbol{\theta}}) \tag{5.22}$$

denote the error signal obtained by extracting from $r^{[L]}(n;\hat{\boldsymbol{\theta}})$ its frequency content in the band I. Since $e^{[L]}(n;\hat{\boldsymbol{\theta}}) = 0$ whenever $\hat{\boldsymbol{\theta}} = \boldsymbol{\theta}$, the estimation scheme we propose minimizes adaptively the power

$$J(\hat{\boldsymbol{\theta}}) = \frac{1}{2} E[|e^{[L]}(n;\hat{\boldsymbol{\theta}})|^2] \tag{5.23}$$

of complex signal $e^{[L]}(n;\hat{\boldsymbol{\theta}})$. This approach is justified rigorously in Section 5.2 by showing that if the complex envelope random process $c^{[L]}(n)$ is WSS, in the vicinity of $\boldsymbol{\theta}$, $J(\hat{\boldsymbol{\theta}})$ can be approximated by a positive definite quadratic function of $\epsilon_i = \hat{\gamma}_i - \gamma_i$ and $\eta_i = \hat{\delta}_i - \delta_i$ for $1 \leq i \leq M-1$, provided $c^{[L]}(n)$ satisfies certain spectral frequency content conditions. This ensures that by minimizing $J(\hat{\boldsymbol{\theta}})$ iteratively, starting with the nominal value

$$\hat{\boldsymbol{\theta}}(0) = \boldsymbol{\theta}_0, \tag{5.24}$$

the iterates will converge to the correct true parameter vector $\boldsymbol{\theta}$.

If the gradient of function $J(\hat{\boldsymbol{\theta}})$ is available, which is typically not the case since the evaluation of the ensemble average in (5.23) requires knowledge of the statistics of the envelope process $c^{[L]}(n)$, $J(\hat{\boldsymbol{\theta}})$ can be minimized by using a steepest descent iteration of the form

$$\hat{\boldsymbol{\theta}}(n+1) = \hat{\boldsymbol{\theta}}(n) - \mu_g(n) \nabla_{\hat{\boldsymbol{\theta}}} J(\hat{\boldsymbol{\theta}}(n)) \tag{5.25}$$

discussed in detail in Section 2.6, where $\mu_g(n) > 0$ denotes the step size at iteration n. In the absence of the gradient of $J(\hat{\boldsymbol{\theta}})$, we apply a stochastic gradient approximation, where

the expectation in (5.23) is replaced by its instantaneous value, which yields the adaptive estimation algorithm

$$\begin{aligned}\hat{\boldsymbol{\theta}}(n+1) &= \hat{\boldsymbol{\theta}}(n) - \mu(n)\nabla_{\hat{\boldsymbol{\theta}}}\big(\frac{1}{2}|e^{[L]}(n;\hat{\boldsymbol{\theta}}(n))|^2\big) \\ &= \hat{\boldsymbol{\theta}}(n) - \mu(n)\Re\{(e^{[L]}(n;\hat{\boldsymbol{\theta}}(n)))^*\,\nabla_{\hat{\boldsymbol{\theta}}}e^{[L]}(n;\hat{\boldsymbol{\theta}}(n))\} \end{aligned} \tag{5.26}$$

with initial condition (5.24). As mentioned in Section 2.6, the value of step size $\mu(n) > 0$ used for this recursion is much smaller than $\mu_g(n)$ for the steepest descent algorithm (5.25).

The recursion (5.26) requires the computation of the gradient of $e^{[L]}(n;\hat{\boldsymbol{\theta}})$ with respect to $\hat{\boldsymbol{\theta}}$, i.e., we need to calculate $\frac{\partial}{\partial\hat{g}_i}e^{[L]}(n;\hat{\boldsymbol{\theta}})$ and $\frac{\partial}{\partial\hat{d}_i}e^{[L]}(n;\hat{\boldsymbol{\theta}})$ for all $1 \le i \le M-1$. To do so, it is convenient to first decompose the error signal $e^{[L]}(n;\hat{\boldsymbol{\theta}})$ using its definition (5.22) and expressions (5.14-5.15) as

$$e^{[L]}(n;\hat{\boldsymbol{\theta}}) = e_0^{[L]}(n;\hat{\boldsymbol{d}}) + \sum_{k=1}^{M-1} e_k^{[L]}(n;\hat{g}_k,\hat{\boldsymbol{d}}) \tag{5.27}$$

with

$$\begin{aligned} e_0^{[L]}(n;\hat{\boldsymbol{d}}) &= x_0^e(n) * h_{0,0}(n) * h_{\mathrm{BP}}(n) + \sum_{l=1}^{M-1}\hat{\delta}_l\big(x_0^e(n) * h_{0,l}(n) * h_{\mathrm{BP}}(n)\big) \\ e_k^{[L]}(n;\hat{g}_k,\hat{\boldsymbol{d}}) &= (1-\hat{\gamma}_k)\big(x_k^e(n) * h_{k,0}(n) * h_{\mathrm{BP}}(n)\big) \\ &\qquad + \sum_{l=1}^{M-1}\hat{\delta}_l\big(x_k^e(n) * h_{k,l}(n) * h_{\mathrm{BP}}(n)\big). \end{aligned} \tag{5.28}$$

We now obtain

$$\frac{\partial}{\partial\hat{g}_i}e^{[L]}(n;\hat{\boldsymbol{\theta}}) = \frac{\partial}{\partial\hat{g}_i}e_i^{[L]}(n;\hat{g}_i,\hat{\boldsymbol{d}}) = -\underbrace{\big(x_i^e(n) * h_{i,0}(n) * h_{\mathrm{BP}}(n)\big)}_{e_{i,0}^{[L]}(n)} = -e_{i,0}^{[L]}(n)\ , \tag{5.29}$$

where we have defined the signal $e_{i,0}^{[L]}(n)$ as shown. Similarly,

$$\begin{aligned}\frac{\partial}{\partial \hat{d}_i} e^{[L]}(n;\hat{\boldsymbol{\theta}}) &= \frac{\partial}{\partial \hat{d}_i} e_0^{[L]}(n;\hat{\boldsymbol{d}}) + \sum_{k=1}^{M-1} \frac{\partial}{\partial \hat{d}_i} e_k^{[L]}(n;\hat{g}_k,\hat{\boldsymbol{d}}) \\ &= \underbrace{\big(x_0^e(n) * h_{0,i}(n) * h_{\mathrm{BP}}(n)\big)}_{e_{0,i}^{[L]}(n)} + \sum_{k=1}^{M-1} \underbrace{\big(x_k^e(n) * h_{k,i}(n) * h_{\mathrm{BP}}(n)\big)}_{e_{k,i}^{[L]}(n)} \\ &= \sum_{k=0}^{M-1} e_{k,i}^{[L]}(n) \end{aligned} \tag{5.30}$$

where we have again defined the signals $e_{k,i}^{[L]}(n)$ for $0 \le k \le M-1$ as shown.

The parameter vector estimate $\hat{\boldsymbol{\theta}}(n)$ is evaluated adaptively by substituting gradient component expressions (5.29) and (5.30) inside recursion (5.26). As shown in Fig. 5.1, the proposed reconstruction and calibration algorithm requires M^2 *fixed* filters $H_{i,l}(e^{j\omega})$ for $0 \le i,l \le M-1$ based on first-order expansions of $H_i(e^{j\omega})$, M^2 copies of the bandpass filter $H_{\mathrm{BP}}(e^{j\omega})$ to extract error signals $e^{[L]}(n;\hat{\boldsymbol{\theta}})$, $e_{0,l}^{[L]}(n)$ for $1 \le l \le M-1$, and $e_{i,l}^{[L]}(n)$ for $1 \le i \le M-1$ and $0 \le l \le M-1$, and M^2-1 taps involving estimated mismatches $\hat{\boldsymbol{\gamma}}$ and $\hat{\boldsymbol{\delta}}$ that need to be adapted. The output $\hat{c}^{[L]}(n)$ is an estimate of the sampled complex envelope $c^{[L]}(n)$ since first order filter expansions in (5.12–5.13) ignore higher order terms. The ideal impulse responses of filters $H_{i,l}(e^{j\omega})$ and $H_{\mathrm{BP}}(e^{j\omega})$ are noncausal and IIR, but causal FIR implementations of these filters can be obtained by windowing and inclusion of appropriate delays. It is also worth observing that the implementation of the copies of bandpass filter $H_{\mathrm{BP}}(e^{j\omega})$ used to generate the error signals is required only during calibration phases. After convergence, if the values of g_i and d_i for $1 \le i \le M-1$ are not expected to change, the estimation algorithm (5.26) and associated bandpass filters can be turned off to save power, until a new calibration update is required. However, if power consumption is not a significant consideration, it may be beneficial to keep running the recursion (5.26) in the background to track drifts in the values of g_i and d_i due to variations in TIADC operating conditions, such as temperature changes. A close-up of the i-th reconstruction channel for $1 \le i \le M-1$ is

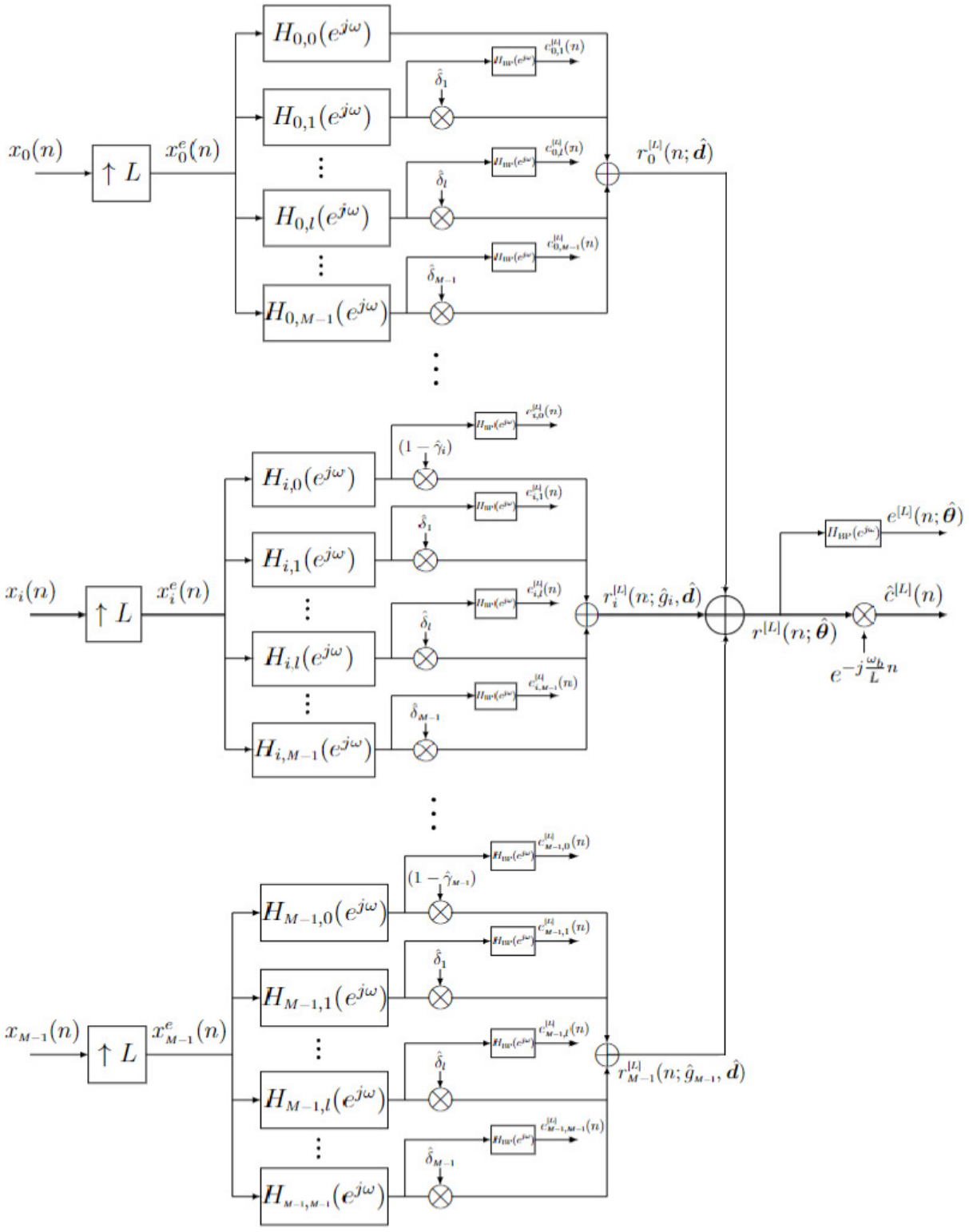


Figure 5.1: Adaptive reconstruction filter implementation and error signal computation, where $1 \leq i \leq M-1$.

shown in Fig. 5.2.

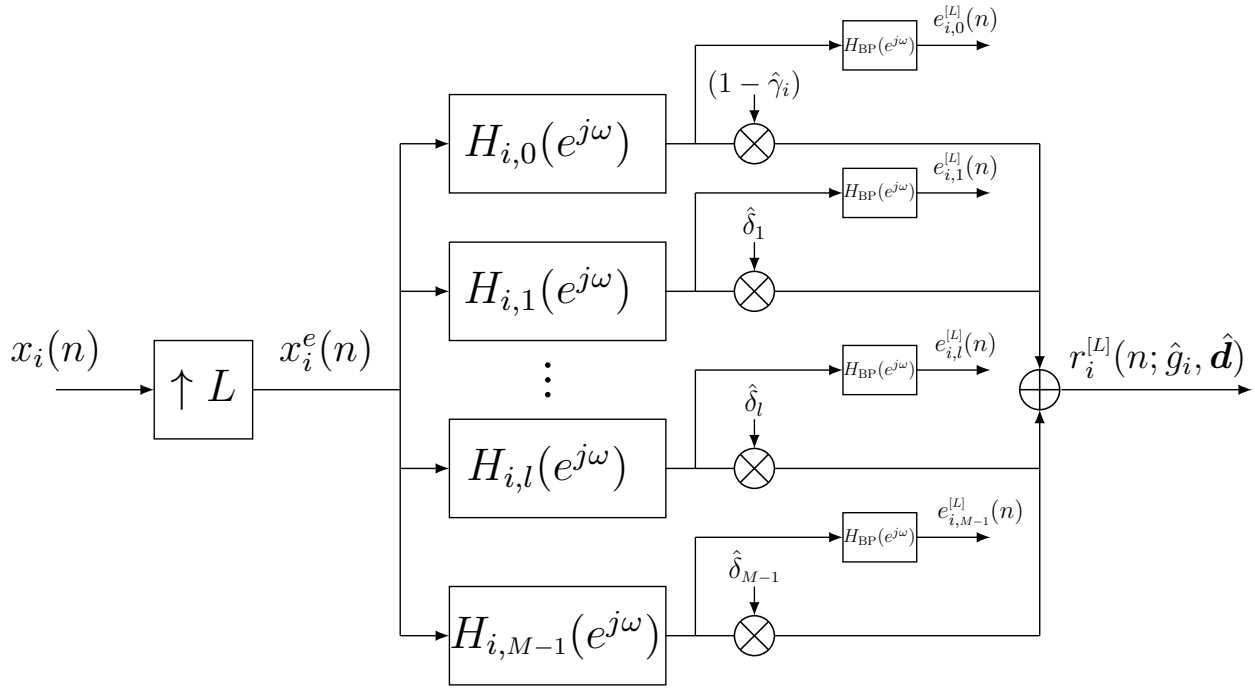


Figure 5.2: Zoomed in i-th reconstruction and calibration channel from Fig. 5.1 for $1 \leq i \leq M-1$.

5.2 Quadratic Approximation of $J(\hat{\boldsymbol{\theta}})$

In this section, we derive a quadratic approximation of $J(\hat{\boldsymbol{\theta}})$ in the vicinity of the true parameter $\boldsymbol{\theta}$. Moreover, we argue that $J(\hat{\boldsymbol{\theta}})$ is convex and achieves its minimum at $\hat{\boldsymbol{\theta}} = \boldsymbol{\theta}$.

We start by recalling from Fig. 3.4 that the DTFT of signal $r^{[L]}(n;\hat{\boldsymbol{\theta}})$ can be expressed as

$$R(e^{j\omega};\hat{\boldsymbol{\theta}}) = \Big[H_0(e^{j\omega};\hat{\boldsymbol{d}}),\ldots,H_i(e^{j\omega};\hat{g}_i,\hat{\boldsymbol{d}}),\ldots,H_{M-1}(e^{j\omega};\hat{g}_{M-1},\hat{\boldsymbol{d}})\Big] \begin{bmatrix} X_0^e(e^{j\omega}) \\ \vdots \\ X_i^e(e^{j\omega}) \\ \vdots \\ X_{M-1}^e(e^{j\omega}) \end{bmatrix} . \quad (5.31)$$

Using (3.39) and (3.47), this expression can be simplified to

$$\begin{aligned} R(e^{j\omega};\hat{\boldsymbol{\theta}}) \;=\; & \Big[1 \;\; 0 \;\; \ldots \;\; 0\Big]\, \mathbf{M}^{\text{inv}}(e^{j\omega};\hat{\boldsymbol{d}}) \\ & \times \text{diag}\big\{1, F_1^{-1}(e^{j\omega};\hat{g}_1,\hat{d}_1),\ldots,F_i^{-1}(e^{j\omega};\hat{g}_i,\hat{d}_i),\ldots,F_{M-1}^{-1}(e^{j\omega};\hat{g}_{M-1},\hat{d}_{M-1})\big\} \\ & \times \text{diag}\big\{1, F_1(e^{j\omega};g_1,d_1),\ldots,F_i(e^{j\omega};g_i,d_i),\ldots,F_{M-1}(e^{j\omega};g_{M-1},d_{M-1})\big\} \\ & \times \mathbf{M}(e^{j\omega};\boldsymbol{d}) \begin{bmatrix} \mathbf{C}(e^{j\omega}) \\ \mathbf{C}^*(e^{-j\omega}) \end{bmatrix} = \mathbf{L}(e^{j\omega};\hat{\boldsymbol{\theta}}) \begin{bmatrix} \mathbf{C}(e^{j\omega}) \\ \mathbf{C}^*(e^{-j\omega}) \end{bmatrix} , \end{aligned} \quad (5.32)$$

where the $L \times 1$ vector $\mathbf{C}(e^{j\omega})$ is given in (3.40) and the $1 \times 2L$ vector $\mathbf{L}(e^{j\omega};\hat{\boldsymbol{\theta}})$ is

$$\begin{aligned} \mathbf{L}(e^{j\omega};\hat{\boldsymbol{\theta}}) = & \Big[1 \;\; 0 \;\; \ldots \;\; 0\Big]\, \mathbf{M}^{\text{inv}}(e^{j\omega};\hat{\boldsymbol{d}}) \\ & \times \text{diag}\big\{1, \tfrac{g_1}{\hat{g}_1} e^{j\omega L(\hat{d}_1 - d_1)} \ldots, \tfrac{g_i}{\hat{g}_i} e^{j\omega L(\hat{d}_i - d_i)},\ldots,\tfrac{g_{M-1}}{\hat{g}_{M-1}} e^{j\omega L(\hat{d}_{M-1} - d_{M-1})}\big\} \mathbf{M}(e^{j\omega};\boldsymbol{d}) . \end{aligned} \quad (5.33)$$

We perform a first-order Taylor series expansion of $\mathbf{L}(e^{j\omega};\hat{\boldsymbol{\theta}})$ in the vicinity of the true parameter vector $\boldsymbol{\theta}$,

$$\mathbf{L}(e^{j\omega};\hat{\boldsymbol{\theta}}) = \mathbf{L}(e^{j\omega};\boldsymbol{\theta}+\boldsymbol{h}) \approx \mathbf{L}(e^{j\omega};\boldsymbol{\theta}) + \boldsymbol{h}^T \nabla_{\hat{\boldsymbol{\theta}}} \mathbf{L}(e^{j\omega};\boldsymbol{\theta}) , \quad (5.34)$$

where

$$\begin{aligned} \boldsymbol{h} = \hat{\boldsymbol{\theta}} - \boldsymbol{\theta} &= \left[\hat{\gamma}_1 - \gamma_1, \ldots, \hat{\gamma}_{M-1} - \gamma_{M-1}, \hat{\delta}_1 - \delta_1, \ldots, \hat{\delta}_{M-1} - \delta_{M-1}\right]^T \\ &= \left[\epsilon_1, \ldots, \epsilon_{M-1}, \eta_1, \ldots, \eta_{M-1}\right]^T \end{aligned} \tag{5.35}$$

is the vector of estimated mismatches. The first term on the right hand side of (5.34) is the simple $1 \times 2L$ row vector

$$\mathbf{L}(e^{j\omega}; \boldsymbol{\theta}) = \begin{bmatrix} 1 & 0 & \ldots & 0 \end{bmatrix}$$

from definition of $\mathbf{L}(e^{j\omega}; \hat{\boldsymbol{\theta}})$ in (5.33). The expansion in (5.34) can then be written as

$$\mathbf{L}(e^{j\omega}; \hat{\boldsymbol{\theta}}) \approx \begin{bmatrix} 1 & 0 & \ldots & 0 \end{bmatrix} + \sum_{i=1}^{M-1} \epsilon_i \mathbf{L}_{\gamma_i}(e^{j\omega}) + \sum_{i=1}^{M-1} \eta_i \mathbf{L}_{\delta_i}(e^{j\omega}) \,, \tag{5.36}$$

with $\mathbf{L}_{\gamma_i}(e^{j\omega})$ and $\mathbf{L}_{\delta_i}(e^{j\omega})$ defined as

$$\begin{aligned} \mathbf{L}_{\gamma_i}(e^{j\omega}) &= \frac{\partial}{\partial \hat{g}_i} \mathbf{L}(e^{j\omega}; \boldsymbol{\theta}) \\ \mathbf{L}_{\delta_i}(e^{j\omega}) &= \frac{\partial}{\partial \hat{d}_i} \mathbf{L}(e^{j\omega}; \boldsymbol{\theta}) \end{aligned} \tag{5.37}$$

for $1 \leq i \leq M-1$. We find

$$\begin{aligned} \mathbf{L}_{\gamma_i}(e^{j\omega}) &= -\begin{bmatrix} 1 & 0 & \ldots & 0 \end{bmatrix} \mathbf{M}^{\text{inv}}(e^{j\omega}; \boldsymbol{d}) \\ &\quad \times \begin{bmatrix} 0 & \cdots & 0 & \cdots & 0 \\ 0 & \cdots & 0 & \cdots & 0 \\ \vdots & \ddots & \vdots & \ddots & \vdots \\ 0 & \cdots & 1/g_i & \cdots & 0 \\ \vdots & \ddots & \vdots & \ddots & \vdots \\ 0 & \cdots & 0 & \cdots & 0 \end{bmatrix} \mathbf{M}(e^{j\omega}; \boldsymbol{d}) \,, \end{aligned} \tag{5.38}$$

($1/g_i$ at the $(i+1, i+1)$ element)

and

$$\mathbf{L}_{\delta_i}(e^{j\omega}) = \begin{bmatrix} 1 & 0 & \dots & 0 \end{bmatrix} \mathbf{M}^{\text{inv}}(e^{j\omega}; \boldsymbol{d}) \times \left(j\omega L \begin{bmatrix} 0 & \cdots & 0 & \cdots & 0 \\ 0 & \cdots & 0 & \cdots & 0 \\ \vdots & \ddots & \vdots & \ddots & \vdots \\ 0 & \cdots & 1 & \cdots & 0 \\ \vdots & \ddots & \vdots & \ddots & \vdots \\ 0 & \cdots & 0 & \cdots & 0 \end{bmatrix} \mathbf{M}(e^{j\omega}; \boldsymbol{d}) - \frac{\partial}{\partial d_i} \mathbf{M}(e^{j\omega}; \boldsymbol{d}) \right) . \quad (5.39)$$

($(i+1, i+1)$ element)

In the last expression

$$\frac{\partial}{\partial d_i} \mathbf{M}(e^{j\omega}; \boldsymbol{d}) = \frac{1}{2L} \begin{bmatrix} \mathbf{Z}(e^{j\omega}; d_i) & \mathbf{Z}^*(e^{-j\omega}; d_i) \end{bmatrix} , \quad (5.40)$$

where $\mathbf{Z}(e^{j\omega}; d_i)$ is of size $M \times L$, and all its rows are zero except the $(i+1)$-th row which is given by

$$\Big[T_0(e^{j\omega}) G_i(e^{j\omega}; d_i), \dots, T_k(e^{j\omega}) f_{i,k}(e^{j\omega}; d_i) G_i(e^{j(\omega - \frac{2\pi}{L}k)}; d_i), \dots, T_{L-1}(e^{j\omega}) f_{i,L-1}(e^{j\omega}; d_i) G_i(e^{j(\omega - \frac{2\pi}{L}(L-1))}; d_i) \Big] . \quad (5.41)$$

Here,

$$T_k(e^{j\omega}) = \frac{\partial}{\partial d_i} \ln\big(f_{i,k}(e^{j\omega}; d_i) G_i(e^{j(\omega - \frac{2\pi}{L}k)}; d_i) \big)$$

for $0 \le k \le L-1$. Evaluating this expression, we obtain

$$T_k(e^{j\omega}) = \begin{cases} -j2\pi(\ell - k + L) & -\pi \le \omega < -\pi + \frac{2\pi}{L}k + \frac{\omega_b}{L} \\ -j2\pi(\ell - k) & -\pi + \frac{2\pi}{L}k + \frac{\omega_b}{L} \le \omega < \pi \end{cases} \quad (5.42)$$

for $\omega_b > 0$ and

$$T_k(e^{j\omega}) = \begin{cases} -j2\pi(\ell - k) & -\pi \le \omega < \pi + \frac{2\pi}{L}k + \frac{\omega_b}{L} \\ -j2\pi(\ell - k - L) & \pi + \frac{2\pi}{L}k + \frac{\omega_b}{L} \le \omega < \pi \end{cases} \tag{5.43}$$

for $\omega_b < 0$.

Using the approximation (5.36) and observing that the bandpass filter $H_{\mathrm{BP}}(e^{j\omega})$ has been selected such that

$$H_{\mathrm{BP}}(e^{j\omega})C(e^{j(\omega - \frac{\omega_b}{L})}) = 0\,, \tag{5.44}$$

the DTFT of error signal $e^{[L]}(n;\hat{\boldsymbol{\theta}})$ can be expressed as

$$\begin{aligned} E(e^{j\omega};\hat{\boldsymbol{\theta}}) &= H_{\mathrm{BP}}(e^{j\omega})R(e^{j\omega};\hat{\boldsymbol{\theta}}) \\ &\approx \sum_{i=1}^{M-1} H_{\mathrm{BP}}(e^{j\omega})\big(\epsilon_i \mathbf{L}_{\gamma_i}(e^{j\omega}) + \eta_i \mathbf{L}_{\delta_i}(e^{j\omega})\big) \cdot \begin{bmatrix} \mathbf{C}(e^{j\omega}) \\ \mathbf{C}^*(e^{-j\omega}) \end{bmatrix} \\ &= \sum_{i=1}^{M-1}\sum_{k=1}^{L-1}\big(\epsilon_i N_{\gamma_{i,k}}(e^{j\omega}) + \eta_i N_{\delta_{i,k}}(e^{j\omega})\big)C(e^{j(\omega - \frac{\omega_b}{L} - \frac{2\pi}{L}k)}) \\ &\qquad + \\ &\quad \sum_{i=1}^{M-1}\sum_{k=0}^{L-1}\big(\epsilon_i \hat{N}_{\gamma_{i,k}}(e^{j\omega}) + \eta_i \hat{N}_{\delta_{i,k}}(e^{j\omega})\big)C^*(e^{-j(\omega + \frac{\omega_b}{L} + \frac{2\pi}{L}k)})\,, \end{aligned} \tag{5.45}$$

with

$$N_{\gamma_{i,k}}(e^{j\omega}) = H_{\mathrm{BP}}(e^{j\omega})\mathbf{L}_{\gamma_i}(e^{j\omega}) \underbrace{\begin{bmatrix} 0 \\ \vdots \\ 1 \leftarrow (k+1)\text{ row} \\ \vdots \\ 0 \\ \mathbf{0}_{L\times 1} \end{bmatrix}}_{2L\times 1} = -H_{\mathrm{BP}}(e^{j\omega}) \begin{bmatrix} 1 & 0 & \dots & 0 \end{bmatrix} \mathbf{M}^{\mathrm{inv}}(e^{j\omega};\boldsymbol{d})$$

$$\times \quad \begin{bmatrix} 0 \\ \vdots \\ \frac{1}{2Lg_i} f_{i,k}(e^{j\omega}; d_i) G_i(e^{j(\omega - \frac{2\pi}{L}k)}; d_i) \leftarrow (i+1)\text{ row} \\ \vdots \\ 0 \end{bmatrix}$$

$$= \quad -\frac{1}{2Lg_i} H_{\mathrm{BP}}(e^{j\omega}) \Phi_i(e^{j\omega}; \boldsymbol{d}) f_{i,k}(e^{j\omega}; d_i) G_i(e^{j(\omega - \frac{2\pi}{L}k)}; d_i) \tag{5.46}$$

where the last equality makes use of definition (3.48). Similar calculations lead to

$$\hat{N}_{\gamma_{i,k}}(e^{j\omega}) \quad = \quad H_{\mathrm{BP}}(e^{j\omega}) \mathbf{L}_{\gamma_i}(e^{j\omega}) \underbrace{\begin{bmatrix} \mathbf{0}_{L\times 1} \\ 0 \\ \vdots \\ 1 \leftarrow (L+k+1)\text{ row} \\ \vdots \\ 0 \end{bmatrix}}_{2L \times 1}$$

$$= \quad -\frac{1}{2Lg_i} H_{\mathrm{BP}}(e^{j\omega}) \Phi_i(e^{j\omega}; \boldsymbol{d}) f^*_{i,k}(e^{-j\omega}; d_i) G^*_i(e^{-j(\omega + \frac{2\pi}{L}k)}; d_i) \ , \tag{5.47}$$

$$N_{\delta_{i,k}}(e^{j\omega}) \quad = \quad H_{\mathrm{BP}}(e^{j\omega}) \mathbf{L}_{\delta_i}(e^{j\omega}) \underbrace{\begin{bmatrix} 0 \\ \vdots \\ 1 \leftarrow (k+1)\text{ row} \\ \vdots \\ 0 \\ \mathbf{0}_{L\times 1} \end{bmatrix}}_{2L \times 1}$$

$$= \quad \frac{j\omega L - T_k(e^{j\omega})}{2L} H_{\mathrm{BP}}(e^{j\omega}) \Phi_i(e^{j\omega}; \boldsymbol{d}) f_{i,k}(e^{j\omega}; d_i) G_i(e^{j(\omega - \frac{2\pi}{L}k)}; d_i) \ , \tag{5.48}$$

and

$$\hat{N}_{\delta_{i,k}}(e^{j\omega}) = H_{\mathrm{BP}}(e^{j\omega})\mathbf{L}_{\delta_i}(e^{j\omega}) \underbrace{\begin{bmatrix} \mathbf{0}_{L\times 1} \\ 0 \\ \vdots \\ 1 \longleftarrow (L+k+1)\text{ row} \\ \vdots \\ 0 \end{bmatrix}}_{2L\times 1}$$

$$= \frac{j\omega L - T_k^*(e^{-j\omega})}{2L} H_{\mathrm{BP}}(e^{j\omega})\Phi_i(e^{j\omega};\boldsymbol{d}) f_{i,k}^*(e^{-j\omega};d_i) G_i^*(e^{-j(\omega+\frac{2\pi}{L}k)};d_i). \quad (5.49)$$

The approximation (5.45) can be alternatively expressed as

$$E(e^{j\omega};\hat{\boldsymbol{\theta}}) \approx \sum_{k=1}^{L-1} A_k(e^{j\omega}) C(e^{j(\omega-\frac{\omega_b}{L}-\frac{2\pi}{L}k)}) + \sum_{k=0}^{L-1} \hat{A}_k(e^{j\omega}) C^*(e^{-j(\omega+\frac{\omega_b}{L}+\frac{2\pi}{L}k)}) \,, \quad (5.50)$$

where

$$\begin{aligned} A_k(e^{j\omega}) &= \sum_{i=1}^{M-1} \epsilon_i N_{\gamma_{i,k}}(e^{j\omega}) + \eta_i N_{\delta_{i,k}}(e^{j\omega}) \\ \hat{A}_k(e^{j\omega}) &= \sum_{i=1}^{M-1} \epsilon_i \hat{N}_{\gamma_{i,k}}(e^{j\omega}) + \eta_i \hat{N}_{\delta_{i,k}}(e^{j\omega}) \end{aligned} \quad (5.51)$$

which indicates that error signal $E(e^{j\omega};\hat{\boldsymbol{\theta}})$ consists of frequency translated variants of the complex envelope of the kind

$$\begin{aligned} q_k^{[L]}(n) = c^{[L]}(n) e^{j(\frac{\omega_b}{L}+\frac{2\pi}{L}k)n} &\overset{\mathcal{FT}}{\longleftrightarrow} Q_k(e^{j\omega}) = C(e^{j(\omega-\frac{\omega_b}{L}-\frac{2\pi}{L}k)}) \\ \hat{q}_k^{[L]}(n) = (c^{[L]}(n))^* e^{-j(\frac{\omega_b}{L}+\frac{2\pi}{L}k)n} &\overset{\mathcal{FT}}{\longleftrightarrow} \hat{Q}_k(e^{j\omega}) = C^*(e^{-j(\omega+\frac{\omega_b}{L}+\frac{2\pi}{L}k)}). \end{aligned} \quad (5.52)$$

In time domain the error signal has the representation

$$e^{[L]}(n;\hat{\boldsymbol{\theta}}) \approx \sum_{k=1}^{L-1} a_k(n) * q_k^{[L]}(n) + \sum_{k=0}^{L-1} \hat{a}_k(n) * \hat{q}_k^{[L]}(n) \,, \quad (5.53)$$

where $a_k(n)$ and $\hat{a}_k(n)$ are the impulse responses of LTI filters $A_k(e^{j\omega})$ and $\hat{A}_k(e^{j\omega})$, respectively.

To evaluate the power of $e^{[L]}(n;\hat{\boldsymbol{\theta}})$, we assume that the complex envelope process $c^{[L]}(n)$ is zero-mean WSS, i.e., that the complex autocorrelation function

$$R_c(m) = E[c^{[L]}(n+m)(c^{[L]}(n))^*] \tag{5.54}$$

depends on m only. The power spectral density (PSD) of $c^{[L]}(n)$ is then defined as the DTFT of $R_c(m)$,

$$S_c(e^{j\omega}) = \sum_{m\in\mathbb{Z}} R_c(m)e^{-j\omega m} \, . \tag{5.55}$$

It is 2π-periodic, non-negative, and real (since $R_c(m) = R_c^*(-m)$) but not necessarily even. Equation (5.53) indicates that to derive the expression for the autocorrelation and PSD of $e^{[L]}(n;\hat{\boldsymbol{\theta}})$, we must first analyze the individual and joint second-order statistics of signals $q_k^{[L]}(n)$ and $\hat{q}_k^{[L]}(n)$. To do so, we start with the observation that the sampled complex envelope possesses the circularity property

$$E[c^{[L]}(n+m)c^{[L]}(n)] = 0 \tag{5.56}$$

which is a consequence of the fact that if $x_c(t)$ is a zero-mean real WSS bandpass process, its complex envelope $c_c(t)$ is zero-mean, circular and WSS, so that the sampled envelope $c^{[L]}(n) = c_c(nT_s'/L)$ has the same properties [119]. The circularity property can also be obtained from Rice's representation for bandpass WSS random signals [120, Sec 8.7]. From this property of $c^{[L]}(n)$ we deduce that for arbitrary integers k and l, $q_k^{[L]}(n)$ and $\hat{q}_l^{[L]}(n)$ are uncorrelated since

$$\begin{aligned} E[q_k^{[L]}(n+m)(\hat{q}_l^{[L]}(n))^*] &= E[c^{[L]}(n+m)c^{[L]}(n)] \\ &\quad \times e^{j(\frac{\omega_b}{L}+\frac{2\pi}{L}k)(n+m)} e^{j(\frac{\omega_b}{L}+\frac{2\pi}{L}l)n} \end{aligned}$$

$$= \quad 0 \tag{5.57}$$

The cross-correlation of $q_k^{[L]}(n)$ and $q_l^{[L]}(n)$ is given by

$$\begin{aligned} R_{q_k q_l}(m,n) &= E[q_k^{[L]}(n+m)(q_l^{[L]}(n))^*] \\ &= E[c^{[L]}(n+m)(c^{[L]}(n))^*]e^{j(\frac{\omega_b}{L}+\frac{2\pi}{L}k)m}e^{j\frac{2\pi}{L}(k-l)n} \\ &= R_c(m)e^{j(\frac{\omega_b}{L}+\frac{2\pi}{L}k)m}e^{j\frac{2\pi}{L}(k-l)n} \\ &= R_c(m)e^{j(\frac{\omega_b}{L}+\frac{2\pi}{L}k)m}e^{j2\pi\alpha n} \end{aligned} \tag{5.58}$$

so for $k = l$ it is WSS, but for $k \neq l$ it is *cyclostationary* [121, Chap. 12] with cycle frequency $\alpha = \frac{k-l}{L}$. Specifically, when viewed as a function of n, $R_{q_k q_l}(m,n)$ is periodic with period L, i.e., $R_{q_k q_l}(m, n+aL) = R_{q_k q_l}(m,n)$ for $a \in \mathbb{Z}$, and thus admits a Discrete Fourier Series (DFS) expansion of the form

$$R_{q_k q_l}(m,n) = \sum_{\alpha} R^{\alpha}_{q_k q_l}(m)e^{j2\pi\alpha n} \tag{5.59}$$

with DFS coefficient

$$R^{\alpha}_{q_k q_l}(m) = \frac{1}{L}\sum_{n=0}^{L-1} R_{q_k q_l}(m,n)e^{-j2\pi\alpha n} \ . \tag{5.60}$$

Comparing the last expression in (5.58) with the DFS (5.59), it is obvious that the expansion includes only a single term at cycle frequency $\alpha = \frac{k-l}{L}$ with the cyclic cross-correlation at cycle frequency α (coefficient) specified by

$$R^{\alpha}_{q_k q_l}(m) = R_c(m)e^{j(\frac{\omega_b}{L}+\frac{2\pi}{L}k)m} \ . \tag{5.61}$$

The cross-cyclic spectrum of $q_k^{[L]}(n)$ and $q_l^{[L]}(n)$ is given by the Fourier transform of $R^{\alpha}_{q_k q_l}(m)$,

$$S^{\alpha}_{q_k q_l}(e^{j\omega}) = S_c(e^{j(\omega-\frac{\omega_b}{L}-\frac{2\pi}{L}k)}) \ , \tag{5.62}$$

where $S_c(e^{j\omega})$ was defined in (5.55). Similarly, the cross-correlation of $\hat{q}_k^{[L]}(n)$ and $\hat{q}_l^{[L]}(n)$ is given by

$$\begin{aligned} R_{\hat{q}_k\hat{q}_l}(m,n) &= E[\hat{q}_k^{[L]}(n+m)(\hat{q}_l^{[L]}(n))^*] \\ &= E[(c^{[L]}(n+m))^* c^{[L]}(n)]e^{-j(\frac{\omega_b}{L}+\frac{2\pi}{L}k)m}e^{-j\frac{2\pi}{L}(k-l)n} \\ &= R_c^*(m)e^{-j(\frac{\omega_b}{L}+\frac{2\pi}{L}k)m}e^{-j\frac{2\pi}{L}(k-l)n} \\ &= R_c^*(m)e^{-j(\frac{\omega_b}{L}+\frac{2\pi}{L}k)m}e^{j2\pi\hat{\alpha}n} \\ &= (R_{q_kq_l}(m,n))^* \ . \end{aligned} \tag{5.63}$$

For $k=l$ it is WSS and for $k\neq l$ it is cyclostationary with cycle frequency $\hat{\alpha}=-\frac{k-l}{L}=-\alpha$. The cyclic cross-correlation at cycle frequency $\hat{\alpha}$ is given by

$$\begin{aligned} R_{\hat{q}_k\hat{q}_l}^{\hat{\alpha}}(m) &= R_c^*(m)e^{-j(\frac{\omega_b}{L}+\frac{2\pi}{L}k)m} \\ &= R_c(-m)e^{-j(\frac{\omega_b}{L}+\frac{2\pi}{L}k)m} \\ &= \frac{1}{L}\sum_{n=0}^{L-1} R_{\hat{q}_k\hat{q}_l}(m,n)e^{-j2\pi\hat{\alpha}n} \ , \end{aligned} \tag{5.64}$$

and the corresponding cross-cyclic spectrum is

$$S_{\hat{q}_k\hat{q}_l}^{\hat{\alpha}}(e^{j\omega}) = S_c(e^{-j(\omega+\frac{\omega_b}{L}+\frac{2\pi}{L}k)}) \ . \tag{5.65}$$

It then follows from (5.53) that $e^{[L]}(n;\hat{\boldsymbol{\theta}})$ is cyclostationary and for $\alpha=\frac{p}{L}$ its cyclic autocorrelation at cycle frequency α is given by

$$\begin{aligned} R_e^{\alpha}(m;\hat{\boldsymbol{\theta}}) \approx & \sum_{k-l=p} a_k(m) * R_{q_kq_l}^{\alpha}(m) * a_l^*(-m) \\ & + \\ & \sum_{k-l=-p} \hat{a}_k(m) * R_{\hat{q}_k\hat{q}_l}^{\hat{\alpha}}(m) * \hat{a}_l^*(-m) \end{aligned} \tag{5.66}$$

and cyclic spectrum

$$S_e^{\alpha}(e^{j\omega};\hat{\boldsymbol{\theta}}) \approx \sum_{k-l=p} A_k(e^{j\omega})A_l^*(e^{j\omega})S_{q_kq_l}^{\alpha}(e^{j\omega}) + \sum_{k-l=-p} \hat{A}_k(e^{j\omega})\hat{A}_l^*(e^{j\omega})S_{\hat{q}_k\hat{q}_l}^{\hat{\alpha}}(e^{j\omega}) \; . \tag{5.67}$$

The error autocorrelation function that is periodic with L

$$R_e(n,m;\hat{\boldsymbol{\theta}}) = E[e^{[L]}(n+m;\hat{\boldsymbol{\theta}})(e^{[L]}(n;\hat{\boldsymbol{\theta}}))^*] = R_e(n+L,m;\hat{\boldsymbol{\theta}}) \tag{5.68}$$

has the DFS expansion

$$R_e(n,m;\hat{\boldsymbol{\theta}}) = \sum_{\alpha} R_e^{\alpha}(m;\hat{\boldsymbol{\theta}})e^{j2\pi\alpha n} \tag{5.69}$$

with $\alpha = \frac{p}{L}$ and

$$R_e^{\alpha}(m;\hat{\boldsymbol{\theta}}) = \frac{1}{L}\sum_{n=0}^{L-1} R_e(n,m;\hat{\boldsymbol{\theta}})e^{-j2\pi\alpha n} \; . \tag{5.70}$$

Evaluating (5.70) for $\alpha = 0$ and $m = 0$, we obtain

$$\begin{aligned} R_e^0(0;\hat{\boldsymbol{\theta}}) &= \frac{1}{L}\sum_{n=0}^{L-1} R_e(n,0;\hat{\boldsymbol{\theta}}) \\ &= \frac{1}{L}\sum_{n=0}^{L-1} E[|e^{[L]}(n;\hat{\boldsymbol{\theta}})|^2] \\ &= E\left[\frac{1}{L}\sum_{n=0}^{L-1} |e^{[L]}(n;\hat{\boldsymbol{\theta}})|^2\right] , \end{aligned} \tag{5.71}$$

where the second equality follows from (5.68). Now, assuming the error process $e^{[L]}(n;\hat{\boldsymbol{\theta}})$ is cycloergodic, by SLLN we have

$$R_e^0(0;\hat{\boldsymbol{\theta}}) = \lim_{N\to\infty} \frac{1}{LN}\sum_{n=0}^{LN-1} |e^{[L]}(n;\hat{\boldsymbol{\theta}})|^2 \approx \frac{1}{T}\sum_{n=0}^{T-1} |e^{[L]}(n;\hat{\boldsymbol{\theta}})|^2 \tag{5.72}$$

for a large T such that $LN \leq T < L(N+1)$. From (5.72) we conclude $R_e^0(0;\hat{\boldsymbol{\theta}})$ is the average power of the error process $e^{[L]}(n;\hat{\boldsymbol{\theta}})$ which we denote as P_e. Equation (5.71) indicates that the computation of P_e requires the second order statistics of $e^{[L]}(n;\hat{\boldsymbol{\theta}})$ at L consecutive time instants. We can equivalently write

$$P_e = E\left[\frac{1}{L}\sum_{k=0}^{L-1}|e^{[L]}(n+k;\hat{\boldsymbol{\theta}})|^2\right], \tag{5.73}$$

and the objective function $J(\hat{\boldsymbol{\theta}})$ then is

$$J(\hat{\boldsymbol{\theta}}) = \frac{1}{2}P_e = \frac{1}{2}E\left[\frac{1}{L}\sum_{k=0}^{L-1}|e^{[L]}(n+k;\hat{\boldsymbol{\theta}})|^2\right] \tag{5.74}$$

instead of (5.23), however the proposed SGD iteration (5.26) can still be used to minimize $J(\hat{\boldsymbol{\theta}})$ as justified in Section 5.3. The average power can also be expressed in frequency domain via the Fourier transform relationship

$$P_e = R_e^0(0;\hat{\boldsymbol{\theta}}) = \frac{1}{2\pi}\int_{-\pi}^{\pi} S_e^0(e^{j\omega};\hat{\boldsymbol{\theta}})d\omega\ . \tag{5.75}$$

We compute this integral to show that

$$J(\hat{\boldsymbol{\theta}}) = \frac{1}{4\pi}\int_{-\pi}^{\pi} S_e^0(e^{j\omega};\hat{\boldsymbol{\theta}})d\omega \tag{5.76}$$

admits a quadratic approximation. Using (5.67), the integrand is given by

$$\begin{aligned} S_e^0(e^{j\omega};\hat{\boldsymbol{\theta}}) \;\approx\; & \sum_{k=1}^{L-1}|A_k(e^{j\omega})|^2 S_c(e^{j(\omega-\frac{\omega_b}{L}-\frac{2\pi}{L}k)}) \\ & + \\ & \sum_{k=0}^{L-1}|\hat{A}_k(e^{j\omega})|^2 S_c(e^{-j(\omega+\frac{\omega_b}{L}+\frac{2\pi}{L}k)}) \end{aligned} \tag{5.77}$$

which requires the evaluation of $|A_k(e^{j\omega})|^2$ and $|\hat{A}_k(e^{j\omega})|^2$.

$$
\begin{aligned}
|A_k(e^{j\omega})|^2 &= A_k(e^{j\omega})A_k^*(e^{j\omega}) \\
&= \Big(\sum_{i=1}^{M-1} \epsilon_i N_{\gamma_{i,k}}(e^{j\omega}) + \eta_i N_{\delta_{i,k}}(e^{j\omega}) \Big) \times \Big(\sum_{l=1}^{M-1} \epsilon_l N^*_{\gamma_{l,k}}(e^{j\omega}) + \eta_l N^*_{\delta_{l,k}}(e^{j\omega}) \Big) \\
&= \frac{|H_{\mathrm{BP}}(e^{j\omega})|^2}{4L^2} \Big\{ \sum_{i=1}^{M-1} \big[\frac{\epsilon_i^2}{g_i^2} + \eta_i^2 |j\omega L - T_k(e^{j\omega})|^2 \big] |\Phi_i(e^{j\omega}; \boldsymbol{d})|^2 + \sum_{\substack{i,l=1 \\ i \neq l}}^{M-1} \big[\frac{\epsilon_i \epsilon_l}{g_i g_l} \\
&+ \eta_i \eta_l |j\omega L - T_k(e^{j\omega})|^2 + \frac{\epsilon_i \eta_l}{g_i} (T_k(e^{j\omega}) - j\omega L)^* + \frac{\eta_i \epsilon_l}{g_l} (T_k(e^{j\omega}) - j\omega L) \big] B^k_{i,l}(e^{j\omega}) \Big\} \quad (5.78)
\end{aligned}
$$

with

$$
\begin{aligned}
B^k_{i,l}(e^{j\omega}) &= \Phi_i(e^{j\omega}; \boldsymbol{d}) \Phi_l^*(e^{j\omega}; \boldsymbol{d}) f_{i,k}(e^{j\omega}; d_i) f^*_{l,k}(e^{j\omega}; d_l) \\
&\quad \times G_i(e^{j(\omega - \frac{2\pi}{L}k)}; d_i) G_l^*(e^{j(\omega - \frac{2\pi}{L}k)}; d_l) \, . \quad (5.79)
\end{aligned}
$$

Similarly,

$$
\begin{aligned}
|\hat{A}_k(e^{j\omega})|^2 &= \hat{A}_k(e^{j\omega}) \hat{A}_k^*(e^{j\omega}) \\
&= \Big(\sum_{i=1}^{M-1} \epsilon_i \hat{N}_{\gamma_{i,k}}(e^{j\omega}) + \eta_i \hat{N}_{\delta_{i,k}}(e^{j\omega}) \Big) \times \Big(\sum_{l=1}^{M-1} \epsilon_l \hat{N}^*_{\gamma_{l,k}}(e^{j\omega}) + \eta_l \hat{N}^*_{\delta_{l,k}}(e^{j\omega}) \Big) \\
&= \frac{|H_{\mathrm{BP}}(e^{j\omega})|^2}{4L^2} \Big\{ \sum_{i=1}^{M-1} \big[\frac{\epsilon_i^2}{g_i^2} + \eta_i^2 |j\omega L - T_k^*(e^{-j\omega})|^2 \big] |\Phi_i(e^{j\omega}; \boldsymbol{d})|^2 + \sum_{\substack{i,l=1 \\ i \neq l}}^{M-1} \big[\frac{\epsilon_i \epsilon_l}{g_i g_l} \\
&+ \eta_i \eta_l |j\omega L - T_k^*(e^{-j\omega})|^2 + \frac{\epsilon_i \eta_l}{g_i} (T_k^*(e^{-j\omega}) - j\omega L)^* + \frac{\eta_i \epsilon_l}{g_l} (T_k^*(e^{-j\omega}) - j\omega L) \big] \hat{B}^k_{i,l}(e^{j\omega}) \Big\}
\end{aligned} \quad (5.80)
$$

with

$$
\begin{aligned}
\hat{B}^k_{i,l}(e^{j\omega}) &= \Phi_i(e^{j\omega}; \boldsymbol{d}) \Phi_l^*(e^{j\omega}; \boldsymbol{d}) f^*_{i,k}(e^{-j\omega}; d_i) f_{l,k}(e^{-j\omega}; d_l) \\
&\quad \times G_i^*(e^{-j(\omega + \frac{2\pi}{L}k)}; d_i) G_l(e^{-j(\omega + \frac{2\pi}{L}k)}; d_l) \, . \quad (5.81)
\end{aligned}
$$

From (5.79) and (5.81), we observe the following quick facts for $i \neq l$,

$$B_{i,l}^k(e^{j\omega}) = \left(B_{l,i}^k(e^{j\omega})\right)^*$$
$$\hat{B}_{i,l}^k(e^{j\omega}) = \left(\hat{B}_{l,i}^k(e^{j\omega})\right)^* .$$

In these expressions "k" is a superscript and not power. With some computation we can then evaluate (5.76) to obtain

$$\begin{aligned} J(\hat{\boldsymbol{\theta}}) \;\approx\; & \sum_{k=1}^{L-1}\left\{ \sum_{i=1}^{M-1} \epsilon_i^2 J_{\gamma_i}^k + \eta_i^2 J_{\delta_i}^k + \sum_{\substack{i,l=1 \\ i\neq l}}^{M-1} \epsilon_i\epsilon_l J_{\gamma_{i,l}}^k + \eta_i\eta_l J_{\delta_{i,l}}^k + \epsilon_i\eta_l J_{\gamma_i\delta_l}^k + \eta_i\epsilon_l J_{\delta_i\gamma_l}^k \right\} \\ & + \\ & \sum_{k=0}^{L-1}\left\{ \sum_{i=1}^{M-1} \epsilon_i^2 \hat{J}_{\gamma_i}^k + \eta_i^2 \hat{J}_{\delta_i}^k + \sum_{\substack{i,l=1 \\ i\neq l}}^{M-1} \epsilon_i\epsilon_l \hat{J}_{\gamma_{i,l}}^k + \eta_i\eta_l \hat{J}_{\delta_{i,l}}^k + \epsilon_i\eta_l \hat{J}_{\gamma_i\delta_l}^k + \eta_i\epsilon_l \hat{J}_{\delta_i\gamma_l}^k \right\}, \end{aligned} \tag{5.82}$$

where again "k" is a superscript, and if $I_m = I \mod (2\pi)$ is defined so that I_m is a subset of $[-\pi, \pi]$, then

$$\begin{aligned} J_{\gamma_i}^k &= \frac{1}{16\pi L^2 g_i^2} \int_{I_m} |\Phi_i(e^{j\omega}; \boldsymbol{d})|^2 S_c(e^{j(\omega - \frac{\omega_b}{L} - \frac{2\pi}{L}k)}) d\omega \\ J_{\delta_i}^k &= \frac{1}{16\pi L^2} \int_{I_m} |j\omega L - T_k(e^{j\omega})|^2 |\Phi_i(e^{j\omega}; \boldsymbol{d})|^2 S_c(e^{j(\omega - \frac{\omega_b}{L} - \frac{2\pi}{L}k)}) d\omega \\ J_{\gamma_{i,l}}^k &= \frac{1}{16\pi L^2 g_i g_l} \int_{I_m} B_{i,l}^k(e^{j\omega}) S_c(e^{j(\omega - \frac{\omega_b}{L} - \frac{2\pi}{L}k)}) d\omega \\ J_{\delta_{i,l}}^k &= \frac{1}{16\pi L^2} \int_{I_m} |j\omega L - T_k(e^{j\omega})|^2 B_{i,l}^k(e^{j\omega}) S_c(e^{j(\omega - \frac{\omega_b}{L} - \frac{2\pi}{L}k)}) d\omega \\ J_{\gamma_i\delta_l}^k &= \frac{1}{16\pi L^2 g_i} \int_{I_m} (T_k(e^{j\omega}) - j\omega L)^* B_{i,l}^k(e^{j\omega}) S_c(e^{j(\omega - \frac{\omega_b}{L} - \frac{2\pi}{L}k)}) d\omega \\ J_{\delta_i\gamma_l}^k &= \frac{1}{16\pi L^2 g_l} \int_{I_m} (T_k(e^{j\omega}) - j\omega L) B_{i,l}^k(e^{j\omega}) S_c(e^{j(\omega - \frac{\omega_b}{L} - \frac{2\pi}{L}k)}) d\omega \; . \end{aligned} \tag{5.83}$$

Since the filter $\Phi_i(e^{j\omega}; \boldsymbol{d})$ for $1 \leq i \leq M-1$ is nonzero, we have $J_{\gamma_i}^k > 0$ and $J_{\delta_i}^k > 0$ as long as the signal $q_k^{[L]}(n)$ has some power in band I_m. The quantities in (5.83) have the following

symmetry relations

$$J^k_{\gamma_{i,l}} = (J^k_{\gamma_{l,i}})^*, \quad J^k_{\delta_{i,l}} = (J^k_{\delta_{l,i}})^*, \quad J^k_{\gamma_i\delta_l} = (J^k_{\delta_l\gamma_i})^* \, .$$

Similarly,

$$\begin{aligned}
\hat{J}^k_{\gamma_i} &= \frac{1}{16\pi L^2 g_i^2} \int_{I_m} |\Phi_i(e^{j\omega}; \boldsymbol{d})|^2 S_c(e^{-j(\omega+\frac{\omega_b}{L}+\frac{2\pi}{L}k)}) d\omega \\
\hat{J}^k_{\delta_i} &= \frac{1}{16\pi L^2} \int_{I_m} |j\omega L - T_k^*(e^{-j\omega})|^2 |\Phi_i(e^{j\omega}; \boldsymbol{d})|^2 S_c(e^{-j(\omega+\frac{\omega_b}{L}+\frac{2\pi}{L}k)}) d\omega \\
\hat{J}^k_{\gamma_{i,l}} &= \frac{1}{16\pi L^2 g_i g_l} \int_{I_m} \hat{B}^k_{i,l}(e^{j\omega}) S_c(e^{-j(\omega+\frac{\omega_b}{L}+\frac{2\pi}{L}k)}) d\omega \\
\hat{J}^k_{\delta_{i,l}} &= \frac{1}{16\pi L^2} \int_{I_m} |j\omega L - T_k^*(e^{-j\omega})|^2 \hat{B}^k_{i,l}(e^{j\omega}) S_c(e^{-j(\omega+\frac{\omega_b}{L}+\frac{2\pi}{L}k)}) d\omega \\
\hat{J}^k_{\gamma_i\delta_l} &= \frac{1}{16\pi L^2 g_i} \int_{I_m} (T_k^*(e^{-j\omega}) - j\omega L)^* \hat{B}^k_{i,l}(e^{j\omega}) S_c(e^{-j(\omega+\frac{\omega_b}{L}+\frac{2\pi}{L}k)}) d\omega \\
\hat{J}^k_{\delta_i\gamma_l} &= \frac{1}{16\pi L^2 g_l} \int_{I_m} (T_k^*(e^{-j\omega}) - j\omega L) \hat{B}^k_{i,l}(e^{j\omega}) S_c(e^{-j(\omega+\frac{\omega_b}{L}+\frac{2\pi}{L}k)}) d\omega
\end{aligned} \tag{5.84}$$

with symmetry relations

$$\hat{J}^k_{\gamma_{i,l}} = (\hat{J}^k_{\gamma_{l,i}})^*, \quad \hat{J}^k_{\delta_{i,l}} = (\hat{J}^k_{\delta_{l,i}})^*, \quad \hat{J}^k_{\gamma_i\delta_l} = (\hat{J}^k_{\delta_l\gamma_i})^* \, ,$$

and $\hat{J}^k_{\gamma_i} > 0$, $\hat{J}^k_{\delta_i} > 0$ if the signal $\hat{q}^{[L]}_k(n)$ has some power in band I_m.

Recalling the definition of the $2(M-1)$ column vector $\boldsymbol{h}$ from (5.35), we can write $J(\hat{\boldsymbol{\theta}})$ in (5.82) in compact matrix form as

$$\begin{aligned}
J(\hat{\boldsymbol{\theta}}) &\approx (\hat{\boldsymbol{\theta}} - \boldsymbol{\theta})^T \Big[\sum_{k=1}^{L-1} \mathbf{J}^k + \sum_{k=0}^{L-1} \hat{\mathbf{J}}^k \Big] (\hat{\boldsymbol{\theta}} - \boldsymbol{\theta}) \\
&= \boldsymbol{h}^T \Big[\sum_{k=1}^{L-1} \mathbf{J}^k + \sum_{k=0}^{L-1} \hat{\mathbf{J}}^k \Big] \boldsymbol{h} \, ,
\end{aligned} \tag{5.85}$$

where $\mathbf{J}^k$ and $\hat{\mathbf{J}}^k$ are matrices of size $2(M-1) \times 2(M-1)$ and can be expressed in block

form as

$$\mathbf{J}^k = \left[\begin{array}{c|c} \mathbf{J}^k_{11} & \mathbf{J}^k_{12} \\ \hline \mathbf{J}^k_{21} & \mathbf{J}^k_{22} \end{array}\right], \quad \hat{\mathbf{J}}^k = \left[\begin{array}{c|c} \hat{\mathbf{J}}^k_{11} & \hat{\mathbf{J}}^k_{12} \\ \hline \hat{\mathbf{J}}^k_{21} & \hat{\mathbf{J}}^k_{22} \end{array}\right]. \tag{5.86}$$

The blocks are of size $(M-1)\times(M-1)$ and are given by

$$\mathbf{J}^k_{11} = \begin{bmatrix} J^k_{\gamma_1} & J^k_{\gamma_{1,2}} & \cdots & J^k_{\gamma_{1,M-1}} \\ J^k_{\gamma_{2,1}} & J^k_{\gamma_2} & \cdots & J^k_{\gamma_{2,M-1}} \\ \vdots & \vdots & \ddots & \vdots \\ J^k_{\gamma_{M-1,1}} & J^k_{\gamma_{M-1,2}} & \cdots & J^k_{\gamma_{M-1}} \end{bmatrix}, \quad \hat{\mathbf{J}}^k_{11} = \begin{bmatrix} \hat{J}^k_{\gamma_1} & \hat{J}^k_{\gamma_{1,2}} & \cdots & \hat{J}^k_{\gamma_{1,M-1}} \\ \hat{J}^k_{\gamma_{2,1}} & \hat{J}^k_{\gamma_2} & \cdots & \hat{J}^k_{\gamma_{2,M-1}} \\ \vdots & \vdots & \ddots & \vdots \\ \hat{J}^k_{\gamma_{M-1,1}} & \hat{J}^k_{\gamma_{M-1,2}} & \cdots & \hat{J}^k_{\gamma_{M-1}} \end{bmatrix}$$

$$\mathbf{J}^k_{22} = \begin{bmatrix} J^k_{\delta_1} & J^k_{\delta_{1,2}} & \cdots & J^k_{\delta_{1,M-1}} \\ J^k_{\delta_{2,1}} & J^k_{\delta_2} & \cdots & J^k_{\delta_{2,M-1}} \\ \vdots & \vdots & \ddots & \vdots \\ J^k_{\delta_{M-1,1}} & J^k_{\delta_{M-1,2}} & \cdots & J^k_{\delta_{M-1}} \end{bmatrix}, \quad \hat{\mathbf{J}}^k_{22} = \begin{bmatrix} \hat{J}^k_{\delta_1} & \hat{J}^k_{\delta_{1,2}} & \cdots & \hat{J}^k_{\delta_{1,M-1}} \\ \hat{J}^k_{\delta_{2,1}} & \hat{J}^k_{\delta_2} & \cdots & \hat{J}^k_{\delta_{2,M-1}} \\ \vdots & \vdots & \ddots & \vdots \\ \hat{J}^k_{\delta_{M-1,1}} & \hat{J}^k_{\delta_{M-1,2}} & \cdots & \hat{J}^k_{\delta_{M-1}} \end{bmatrix}$$

$$\mathbf{J}^k_{21} = \begin{bmatrix} 0 & J^k_{\delta_1\gamma_2} & \cdots & J^k_{\delta_1\gamma_{M-1}} \\ J^k_{\delta_2\gamma_1} & 0 & \cdots & J^k_{\delta_2\gamma_{M-1}} \\ \vdots & \vdots & \ddots & \vdots \\ J^k_{\delta_{M-1}\gamma_1} & J^k_{\delta_{M-1}\gamma_2} & \cdots & 0 \end{bmatrix}, \quad \hat{\mathbf{J}}^k_{21} = \begin{bmatrix} 0 & \hat{J}^k_{\delta_1\gamma_2} & \cdots & \hat{J}^k_{\delta_1\gamma_{M-1}} \\ \hat{J}^k_{\delta_2\gamma_1} & 0 & \cdots & \hat{J}^k_{\delta_2\gamma_{M-1}} \\ \vdots & \vdots & \ddots & \vdots \\ \hat{J}^k_{\delta_{M-1}\gamma_1} & \hat{J}^k_{\delta_{M-1}\gamma_2} & \cdots & 0 \end{bmatrix}$$

$$\mathbf{J}^k_{12} = \begin{bmatrix} 0 & J^k_{\gamma_1\delta_2} & \cdots & J^k_{\gamma_1\delta_{M-1}} \\ J^k_{\gamma_2\delta_1} & 0 & \cdots & J^k_{\gamma_2\delta_{M-1}} \\ \vdots & \vdots & \ddots & \vdots \\ J^k_{\gamma_{M-1}\delta_1} & J^k_{\gamma_{M-1}\delta_2} & \cdots & 0 \end{bmatrix}, \quad \hat{\mathbf{J}}^k_{12} = \begin{bmatrix} 0 & \hat{J}^k_{\gamma_1\delta_2} & \cdots & \hat{J}^k_{\gamma_1\delta_{M-1}} \\ \hat{J}^k_{\gamma_2\delta_1} & 0 & \cdots & \hat{J}^k_{\gamma_2\delta_{M-1}} \\ \vdots & \vdots & \ddots & \vdots \\ \hat{J}^k_{\gamma_{M-1}\delta_1} & \hat{J}^k_{\gamma_{M-1}\delta_2} & \cdots & 0 \end{bmatrix} \tag{5.87}$$

The zeros on the diagonal of $\mathbf{J}_{12}^k$, $\hat{\mathbf{J}}_{12}^k$, $\mathbf{J}_{21}^k$, and $\hat{\mathbf{J}}_{21}^k$ come from the fact that $J_{\gamma_i\delta_l}^k = J_{\delta_i\gamma_l}^k = 0$ for all $i = l$. From the symmetry relations, it follows that the matrices in (5.86) are Hermitian, i.e.,

$$\mathbf{J}^k = (\mathbf{J}^k)^H, \quad \hat{\mathbf{J}}^k = (\hat{\mathbf{J}}^k)^H$$

which implies that they have real eigenvalues with orthogonal eigenvectors. If we let

$$\boldsymbol{\mathcal{J}} = \sum_{k=1}^{L-1} \mathbf{J}^k + \sum_{k=0}^{L-1} \hat{\mathbf{J}}^k, \tag{5.88}$$

then the desired quadratic approximation for $J(\hat{\boldsymbol{\theta}})$ can be simply expressed as

$$J(\hat{\boldsymbol{\theta}}) \approx (\hat{\boldsymbol{\theta}} - \boldsymbol{\theta})^T \boldsymbol{\mathcal{J}} (\hat{\boldsymbol{\theta}} - \boldsymbol{\theta}) = \boldsymbol{h}^T \boldsymbol{\mathcal{J}} \boldsymbol{h} \, . \tag{5.89}$$

It is obvious that $\boldsymbol{h} = 0$ (corresponding to $\hat{\boldsymbol{\theta}} = \boldsymbol{\theta}$) is the stationary point of $J(\hat{\boldsymbol{\theta}})$ since

$$\nabla_{\hat{\boldsymbol{\theta}}} J(\hat{\boldsymbol{\theta}}) = \nabla_{\boldsymbol{h}} J(\hat{\boldsymbol{\theta}}) \approx 2\boldsymbol{\mathcal{J}} \boldsymbol{h} \, .$$

Thus, it simply remains to show that $J(\hat{\boldsymbol{\theta}})$ achieves a minimum at $\boldsymbol{h} = 0$. We can accomplish this by showing the Hessian matrix

$$\mathbf{H}(\hat{\boldsymbol{\theta}}) = \nabla_{\hat{\boldsymbol{\theta}}}^2 J(\hat{\boldsymbol{\theta}}) \approx 2\boldsymbol{\mathcal{J}} \tag{5.90}$$

is positive definite. Computing the eigenvalues of $\boldsymbol{\mathcal{J}}$ and proving they are all positive is no easy task. Fortunately, we can recall from (5.74) that $J(\hat{\boldsymbol{\theta}})$ is the scaled power of error process $e^{[L]}(n; \hat{\boldsymbol{\theta}})$ and is thus strictly positive unless the error signal is zero. If at least one of the signals $q_k^{[L]}(n)$, $1 \leq k \leq L-1$ and $\hat{q}_k^{[L]}(n)$, $0 \leq k \leq L-1$ has some power in band I_m, then $J(\hat{\boldsymbol{\theta}}) \neq 0$ according to (5.82). In this case $J(\hat{\boldsymbol{\theta}}) > 0$, $\boldsymbol{h}^T \boldsymbol{\mathcal{J}} \boldsymbol{h} > 0$ from (5.89), and the matrix $\boldsymbol{\mathcal{J}}$ is positive definite implying that $J(\hat{\boldsymbol{\theta}})$ is a strictly convex function with a with a minimum at $\boldsymbol{h} = 0$. Therefore, $J(\hat{\boldsymbol{\theta}})$ is minimized when $\epsilon_i = \eta_i = 0$, i.e., when the

estimated gain $\hat{\gamma}_i$ and timing $\hat{\delta}_i$ mismatches correspond to the true mismatch values γ_i and δ_i for $1 \leq i \leq M-1$.

The signal $q_k^{[L]}(n) = c^{[L]}(n)e^{j(\frac{\omega_b}{L}+\frac{2\pi}{L}k)n}$ for $1 \leq k \leq L-1$ has power in band I_m if $c^{[L]}(n)$ has power in the band

$$I_T^k = \left[(1-\alpha)\pi - \frac{2\pi}{L}k, (1+\alpha)\pi - \frac{2\pi}{L}k\right] \mod (2\pi)\,. \tag{5.91}$$

Similarly, $\hat{q}_k^{[L]}(n) = (c^{[L]}(n))^* e^{-j(\frac{\omega_b}{L}+\frac{2\pi}{L}k)n}$ for $0 \leq k \leq L-1$ has power in I_m if $c^{[L]}(n)$ has power in the band

$$\hat{I}_T^k = \left[(1-\alpha)\pi - \frac{2\omega_b}{L} - \frac{2\pi}{L}k, (1+\alpha)\pi - \frac{2\omega_b}{L} - \frac{2\pi}{L}k\right] \mod (2\pi)\,. \tag{5.92}$$

We recall that due to oversampling the sampled complex envelope $c^{[L]}(n)$ has a nonzero spectral support only in the band $I_c = [-(1-\alpha)\pi, (1-\alpha)\pi]$. It is then easy to show that

$$I_c \cap I_T^k \neq \emptyset$$

for any $1 \leq k \leq L-1$, and therefore $q_k^{[L]}(n)$ will always have power in band I_m. With some effort it can be shown that

$$I_c \cap \hat{I}_T^k = \hat{I}_T^k$$

for all $0 \leq k \leq L-1$, i.e., $\hat{I}_T^k \subset I_c$ when ω_b satisfies

$$\max\left(-\pi, \pi(\alpha L - \mathrm{sgn}(\omega_b)k)\right) < |\omega_b| < \min\left(\pi, \pi(L - \alpha L - \mathrm{sgn}(\omega_b)k)\right)\,. \tag{5.93}$$

Outside this bound on ω_b, $\hat{I}_T^k$ only partially fits inside I_c which still guarantees $I_c \cap \hat{I}_T^k \neq \emptyset$. Extra precaution must be taken in the cases when $\omega_b = 0, \pm\pi$ since

$$\omega_b = 0 \Rightarrow I_c \cap \hat{I}_T^0 = \emptyset$$

$$\omega_b = -\pi \Rightarrow I_c \cap \hat{I}_T^1 = \emptyset$$
$$\omega_b = +\pi \Rightarrow I_c \cap \hat{I}_T^{L-1} = \emptyset \; .$$

This is generally of no dire consequence since it simply implies that the single signal $\hat{q}_k^{[L]}(n)$ for $k = 0$ if $\omega_b = 0$, $k = 1$ if $\omega_b = -\pi$, or $k = L-1$ if $\omega_b = +\pi$ does not have any power in band I_m and hence does not contribute to $J(\hat{\boldsymbol{\theta}})$. The corresponding matrix $\hat{\mathbf{J}}^k$ has all zero elements and drops out of the sum in (5.88). A major issue arises in the case $M = 2, 3$ with $L = 1, k = 0$ when $\omega_b = 0, \pm\pi$ since the only signal $\hat{q}_0(n) = c^*(n)e^{-j\omega_b n}$ comprising the error has no power in band I. In this situation, the described calibration technique will not work as described. To circumvent this issue, we can identify another frequency band other than I where the signal $r(n;\boldsymbol{\theta}) = c(n)e^{j\omega_b n}$ is free of energy, extract the error $e(n;\hat{\boldsymbol{\theta}})$ in this new band, and then perform minimization of $J(\hat{\boldsymbol{\theta}})$.

5.3 Calibration Analysis

Proposed Iteration Justification

We wish to minimize the objective function

$$J(\hat{\boldsymbol{\theta}}) = \frac{1}{2}E\left[\frac{1}{L}\sum_{k=0}^{L-1}|e^{[L]}(n+k;\hat{\boldsymbol{\theta}})|^2\right] \tag{5.94}$$

over $\hat{\boldsymbol{\theta}} \in \mathbb{R}^{2(M-1)}$. We proposed the following SGD iteration to perform this minimization

$$\hat{\boldsymbol{\theta}}(n+1) = \hat{\boldsymbol{\theta}}(n) - \mu(n)\nabla_{\hat{\boldsymbol{\theta}}}\big(\frac{1}{2}|e^{[L]}(n;\hat{\boldsymbol{\theta}}(n))|^2\big), \tag{5.95}$$

where for the purpose of analysis $\mu(n) = \mu$ is assumed to be a very small constant step size. The estimate after L iterations can be expressed as

$$\begin{aligned}\hat{\boldsymbol{\theta}}(n+L) &= \hat{\boldsymbol{\theta}}(n) - \frac{\mu}{2}\nabla_{\hat{\boldsymbol{\theta}}}\Big(\sum_{k=0}^{L-1}|e^{[L]}(n+k;\hat{\boldsymbol{\theta}}(n+k))|^2\Big) \\ &\approx \hat{\boldsymbol{\theta}}(n) - \frac{\mu}{2}\nabla_{\hat{\boldsymbol{\theta}}}\Big(\sum_{k=0}^{L-1}|e^{[L]}(n+k;\hat{\boldsymbol{\theta}}(n))|^2\Big), \end{aligned} \tag{5.96}$$

where we have used the approximation $\hat{\boldsymbol{\theta}}(n+k) \approx \hat{\boldsymbol{\theta}}(n)$ for $0 \leq k \leq L-1$ since μ is very small. Letting $\widehat{\mu} = \mu L$, the expression (5.96) can be rewritten as

$$\hat{\boldsymbol{\theta}}(n+L) \approx \hat{\boldsymbol{\theta}}(n) - \frac{\widehat{\mu}}{2}\nabla_{\hat{\boldsymbol{\theta}}}\Big(\frac{1}{L}\sum_{k=0}^{L-1}|e^{[L]}(n+k;\hat{\boldsymbol{\theta}}(n))|^2\Big), \tag{5.97}$$

from which we deduce that L iterations of our proposed SGD (5.95) collectively behave as a single SGD iteration for minimizing $J(\hat{\boldsymbol{\theta}})$ in (5.94). Now consider the estimate after LP iterations which using (5.97) can be expressed as

$$\hat{\boldsymbol{\theta}}(n+LP) \approx \hat{\boldsymbol{\theta}}(n) - \frac{\widehat{\mu}}{2}\nabla_{\hat{\boldsymbol{\theta}}}\Big(\frac{1}{L}\sum_{m=0}^{P-1}\sum_{k=0}^{L-1}|e^{[L]}(n+k+mL;\hat{\boldsymbol{\theta}}(n+mL))|^2\Big). \tag{5.98}$$

Again, if $\widehat{\mu}$ is fairly small, then $\hat{\boldsymbol{\theta}}(n+mL) \approx \hat{\boldsymbol{\theta}}(n)$ for $m = 0, \ldots, P-1$, and provided the cyclostationary process $e^{[L]}(n;\hat{\boldsymbol{\theta}})$ satisfies a strong mixing property of the type discussed in [122], the cycloergodicity property

$$\sum_{m=0}^{P-1}\sum_{k=0}^{L-1}|e^{[L]}(n+k+mL;\hat{\boldsymbol{\theta}}(n))|^2 \approx P \cdot \underbrace{E\Big[\sum_{k=0}^{L-1}|e^{[L]}(n+k;\hat{\boldsymbol{\theta}}(n))|^2\Big]}_{2LJ(\hat{\boldsymbol{\theta}}(n))} \tag{5.99}$$

holds for a sufficiently large P. The equation (5.98) can then be approximated with the iteration

$$\hat{\boldsymbol{\theta}}(n+LP) \approx \hat{\boldsymbol{\theta}}(n) - \tilde{\mu}\nabla_{\hat{\boldsymbol{\theta}}}J(\hat{\boldsymbol{\theta}}(n)) \tag{5.100}$$

of step size $\tilde{\mu} = \widehat{\mu}P = \mu LP$, which has the familiar form of steepest descent. We conclude that blocks of LP iterations of our proposed SGD approximately act as a single iteration of steepest descent for minimizing $J(\hat{\boldsymbol{\theta}})$. As expected, $\mu << \tilde{\mu}$.

Convergence Analysis

We examine L consecutive steps of our proposed estimation algorithm (5.95) which from (5.97) can be expressed as

$$\hat{\boldsymbol{\theta}}(n+L) \approx \hat{\boldsymbol{\theta}}(n) + \widehat{\mu}\, \mathbf{T}(n; \hat{\boldsymbol{\theta}}(n)) \tag{5.101}$$

with

$$\mathbf{T}(n; \hat{\boldsymbol{\theta}}) = -\nabla_{\hat{\boldsymbol{\theta}}} \left(\frac{1}{2L} \sum_{k=0}^{L-1} |e^{[L]}(n+k; \hat{\boldsymbol{\theta}})|^2 \right). \tag{5.102}$$

The convergence and steady-state behavior of this algorithm can be analyzed by using the stochastic averaging or ODE method discussed in Section 2.6 applicable to adaptive algorithms with a small step size. Note that since the gain and timing mismatches we seek to estimate are small, and since the fluctuations of the adaptive estimates about the correct mismatch values need to be even smaller, the small $\widehat{\mu}$ assumption is well adapted to our application. The ODE method interprets the trajectories of adaptive algorithm (5.101) as random fluctuations about trajectories of the differential equation

$$\frac{d\hat{\boldsymbol{\theta}}}{dt} = \boldsymbol{t}(\hat{\boldsymbol{\theta}}) \tag{5.103}$$

with

$$\boldsymbol{t}(\hat{\boldsymbol{\theta}}) = E[\mathbf{T}(n; \hat{\boldsymbol{\theta}})]\,, \tag{5.104}$$

where in evaluating the expectation (5.104), the vector $\hat{\boldsymbol{\theta}}$ is viewed as fixed and nonrandom. For the case at hand, by exchanging the expectation and differentiation operations and

applying definition (5.94), we obtain

$$\boldsymbol{t}(\hat{\boldsymbol{\theta}}) = -\nabla_{\hat{\boldsymbol{\theta}}} J(\hat{\boldsymbol{\theta}}) \tag{5.105}$$

so that as expected for stochastic gradient algorithms, the ODE (5.103) is a gradient flow, i.e., its trajectories follow steepest descent lines of $J(\hat{\boldsymbol{\theta}})$. Accordingly, since it was shown in previous section that under certain spectral content conditions for $c^{[L]}(n)$, $J(\hat{\boldsymbol{\theta}})$ can be approximated by a positive definite quadratic form in the vicinity of $\boldsymbol{\theta}$, we can deduce that for all initial conditions $\hat{\boldsymbol{\theta}}(0)$ located close to $\boldsymbol{\theta}$, all trajectories of differential equation (5.103) will converge to the true parameter vector $\boldsymbol{\theta}$.

In addition, it is shown in Theorem 2 of Chap 3 of [72] that when the negative Hessian matrix

$$\mathbf{A}(\boldsymbol{\theta}) = -\nabla^2_{\hat{\boldsymbol{\theta}}} J(\hat{\boldsymbol{\theta}})\big|_{\hat{\boldsymbol{\theta}}=\boldsymbol{\theta}} \tag{5.106}$$

is stable in the sense of continuous-time systems, i.e., its eigenvalues have a strictly negative real part, then for large n and vanishingly small $\widehat{\mu}$

$$\hat{\boldsymbol{\theta}}(n) \sim N(\boldsymbol{\theta}, \widehat{\mu}\mathbf{P}) \,, \tag{5.107}$$

where the covariance matrix $\mathbf{P} > 0$ satisfies a Lyapunov equation. In other words, $\hat{\boldsymbol{\theta}}(n)$ admits asymptotically a Gaussian distribution about the true parameter vector $\boldsymbol{\theta}$ and the fluctuations have a standard deviation proportional to $\widehat{\mu}^{1/2}$. For the case at hand

$$\mathbf{A}(\boldsymbol{\theta}) \approx -2\boldsymbol{\mathcal{J}} = -2\Big[\sum_{k=1}^{L-1} \mathbf{J}^k + \sum_{k=0}^{L-1} \hat{\mathbf{J}}^k\Big] < 0 \tag{5.108}$$

and is stable since $\boldsymbol{\mathcal{J}} > 0$ (when $c^{[L]}(n)$ satisfies appropriate spectral conditions). Unfortunately, the Lyapunov equation statisfied by $\mathbf{P}$ (not described here) does not appear to admit a closed form solution.

5.4 Simulations

We illustrate the proposed TIADC calibration method for the two-channel case with different types of signals. The reconstruction and calibration filters (5.12–5.13) in Fig. 5.1 when $M = 2$ are specified in Appendix B.

Sum of Complex Tones Complex Envelope

We consider first the bandpass signal from Section 3.4 with carrier frequency $F_c = \Omega_c/(2\pi) =$ 5.15 GHz, multi-tone complex envelope given in (3.102), and bandwidth $B/(2\pi) = 800$ MHz. The chosen sub-ADC sampling frequency $F'_s = \Omega'_s/(2\pi) = 1$ GHz is above $B/(2\pi)$ as per (3.5), and the oversampling ratio (5.16) is thus $\alpha = 0.2$. We have $\ell = 5$, $\omega_b = 0.3\pi$, and the sampled envelope $c(n)$ expressed in (3.103) that has four tones located at $\pm 0.8\pi$ and $\pm 0.35\pi$. The frequency support of $c(n)$ lies in the interval $I_c = [-0.8\pi, 0.8\pi]$ and given

$$\hat{I}_T = [0.8\pi, 1.2\pi] - 0.6\pi = [0.2\pi, 0.6\pi]$$

from (5.92), the calibration method should work satisfactorily since the set $I_c \cap \hat{I}_T = 0.35\pi$ is not empty. The passband of the bandpass filter $H_{\rm BP}(e^{j\omega})$ defined in (5.20) is $I = [0.8\pi, 1.2\pi] + 0.3\pi \mod (2\pi) = [-0.9\pi, -0.5\pi]$.

Let $d^0 = 0.425$ be the nominal timing skew of the two-channel TIADC which has gain and timing mismatches in the amounts $\gamma = g - 1 = 0.01$ and $\delta = d - d^0 = -0.0025$. The two sub-ADC sequences according to (5.2–5.3) are given by

$$\begin{aligned} x_0(n) &= \Re\{c(n)e^{j\omega_b n}\} + v_0(n) \\ x_1(n) &= g \times \Re\{c(n-d)e^{j\omega_b(n-d)}e^{-j2\pi\ell d}\} + v_1(n)\ , \end{aligned} \tag{5.109}$$

where the zero mean white noises $v_0(n)$ and $v_1(n)$ model the effect of thermal and quantization noises. The sub-ADC SNR is 61.8dB.

The FIR versions of reconstruction filters $H_{i,l}(e^{j\omega})$ with $i, l = 0, 1$ appearing in Fig. 5.1 are obtained by windowing their impulse responses calculated in Appendix B with a Kaiser window of order $N = 60$ and parameter $\beta = 6$. The magnitudes of the frequency responses of the resulting FIR filters are shown in Fig. 5.3. The small notches of these filters (except for $H_{0,1}$) at the frequency $\pm(\pi - |\omega_b|) = \pm 0.7\pi$ are due to phase discontinuities of the reconstruction filters (except for $H_{0,1}$) at this frequency. Note that the gradient filters $H_{0,1}$ and $H_{1,1}$ have large magnitudes. To ensure that the transition region of the bandpass filter $H_{\mathrm{BP}}(e^{j\omega})$ does not extend outside $[-0.9\pi, -0.5\pi]$, we select a value $\alpha = 0.15$ (corresponding to a narrower passband of $[-0.85\pi, -0.55\pi]$) in the impulse response $h_{\mathrm{BP}}(n)$ and employ a Kaiser window of length 81 and parameter $\beta = 8$. The magnitude of the resulting FIR filter is shown in Fig. 5.4.

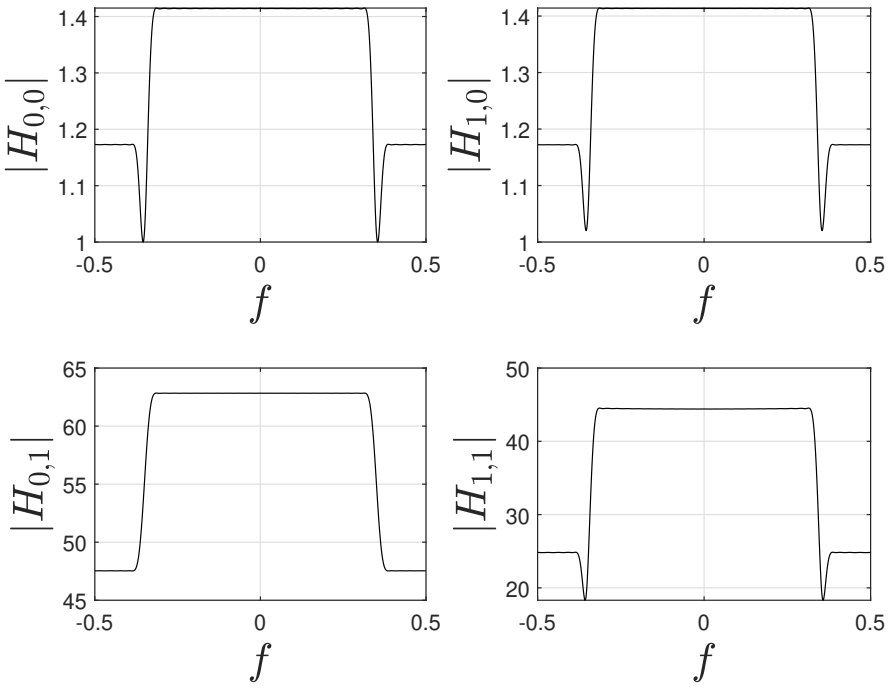


Figure 5.3: Magnitudes of FIR approximation of reconstruction filters $H_{i,l}(e^{j\omega})$ with $i, l = 0, 1$ for a Kaiser window of length $N + 1 = 61$ and parameter $\beta = 6$.

To quantify the loss of performance associated with the use of first-order approximations (5.12) and (5.13) instead of the exact reconstruction filters $H_0(e^{j\omega}; d)$ and $H_1(e^{j\omega}; g, d)$,

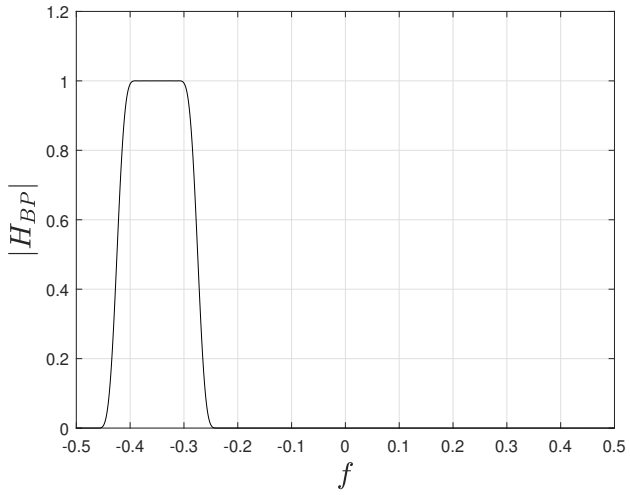


Figure 5.4: Magnitude of bandpass FIR filter H_{BP} obtained by using a window of length 81 and parameter $\beta = 8$.

the Fig. 5.5 and Fig. 5.6 show the PSDs of the estimated sampled complex envelope $\hat{c}(n)$ obtained respectively with the filters $H_0(e^{j\omega}; d)$ and $H_1(e^{j\omega}; g, d)$ corresponding to the true ADC parameters, and the first order approximations (5.12) and (5.13) used in Fig. 5.1 with true mismatches γ, δ. The PSDs are computed with the complex periodogram method for a data block of length 10^4, and filters of order $N = 60$ are used in both figures. The MSE between the theoretical and estimated envelope when reconstruction filters with the true TIADC parameters are used in computation is -53.03dB which as expected is very similar to the MSE obtained in Table 3.2, whereas the first-order approximation used in Fig. 5.1 yields a MSE of -39.93dB only. A closer look at Fig. 5.5 and Fig. 5.6 reveals a SFDR of about 68dB with exact reconstruction filters and only 45dB for a first-order approximation of these filters in the vicinity of (g^0, d^0).

Next, for the four-tone complex envelope considered, the blind estimation algorithm (5.26) is applied to a sequence of length $L_s = 5 \times 10^4$ samples. The initial mismatches are selected as $\hat{\gamma} = 0$ and $\hat{\delta} = 0$, which corresponds to selecting the nominal TIADC parameters (g^0, d^0) as the starting point. Instead of using the same step size for both the gain and timing skew iterations, we select two different constant step sizes $\mu_\gamma = 10^{-3}$ for gain and $\mu_\delta = 10^{-5}$

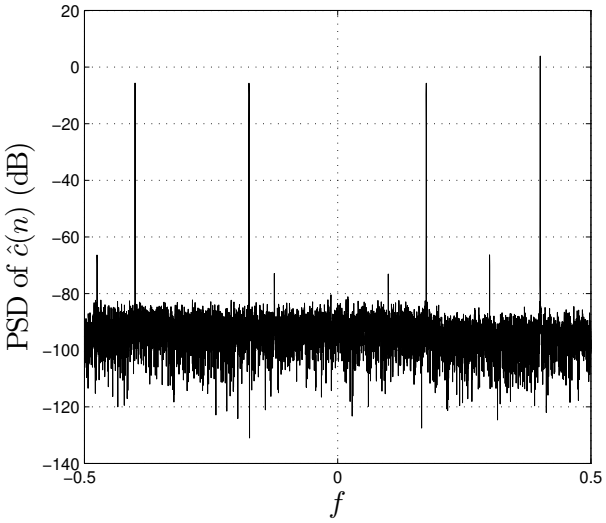


Figure 5.5: PSD of the estimated envelope $\hat{c}(n)$ computed with FIR approximations of order $N = 60$ of reconstruction filters H_0 and H_1 for the true TIADC parameters g and d.

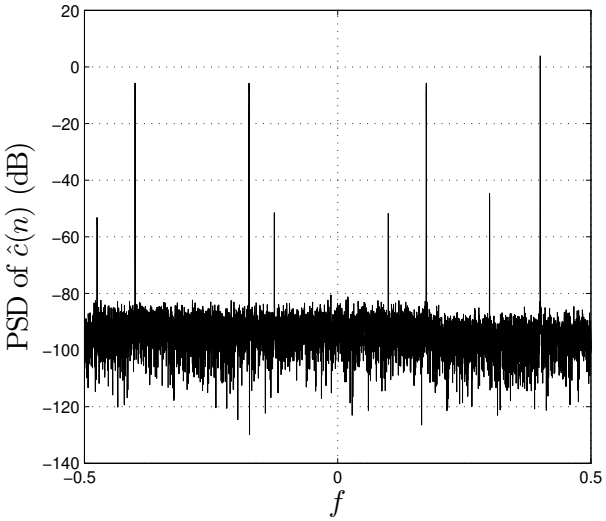


Figure 5.6: PSD of the estimated envelope $\hat{c}(n)$ computed with first order structure of Fig. 5.1 for nominal TIADC parameters $g^0 = 1$, $d^0 = 0.425$ and actual mismatches $\gamma = 0.01$, $\delta = -0.0025$ using filters of order $N = 60$.

for timing skew iterations to improve speed of convergence and estimation accuracy. This choice can be interpreted as replacing the steepest descent algorithm by a quasi-Newton algorithm. The resulting gain and time skew mismatches are shown in Fig. 5.7 and Fig. 5.8, respectively. Note that the final estimated gain mismatch value $\hat{\gamma}(L_s) = 0.77 \times 10^{-2}$

underestimates the gain mismatch γ by more than 20%, but the estimated timing skew mismatch $\hat{\delta}(L_s) = -0.27 \times 10^{-2}$ is very close to the exact mismatch value δ.

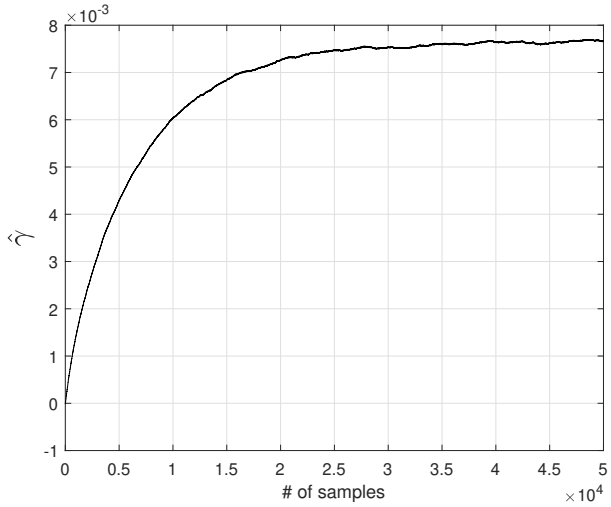


Figure 5.7: Gain mismatch estimates for a four-tone complex input sequence of length $L_s = 5 \times 10^4$ samples, and constant adaptation step sizes $\mu_\gamma = 10^{-3}$ amd $\mu_\delta = 10^{-5}$.

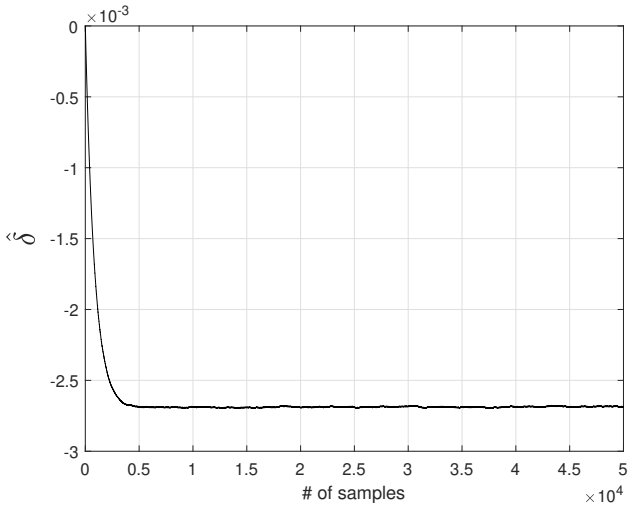


Figure 5.8: Timing skew mismatch estimates for a four-tone complex input sequence of length $L_s = 5 \times 10^4$ samples, and constant adaptation step sizes $\mu_\gamma = 10^{-3}$ amd $\mu_\delta = 10^{-5}$.

To demonstrate the performance improvement of the proposed calibration algorithm, Fig. 5.9 and Fig. 5.10 show the PSDs of the reconstructed envelope $\hat{c}(n)$ obtained before and after calibration. Before calibration, the sampled envelope is computed by using the

initial estimates $\hat{\gamma}(0) = \hat{\delta}(0) = 0$ corresponding to the nominal TIADC values, whereas the calibrated sequence $\hat{c}(n)$ uses the last 10^4 estimates $\hat{\gamma}(n)$ and $\hat{\delta}(n)$ produced by the blind estimation algorithm. Note that as indicated by Fig. 5.7 and Fig. 5.8, the blind estimation algorithm converges quickly, so that the mismatch estimates obtained during the final 10^4 simulation samples fluctuate around the final values. The MSE and SFDR before calibration are -17.80dB and 22dB, and -35.97dB and 40dB after calibration, respectively. Thus calibration yields about 18dB in MSE and SFDR improvement. Note that the MSE performance of the calibration algorithm is within 4dB of the MSE for the simulation of Fig. 5.6 for the first-order reconstruction approximation with the correct TIADC parameters.

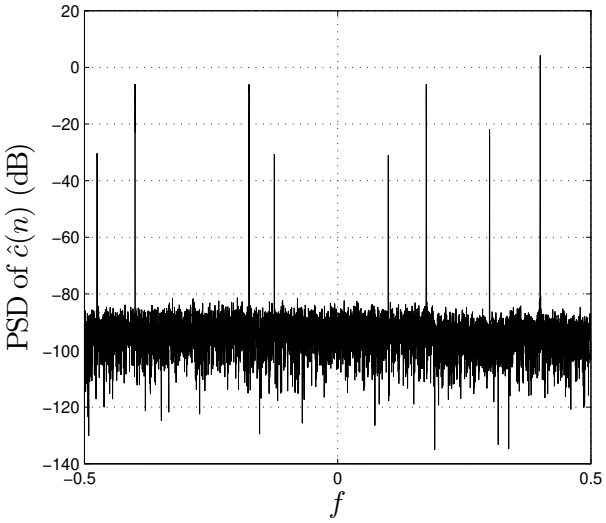


Figure 5.9: PSD of the estimated envelope $\hat{c}(n)$ before calibration.

Consider the same exact calibration setup but the SGD iterations now have time-decaying step sizes $\mu_\gamma(n) = 5/n$ and $\mu_\delta(n) = (2 \times 10^{-3})/n$. Calibration is run again for $L_s = 5 \times 10^4$ samples, but the gain and timing skew mismatch estimates are shown in Fig. 5.11 and Fig. 5.12 only for the first 5×10^3 and 3×10^4 samples, respectively, after which they do not change considerably. The gain mismatch estimate converges to its final value $\hat{\gamma}(L_s) = 0.82 \times 10^{-2}$ very quickly in comparison to the constant step size case in Fig. 5.7. It is also slightly more accurate. The timing skew mismatch takes longer to settle, but converges to the

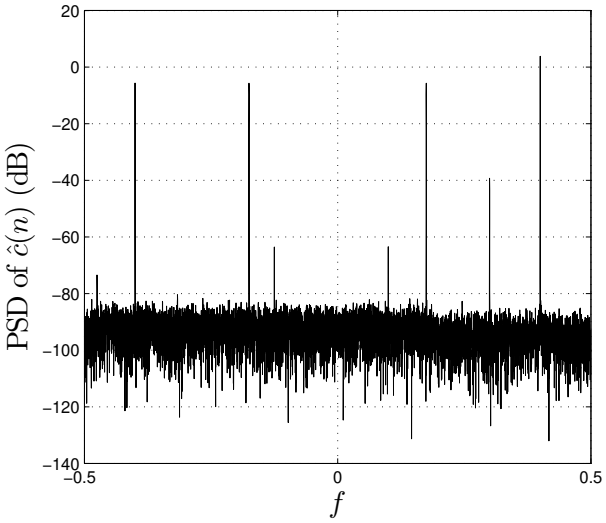


Figure 5.10: PSD of the estimated envelope $\hat{c}(n)$ after calibration with constant adaptation step sizes.

true mismatch parameter $\hat{\delta}(L_s) = \delta = -.25 \times 10^{-2}$. It is then not suprising that the MSE after calibration is -39.45dB which is within half dB of the MSE obtained for first-order approximation with true mismatch values. The PSD after calibration is shown in Fig. 5.13. The SFDR is 45dB. Since the overall reconstruction performance is limited by first-order filter approximations, between calibration phases it may be preferable to use the exact nonlinearized reconstruction filters at the current estimates $\hat{g}$ and $\hat{\delta}$, i.e., $H_0(e^{j\omega}; \hat{d})$ and $H_1(e^{j\omega}; \hat{g}, \hat{d})$ instead of their linearized versions around the nominal point (g^0, d^0).

Finally, to assess the effect of the image band index ℓ on the performance of the proposed calibration algorithm, we perform simulations for values of the carrier frequency F_c equal to $2.15, 3.15, 4.15, \ldots, 10.15, 15.15, 20.15$ GHz. The sub-ADC sampling frequency is held constant at $F_s' = 1$ GHz, so that the values of the carrier frequency correspond to signals in image bands $\ell = 2, 3, 4, \ldots, 10, 15, 20$, and $\omega_b = 0.3\pi$ in all cases. For these signals, we select a nominal timing skew value equal to

$$d^0 = 1/2 - 3/(8\ell)$$

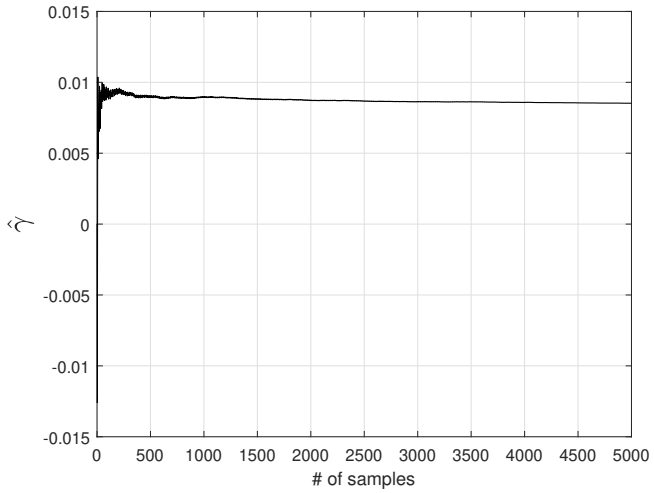


Figure 5.11: Gain mismatch estimates for a four-tone complex input sequence of length $L_s = 5 \times 10^4$ samples, and time-varying adaptation step sizes $\mu_\gamma(n) = 5/n$ and $\mu_\delta(n) = (2 \times 10^{-3})/n$.

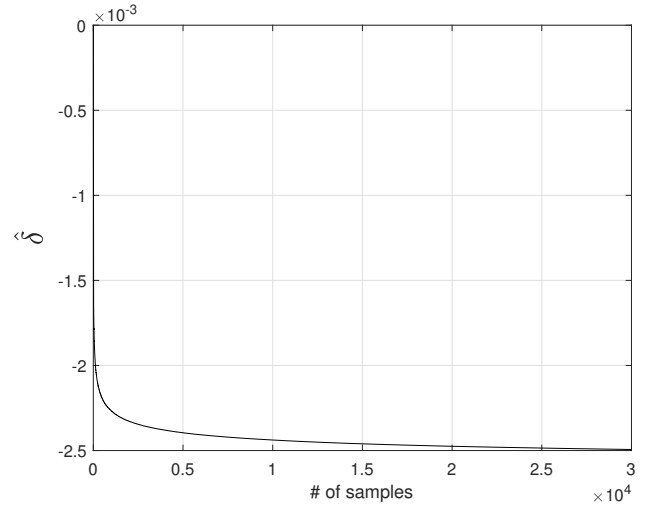


Figure 5.12: Timing skew mismatch estimates for a four-tone complex input sequence of length $L_s = 5 \times 10^4$ samples, and time-varying adaptation step sizes $\mu_\gamma(n) = 5/n$ and $\mu_\delta(n) = (2 \times 10^{-3})/n$.

which ensures d^0 does not correspond to a forbidden value. The gain and timing mismatches are still selected as $\gamma = 10^{-2}$ and $\delta = -0.25 \times 10^{-2}$, and calibration is performed with constant step sizes $\mu_\gamma = 10^{-3}$, $\mu_\delta = 10^{-5}$. Table 5.1 shows the reconstruction MSE before calibration and MSE along with final estimated mismatches after calibration for all image band indices ℓ. The table indicates that the performance of the calibration algorithm de-

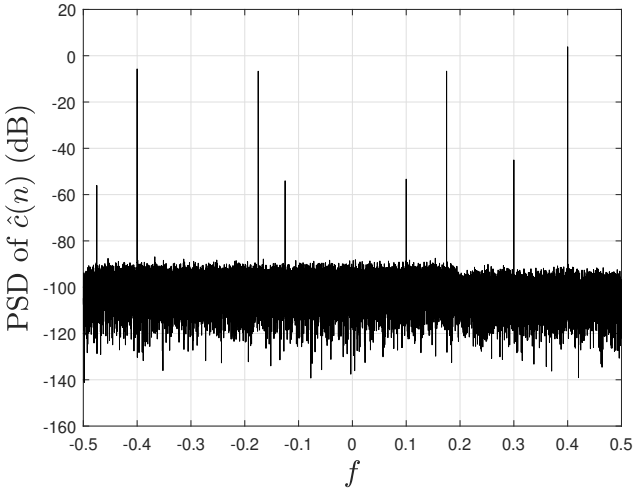


Figure 5.13: PSD of the estimated envelope $\hat{c}(n)$ after calibration with time-varying adaptation step sizes.

grades progressively as ℓ increases. The main reason for this loss in performance is that the first order approximations of reconstruction filters become progressively less accurate as ℓ increases. Thus, for large ℓ it may be desirable to include second-order terms in expansions (5.12–5.13). An alternative approach is to employ *iterative calibration* where reconstruction filters are relinearized around an estimate obtained in the calibration, and a new calibration is started with this estimate as an improved initial starting point. For example, the second calibration shown in Table 5.1 is performed by linearizing reconstruction filters $H_0(e^{j\omega}; \hat{d})$ and $H_1(e^{j\omega}; \hat{g}, \hat{d})$ around a new point (g^p, d^p) obtained in the first calibration, as shown in Appendix C such that

$$|g - g^p| < |g - g^0|$$
$$|d - d^p| < |d - d^0| \,,$$

i.e., (g^p, d^p) is an improvement over the first linearization point (g^0, d^0). As further elaborated in Appendix C, the adaptive equations for $\hat{g}$ and $\hat{d}$ need to be rederived taking into account the new initial vector (g^p, d^p). For the values of ℓ in Table 5.1, one or two calibrations are sufficient to achieve comparable performance in all image bands. For higher ℓ, more than

two calibrations may be needed to attain a satisfactory result. If either $\hat{\gamma}(n)$ or $\hat{\delta}(n)$, but not both, do not converge to any value in one calibration, their final value can be ignored, and a new calibration can begin with improvement in only one of these estimates. This is observed in Table 5.1 where the gain mismatch estimate $\hat{\gamma}(n)$ does not converge (denoted as "NA" in the table) for $\ell = 9, 10, 15, 20$ in the first calibration, but improvement in $\hat{\delta}(n)$ can be used to start a new calibration resulting in a final estimate $\hat{\gamma}(L_s)$ very close to the true gain mismatch γ.

	Carrier Freq. (GHz)	2.15	3.15	4.15	5.15	6.15	7.15	8.15	9.15	10.15	15.15	20.15
	ℓ	2	3	4	5	6	7	8	9	10	15	20
No Calibration	MSE (dB)	-25.49	-22.23	-19.75	-17.80	-16.17	-14.80	-13.61	-12.56	-11.63	-8.04	-5.48
First Calibration	$\hat{\gamma}(L_s)(\times 10^{-3})$	10.5	10.1	9.4	8.3	6.9	5.1	3	NA	NA	NA	NA
	$\hat{\delta}(L_s)(\times 10^{-3})$	-2.5	-2.58	-2.63	-2.70	-2.73	-2.8	-2.85	-2.9	-2.97	-3.27	-3.8
	MSE (dB)	-45.54	-42.73	-39.36	-35.85	-32.57	-29.5	-26.87	-24.5	-22.42	-14	-7.63
Second Calibration	$\hat{\gamma}(L_s)(\times 10^{-3})$	-	-	10.5	10.6	10.1	9.9	10.4	10.5	10.5	10	10.3
	$\hat{\delta}(L_s)(\times 10^{-3})$	-	-	-2.5	-2.51	-2.53	-2.53	-2.5	-2.5	-2.5	-2.5	-2.5
	MSE (dB)	-	-	-44	-43.64	-42.1	-41.75	-42.3	-42.28	-42.45	-40.16	-40.2

Table 5.1: The MSE and final estimated mismatches after one and two calibrations (with constant adaptation step sizes) as the image band index ℓ increases.

Bandlimited White Noise Compex Envelope

For a signal with a carrier frequency $F_c = 5.15$ GHz, we consider the case where the complex envelope $c_c(t)$ is a bandlimited white noise signal with bandwidth $B/(4\pi) = 400$ MHz. The sub-ADC sampling frequency remains $F_s' = 1$ GHz, so that the oversampling ratio is again $\alpha = 0.2$. The PSD of the sampled complex envelope is shown in Fig. 5.14. The nominal TIADC parameters $g^0 = 1$, $d^0 = 0.425$, and mismatches γ and δ are the same as before. Since $\omega_b = 0.3\pi$ and $\ell = 5$, the reconstruction filters $H_{i,l}(e^{j\omega})$ with $i, l = 0, 1$ and bandpass filter $H_{\text{BP}}(e^{j\omega})$ are the same as for the multi-tone signal example, and we use FIR filters with the same orders. Finally, Fig. 5.14 indicates that $c(n)$ has power in the band $\hat{I}_T = [0.2\pi, 0.6\pi]$ which is necessary for calibration to work.

The blind estimation algorithm is applied to a data block of length $L_s = 10^5$ samples with constant adaptation step sizes $\mu_\gamma = 5 \times 10^{-4}$ and $\mu_\delta = 5 \times 10^{-6}$ and zero initial mismatch values corresponding to nominal TIADC parameters. The resulting estimated mismatches

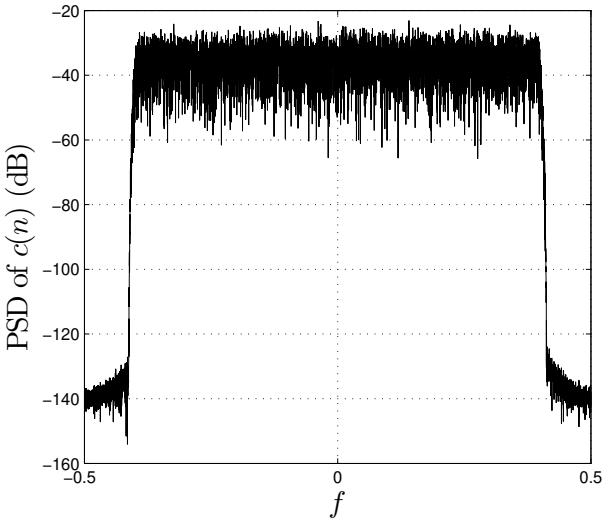


Figure 5.14: PSD of the actual sampled bandlimited white noise complex envelope.

are shown as a function of time in Fig. 5.15 and Fig. 5.16. The final estimated gain and timing skew mismatches estimates are $\hat{\gamma}(L_s) = 0.83 \times 10^{-2}$ and $\hat{\delta}(L_s) = -0.24 \times 10^{-2}$. As in the case of a sum of complex tones envelope, the gain mismatch is underestimated, but slightly less so than in the complex tones case, and the timing skew mismatch is estimated quite accurately. The MSE of the complex envelope error is -37.56dB.

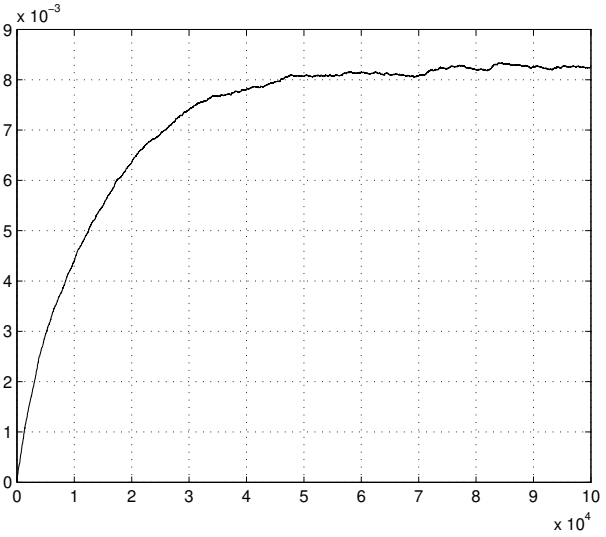


Figure 5.15: Gain mismatch estimates for a bandlimited white noise complex envelope, with $L_s = 10^5$ samples, and constant adaptation step sizes $\mu_\gamma = 5 \times 10^{-4}$ and $\mu_\delta = 5 \times 10^{-6}$.

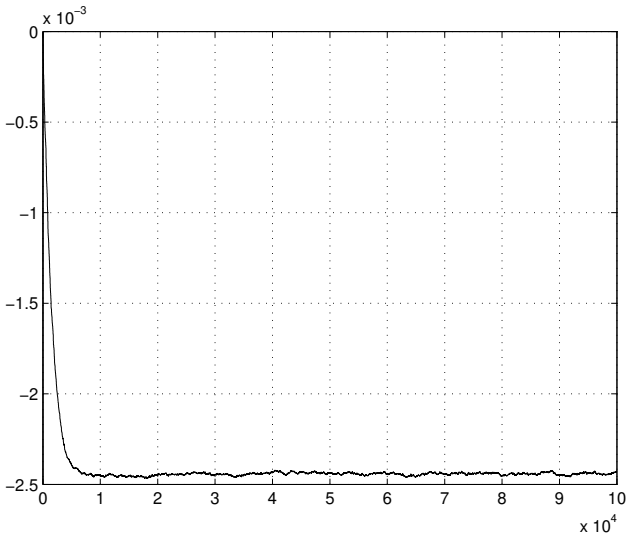


Figure 5.16: Timing skew mismatch estimates for a bandlimited white noise complex envelope, with $L_s = 10^5$ samples, and constant adaptation step sizes $\mu_\gamma = 5 \times 10^{-4}$ and $\mu_\delta = 5 \times 10^{-6}$.

The PSD of the complex envelope after calibration is shown in Fig. 5.17. It is computed by selecting the final block of length 10^4 samples of the blind calibration simulation, after the estimation algorithm has converged.

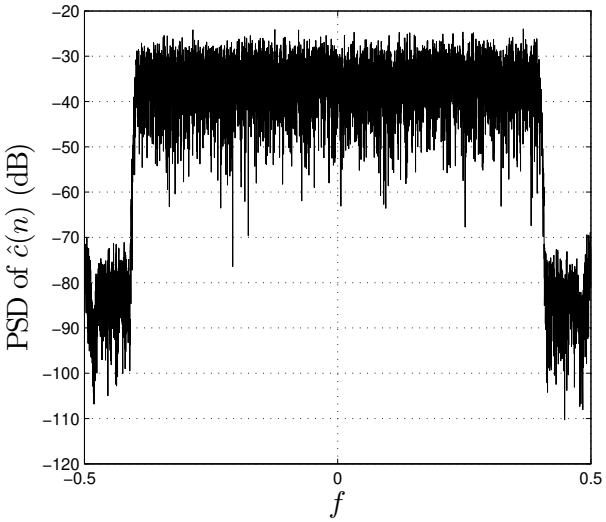


Figure 5.17: PSD of the sampled bandlimited white noise complex envelope after calibration with constant adaptation step sizes.

MSK Envelope

Consider a MSK signal with carrier frequency $F_c = 5.15$ GHz, complex envelope $c_c(t)$ specified in (3.107), and bandwidth $B/(2\pi) = 800$ MHz. As in the last two examples, setting sub-ADC sampling frequency to $F_s' = 1$ GHz results in oversampling ratio $\alpha = 0.2$. The sampled complex envelope has a continuous PSD as shown in Fig. 5.18. Due to oversampling, energy levels are lower in the band $[0.8\pi, 1.2\pi] \mod (2\pi)$ than outside this band but not entirely zero. The TIADC has the same nominal parameters $g^0 = 1$ and $d^0 = 0.425$ as in the previous examples, but this time contains $\gamma = 0.03$ and $\delta = -0.30 \times 10^{-2}$ mismatches. We use the same reconstruction/calibration filters with same orders as before since $\ell = 5$ and $\omega_b = 0.3\pi$, but the bandpass filter has a smaller passband set by selecting $\alpha = 0.1 < 0.2$ to allow for the transition region and avoid picking up higher energy levels of $C(e^{j(\omega-\omega_b)})$. A passband too small, however, should be avoided since in that case $h_{\text{BP}}(n)$ extracts too little power from the error signal $C^*(e^{-j(\omega+\omega_b)})$ needed for calibration to work properly. The continuous PSD of $c(n)$ assures it contains power across all $\hat{I}_T = [0.2\pi, 0.6\pi]$.

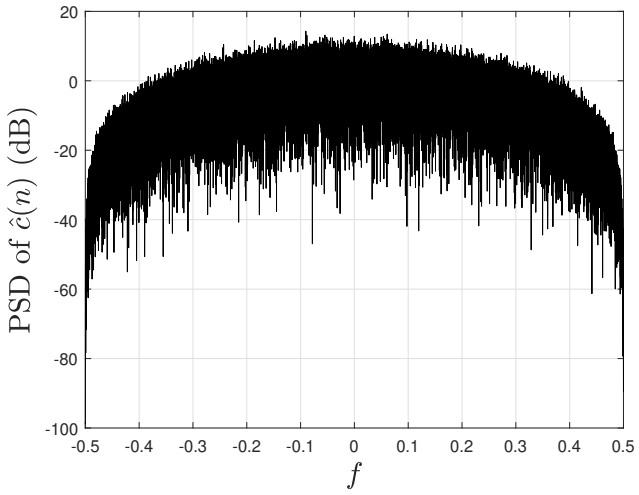


Figure 5.18: PSD of the sampled MSK envelope.

The results of the blind calibration algorithm for estimated mismatches with $L_s = 10^5$ samples, constant adaptation step sizes $\mu_\gamma = 1.2 \times 10^{-3}$ and $\mu_\delta = 0.15 \times 10^{-5}$, and zero initial mismatches are shown in Fig. 5.19 and Fig. 5.20. The final estimated gain mismatch

$\hat{\gamma}(L_s) = 0.0361$ slightly overestimates γ, while the final estimate timing mismatch $\hat{\delta}(L_s) = -0.30 \times 10^{-2}$ is extremely accurate. The PSD of the complex envelope after calibration is shown in Fig. 5.21 which is computed using the last 10^4 samples of the blind calibration simulation after the algorithm has converged. The MSE of reconstruction after calibration is -38.2dB which is very close to -39.95dB obtained in the simulation (not shown here) for first-order approximation with true mismatch values.

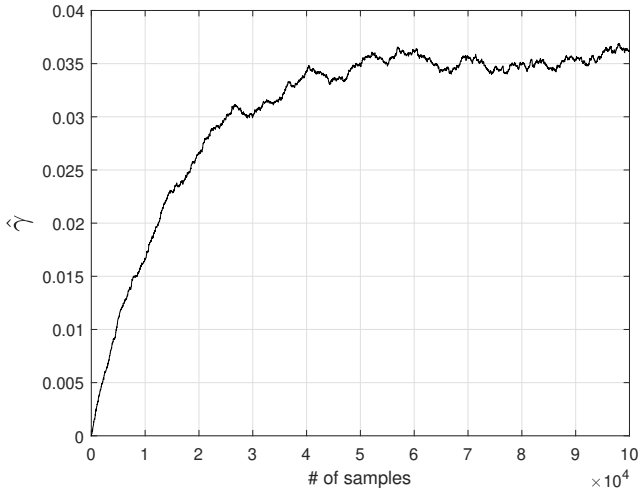


Figure 5.19: Gain mismatch estimates for MSK complex envelope, with $L_s = 10^5$ samples, and constant adaptation step sizes $\mu_\gamma = 1.2 \times 10^{-3}$ and $\mu_\delta = 0.15 \times 10^{-5}$.

As highlighted in Chapter 3, timing skew mismatches play a larger role in degrading reconstruction performance than gain mismatches do. For this reason, we analyze calibration performance for various timing mismatches. The results before and after calibration are shown in Table 5.2. $L_s = 10^5$ samples and constant adaptation step size $\mu_\delta = 0.15 \times 10^{-5}$ are used to perform estimation. Except for the case of 0.10% timing skew mismatch, calibration is all other cases roughly doubles the MSE performance. In all cases, the estimate $\hat{\delta}(n)$ converges to the true parameter δ.

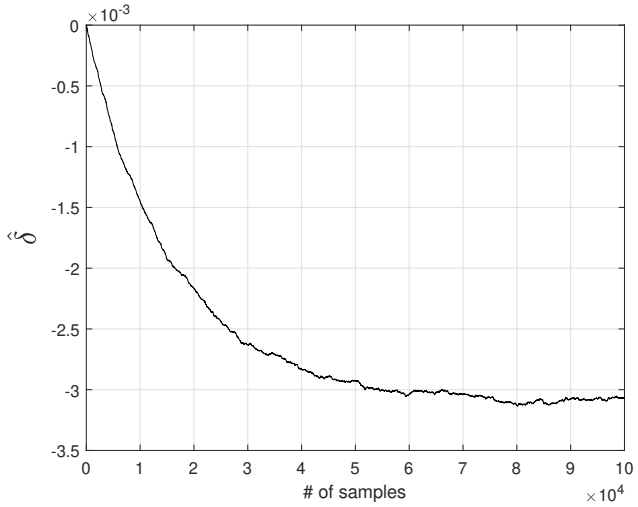


Figure 5.20: Timing skew mismatch estimates for MSK complex envelope, with $L_s = 10^5$ samples, and constant adaptation step sizes $\mu_\gamma = 1.2 \times 10^{-3}$ and $\mu_\delta = 0.15 \times 10^{-5}$.

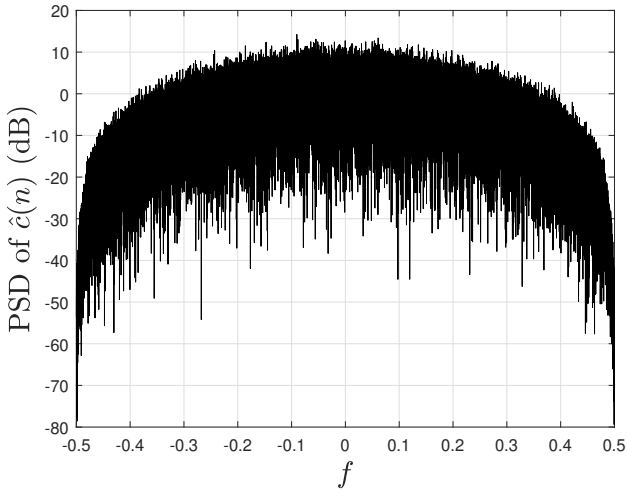


Figure 5.21: PSD of the sampled MSK complex envelope after calibration with constant adaptation step sizes.

Timing Skew Mismatch δ	MSE(dB) before calibration	MSE(dB) after calibration
0.10%	-29.99	-47.63
0.25%	-22.07	-43.11
0.50%	-16.09	-31.91
0.75%	-12.56	-24.89
1%	-10.08	-19.41

Table 5.2: MSK complex envelope reconstruction performance (MSE) before and after calibration (with constant adaptation step size) for various timing skew mismatches.

Chapter 6

Conclusions and Future Work

In this dissertation we have described a flexible technique for computing the sampled complex envelope of a bandpass signal from nonuniform samples of the signal taken on the order of Nyquist rate by a M-channel TIADC. A discrete-time model establishing the relationship between the sampled complex envelope and data sequences generated by the sub-ADCs was presented. It was shown that reconstruction of the envelope generally requires M complex-valued FIR filters and a discrete-time modulator. Some TIADC timing skews are forbidden as they cause the reconstruction process to collapse. Higher number of channels allow for lower sub-ADC sampling rates but at the cost of increasing reconstruction filter complexity. A careful analysis was provided for the practical cases $M = 2, 3, 4$. Extensive simulations with multi-tone and MSK signals demonstrated robust method performance. Degradation in performance was observed near forbidden timing skews and in the presence of TIADC gain and timing skew mismatches. It was also shown that reconstruction is more sensitive to timing than gain mismatches highlighting the need for timing skew calibration.

A special case of $M = 2$ known as quadrature sampling assumes certain relations between the signal carrier frequency and sub-ADC sampling rate and moreover between the carrier period and TIADC timing offset. It requires the implementation of only one reconstruction filter which can be used to estimate the complex envelope even when the carrier

frequency is not exactly an integer multiple of the sub-ADC sampling frequency as required for quadrature sampling. Simulations demonstrated this approach to be an effective and robust approximation dependent on the order of reconstruction filter. The approximation suffered when due to sub-ADC mismatches the timing skew deviated from its ideal value set by quadrature sampling.

To address performance loss due to TIADC gain and timing skew mismatches, we proposed a blind calibration method that requires the bandpass signal to be slightly oversampled so that there exists a frequency band in which the sampled complex envelope has no power. By extracting the component of the reconstructed envelope corresponding to this frequency band, an error signal was obtained with cyclostationary second-order statistics (assuming a WSS envelope random process). We proved rigorously that the scaled power of the error process admits a positive definite quadratic approximation and can be minimized adaptively by using the stochastic gradient approach in order obtain estimates of the TIADC gain and timing skew mismatches. The overall joint reconstruction and calibration architecture requires a total of $2M^2$ fixed FIR filters and $M^2 - 1$ adaptive taps. Reconstruction performance substantially improves after calibration as was demonstrated with simulations using multi-tone, MSK, and bandlimited white noise signals.

In conjunction with recent advances in the design of wide bandwidth sample-and-hold circuits of the type reported in [5], the proposed sampling technique has the potential to simplify greatly RF communications and radar receiver front-ends by removing all mixing and filtering hardware typically used to extract the I and Q components of the received signal prior to sampling. As was noted in [74], the use of a nonuniform TIADC has also the advantage that sampling a bandpass signal of bandwidth B becomes possible at all rates greater than or equal to $2B$, independently of the frequency band $[\Omega_L, \Omega_H]$ where the signal is located. Thus the proposed TIADC and reconstruction/calibration architecture could be implemented as a software radio front end capable of digitizing signals in different bands.

6.1 Suggestions for Further Research

There are several research directions we can take to broaden the presented reconstruction/calibration technique. We highlight three possibilities.

- Extend the sampling technique to multi-band signals of the type considered in [75, 80] where the spectrum consists of several disjoint components in an interval of length B. The goal then would be to achieve sampling rates below the Nyquist rate $2B$ since the presence of "holes" in the spectrum indicates the effective signal bandwidth is less than B. This problem can be considered as sampling directly multiple RF signals with nonoverlapping spectra. The work in [123] proposes a minimum sampling frequency bound for such a case but only when a single ADC is used in sampling. It would be of interest to see what lower bound on the sampling frequency can be derived in the general M-channel case with no assumptions (unlike multicoset sampling) on the TIADC timing skews.

- Extend the calibration method to include correction of bandwidth mismatches. As stated in Chapter 1, bandwidth mismatches arise due to mismatches in channel S/H circuits. Given our sampling method is direct and requires wide bandwidth S/H circuits [5] operating at high frequencies, it is very likely that bandwidth mismatches contribute significantly to overall TIADC performance loss. It remains to be seen if the filter-bank bandwidth calibration approach developed in [20, Chap. 4], which similar to our gain and timing mismatch correction also relies on power minimization in a certain frequency band, can be extended to the bandpass case.

- Consider calibration in the case when the channel gains are complex-valued, i.e., when gain mismatches introduce a phase in addition to amplitude mismatch in each channel. Linearization of reconstruction filters would then involve some form of complex gradients. In this context, it would be of interest to determine if timing skew mismatches still dominate TIADC performance loss when the gain mismatches have two

parameters (magnitude and phase) that need to be estimated.

Appendix A

Reconstruction Filters for the Four-Channel TIADC

Reconstruction filters and their impulse responses when $\ell = 5$, $\omega_b = \pi/2$, $d_1 = 0.375$, $d_2 = 0.625$, and $d_3 = 0.875$.

$$\Phi_0(e^{j\omega}) = \begin{cases} 2 & -\pi \le \omega < -\frac{3\pi}{4} \\ 1.4142 + j0.5858 & -\frac{3\pi}{4} \le \omega < -\frac{\pi}{4} \\ 0 & -\frac{\pi}{4} \le \omega < \frac{\pi}{4} \\ 0.5858 + j1.4142 & \frac{\pi}{4} \le \omega < \frac{3\pi}{4} \\ 2 & \frac{3\pi}{4} \le \omega < \pi \end{cases} \tag{A.1}$$

$$\phi_0(n) = \frac{2}{\pi n}\Big[(1+j)\sin\big(\frac{\pi n}{4}\big)\big(\cos\big(\frac{\pi n}{2}\big) - 0.4142\sin\big(\frac{\pi n}{2}\big)\big) - \sin\big(\frac{3\pi n}{4}\big)\Big] \tag{A.2}$$

for $n \neq 0$ and $\phi_0(0) = 1 + j0.5$,

$$h_0(n) = \phi_0(n). \tag{A.3}$$

$$\Phi_1(e^{j\omega}) = \begin{cases} 0.2929 - j1.7071 & -\pi \le \omega < -\frac{3\pi}{4} \\ 0.7071 - j1.1213 & -\frac{3\pi}{4} \le \omega < -\frac{\pi}{4} \\ 1.4142 & -\frac{\pi}{4} \le \omega < \frac{\pi}{4} \\ 0.2929 - j0.7071 & \frac{\pi}{4} \le \omega < \frac{3\pi}{4} \\ 1.7071 + j0.2929 & \frac{3\pi}{4} \le \omega < \pi \end{cases} \tag{A.4}$$

$$\begin{aligned} \phi_1(n) &= \frac{1}{2\pi n}\Big[(-1 + e^{j\frac{\pi}{4}n})\big((0.2929 - j1.7071)e^{j\frac{3\pi}{4}n} \\ &\quad -(1.7071 + j0.2929)(-1)^n\big) - (-1 + e^{j\frac{\pi}{2}n})\big((.7071 + j0.2929)e^{j\frac{\pi}{4}n} \\ &\quad +(1.1213 + j0.7071)e^{-j\frac{3\pi}{4}n} + j1.4142e^{-j\frac{\pi}{4}n}\big)\Big] \end{aligned} \tag{A.5}$$

for $n \neq 0$ and $\phi_1(0) = 0.8535 - j0.6339$,

$$h_1(n) = \phi_1(n + 2d_1). \tag{A.6}$$

$$\Phi_2(e^{j\omega}) = \begin{cases} 1 + j & -\pi \le \omega < -\frac{3\pi}{4} \\ 0.4142 + j & -\frac{3\pi}{4} \le \omega < -\frac{\pi}{4} \\ 1.4142 + j1.4142 & -\frac{\pi}{4} \le \omega < \frac{\pi}{4} \\ 1 + j0.4142 & \frac{\pi}{4} \le \omega < \frac{3\pi}{4} \\ 1 - j & \frac{3\pi}{4} \le \omega < \pi \end{cases} \tag{A.7}$$

$$\begin{aligned} \phi_2(n) &= \frac{1}{2\pi n}\Big[2\big(\cos(\frac{3\pi}{4}n) - \sin(\frac{3\pi}{4}n) - (-1)^n\big) + (-1 + e^{j\frac{\pi}{2}n}) \times \\ &\quad \big((0.4142 - j)e^{j\frac{\pi}{4}n} + (1 - j0.4142)e^{-j\frac{3\pi}{4}n} + (1.4142 - j1.4142)e^{-j\frac{\pi}{4}n}\big)\Big] \end{aligned} \tag{A.8}$$

for $n \neq 0$ and $\phi_2(0) = 0.9571 + j0.7071$,

$$h_2(n) = \phi_2(n + 2d_2). \tag{A.9}$$

$$\Phi_3(e^{j\omega}) = \begin{cases} 0.7071 + j0.7071 & -\pi \leq \omega < -\frac{3\pi}{4} \\ 0.2929 + j0.7071 & -\frac{3\pi}{4} \leq \omega < -\frac{\pi}{4} \\ j1.4142 & -\frac{\pi}{4} \leq \omega < \frac{\pi}{4} \\ -0.7071 + j1.7071 & \frac{\pi}{4} \leq \omega < \frac{3\pi}{4} \\ -0.7071 + j0.7071 & \frac{3\pi}{4} \leq \omega < \pi \end{cases} \tag{A.10}$$

$$\begin{aligned} \phi_3(n) &= \frac{1}{2\pi n}\Big[(-1 + e^{j\frac{\pi}{4}n})\big((0.7071 + j0.7071)e^{j\frac{3\pi}{4}n} \\ &\quad +(0.7071 - j0.7071)(-1)^n\big) + (-1 + e^{j\frac{\pi}{2}n})\big((1.7071 + j0.7071)e^{j\frac{\pi}{4}n} \\ &\quad +(0.7071 - j0.2929)e^{-j\frac{3\pi}{4}n} + 1.4142e^{-j\frac{\pi}{4}n}\big)\Big] \end{aligned} \tag{A.11}$$

for $n \neq 0$ and $\phi_3(0) = -0.1036 + j1.1339$,

$$h_3(n) = \phi_3(n + 2d_3). \tag{A.12}$$

Appendix B

Impulse Responses of the Gradient Filters for the Two-Channel TIADC

For the two-channel TIADC, first-order filter expansions (5.12 – 5.13) involve filters

$$\begin{aligned} H_{0,0}(e^{j\omega}) &= H_0(e^{j\omega}; d^0) \\ H_{0,1}(e^{j\omega}) &= \frac{\partial}{\partial d} H_0(e^{j\omega}; d^0) \\ H_{1,0}(e^{j\omega}) &= H_1(e^{j\omega}; g^0, d^0) \\ H_{1,1}(e^{j\omega}) &= \frac{\partial}{\partial d} H_1(e^{j\omega}; g^0, d^0) \, . \end{aligned}$$

The impulse responses of $H_{0,0}(e^{j\omega})$ and $H_{1,0}(e^{j\omega})$ are given in (3.62–3.66) with the simple substitution d^0 for d. Taking the partial derivatives with respect to d of correction filters (3.62–3.66) and then evaluating at d^0 provides the impulse responses of $H_{0,1}(e^{j\omega})$ and $H_{1,1}(e^{j\omega})$. This gives

$$\Re\{h_{0,1}(n)\} = \Re\{h_{1,1}(n)\} = 0 \, ,$$

$$\begin{aligned} \Im\{h_{0,1}(n)\} &= \pi(2\ell + \mathrm{sgn}(\omega_b)) \csc^2(\pi(2\ell + \mathrm{sgn}(\omega_b))d^0)\delta(n) \\ &\quad + \pi[2\ell \csc^2(2\pi\ell d^0) - (2\ell + \mathrm{sgn}(\omega_b)) \csc^2(\pi(2\ell + \mathrm{sgn}(\omega_b))d^0)] \times \frac{\sin((\pi - |\omega_b|)n)}{\pi n}, \end{aligned} \quad \text{(B.1)}$$

and

$$\begin{aligned}
\Im\{h_{1,1}(n)\} &= \frac{1}{\pi(n+d^0)} \times \Big[(\pi - |\omega_b|)\frac{\cos((\pi - |\omega_b|)(n+d^0))}{\sin(2\pi\ell d^0)} \\
&- 2\pi\ell\frac{\sin((\pi - |\omega_b|)(n+d^0))\cos(2\pi\ell d^0)}{\sin^2(2\pi\ell d^0)} + |\omega_b|\frac{\cos((\pi - |\omega_b|)(n+d^0) - \pi d^0)}{\sin(\pi(2\ell + \mathrm{sgn}(\omega_b))d^0)} \\
&+ \pi(2\ell + \mathrm{sgn}(\omega_b))\sin((\pi - |\omega_b|)(n+d^0) - \pi d^0) \times \frac{\cos(\pi(2\ell + \mathrm{sgn}(\omega_b))d^0)}{\sin^2(\pi(2\ell + \mathrm{sgn}(\omega_b))d^0)}\Big] \\
&- \frac{1}{(n+d^0)^2}\Big[\frac{\sin((\pi - |\omega_b|)(n+d^0))}{\pi\sin(2\pi\ell d^0)} - \frac{\sin((\pi - |\omega_b|)(n+d^0) - \pi d^0)}{\pi\sin(\pi(2\ell + \mathrm{sgn}(\omega_b))d^0)}\Big] .
\end{aligned} \tag{B.2}$$

Appendix C

Linearization of Reconstruction Filters around a General Point (g^p, d^p) Close to the True Parameter (g, d) for the Two-Channel TIADC

The mismatches are given by

$$\gamma = g - g^p$$
$$\delta = d - d^p \ ,$$

and estimated mismatches can be expressed as

$$\hat{\gamma} = \hat{g} - g^p$$
$$\hat{\delta} = \hat{d} - d^p \ ,$$

where $(\hat{g}, \hat{d})$ are estimates of true parameters (g, d). Linearzing the filters $H_0(e^{j\omega}; \hat{d})$ and $H_1(e^{j\omega}; \hat{g}, \hat{d})$ around the point (g^p, d^p) that is close to (g, d), we obtain first-order expansions

$$
\begin{aligned}
H_0(e^{j\omega};\hat{d}) &= H_0(e^{j\omega};d^p+\hat{\delta}) \\
&= \underbrace{H_0(e^{j\omega};d^p)}_{H^p_{0,0}(e^{j\omega})} + \hat{\delta}\,\underbrace{\frac{\partial H_0}{\partial \hat{d}}(e^{j\omega};d^p)}_{H^p_{0,1}(e^{j\omega})}\,, \qquad \text{(C.1)}
\end{aligned}
$$

and

$$
\begin{aligned}
H_1(e^{j\omega};\hat{g},\hat{d}) &= H_1(e^{j\omega};g^p+\hat{\gamma},d^p+\hat{\delta}) \\
&= H_1(e^{j\omega};g^p,d^p) + \hat{\gamma}\frac{\partial H_1}{\partial \hat{g}}(e^{j\omega};g^p,d^p) + \hat{\delta}\frac{\partial H_1}{\partial \hat{d}}(e^{j\omega};g^p,d^p) \\
&= (1-\frac{\hat{\gamma}}{g^p})\,\underbrace{H_1(e^{j\omega};g^p,d^p)}_{H^p_{1,0}(e^{j\omega})} + \hat{\delta}\,\underbrace{\frac{\partial H_1}{\partial \hat{d}}(e^{j\omega};g^p,d^p)}_{H^p_{1,1}(e^{j\omega})}\,, \qquad \text{(C.2)}
\end{aligned}
$$

where the last equality follows from the fact that

$$
\frac{\partial H_1}{\partial \hat{g}}(e^{j\omega};\hat{g},\hat{d}) = -\frac{1}{\hat{g}}H_1(e^{j\omega};\hat{g},\hat{d})\,.
$$

The impulse responses of the filters are given by

$$
\begin{aligned}
\Re\{h^p_{0,0}(n)\} &= \delta(n) \\
\Im\{h^p_{0,0}(n)\} &= -\cot(\pi(2\ell+\mathrm{sgn}(\omega_b))d^p)\delta(n) \\
&\quad +(\cot(\pi(2\ell+\mathrm{sgn}(\omega_b))d^p)-\cot(2\pi\ell d^p))\times\frac{\sin((\pi-|\omega_b|)n)}{\pi n}\,. \qquad \text{(C.3)}
\end{aligned}
$$

$$
\begin{aligned}
\Re\{h^p_{1,0}(n)\} &= 0 \\
\Im\{h^p_{1,0}(n)\} &= \frac{\sin((\pi-|\omega_b|)(n+d^p))}{g^p\pi\sin(2\pi\ell d^p)(n+d^p)} - \frac{\sin((\pi-|\omega_b|)(n+d^p)-\pi d^p)}{g^p\pi\sin(\pi(2\ell+\mathrm{sgn}(\omega_b))d^p)(n+d^p)}\,. \qquad \text{(C.4)}
\end{aligned}
$$

$$
\begin{aligned}
\Re\{h^p_{0,1}(n)\} &= 0 \\
\Im\{h^p_{0,1}(n)\} &= \pi(2\ell + \mathrm{sgn}(\omega_b))\csc^2(\pi(2\ell + \mathrm{sgn}(\omega_b))d^p)\delta(n) \\
&\quad +\pi[2\ell\csc^2(2\pi\ell d^p) - (2\ell + \mathrm{sgn}(\omega_b))\csc^2(\pi(2\ell + \mathrm{sgn}(\omega_b))d^p)] \\
&\quad \times\frac{\sin((\pi - |\omega_b|)n)}{\pi n} \ .
\end{aligned} \tag{C.5}
$$

$$
\begin{aligned}
\Re\{h^p_{1,1}(n)\} &= 0 \\
\Im\{h^p_{1,1}(n)\} &= \frac{1}{g^p\pi(n+d^p)} \times \Big[(\pi - |\omega_b|)\frac{\cos((\pi - |\omega_b|)(n+d^p))}{\sin(2\pi\ell d^p)} \\
&- 2\pi\ell\frac{\sin((\pi - |\omega_b|)(n+d^p))\cos(2\pi\ell d^p)}{\sin^2(2\pi\ell d^p)} + |\omega_b|\frac{\cos((\pi - |\omega_b|)(n+d^p) - \pi d^p)}{\sin(\pi(2\ell + \mathrm{sgn}(\omega_b))d^p)} \\
&+ \pi(2\ell + \mathrm{sgn}(\omega_b))\sin((\pi - |\omega_b|)(n+d^p) - \pi d^p) \times \frac{\cos(\pi(2\ell + \mathrm{sgn}(\omega_b))d^p)}{\sin^2(\pi(2\ell + \mathrm{sgn}(\omega_b))d^p)}\Big] \\
&- \frac{1}{g^p(n+d^p)^2}\Big[\frac{\sin((\pi - |\omega_b|)(n+d^p))}{\pi\sin(2\pi\ell d^p)} - \frac{\sin((\pi - |\omega_b|)(n+d^p) - \pi d^p)}{\pi\sin(\pi(2\ell + \mathrm{sgn}(\omega_b))d^p)}\Big].
\end{aligned} \tag{C.6}
$$

With these filters, the error signal defined in (5.22) can be expressed as

$$
e(n;\hat{g},\hat{d}) = e_0(n;\hat{d}) + e_1(n;\hat{g},\hat{d}) \ , \tag{C.7}
$$

where

$$
e_0(n;\hat{d}) = e^p_{0,0}(n) + \hat{\delta}e^p_{0,1}(n) \tag{C.8}
$$

with

$$
\begin{aligned}
e^p_{0,0}(n) &= x_0(n) * h^p_{0,0}(n) * h_{\mathrm{BP}}(n) \\
e^p_{0,1}(n) &= x_0(n) * h^p_{0,1}(n) * h_{\mathrm{BP}}(n) \ ,
\end{aligned}
$$

and

$$e_1(n;\hat{g},\hat{d}) = \big(1 - \frac{\hat{\gamma}}{g^p}\big)e^p_{1,0}(n) + \hat{\delta}e^p_{1,1}(n) \tag{C.9}$$

with

$$e^p_{1,0}(n) = x_1(n) * h^p_{1,0}(n) * h_{\mathrm{BP}}(n)$$
$$e^p_{1,1}(n) = x_1(n) * h^p_{1,1}(n) * h_{\mathrm{BP}}(n)\ .$$

The partial derivatives needed in the iteration (5.26) are calculated to be

$$\begin{aligned} \frac{\partial}{\partial\hat{g}}e(n;\hat{g},\hat{d}) &= -\frac{1}{g^p}e^p_{1,0}(n) \\ \frac{\partial}{\partial\hat{d}}e(n;\hat{g},\hat{d}) &= e^p_{0,1}(n) + e^p_{1,1}(n)\ . \end{aligned} \tag{C.10}$$

Bibliography

[1] S. Mirabassi and K. Martin, "Classical and modern receiver architectures," *IEEE Communic. Magazine*, Nov. 2000.

[2] J. Rudell, J.-J. Ou, T. Cho, G. Chien, F. Brianti, J. Weldon, and P. Gray, "A 1.9-GHz wide-band IF double conversion CMOS receiver for cordless telephone applications," *IEEE Journal of Solid-State Circuits*, vol. 32, no. 12, pp. 2071–2088, 1997.

[3] B. Razavi, "Design considerations for direct-conversion receivers," *IEEE Transactions on Circuits and Systems II: Analog and Digital Signal Processing*, vol. 44, no. 6, pp. 428–435, 1997.

[4] J. H. Reed, *Software Radio– A Modern Approach to Radio Engineering*. Upper Saddle River, NJ: Prentice Hall, 2002.

[5] S. Daneshgar, Z. Griffith, M. Seo, and M. J. W. Rodwell, "Low distortion 50 GSamples/s track-hold and sample-hold amplifiers," *IEEE J. Solid-State Circuits*, vol. 49, pp. 2114–2126, Oct. 2014.

[6] N. B. Zhang, Z. L. Deng, and J. M. Huang, "A novel tunable band-pass filter using MEMS technology," in *The 2010 IEEE International Conference on Information and Automation*, pp. 1510–1515, 2010.

[7] N. Zhang, Z. Deng, C. Shu, and H. Wang, "Design and analysis of a tunable bandpass filter employing RF MEMS capacitors," *IEEE Electron Device Letters*, vol. 32, no. 10, pp. 1460–1462, 2011.

[8] L. Zhao, M. Miao, J. Bu, and Y. Jin, "A 10–14 GHz RF MEMS tunable bandpass filter," in *2008 9th International Conference on Solid-State and Integrated-Circuit Technology*, pp. 2516–2519, 2008.

[9] K. Kawai, H. Okazaki, and S. Narahashi, "Center frequency and bandwidth tunable filter employing MEMS digitally tunable capacitors," in *2013 Asia-Pacific Microwave Conference Proceedings (APMC)*, pp. 188–190, 2013.

[10] E. Venosa, F. J. Harris, and F. A. N. Palmieri, *Software Radio– Sampling Rate Selection, Design and Synchronization.* New York: Springer, 2012.

[11] A. Kohlenberg, "Exact interpolation of band-limited functions," *J. Applied Physics*, vol. 24, pp. 1432–1436, Dec. 1953.

[12] R. G. Vaughan, N. L. Scott, and D. R. White, "The theory of bandpass sampling," *IEEE Trans. Sig. Proc.*, vol. 39, pp. 1973–1984, Sept. 1991.

[13] J. G. Proakis and D. G. Manolakis, *Digital Signal Processing: Principles, Algorithms, and Applications, 4th edition.* Upper Saddle River, NJ: Prentice-Hall, 2007.

[14] D. A. Linden, "A discussion of sampling theorems," *Proceedings of the IRE*, vol. 47, no. 7, pp. 1219–1226, 1959.

[15] H. Zhang and B. Arigong, "A novel frequency reconfigurable RF Hilbert transformer for real-time analog signal processing," *IEEE Transactions on Circuits and Systems II: Express Briefs*, vol. 70, no. 4, pp. 1361–1365, 2023.

[16] W. Black and D. Hodges, "Time interleaved converter arrays," *IEEE Journal of Solid-State Circuits*, vol. 15, no. 6, pp. 1022–1029, 1980.

[17] C. Su, "Time-interleaved SAR ADC with signal independent background timing calibration," *Thesis (Ph.D.)–University of California, Davis*, 2020.

[18] C. Vogel and H. Johansson, "Time-interleaved analog-to-digital converters: status and future directions," in *2006 IEEE International Symposium on Circuits and Systems*, pp. 4 pp.–3389, 2006.

[19] H. Jin and E. Lee, "A digital-background calibration technique for minimizing timing-error effects in time-interleaved ADCs," *IEEE Transactions on Circuits and Systems II: Analog and Digital Signal Processing*, vol. 47, no. 7, pp. 603–613, 2000.

[20] P. Satarzadeh, "Digital calibration methods for sample-and-hold circuits," *Thesis (Ph.D.)–University of California, Davis*, 2009.

[21] Y.-C. Jenq, "Digital spectra of nonuniformly sampled signals: fundamentals and high-speed waveform digitizers," *IEEE Transactions on Instrumentation and Measurement*, vol. 37, no. 2, pp. 245–251, 1988.

[22] Y.-C. Jenq, "Digital spectra of nonuniformly sampled signals: a robust sampling time offset estimation algorithm for ultra high-speed waveform digitizers using interleaving," *IEEE Transactions on Instrumentation and Measurement*, vol. 39, no. 1, pp. 71–75, 1990.

[23] A. Petraglia and S. Mitra, "Analysis of mismatch effects among A/D converters in a time-interleaved waveform digitizer," *IEEE Transactions on Instrumentation and Measurement*, vol. 40, no. 5, pp. 831–835, 1991.

[24] N. Kurosawa, H. Kobayashi, K. Maruyama, H. Sugawara, and K. Kobayashi, "Explicit analysis of channel mismatch effects in time-interleaved ADC systems," *IEEE Transactions on Circuits and Systems I: Fundamental Theory and Applications*, vol. 48, no. 3, pp. 261–271, 2001.

[25] C. Vogel, "The impact of combined channel mismatch effects in time-interleaved ADCs," *IEEE Transactions on Instrumentation and Measurement*, vol. 54, no. 1, pp. 415–427, 2005.

[26] M. El-Chammas and B. Murmann, "General analysis on the impact of phase-skew in time-interleaved ADCs," *IEEE Transactions on Circuits and Systems I: Regular Papers*, vol. 56, no. 5, pp. 902–910, 2009.

[27] B. Razavi, "Problem of timing mismatch in interleaved ADCs," in *Proceedings of the IEEE 2012 Custom Integrated Circuits Conference*, pp. 1–8, 2012.

[28] Y. Feng, H. Deng, Q. Fan, R. Zhang, P. Bikkina, and J. Chen, "A 6-b 20-GS/s 2-way time-interleaved flash ADC with automatic comparator offset calibration in 28-nm FDSOI," in *2020 IEEE International Symposium on Circuits and Systems (ISCAS)*, pp. 1–4, 2020.

[29] K. Dyer, D. Fu, S. Lewis, and P. Hurst, "An analog background calibration technique for time-interleaved analog-to-digital converters," *IEEE Journal of Solid-State Circuits*, vol. 33, no. 12, pp. 1912–1919, 1998.

[30] D. Fu, K. Dyer, S. Lewis, and P. Hurst, "A digital background calibration technique for time-interleaved analog-to-digital converters," *IEEE Journal of Solid-State Circuits*, vol. 33, no. 12, pp. 1904–1911, 1998.

[31] J.-E. Eklund and F. Gustafsson, "Digital offset compensation of time-interleaved ADC using random chopper sampling," in *2000 IEEE International Symposium on Circuits and Systems (ISCAS)*, vol. 3, pp. 447–450 vol.3, 2000.

[32] J. Elbornsson, F. Gustafsson, and J.-E. Eklund, "Blind equalization of time errors in a time-interleaved ADC system," *IEEE Transactions on Signal Processing*, vol. 53, no. 4, pp. 1413–1424, 2005.

[33] S. Huang and B. C. Levy, "Adaptive blind calibration of timing offset and gain mismatch for two-channel time-interleaved A/D converters," *IEEE Trans. Circuits Syst. I*, vol. 53, pp. 1278–1288, June 2006.

[34] V. Divi and G. W. Wornell, "Blind calibration of timing skew in time-interleaved analog-to-digital converters," *IEEE Journal of Selected Topics in Signal Processing*, vol. 3, no. 3, pp. 509–522, 2009.

[35] Y. A. Tavares, S. Kim, and M. Lee, "A background M-channel time-interleaved ADC calibration for multilevel modulations based on the probability density function difference and a greedy algorithm," *IEEE Transactions on Signal Processing*, vol. 70, pp. 4140–4155, 2022.

[36] T.-H. Tsai, P. J. Hurst, and S. H. Lewis, "Bandwidth mismatch and its correction in time-interleaved analog-to-digital converters," *IEEE Trans. Circuits Syst. II*, vol. 53, pp. 1133–1137, Oct. 2006.

[37] P. Satarzadeh, B. C. Levy, and P. J. Hurst, "Adaptive semiblind calibration of bandwidth mismatch for two-channel time-interleaved ADCs," *IEEE Trans. Circuits Syst. I*, vol. 56, pp. 2075–2088, Sept. 2009.

[38] C. Vogel and S. Mendel, "A flexible and scalable structure to compensate frequency response mismatches in time-interleaved ADCs," *IEEE Transactions on Circuits and Systems I: Regular Papers*, vol. 56, no. 11, pp. 2463–2475, 2009.

[39] H. Johansson, "A polynomial-based time varying filter structure for the compensation of frequency-response mismatch errors in time-interleaved ADCs," *Selec. Topics in Signal Proc.*, vol. 3, pp. 384–396, 2009.

[40] S. Saleem and C. Vogel, "Adaptive blind background calibration of polynomial-represented frequency response mismatches in a two-channel time-interleaved ADC," *IEEE Trans. Circuits Syst. I*, vol. 58, pp. 1300–1310, June 2011.

[41] Y. Park, J. Kim, and C. Kim, "A scalable bandwidth mismatch calibration technique for time-interleaved ADCs," *IEEE Transactions on Circuits and Systems I: Regular Papers*, vol. 63, no. 11, pp. 1889–1897, 2016.

[42] A. V. Oppenheim and R. W. Schafer, *Discrete-Time Signal Processing, 3rd edition*. USA: Prentice Hall Press, 2009.

[43] B. Lathi and R. Green, *Signal Processing and Linear Systems, 2nd edition*. USA: Oxford University Press, 2021.

[44] S. Mallat, *A Wavelet Tour of Signal Processing, Third Edition: The Sparse Way*. USA: Academic Press, Inc., 2009.

[45] M. J. Lighthill, *An introduction to Fourier analysis and generalised functions*. Cambridge monographs on mechanics, Cambridge: Cambridge University Press, 1958.

[46] E. T. Whittaker, "On the functions which are represented by the expansions of the interpolation-theory," *Proceedings of the Royal Society of Edinburgh*, vol. 35, p. 181–194, 1915.

[47] H. Nyquist, "Certain topics in telegraph transmission theory," *Transactions of the American Institute of Electrical Engineers*, vol. 47, no. 2, pp. 617–644, 1928.

[48] V. A. Kotel'nikov, "On the carrying capacity of the "Ether" and wire in telecommunications," in *Material for the First All-Union Conference on Questions of Communication (Russian), Izd. Red. Upr. Svyzai RKKA, Moscow*, 1933.

[49] H. Raabe, "Untersuchungen an der wechselzeitigen mehrfachübertragung (multiplexübertragung)," *Dissertation, TH Berlin*, 1939.

[50] C. E. Shannon, "A mathematical theory of communication," *The Bell System Technical Journal*, vol. 27, no. 3, pp. 379–423, 1948.

[51] H. Ogawa, "Sampling theory and Isao Someya: A historical note," *Sampling Theory in Signal and Image Processing*, vol. 5, 2006.

[52] K. Ogura, "On a certain transcendetal integral function in the theory of interpolation," *Tôhoku Math J.*, vol. 17, pp. 64–72, 1920.

[53] P. Butzer, P. Ferreira, J. Higgins, S. Saitoh, G. Schmeisser, and R. Stens, "Interpolation and sampling: E.T. Whittaker, K. Ogura and their followers," *J Fourier Anal Appl*, vol. 17, pp. 320–354, 2011.

[54] P. L. Butzer, S. Ries, and R. L. Stens, *Shannon's Sampling Theorem Cauchy's Integral Formula, and Related Results*, pp. 363–377. Basel: Birkhäuser Basel, 1984.

[55] M. Vetterli and J. Kovačevic, *Wavelets and Subband Coding*. USA: Prentice-Hall, Inc., 1995.

[56] A. Papoulis, "Generalized sampling expansion," *IEEE Transactions on Circuits and Systems*, vol. 24, no. 11, pp. 652–654, 1977.

[57] M. Unser, "Sampling-50 years after Shannon," *Proceedings of the IEEE*, vol. 88, no. 4, pp. 569–587, 2000.

[58] P. Vaidyanathan, "Generalizations of the sampling theorem: Seven decades after Nyquist," *IEEE Transactions on Circuits and Systems I: Fundamental Theory and Applications*, vol. 48, no. 9, pp. 1094–1109, 2001.

[59] Y. C. Eldar, *Sampling Theory: Beyond Bandlimited Systems*. Cambridge University Press, 2015.

[60] P. P. Vaidyanathan, *Multirate Systems and Filter Banks*. USA: Prentice-Hall, Inc., 1993.

[61] M. Mottaghi-Kashtiban, S. Farazi, and M. G. Shayesteh, "Optimum structures for sample rate conversion from CD to DAT and DAT to CD using multistage interpolation

and decimation," in *2006 IEEE International Symposium on Signal Processing and Information Technology*, pp. 633–637, 2006.

[62] J. Dugundji, "Envelopes and pre-envelopes of real waveforms," *IRE Transactions on Information Theory*, vol. 4, no. 1, pp. 53–57, 1958.

[63] R. Boute, "The geometry of bandpass sampling: A simple and safe approach [lecture notes]," *IEEE Signal Processing Magazine*, vol. 29, no. 4, pp. 90–96, 2012.

[64] B. C. Levy, *EEC263 Lecture Notes on Optimal Filtering, Adaptive Filtering and Parameter Learning*. Dept of Electrical and Computer Eng, UC Davis, Dec 2019.

[65] S. Boyd and L. Vandenberghe, *Convex Optimization*. Cambridge University Press, March 2004.

[66] M. Bartholomew-Biggs, *Nonlinear Optimization with Engineering Applications*. Springer New York, NY, 2008.

[67] J. Nocedal and S. J. Wright, *Numerical Optimization*. New York, NY, USA: Springer, 2e ed., 2006.

[68] H. Robbins and S. Monro, "A stochastic approximation method," *Annals Math. Stat.*, vol. 22, pp. 400–407, 1951.

[69] A. Sayed, *Adaptive Filters*. John Wiley & Sons, Ltd, 2008.

[70] L. Ljung, "Analysis of recursive stochastic algorithms," *IEEE Transactions on Automatic Control*, vol. 22, no. 4, pp. 551–575, 1977.

[71] L. Ljung and T. Soderstrom, *Theory and Practice of Recursive Identification*. Cambridge, MA: MIT Press, 1983.

[72] A. Benveniste, M. Métivier, and P. Priouret, *Adaptive Algorithms and Stochastic Approximations*. Berlin: Springer Verlag, 1990.

[73] T. Kida and T. Kuroda, "Relations between the possibility of restoration of bandpass-type band-limited waves by interpolation and arrangement of sampling points," *Electronics and Communications in Japan (Part I: Communications)*, vol. 69, no. 1, pp. 1–10, 1986.

[74] A. J. Coulson, "A generalization of nonuniform bandpass sampling," *IEEE Trans. Sig. Proc.*, vol. 41, pp. 694–704, Mar. 1995.

[75] Y.-P. Lin and P. Vaidyanathan, "Periodically nonuniform sampling of bandpass signals," *IEEE Transactions on Circuits and Systems II: Analog and Digital Signal Processing*, vol. 45, no. 3, pp. 340–351, 1998.

[76] M. Wahab and B. C. Levy, "Direct complex envelope sampling of bandpass signals with M-Channel Time-Interleaved ADCs," *IEEE Transactions on Signal Processing*, vol. 70, pp. 4804–4819, 2022.

[77] A. J. Laub, *Matrix Analysis for Scientists And Engineers*. Philadelphia, PA: SIAM, 2004.

[78] Z. Cvetkovic, I. Daubechies, and B. F. Logan, "Single-bit oversampled A/D conversion with exponential accuracy in the bit rate," *IEEE Transactions on Information Theory*, vol. 53, no. 11, pp. 3979–3989, 2007.

[79] R. Venkataramani and Y. Bresler, "Sub-Nyquist sampling of multiband signals: perfect reconstruction and bounds on aliasing error," in *Proceedings of the 1998 IEEE International Conference on Acoustics, Speech and Signal Processing, ICASSP '98 (Cat. No.98CH36181)*, vol. 3, pp. 1633–1636 vol.3, 1998.

[80] R. Venkataramani and Y. Bresler, "Perfect reconstruction formulas and bounds on aliasing error in sub-Nyquist nonuniform sampling of multiband signals," *IEEE Transactions on Information Theory*, vol. 46, no. 6, pp. 2173–2183, 2000.

[81] R. Venkataramani and Y. Bresler, "Optimal sub-Nyquist nonuniform sampling and reconstruction for multiband signals," *IEEE Transactions on Signal Processing*, vol. 49, no. 10, pp. 2301–2313, 2001.

[82] H. Landau, "Necessary density conditions for sampling and interpolation of certain entire functions," *Acta Mathematica*, vol. 117, pp. 37–52, 1967.

[83] T. Aulin and C. Sundberg, "Continuous phase modulation - Part I: Full response signaling," *IEEE Transactions on Communications*, vol. 29, no. 3, pp. 196–209, 1981.

[84] J. G. Proakis and M. Salehi, *Digital Communications, 5th edition*. New York, NY: McGraw-Hill Education, 2007.

[85] O. D. Grace and S. P. Pitt, "Quadrature sampling of high frequency waveforms," *J. Acoust. Soc. Amer.*, vol. 44, pp. 1453–1454, 1968.

[86] J. L. Brown, Jr., "On quadrature sampling of bandpass signals," *IEEE Trans. Aerospace Elec. Syst.*, vol. 15, May 1979.

[87] J. L. Brown, Jr., "A simplified approach to optimum quadrature sampling," *J. Acoust. Soc. Amer.*, vol. 67, pp. 1659–1662, May 1980.

[88] Y.-R. Sun and S. Signell, "Generalized bandpass sampling with FIR filtering," in *Proc. 2005 IEEE Internat. Symp. Circuits Systems*, (Kobe, Japan), pp. 4429–4432, May 2005.

[89] Y.-R. Sun, *Generalized bandpass sampling receivers of software defined radio*. PhD thesis, Royal Institute of Technology, Stockholm, Sweden, 2006.

[90] M. Wahab and B. C. Levy, "Quadrature filter approximation for reconstructing the complex envelope of a bandpass signal sampled directly with a two-channel TIADC," *IEEE Transactions on Circuits and Systems II: Express Briefs*, vol. 69, no. 6, pp. 3017–3021, 2022.

[91] A. G. Dempster, "Quadrature bandpass sampling rules for single- and multiband communications and satellite navigation receivers," *IEEE Trans. Aerospace Elec. Syst.*, vol. 47, Oct. 2011.

[92] W. Namgoong, "Finite-length synthesis filters for non-uniformly time-interleaved analog-to-digital converter," in *Proc. 2002 IEEE Internat. Conf. Circuits and Systems*, vol. 4, (Scottsdale, AZ), pp. 815–818, May 2002.

[93] F. Xu, "Perfect data reconstruction algorithm of time interleaved ADC," in *Proc. 2006 IEEE Internat. Test Conference*, (Santa Clara, CA), pp. 1–6, 2006.

[94] M. Seo, M. Rodwell, and U. Madhow, "Comprehensive digital correction of mismatch errors for a 400-Msamples/s 80-dB SFDR time-interleaved analog-to-digital converter," *IEEE Transactions on Microwave Theory and Techniques*, vol. 53, no. 3, pp. 1072–1082, 2005.

[95] M. Chakravarthi and C. M. Bhuma, "Detection and correction of sampling-time-errors in an N-channel time-interleaved ADC using genetic algorithm," in *2017 14th IEEE India Council International Conference (INDICON)*, pp. 1–6, 2017.

[96] Y. A. Tavares and M. Lee, "A foreground calibration for M-channel time-interleaved analog-to-digital converters based on genetic algorithm," *IEEE Transactions on Circuits and Systems I: Regular Papers*, vol. 68, no. 4, pp. 1444–1457, 2021.

[97] V. Divi and G. Wornell, "Signal recovery in time-interleaved analog-to-digital converters," in *2004 IEEE International Conference on Acoustics, Speech, and Signal Processing*, vol. 2, pp. ii–593, 2004.

[98] V. Divi and G. Wornell, "Scalable blind calibration of timing skew in high-resolution time-interleaved ADCs," in *2006 IEEE International Symposium on Circuits and Systems*, pp. 4 pp.–3393, 2006.

[99] S. Huang and B. C. Levy, "Blind calibration of timing offsets for four-channel time-interleaved A/D converters," *IEEE Trans. Circuits Syst. I*, vol. 54, pp. 863–876, Apr. 2007.

[100] S. Saleem and C. Vogel, "LMS-based identification and compensation of timing mismatches in a two-channel time-interleaved analog-to-digital converter," in *Norchip 2007*, pp. 1–4, 2007.

[101] C. Vogel, S. Saleem, and S. Mendel, "Adaptive blind compensation of gain and timing mismatches in M-channel time-interleaved ADCs," in *2008 15th IEEE International Conference on Electronics, Circuits and Systems*, pp. 49–52, 2008.

[102] P. Satarzadeh, B. C. Levy, and P. J. Hurst, "A parametric polyphase domain approach to blind calibration of timing mismatches for M-channel time-interleaved ADCs," in *Proc. 2010 IEEE Internat. Symp. Circuits Systems*, (Paris, France), pp. 4053–4056, May 2010.

[103] J. Elbornsson, F. Gustafsson, and J.-E. Eklund, "Blind adaptive equalization of mismatch errors in a time-interleaved A/D converter system," *IEEE Transactions on Circuits and Systems I: Regular Papers*, vol. 51, no. 1, pp. 151–158, 2004.

[104] D. Marelli, K. Mahata, and M. Fu, "Linear LMS compensation for timing mismatch in time-interleaved ADCs," *IEEE Transactions on Circuits and Systems I: Regular Papers*, vol. 56, no. 11, pp. 2476–2486, 2009.

[105] M. Seo, M. Rodwell, and U. Madhow, "Blind correction of gain and timing mismatches for a two-channel time-interleaved analog-to-digital converter," in *Conference Record of the Thirty-Ninth Asilomar Conference on Signals, Systems and Computers, 2005.*, pp. 1121–1125, 2005.

[106] M. Yin and Z. Ye, "First order statistic based fast blind calibration of time skews for time-interleaved ADCs," *IEEE Transactions on Circuits and Systems II: Express Briefs*, vol. 67, no. 1, pp. 162–166, 2020.

[107] Y. X. Zou and X. J. Xu, "Blind timing skew estimation using source spectrum sparsity in time-interleaved ADCs," *IEEE Transactions on Instrumentation and Measurement*, vol. 61, no. 9, pp. 2401–2412, 2012.

[108] S. Liu, N. Lyu, J. Cui, and Y. Zou, "Improved blind timing skew estimation based on spectrum sparsity and ApFFT in time-interleaved ADCs," *IEEE Transactions on Instrumentation and Measurement*, vol. 68, no. 1, pp. 73–86, 2019.

[109] F. Harris, X. Chen, E. Venosa, and F. A. N. Palmieri, "Two-channel TI-ADC for communication signals," in *Proc. 2001 IEEE 12th Internat. Workshop on Signal Proc. Advances in Wireless communications (SPAWC' 11)*, (San Francisco, CA), pp. 576–580, June 2011.

[110] F. J. Harris, "Artifact-corrected time-interleaved ADC." US Patent No. 8,957,798, Feb. 2015.

[111] M. Waltari, "Time-interleaved analog-to-digital converter for signals in any Nyquist zone." US Patent No. 8,654,000, Feb. 2014.

[112] H. L. Duc, C. Jabbour, P. Desgreys, O. Jamin, and N. Van Tam, "A fully digital background calibration of timing skew in undersampling TI-ADC," in *2014 IEEE 12th International New Circuits and Systems Conference (NEWCAS)*, 2014.

[113] H. Le Duc, D. M. Nguyen, C. Jabbour, T. Graba, P. Desgreys, O. Jamin, and V. T. Nguyen, "All-digital calibration of timing skews for TIADCs using the polyphase decomposition," *IEEE Transactions on Circuits and Systems II: Express Briefs*, vol. 63, no. 1, pp. 99–103, 2016.

[114] H. Le Duc, D. M. Nguyen, C. Jabbour, P. Desgreys, O. Jamin, and V. Tam Nguyen, "Fully digital feedforward background calibration of clock skews for sub-sampling TIADCs using the polyphase decomposition," *IEEE Transactions on Circuits and Systems I: Regular Papers*, vol. 64, no. 6, pp. 1515–1528, 2017.

[115] V.-T. Ta, V.-P. Hoang, V.-P. Pham, and C.-K. Pham, "An improved all-digital background calibration technique for channel mismatches in high speed time-interleaved analog-to-digital converters," *Electronics*, vol. 9, no. 1, 2020.

[116] M. Hu and P. Yi, "Digital calibration for gain, time skew, and bandwidth mismatch in under-sampling time-interleaved system," *Applied Sciences*, vol. 12, no. 21, 2022.

[117] J.-A. Vernhes, M. Chabert, B. Lacaze, G. Lesthievent, R. Baudin, and M.-L. Boucheret, "Adaptive estimation and compensation of the time delay in a periodic non-uniform sampling scheme," in *2015 International Conference on Sampling Theory and Applications (SampTA)*, pp. 473–477, 2015.

[118] J.-A. Vernhes, M. Chabert, B. Lacaze, G. Lesthievent, R. Baudin, and M.-L. Boucheret, "Blind estimation of unknown time delay in periodic non-uniform sampling: Application to desynchronized time interleaved-ADCs," in *2016 IEEE International Conference on Acoustics, Speech and Signal Processing (ICASSP)*, pp. 4478–4482, 2016.

[119] D. R. Fuhrmann, "Complex random variables and stochastic processes." in V. Madisetti and D. Williams, eds., *Digital Signal Processing Handbook*, CRC Press, 1998.

[120] B. C. Levy, *Random Processes with Applications to Circuits and Communications*. Springer, 2020.

[121] W. Gardner, *Introduction to Random Processes: With Applications to Signals and Systems*. Macmillan Publishing Company, 1986.

[122] J. Leskow and A. Weron, "Ergodic behavior and estimation for periodically correlated processes," *Statistics & Probability Letters*, vol. 15, no. 4, pp. 299–304, 1992.

[123] D. M. Akos, M. Stockmaster, J. B. Y. Tsui, and J. Caschera, "Direct bandpass sampling of multiple distinct RF signals," *IEEE Trans. Commun.*, vol. 47, pp. 983–988, July 1999.